Vibrational spectroscopy and density functional theory calculations on biological molecules

Dissertation

zur Erlangung des

Naturwissenschaftlichen Doktorgrades

der Bayerischen Julius-Maximilians-Universität Würzburg

vorgelegt von

Niculina Peica

aus

Potcoava, Rumänien

Würzburg 2006

II

Eingerichtet am: ……………………………………………………….

bei der Fakultät für Chemie und Pharmazie

1. Gutachter: ……………………………………………………….

2. Gutachter: ……………………………………………………….

der Dissertation

1. Prüfer ……………………………………………………….

2. Prüfer ……………………………………………………….

3. Prüfer ……………………………………………………….

des Öffentlichen Promotionskolloquiums

Tag der mündlichen Prüfung: …………………………………………….

Doktorurkunde ausgehändigt am: ……..…………………………………...

in memory of my father

to my family

IV

Table of Contents

Abbreviations and Symbols

°	degree
Å	1 Ångstrom = 10^{-10} m
a_0	atomic unit of length = 0.529 177 2108 x 10^{-10} m
Ag	silver
amu	atomic mass unit = 1.660 538 73 x 10^{-27} kilograms
ANT	unbuffered aspirin
AO	Atomic Orbital
ASA	buffered aspirin
Au	gold
a.u.	atomic unit of energy = 27.211 3845 eV=4.359 744 17 x 10^{-18} Joules
c	speed of light in vacuum = 299 792 458 m·s^{-1}
ca.	circa
cal	calorie = 4.184 Joules
Calcd.	calculated
CCD	Charge-Coupled Device
CGTO	Contracted Gaussian Type Orbitals
CQ	chloroquine diphosphate
CT	Charge Transfer
DFT	Density Functional Theory
DNA	Deoxyribonucleic Acid
e	elementary charge = 1.602 176 53 x 10^{-19} Coulomb
ECP	Effective Core Potential
e.g.	*exempli gratia* (for example)

X *Abbreviations and Symbols*

EM	Electromagnetic
EryB	erythrosine B
et al.	et alii (and others)
etc.	etcetera
eV	1 electron Volt = 1.602 176 53 x 10^{-19} Joules
Exp.	experimental
E102	tartrazine
E127	erythrosine B
E132	indigo carmine
E211	sodium benzoate
E621	monosodium glutamate
FDA	Food and Drug Administration
freqs.	frequencies
FT	Fourier Transform
FWHM	Full Width at Half Maximum
GTO	Gaussian Type Orbitals
h	Planck's constant (h = 6.626 068 76 x 10^{-34} Joule·s)
HAOA	5-aminoorotic acid
HF	Hartree-Fock
HOA	orotic acid
HPy	3,5-pyrazoledicarboxylic acid
Hz	Hertz
i.e.	*id est* (that is)
IR	infrared
J	Joule = $m^2 \cdot Kg \cdot s^{-2}$
KS	Kohn-Sham
LANL2DZ	Los Alamos National Laboratory 2 Double-Zeta
Ln	Lanthanide
LSDA	Local Spin Density Approximation
M	molarity = $mol \cdot l^{-1}$

mg	milligram = 10^{-3} g
MIR	mid-infrared spectroscopy
ml	milliliter = 10^{-3} l
MO	Molecular Orbital
MP	Møller-Plesset
MQ	mefloquine hydrochloride
MS	Mass Spectrometry
MSG	monosodium glutamate
mW	milliwatt
NIR	near-infrared spectroscopy
nm	nanometer = 10^{-9} m
NMR	Nuclear Magnetic Resonance
NPA	Natural Population Analysis
ORC	Oxidation-Reduction Cycle
PGTO	Primitive Gaussian Type Orbitals
pk_a	acid-dissociation constant
pm	picometer = 10^{-12} m
PZ	Perdew and Zunger
RNA	Ribonucleic acid
RR	Resonance Raman
RRS	Resonance Raman Scattering
SCF	Self-Consistent Field
SERS	Surface-Enhanced Raman Scattering
SERRS	Surface-Enhanced Resonance Raman Scattering
S/N	signal-to-noise ratio
STO	Slater Type Orbitals
THF	tetrahydrofuran
UV	Ultra-Violet
v.a.	vor allem
VIS	visible

XII *Abbreviations and Symbols*

vs.	versus
VWN	Vosko, Wilk, and Nusair
w/v	weigh-to-volume ratio
XC	Exchange and Correlation
YAG	Yttrium Aluminum Garnet
z.B.	Zum Beispiel
μm	micrometer = 10^{-6} m

Chapter I

Introduction

"Imagination is more important than knowledge…"

Albert Einstein (1879-1955)

"In physics, your solution should convince a reasonable person. In math, you have to convince a person who's trying to make trouble. Ultimately, in physics, you're hoping to convince Nature. And I've found Nature to be pretty reasonable."

Franck Wilczek (1951-)

Infrared (IR) and Raman spectroscopy are among the most widely used techniques in the physical and natural sciences today. Vibrational spectroscopy, including IR and Raman spectroscopy, has both a long and interesting history and an illustrious record of contributions to science. Spectroscopy in the pharmaceutical industry is dominated by techniques such as nuclear magnetic resonance (NMR) and mass spectrometry (MS) for the elucidation of chemical structures. Despite this, the versatility of infrared spectroscopy ensures it still remains a key technique in quality control laboratories, and in applications where solid form characterization or minimal sample preparation is a necessity. Raman spectroscopy has many uses in the pharmaceutical and chemical industry, but its strengths is in solid form analysis. It is regularly used to identify compounds, and results are used in the release of pharmaceutical and chemical products.

Vibrational spectroscopy can be applied to both qualitative and quantitative analysis of foods and food products. Within the food industry, the primary applications of vibrational spectroscopy are related to quantitative analysis by near-infrared (NIR) spectroscopy of the major components found in foods. However, with recent advances in technology associated with Fourier transform (FT) instrumentation, sampling, laser sources as well as detectors, new avenues of applications have been opened to apply mid-infrared (MIR) and Raman spectroscopy for quantitative analysis as well as qualitative analysis to characterize food components and to investigate their structure-function relationships[65].

Raman spectroscopy has long been regarded as a valuable diagnosis tool for investigation of chemical and biological samples. Based on vibrational transitions, the fine structure inherent in Raman spectra enables the elucidation of molecular structure, surface processes, and interface reactions. The Raman process is associated with a low photon scattering efficiency because of its two-photon nature, although multichannel photon detectors enhance Raman sensitivities. Due to the low scattering cross-section and the possibility of high background-fluorescence interference, the application of Raman spectroscopy to trace analysis is limited. Therefore, there was a great need for a technique that can overcome this limitation. The renewal of interest has been, in large part, due to the observations of enormous Raman signal enhancements for molecules adsorbed on special metallic surfaces. The name of this phenomenon is surface-enhanced Raman scattering (SERS), which was in 1974 discovered on pyridine by Fleischmann and coworkers[86]. The groups of Jeanmaire and Van Duyne[87], and Albrecht and Creighton[88] later confirmed the enhancement up to 8 orders of magnitude and attributed the effect to complex surface enhancement processes, which, to this day, are still under intensive investigation. Recent reports have cited the SERS enhancements from 13 to 15 orders of magnitude, thus demonstrating the potential for single-molecule detection with SERS[133]. Lately, was discussed surface-enhanced Raman scattering at extremely high enhancement levels that can occur for molecules attached to silver and gold nanoclusters. Strongly enhanced and highly confined local optical fields enable surface-enhanced Stokes and anti-Stokes Raman spectroscopy of single molecules even under nonresonant excitation conditions as well as extremely large effective cross sections in two-photon excited Raman spectroscopy. The ability for very sensitive and spatially confined molecular structural probing makes gold and silver nanoclusters very promising tools for studies of small structures in biological materials, (cellular compartments)[133].

But, the direct assignment of infrared or Raman bands of relatively complex molecules, as biological or lanthanide complexes of biological molecules, is quite difficult. Theoretical calculations may certainly assist to obtain a deeper understanding of the vibrational spectra of such molecules. In the last twenty years, quantum mechanical methods have been developed which now are indispensable complements of experimental studies in chemistry. Particularly, recent developments in Density Functional Theory (DFT) have been made through this method, since they are much less computationally demanding and take account of the effects of electron correlations. Because DFT includes corrections to Hartree-Fock (HF) energies for the correlation energy, the structures and relative energies become much more reliable, while computations using Kohn-Sham orbitals become simpler.

This work consists of 8 chapters, which cover the vibrational spectroscopy beginning with the theory and instrumentation, continuing with the experimental setup and probes description, and completing with results and discussions of the experiments.

The first chapter of this work introduces Raman spectroscopy as a dominant technique used in pharmaceutical and chemical industry. The theoretical background regarding vibrational spectroscopy (IR and Raman) is accounted for in the second chapter of this work, while the samples presentation, the experimental procedures, and the description of the apparatus together with the computational details are briefly specified in the third chapter.

The fourth chapter investigates the concentration dependent wavenumber shifts and linewidth changes of tetrahydrofuran in a binary system. Many of the applications in food science rely heavily on Raman spectroscopy, often preceding the biomedical applications. The characterization and identification of food additives using Raman, surface-enhanced Raman spectroscopy, and theoretical calculations is in detail depicted in the fifth chapter, whereas in the sixth and seventh chapters the monitoring of several medicines and various lanthanide complexes with anticancer properties, respectively, employing IR and Raman techniques are treated. These last two chapters address applications of vibrational spectroscopy to pharmaceutical products, and include the use of vibrational spectroscopy in combinatorial chemistry and density functional theory, a modality increasingly used by the pharmaceutical industry for the discovery if new pharmacologically active substances.

Chapter II

_____

Theoretical background

_____

Theory...
"An extremely well-substantiated explanation of some
aspects of the natural world that incorporates facts, laws,
predictions, and tested hypotheses."
(Albert Einstein, 1916)

II.1 Ultra-violet and visible spectroscopy

"The first event was God Said „let there be light". But Light is really the core of spectroscopy. Hard to describe what it is – but if you can see, you know it is there. Scientists call it electromagnetic radiation, and have described it waves with electric and magnetic components. They include not only visible light, but slow & wide radio waves and fast & narrow gamma rays."

("Secrets of Spectroscopy Revealed", Sue Cardinal, librarian at the University of Rochester, June 11, 2002)

II.1.1 Basic concepts of electronic spectroscopy

The electronic spectra of molecules are found in the wavelength range 100-800 nm of the electromagnetic spectrum. The electromagnetic radiation is characterized by a wavelength or frequency. The wavelength is defined as the distance between adjacent peaks and may be designated in meters, centimeters or nanometers. The frequency is the number of wave cycles that past a fixed point per unit of time, and is usually given in cycles per second, or Hertz (Hz).
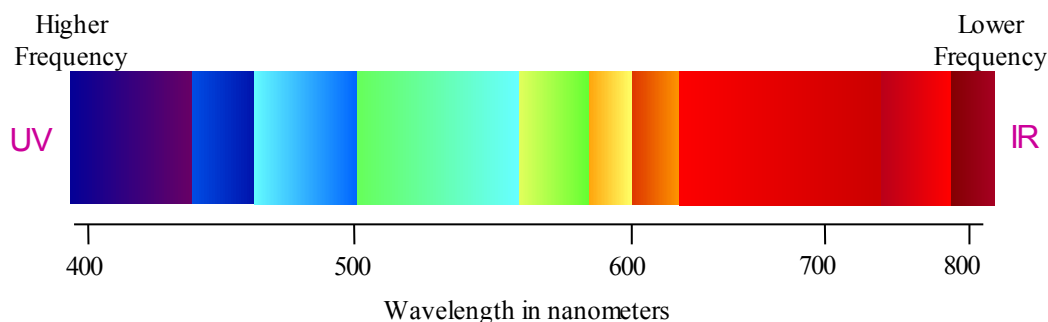
Figure II.1.1.1. The VIS spectrum from higher to lower frequencies.

The UV and VIS radiation interacts with mater causing electronic transitions (promotion of electrons from the ground state to a high energy state). The VIS region to which the human eye is sensitive, corresponds to the range of wavelength between 400 nm and 800 nm. The longest VIS wavelength is red and the shortest is violet (Fig. II.1.1.1). The UV region is subdivided into two spectral regions; the range between 200 nm and 400 nm is referred to as the near UV region, while the region below 200 nm, is called the far or vacuum UV region[1].

The electromagnetic spectrum ranges from very short wavelengths (including gamma and X-rays) to very long wavelengths (including microwaves and broadcast radio waves) (Fig. II.1.1.2)[2]. The electronic spectra are classified in two classes, namely emission and absorption spectra. An emission

spectrum is obtained through the spectroscopic analysis of the light transmitted by an absorbing medium which is placed between the light source and the spectroscope[3].
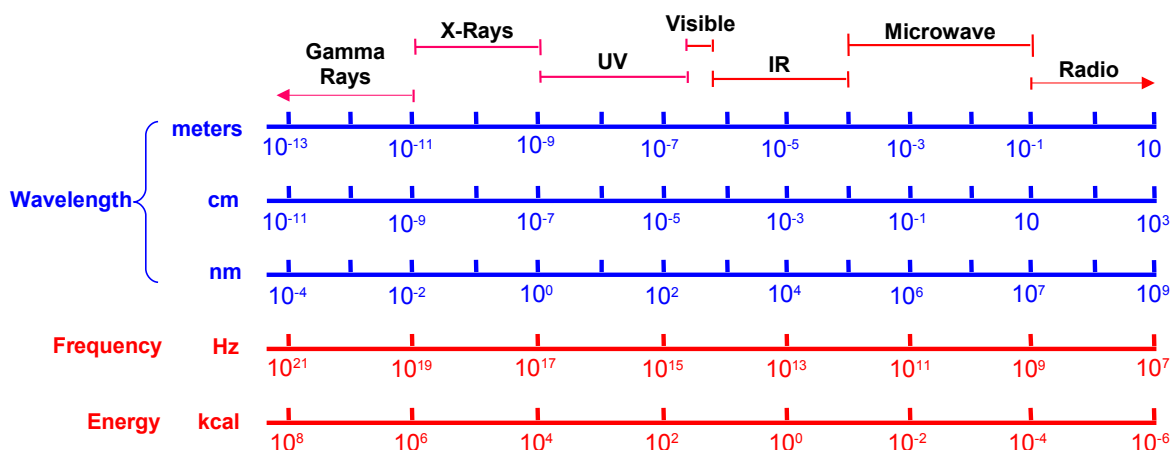
Figure II.1.1.2. The electromagnetic spectrum and the the inverse relationship
between wavelength and frequency.

When a molecule absorbs radiation, its energy increases. This increase is equal to the energy of the photon as expressed by the relation:

$$\Delta E = h \cdot \upsilon = h \cdot c / \lambda$$

where h is the Planck's constant, υ and λ are the frequency and the wavelength of the radiation, respectively, and c is the velocity of light.

Before the development of adequate theory, Beer and Lambert had proposed laws of light absorption. These laws are well-known in their combined form as the *Beer-Lambert law of light absorption*, which states that the fraction of the incident light absorbed is proportional to the number of molecules in the path[4]. That is, if a substance is dissolved in a solvent, the absorption by the solution will be proportional to its molecular concentration, provided the solvent itself does not have any absorption in that region. This law is expressed as:

$$A = log_{10}(I_0/I) = \varepsilon \cdot c \cdot l$$

where A is the absorbance (extinction or optical density), I_0 is the initial light intensity, I is the light intensity after it passes through the sample, ε is the absorption coefficient, l is path length, and c is the concentration (Fig. II.1.1.3). The data on absorption spectra are usually presented as absorption curves.
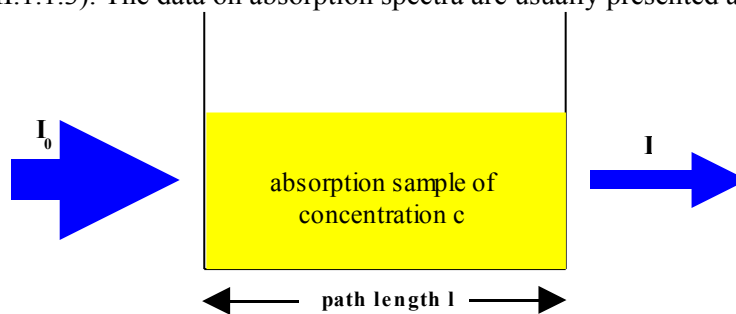
Figure II.1.1.3. The schematic representation of the absorption of light by a sample.

The units of absorption are plotted as ordinates and the units of wavelength as abscissae. The convention normally employed is to plot ε and *log ε* against the wavelength in nm.

The basic parts of any type of spectroscopic equipment are the radiation source, the sample container, the monochromator, the detector and the detector output measuring instrument. In the UV and VIS regions, the sources are incandescent lamps or discharge tubes. Prisms or gratings are used as monochromators. If prisms are used, the prism material will vary from one region of electronic spectra to the other. Calcium fluoride or lithium fluoride prisms are used in the vacuum UV region, while quartz prisms are used in the near UV region. For the VIS region, glass prisms are employed. The eye, the photographic plate, and the photoelectric cells are used as detectors for the VIS region and the last two also for the UV region. The optical system of a typical photoelectric spectrophotometer is shown in its simple form in Fig. II.1.1.4[5].
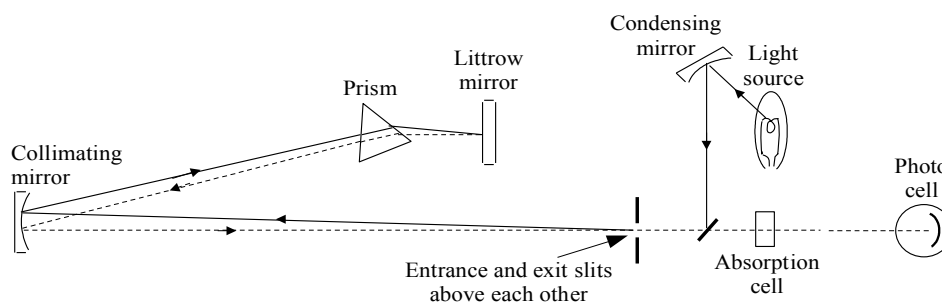
Figure II.1.1.4. Optical system on a simple photoelectric spectrophotometer.

II.1.2 Chromophores and transitions

The absorption of UV or VIS radiation corresponds to the excitation of outer electrons. There are three types of electronic transition, which can be considered (Fig. II.1.2.1):

- transition involving π, σ, and n electrons;
- transition involving charge-transfer electrons;
- transitions involving d and f electrons (not covered in this Unit).
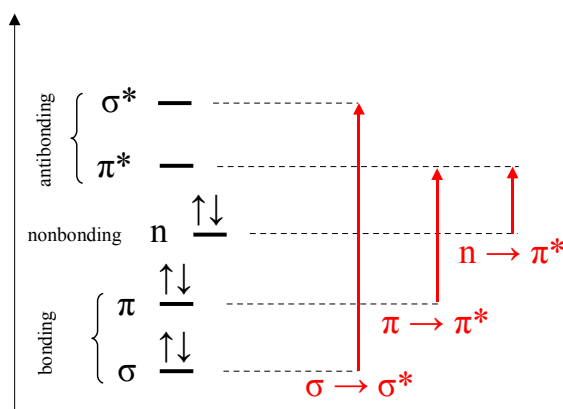
Figure II.1.2.1. Possible electronic transitions of π, σ, and n electrons.

When an atom or molecule absorbs energy, electrons are promoted from their ground state to an excited state. In a molecule, the atoms can rotate and vibrate with respect to each other. These vibrations and rotations also have discrete energy levels, which can be considered as being packed on top of each electronic level.

It has been known for quite some time that colored substances owe their color to the presence of one or more unsaturated linkages. These linkages or groups conferring color on substances were called *chromophores*. Some groups which by themselves did not confer color on a substance were found to increase the coloring power of a chromophore. Such groups were called *auxochromes*. Typical examples of *chromophores* would be, C=C, C=O, N=N etc. and of *auxochromes*, C-Br, C-OH, C-NH$_2$ etc.[5].

If one surveys the data on the electronic spectra of organic molecules, some generalities become evident. Saturated organic molecules do not exhibit any absorption in the near UV and VIS (200-800 nm). Introduction of an *auxochrome* in a saturated system usually shifts the absorption maximum to a longer wavelength.

UV and VIS spectrophotometry can be effectively used for the control of purification and specification of compounds purity. The identity of a synthetic product is often established by comparison of its absorption curve with that of the natural product or another standard sample. The absorption spectra of optically active (*d* or *l*), racemic and inactive isomers are generally found to be similar. Optical isomerism has no effect on λ_{max} or ε_{max}[6]. Whenever two or more readily inconvertible isomers of a substance are in dynamic equilibrium, there will generally be migration of double bonds. The most often encountered tautomerism is between the keto and the enol forms of an oxygen-containing compound. UV and VIS spectrophotometry have been widely used for the quantitative determination of substances. A mixture of substances with widely separated absorption maxima may be readily analyzed using the Beer's law plot for each component independently.

If a compound forms a derivative with a reagent which has characteristic absorption band of high intensity at a wavelength where the compound does not absorb, then the extinction coefficient of the derivative is usually the same as that of the reagent. Determination of the dissociation constants of acids and bases is one of the important methods in the elucidation of the structures of organic molecules[7] and the spectrophotometric method offers an accurate method for the determination of the dissociation constants. If the absorption spectra of the reactants and products are considerably different, spectrophotometry may be employed to follow the changes in the concentration of either the products or reactants during a reaction.

II.1.3 Fluorescence

Fluorescence is the process of emission of light which accompanies the spontaneous transition of a molecule from an excited state to a lower energy level. The distribution of wavelength-dependent intensity that causes fluorescence is known as the fluorescence excitation spectrum, and the distribution of wavelength-dependent intensity of the emitted energy is known as the fluorescence emission spectrum[8].

Fluorescence is the emission of light from singlet-excited states, in which the electron in the excited orbital is paired (of opposite sign) to the second electron in the ground-state orbital. Return to the ground-state is spin-allowed and occurs rapidly by emission of a photon. The emission rates of fluorescence are typically 10^8 s^{-1}, so that a typical fluorescence lifetime is about 10 ns. Fluorescence

spectral data are generally presented as emission spectra. Emission spectra vary widely and are dependent upon the chemical structure of the fluorophore and the solvent in which it is dissolved[9].

Fluorescence detection has three major advantages over other light-based investigation methods: high sensitivity, high speed, and safety. The point of safety refers to the fact that samples are not affected or destroyed in the process, and no hazardous products can be generated.

Fluorescence is a powerful technique for studying molecular interactions in analytical chemistry, biochemistry, cell biology, physiology, nephrology, cardiology, photochemistry, and environmental science. It boasts phenomenal sensitivity for the analytical chemist or the life scientist working at nanomolar concentrations. New developments in instrumentation, software, probes, and applications have resulted in a burst of popularity for a technique that was first observed over 150 years ago.

Fluorescence is radically affected by chemical elements and changes in physical environment, which cause a decrease in intensity, duration of emission or width of the bands. This process is known as quenching. Fluorescence quenching refers to any process that decreases the fluorescence intensity of a sample. Quenching involves processes like internal quenching or concentration quenching[10,11].

Quenching is basically of two types: static and dynamic (collisional). Both types require an interaction between the fluorophore and the quencher. In the case of dynamic quenching, the quencher must diffuse to the fluorophore during the lifetime of the excited state. Upon contact, the fluorophore returns to the ground-state without emission of a photon. In the case of static quenching a complex forms between the fluorophore and the quencher and this complex is non-fluorescent. The formation of this complex does not rely upon population of the excited state[12].

II.1.4 Solvent effects

The wavelength and the intensity of absorption bands are both affected when a molecule is in a solvent environment compared with its spectrum in the gas phase. This is due to an unequal perturbation of the ground and excited states of the molecule, which depends on the nature of the solvent-solute interactions in the two states. The absorption spectra in highly non-polar solvents generally retains most of the features of the gas phase spectra and the position and intensity of the absorption maxima are scarcely affected. The interpretation of the solvent effects is often made difficult because they are small and not easy to measure precisely and also because several individual effects, superimposed on one another, contribute to the observed changes.

The limitation of the solvents is, in general, their solubility. In this way, the more polar solvents such as chloroform and acetonitrile have often to be employed. The increased background problem due to the additional solvent frequencies can be overcome by choosing several solvents with appropriate "windows". The second problem is the solvent-solute interaction, which is magnified with increasing polarity of the solvent[13].

The transition from the gaseous state to the state of solution produces three characteristic effects in the vibrational spectrum of the solute: the rotational structure of the bands disappears or is replaced by a very simple contour[14-16], the band positions do not correspond with the pure vibrational frequencies of

the molecule in the gaseous state[17-19], and the band half-widths are changed and their band intensities are enhanced[20,21].

Kasha[22] and McConnell[23] have proposed solvent effects as a criterion for distinguishing the $n{\rightarrow}\pi^*$ and the $\pi{\rightarrow}\pi^*$ transitions. They defined bands as *red shift* or *blue shift* bands according to their displacement in the solvent order, paraffin, alcohol, water, without reference to the gas phase frequency. McConnell[23] and other authors have found that all the known $n{\rightarrow}\pi^*$ transitions give blue shift bands, while all the $\pi{\rightarrow}\pi^*$ transitions do not necessarily give rise to red shift bands.

Later, Bayliss and McRae[24] have presented a scheme by which the solvent effects on absorption spectra can be interpreted qualitatively in terms of dipole-polarization and hydrogen bonding forces between the solute and the solvent, superimposed on one another.

II.1.5 Hydrogen bonding

Hydrogen bonding is among the most fundamental interactions in biology and chemistry, providing an extra stabilization of 4.184-167.36 KJ/mol to the molecular systems involved. This wide range of stabilization energy underlines the need for a general and comprehensive theory that will explain the formation of hydrogen bonds.

Hydrogen bonding occurs when an atom of hydrogen is attracted by rather strong forces to two atoms instead of only one, so that it may be considered to be acting as a bond between them[25]. A hydrogen bond is an interaction between a functional proton-donor group *(X-H)* and an electron-donor atom *Y* in the same or a different molecule, and is generally symbolized *[X-H···Y]*. Both *X* and *Y* are usually electronegative atoms; *Y* has either a lone pair electrons or is a group with π-electrons. The energy of a hydrogen bond is of the order of a few KJ, weaker by a factor of ten than covalent bonds between atoms. The strongest hydrogen bonds are found in the bifluoride ion, *[F-H···F-]* and in hydrogen fluoride. Less strong but often encountered, are those in which the proton is donated by a carboxyl, hydroxyl, amine or amide group. Weaker hydrogen bonds are found with *(C-H)* and *(S-H)* groups, especially when *C* or *S* atom bound to a strongly electronegative group. The common electron donor atoms are *O* atoms in carbonyl and other groups, *N* atoms in amines and *N*-heterocyclics, and halogen atoms[13].

Three types of hydrogen bonding may be studied by spectroscopic methods: intermolecular hydrogen bonding between solute molecules, intermolecular hydrogen bonding between solute and solvent molecules, and intramolecular hydrogen bonding. The effects of hydrogen bonding on electronic absorption spectra have been studied to a lesser extent than on IR spectra. Most of the studies on electronic spectra reported in the literature relate to solute-solvent hydrogen bonding[26,27]. In the vibrational spectra, the most unique manifestation of the hydrogen bond is the perturbation of its stretching mode. This perturbation can be observed through the wavenumber shift, the increase in band width, and the enhancement of intensity[28,29].

In the condensed phases the uncertainties in the number and nature of the polymeric species are frequently big enough to cause considerable difficulties in spectral interpretation. This is not always sufficiently appreciated since, from the practical standpoint, the liquid state is the most amenable to study

and many investigations of hydrogen bonding in pure liquids and mixtures have been reported[30-42]. The results can be summarized by saying that in the *v(X-H)* region the absorptions of the many hydrogen bonded species, generally, coalesce into a single broad band of considerable width[33].

Since hydrogen bonding involves electronegative proton donor and acceptor atoms by definition, the first models were developed on a purely electrostatic basis. This model was qualified by Gilli et al.[43] as the simple electrostatic model. After that, Coulson[44] has introduced the valence bond theory into hydrogen bonding. In this way the electrostatic picture was further modulated by delocalizational, repulsive, and dispersive contributions, which were revised by Morokuma[45] and others using molecular orbital theory. Taking into account Morokuma's decomposition method, the hydrogen bond energy can be decomposed into electrostatic, exchange repulsion, polarization, change transfer, and coupling terms, the first two terms being dominant. The insufficiency of the simple electrostatic model in describing the resonance-assisted hydrogen bonding, among others observed in the *O-H⋯O* type of bonds, has led Gilli et al. to focus more on the covalent nature of the hydrogen bonding, which was already suggested occasionally on the basis of both X-Ray and neutron diffraction experiments[46] and *ab initio* and semiempirical calculations[47-49]. The conclusion pronounced that "forces determining the hydrogen bond strength are a mixture of both electrostatic and covalent contributions" forms the basis of the electrostatic-covalent hydrogen bond model[43].

The density functional theory[50-52] concentrates on the extraction of chemically relevant concepts such as electronegativity[53], electronic chemical potential[54], hardness[55], and softness. The density functional theory can be considered the technique of choice to achieve the properties and the principles[56] of the hydrogen bonded systems and also of hydrogen bond detection[57].

II.2 Vibrational spectroscopy

"These dark days in Stockholm emphasize the importance of light in our lives. It is equally important in our literature. The word, "light", has vastly many meanings. Shakespeare, in *Love's Labours Lost*, has one of his cleverer characters make fun of that by speaking the line, "Light, seeking light, doth light of light beguile ..." Loosely translated, that means: Intellect, seeking understanding, easily fools reason. - Or perhaps it's the other way around."

(Roy J. Glauber – half of the Nobel Prize in Phisics for his theoretical description of the behaviour of light particles, speech at the Nobel Banquet, December 10, 2005)

II.2.1 Scattering of light

Scattering refers to light being deflected from the direction of incident light propagation. The interaction of the electric vector of an electromagnetic wave with the electrons of a compound results in the scattering of the incident light. Such interactions induce periodic vibrations in the electrons of a compound, thereby producing oscillating electric moments. Such oscillating electrons become new sources for emitting radiation, that is, the scattered light[58-60]. There are three basic types of scattering:

- Elastic. Same frequency (wavelength) as the incident light – Rayleigh scattering.
- Inelastic. Lower frequency (longer wavelength) than that of the incident light – Stokes Raman scattering.
- Inelastic. Higher frequency (shorter wavelength) than that of the incident light – anti-Stokes Raman scattering.

The Raman scattering effect appears when there is an exchange of energy between the photon and the molecule, leading to the emission of another photon with a different frequency than the incident photon. Worded differently, one can distinguish two types of Raman scattering. The first type of Raman scattering corresponds to the scattered light which has lower energy than the incident light, hence it has lower frequency and the effect is called Stokes Raman scattering. When the scattered light has higher energy than the incident light, hence it has higher frequency than that of the incident light, the effect is called anti-Stokes Raman scattering. Rayleigh scattering denominates the effect when the photon simply "bounces" off the molecule, with no exchange in energy. The vast majority of photons will be scattered in this way (Fig. II.2.1.1)[61-63]. Rayleigh scattering is most familiar as we are able to see objects in everyday life as a results of light scattering. Experiments show that the scattering efficiency is inversely

proportional to the fourth power of wavelength. Sunlight includes light of many wavelengths. The blue light is scattered more than the red light because of its shorter wavelength.
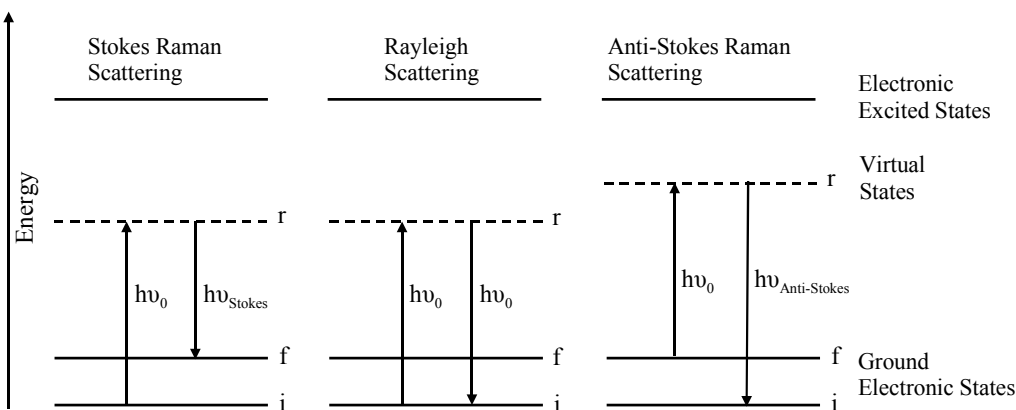
Figure II.2.1.1. The energy diagram of a molecule showing the origin of Raman scattering (non-resonance Raman effect).

Compared to Rayleigh scattering, Raman scattering is less common in our daily lives and is important for the scientists who are interested in vibrational and rotational states of molecules. The Raman process involves two photons (incident and scattered) with different energies. This difference is due to the change in the vibrational or the rotational state of a molecule caused by interaction with incident photons. For this reason, analysis of the Raman spectra provide information about molecular properties and type of vibrations[64,65].

II.2.2 Infrared and Raman spectroscopy

Due to the complementary nature of IR and Raman spectroscopy for studying the vibrational and rotational energies of molecules, it is interesting to compare these two techniques in terms of sample handling, instrumentation, and applications[66].

IR and Raman spectra result from transitions between quantized vibrational energy states. Molecular vibrations can range from the simple coupled motion of the two atoms of a diatomic molecule to the much more complex motion of every atom in a large polyfunctional molecule. The *N* atomic molecules have *3N* degrees of freedom, three of which represent translational motion in mutually perpendicular directions (the *x*-, *y*-, and *z*- axes) and three represent rotational motion about the *x*-, *y*-, and *z*- axes. The remaining *3N-6* (*3N-5* for a linear molecule) degrees of freedom give the number of ways that the atoms in the molecule can vibrate, i.e. the number of *vibrational modes*[63,65,67-73]. Each mode *i* involves approximate harmonic displacements of the atoms from their equilibrium positions (v_i). The potential energy, *V(x)*, of a harmonic oscillator appears as a function of the distance between the atoms, *x*, as the broken line in Fig. II.2.2.1. For any mode in which the atoms vibrate with simple harmonic motion, considering Hooke's law, the vibrational energy states, V_{iv} , can be expressed by the equation (II.2.2.1):

$$V_{iv} = hv\left(v_i + \frac{1}{2}\right)$$ (II.2.2.1)

where h is Planck's constant, v_i is the *fundamental frequency* (in Hz) of the particular mode and υ_i is the *vibrational quantum number* of the ith mode $(\upsilon_i = 0, 1, 2, \ldots)$. The energy difference for transitions between the ground state $(\upsilon_i = 0)$ and the first excited state $(\upsilon_i = 1)$ of most vibrational modes corresponds to the energy of radiation in the MIR spectrum (400-4000 cm^{-1})[65,68]. The classical vibrational frequency v is related to the reduced mass $\mu = \left[m_1 m_2 / (m_1 + m_2) \right]$, were m$_1$, m$_2$ are the atomic masses and the force constant k by:

$$v = \frac{1}{2\pi} \left(\frac{k}{\mu} \right)^{1/2} \tag{II.2.2.2}$$

In a diatomic molecule the requirement of a dipole change leads to the simple requirement that the molecule must have a dipole moment. For small displacements of the atoms from their equilibrium positions, the forces on the nuclei are linearly proportional to the displacement x (Hooke's law), and for displacements from equilibrium these must be towards the rest position, i.e. negative. Since force equals mass times acceleration, the force constant can be described by the formula:

$$Force = -fx = -\left(\frac{\partial V^2}{\partial x^2} \right) \cdot x = \mu \frac{\partial^2 x}{\partial t^2} \tag{II.2.2.3}$$

where the reduced mass was previously described and t being the time. The solution of this equation is:

$$x = x_0 \cos \left(2\pi v t + \theta \right) \tag{II.2.2.4}$$

$$\frac{v}{c} = \widetilde{v} = \frac{1}{2\pi c} \sqrt{\frac{f}{\mu}} \tag{II.2.2.5}$$

where θ is an arbitrary phase angle, v is the frequency of the vibration and $\widetilde{v}$ is the wavenumber. It appears that for first-row elements and hydrogen the force constant, $f = \partial^2 V / \partial x^2$, is reasonably proportional to the bond order, and one can consider that for the single bonds the frequency is inverse proportional, to a first approximation, to the inverse square root of the reduced mass. The terms wavenumber and frequency may be used interchangeably, but one can realise that they are dimensionally different and are strictly proportional only as long as the wavelength is measured in a vacuum or in constant atmospheric conditions so that the velocity of light is constant. In accordance with this, one can rationalize the relative positions of many of the bands arising in the spectra of complex molecules[65,67].

The motion of the atoms during a vibration is normally described considering the *normal coordinate*, Q. The molecule is only promoted to the excited state if its dipole moment, μ, changes during the vibration. This change can be provided by the relation: $\partial \mu / \partial Q \neq 0$ [67-73]. For molecules with certain elements of symmetry, some vibrational modes may be degenerate, so that more than one mode has a given vibrational frequency while others may be completely forbidden. Thus because of degeneracy, the number of fundamental absorption bands to be observed is often less than *3N-6*[67-73]. The present variation of the potential energy as a function of the displacement of the atoms from their equilibrium positions is shown in Fig. II.2.2.1. From this curve it can be seen that equation (II.2.2.1) is only valid for low values of the vibrational quantum number, and is not valid when υ_i is large. Practically, V_{iv} must be described

using an *anharmonic* (Morse type) potential function. This behaviour can be observed on Fig. II.2.2.1 as the solid line, and the potential energy is given to a first approximation by equation:

$$V_{iv} = h\nu_i \left(\nu_i + \frac{1}{2} \right) + h\nu_i x_i \left(\nu_i + \frac{1}{2} \right)^2 \qquad (\text{II.2.2.6})$$

where x_i is the *anharmonicity constant*. x_i is dimensionless and typically has values between –0.001 and –0.02 depending on the mode.
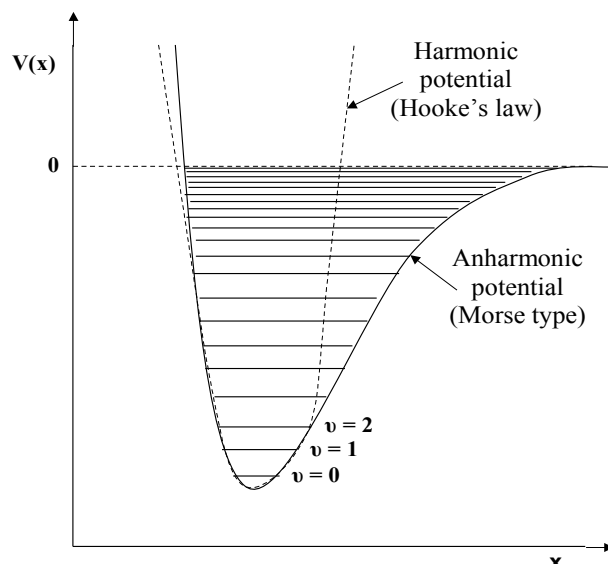
Figure II.2.2.1. Potential energy of a diatomic molecule as a function of the atomic displacement during a vibration for a harmonic oscillator (broken line) and an anharmonic oscillator(solid line).

A molecule may show both electrical and mechanical anharmonicity but the latter is generally much more important and it is usual to define a harmonic oscillator as one which is harmonic in the mechanical sense. It is possible, therefore, that a harmonic oscillator may show electrical anharmonicity.

One effect of mechanical anharmonicity is to modify the $\Delta\nu = \pm 1$ infrared and Raman selection rule to $\Delta\nu = \pm 1, \pm 2, \pm 3, \cdots$, but the overtone transitions with $\Delta\nu = \pm 2, \pm 3, \cdots$ are usually weak compared to those with $\Delta\nu = \pm 1$. Since electrical anharmonicity also has this effect both types of anharmonicity may contribute to overtone intensities[68]. If all vibrational modes were strictly harmonic, no transitions involving changes in ν_i by more than ± 1 would be allowed. The effect of anharmonicity is to relax this selection rule, namely to allow bands caused by $|\Delta\nu_i| > 1$ to become allowed. Thus overtone $(\Delta\nu_i = 2, 3, \cdots)$ and combination $(\Delta\nu_i = 1, 2, \cdots; \Delta\nu_j = 1, 2, \cdots)$, where j represents a different mode, bands commonly appear weakly in the MIR spectrum of organic compounds along with the bands due to fundamental transitions $(\Delta\nu_i = 1)$ [67-73]. The *3N-6* normal vibrations of a non-linear molecule with N atoms, may absorb infrared radiation if they modulate the molecular dipole moment μ. The molecular dipole moment, μ, can be expanded as a Taylor series in the molecular distortions Q[68,74]:

$$\mu = \mu_0 + \frac{\partial \mu}{\partial Q}Q + \frac{1}{2}\frac{\partial^2 \mu}{\partial^2 Q}Q^2 + \textit{higher terms} \qquad (\text{II.2.2.7})$$

The term in Q^2 exists for a change in the vibrational quantum number of 2, and therefore overtones will occur if the second derivative of the dipole moment is non-zero. Since the total molecular wavefunction can be written as a product over all states, then the condition for combination bands to occur (simultaneous changes in two different quantum numbers) is that $\partial^2 \mu / \partial Q_i \partial Q_j \neq 0$. Seldom combination bands appear with considerable strength due to mixing with a nearby fundamental transition of the same symmetry (Fermi resonance). Using Boltzmann statistic calculations, one can observe that the intensity of fundamental bands in IR spectra is proportional to $\left(\partial \mu / \partial Q \right)^2$:

$$\Gamma_i = \frac{N\pi}{3c\nu_i \epsilon_0} \left(\frac{\partial \mu}{\partial Q_i} \right)^2 \tag{II.2.2.8}$$

where Γ_i is the integrated absorption intensity of mode i (for an ensemble of randomly oriented molecules) and ϵ_0 is the permittivity of the free space[68]. Every molecule has slightly different vibrational modes from all other molecules (with the exception of enantiomers). Thus the vibrational spectrum of a given molecule is unique and can be used to identify that molecule. But not all vibrations may give rise to absorption bands in the IR spectrum. The interaction of matter with electromagnetic radiation is subject to selection rules[67-73]. That is, the stretching vibrations of homonuclear diatomic molecules (such as H_2, O_2, etc.) or the totally symmetric vibrations of larger molecules having a centre of symmetry, as well as any other vibrations which do not generate a vibrating dipole, are IR inactive. In order to detect such vibrations, it is necessary to consider the inelastic scattering of light, a phenomena that is referred as Raman scattering. This is governed by different selection rules compared to the absorption of light[67-73].

In Raman spectrometry, the sample is illuminated with a monochromatic beam of radiation of wavenumber $\tilde{\nu}_0$. All of the photons that interact with the sample cause the potential energy of a molecule to be raised to a virtual state, $h\nu_0$ above the ground state. Almost immediately most molecules return to the ground state through the emission of a photon of the same wavelength as that of the incident photon. Since the energy of the incident and scattered photons are identical, this process is a form of inelastic scattering and is often referred to as *Rayleigh scattering* (Fig. II.2.1.1)[65,67-73]. A small fraction of the incident photons drop back to the first excited vibrational state of the ith vibrational mode of the molecule, so that the energy of the scattered photon is $h(\nu_0 - \nu_i)$, i.e. it will be observed at a wavenumber of $(\tilde{\nu}_0 - \tilde{\nu}_i)$, where $\tilde{\nu}_i$ is the wavenumber of the ith vibrational mode. Since the energy of the incident and scattered photons are different, the scattering is inelastic and the process is called *Stokes Raman scattering* (Fig. II.2.1.1)[65,67-73]. Because a given molecule has many different vibrational modes, a measurement of the spectrum from $\tilde{\nu}_0$ to $(\tilde{\nu}_0 - 4000)$ cm^{-1} allows all Raman-active vibrational bands to be measured. Molecules that are in an excited vibrational state will undergo analogous effects when illuminated by a laser. Once more, the largest number of these molecules will undergo Rayleigh scattering, but a small number will return from the virtual state to the ground vibrational state. In this

case, in which the radiation will be observed at a wavenumber of $\left(\widetilde{v}_0 + \widetilde{v}_i\right)$, the process is known as *anti-Stokes scattering* (Fig. II.2.1.1)[65,67-73]. In practice, anti-Stokes-shifted Raman bands are only seen for bands where $\widetilde{v}_i$ is low, usually below 1000 cm^{-1}, because only for these bands is the Boltzmann population of the excited vibrational state populated with more than 1% as compared to the population at ambient temperature.

The classical theory of Rayleigh and Raman scattering is based on the concept that scattered light is generated by oscillating electric dipoles induced by electric field of incident (exciting) radiation. The relation between the induced dipole moment vector μ and the electric field vector E can be written in the form of the following power series:

$$\mu = \alpha E + \frac{1}{2}\beta EE + \frac{1}{6}\gamma EEE + \cdots \tag{II.2.2.9}$$

where α is the polarizability, β the hyperpolarizability, and γ the second hyperpolarizability of the molecule. Polarizabilities α, β, and γ are tensors of rank 2, 3, and 4, respectively. The polarizabilities can be regarded as the measure of the flexibility of the electron cloud: the ease with which the electron cloud of the molecule can be deformed or displaced to produce an electric dipole under the influence of the external electric field. The nonlinear terms in equation (II.2.2.9) are usually so small compared to the linear term that they do not play a role in normal, linear Raman scattering. If we restrict the discussion to the linear term in equation (II.2.2.9), that means:

$$\mu = \alpha E \tag{II.2.2.10}$$

then it can be written in the form of three linear equation[60,65],

$$\left.\begin{aligned}
\mu_x &= \alpha_{xx}E_x + \alpha_{xy}E_y + \alpha_{xz}E_z \\
\mu_y &= \alpha_{yx}E_x + \alpha_{yy}E_y + \alpha_{yz}E_z \\
\mu_z &= \alpha_{zx}E_x + \alpha_{zy}E_y + \alpha_{zz}E_z
\end{aligned}\right\} \tag{II.2.2.11}$$

All α_{ij} are components of a tensor α, which projects one vector, the electric field vector E, to produce another vector μ, the induced dipole moment. This can be written in matrix notation as[74]:

$$\begin{bmatrix} \mu_x \\ \mu_y \\ \mu_z \end{bmatrix} = \begin{bmatrix} \alpha_{xx} & \alpha_{xy} & \alpha_{xz} \\ \alpha_{yx} & \alpha_{yy} & \alpha_{yz} \\ \alpha_{zx} & \alpha_{zy} & \alpha_{zz} \end{bmatrix} \cdot \begin{bmatrix} E_x \\ E_y \\ E_z \end{bmatrix}. \tag{II.2.2.12}$$

The polarizability tensor can be described by a real, symmetric matrix, where all $\alpha_{ij} = \alpha_{ji}$. Thus it has three diagonal and three off-diagonal. This matrix is only necessarily symmetric in the case of nonresonant Raman scattering. The dependence of the molecular polarizability on the normal coordinates can be expressed in the form of Taylor series[60,74]:

$$\alpha_{ij} = \left(\alpha_{ij}\right)_0 + \sum_k \left(\frac{\partial \alpha_{ij}}{\partial Q_k}\right)_0 Q_k + \frac{1}{2}\sum_{k,l}\left(\frac{\partial^2 \alpha_{ij}}{\partial Q_k \partial Q_l}\right)_0 Q_k Q_l + \cdots, \tag{II.2.2.13}$$

where α_{ij} is a component of the polarizability tensor, with $\left(\alpha_{ij}\right)_0$ being its value at the equilibrium configuration, Q_k is the kth normal coordinate associated with vibration wavenumber $\widetilde{v}_k$, the subscripts 0 refer to derivatives taken at the equilibrium configuration.

In order to further simplify the treatment, the double harmonic approximation is adopted which neglects both mechanical and electrical anharmonicity. On the one hand, instead of equation (II.2.2.13), linear dependence of polarizability on each vibrational coordinate (for small amplitude vibrations near the equilibrium) is assumed, that is:

$$\alpha_k = \alpha_0 + \left(\frac{\partial \alpha}{\partial Q_k}\right)_0 Q_k. \tag{II.2.2.14}$$

On the other hand, the normal vibrations are treated as being harmonic, meaning:

$$Q_k = Q_{k0} \cos 2\pi\, c\tilde{v}_k\, t. \tag{II.2.2.15}$$

Considering the time dependence of the induced electric dipole moment μ, generated under the influence of the electric field of incident radiation of wavenumber $\tilde{v}_0$ (which is normally much higher than $\tilde{v}_k$) in a vibrating molecule. The variation of the electric field strength with time is given by:

$$E = E_0 \cos 2\pi\, c\tilde{v}_k\, t. \tag{II.2.2.16}$$

Inserting equations (II.2.2.14)–(II.2.2.16) into equation (II.2.2.10) gives, for the kth vibration,

$$\mu = \alpha_0 E_0 \cos 2\pi\, c\tilde{v}_0\, t + \left(\frac{\partial \alpha}{\partial Q_k}\right)_0 \times Q_{k0} E_0 \cos 2\pi\, c\tilde{v}_0\, t \times \cos 2\pi\, c\tilde{v}_k\, t. \tag{II.2.2.17}$$

As a consequence of irradiation, the magnitude of the electric field vector is modulated with the frequency $\tilde{v}_0$, and shows the induced dipole moment. Trigonometric transformation yields:

$$\mu = \alpha_0 E_0 \cos 2\pi\, c\tilde{v}_0\, t + \frac{1}{2}\left(\frac{\partial \alpha}{\partial Q_k}\right)_0 Q_{k0} E_0 \times \left[\cos 2\pi\, c(\tilde{v}_0 - \tilde{v}_k)t + \cos 2\pi\, c(\tilde{v}_0 + \tilde{v}_k)t\right]. \tag{II.2.2.17}$$

The three cosine functions' different arguments in this equation mean that the induced dipole oscillates with three distinct frequencies simultaneously, therefore it generates radiation at $\tilde{v}_0$ (the Rayleigh scattering) and also at wavenumbers shifted by $\pm \tilde{v}_k$ (the Stokes and anti-Stokes Raman scattering). These so-called beat frequencies are produced when the dipole oscillating at $\tilde{v}_0$ is modulated by the molecular vibration at wavenumber $\tilde{v}_k$. From equation (II.2.2.17) it seems to be clear that the derived polarizability tensor serves as the measure of Raman activity. Those vibrations for which $\alpha'_k = 0$ (meaning that all tensor components are zero) are inactive in Raman scattering, and those normal vibrations for which at least one component of α'_k differs from zero, i.e.:

$$\left(\alpha'_{ij}\right)_k = \left(\frac{\partial \alpha_{ij}}{\partial Q_k}\right)_0 \neq 0 \tag{II.2.2.18}$$

are Raman active[60,65,67-74]. The intensity of bands in Raman spectrum of a compound is governed by change in *polarizability*, α, that occurs during the vibration. The intensity of any band in the Raman spectrum is given by equation (II.2.2.19):

$$I_{Raman} = KI_L(\tilde{v}_0 - \tilde{v}_k)^4\left(\frac{d\alpha}{dQ}\right)^2, \tag{II.2.2.19}$$

where I_L is the power of the laser at the sample, $\left(\widetilde{v}_0 - \widetilde{v}_k \right)$ is the wavenumber at which the band is measured and $\left(d\alpha / dQ \right)$ is the change in polarizability with the normal coordinate of the vibration. The value of the constant of proportionality, K, is dependent on the efficiency at which Raman-scattered light may be collected, as well as some other factors. The most pronounced difference between classical and quantum mechanical treatments of Raman scattering is found in the relative intensities of the corresponding Stokes and anti-Stokes Raman lines:

$$\frac{I_{Stokes}}{I_{anti-Stokes}} = \frac{I_{\widetilde{v}_0 - \widetilde{v}_k}}{I_{\widetilde{v}_0 + \widetilde{v}_k}} = \frac{\left(\widetilde{v}_0 - \widetilde{v}_k \right)^4}{\left(\widetilde{v}_0 + \widetilde{v}_k \right)^4} e^{-\left(\frac{hc\widetilde{v}_k}{kT} \right)},$$ (II.2.2.20)

where h is the Planck's constant, c is velocity of light, k is Boltzmann constant, and T is temperature in Kelvin.

The Boltzmann exponential factor is the dominant term of the equation (II.2.2.20), which makes the anti-Stokes features of the spectra much weaker than the corresponding Stokes lines.

The relatives intensities and polarization properties of spectral lines in scattered radiation depend on different factors, such as the scattering geometry, the orientation of the molecule with respect to the incident light, and the state of polarization of the incident light. Determination of the state of polarization may be of great importance because it can be correlated with the symmetry of the scattering species and the symmetry of the individual vibrational modes[65,67-74]. The radiant intensity I of the light scattered at an angle θ and its polarization characteristics described by the so-called depolarization ratio ρ are also interesting in defining of the scattering geometry (Fig. II.2.2.2). The latter quantity can be defined in different ways. For the case of illumination with radiation polarized perpendicular to the scattering plane, it is denoted $\rho_\perp$ and defined as[60,65]:

$$\rho_\perp(\theta) = \frac{^\perp I_\parallel(\theta)}{^\perp I_\perp(\theta)},$$ (II.2.2.21)

where the superscript preceding I refers to polarization of the incident radiation (perpendicular to the scattering plane for both $^\perp I_\parallel$ and $^\perp I_\perp$), and the subscript following I stands for the direction of polarization of the scattered light (parallel and perpendicular, respectively, to the scattering plane).

Similarly, if the electric vector of incident light were polarized parallel to the scattering plane, the corresponding depolarization ratio $\rho_\parallel$ would be defined as[60,65]:

$$\rho_\parallel(\theta) = \frac{^\parallel I_\perp(\theta)}{^\parallel I_\parallel(\theta)}.$$ (II.2.2.22)

The common governing principle in equations (II.2.2.21) and (II.2.2.22) is that the intensity of depolarized scattering is rationed against the intensity of scattering with unaltered polarization, the states of polarization being considered with respect to that of the incident light. This allows for a simpler definition of the depolarization ratio as[60,65]:

$$\rho(\theta) = \frac{I_\perp(\theta)}{I_\parallel(\theta)},$$ (II.2.2.23)

where subscripts ⊥ and ‖ refer to the mutual orientation of the electric vectors of the incident radiation and the scattered light.
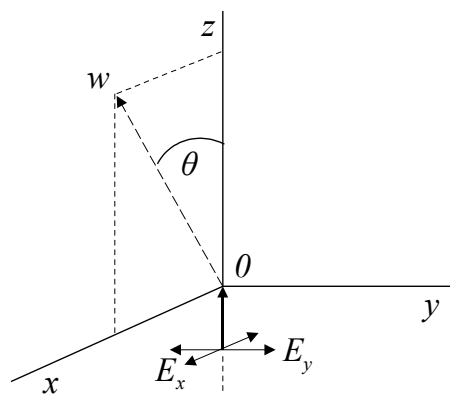
Figure II.2.2.2. Orientation of axes for definition of illumination and observation geometry, where xz is the scattering plane.

The intervals of the possible depolarization ratio values are[60,65]:

$$0 \leq \rho_{\perp}\left(\frac{\pi}{2}\right) \leq \frac{3}{4}. \tag{II.2.2.24}$$

Depolarization results are, in principle, the same for 180° scattering when using polarized exciting radiation (namely for $\rho_{\perp}(\pi)$) as for 90° scattering with incident light perpendicularly polarized with respect to the scattering plane ($\rho_{\perp}(\pi/2)$)[60,65]:

$$0 \leq \rho_{\perp}(\pi) \leq \frac{3}{4} \tag{II.2.2.25}$$

The actual values of $\rho_{\perp}$ are determined by the symmetry properties of the derived polarizability tensor, that reflect the symmetry of the corresponding normal mode of vibration. Thus, the following cases can be distinguished[60,65,67-74]:

(a) For nontotally symmetric vibrations $\rho_{\perp} = 3/4$ and such Raman bands are said to be depolarized.

(b) For totally symmetric vibrations $\rho_{\perp} < 3/4$ and such Raman bands are said to be partially polarized.

(c) At an extreme, for totally symmetric vibrations of molecules belonging to cubic point groups $\rho_{\perp} = 0$ and the observed band is considered completely polarized.

Before the mid-1980s, Raman spectroscopy was often considered to be less desirable than IR absorption spectroscopy for two reasons: the first one because only one out of about 10^8 of the incident photons undergoes Raman scattering and because until about 1985, Raman spectrometry was considered to be a relatively insensitive and/or time-consuming technique. However, the distinct advantages of Raman to IR are that in Raman there is little or no sample preparation as well as the ability to use glass optics and work in aqueous media. Therefore, the probes can often be examined in the form in which they are submitted, and can usually be returned unaffected after measurements. Furthermore low wavenumber measurements are possible and hence, signals can be easily observed below 100 cm^{-1}. In this way, IR and

Raman spectroscopy are powerful complementary tools for obtaining precise and detailed information about the structure of molecules and complexes, particularly since lasers have been developed in optical spectroscopy[60,65,67-74].

II.2.3 Fourier-transform Raman spectroscopy

The advent of multiplex (usually FT) and multichannel (monochromators with array detectors) techniques have greatly increased the sensitivity of modern Raman spectrometry. A great problem is that the high frequency of the laser irradiation (radiation from an Ar^+ laser at 488 nm) in the visible region may lead to photochemical reactions in the laser focus. In addition to this difficulty, fluorescence can often cover the whole Raman spectrum. Such problems can be avoided by using an excitation wavelength in the near infrared (NIR) region. The most popular NIR laser is the Nd:YAG laser operating at 1064 nm. Deficits arising from the ν^4 dependence of the Raman intensity and the lower sensitivity of NIR detectors are compensated by the Fourier-Transform (FT) technique, which is widely extended in IR spectroscopy[65,69,75-77].

The high intensities required to drive stimulated Raman processes efficiently is a factor that works against the ready production of very narrow band widths. One way to get around this is to employ interferometric, FT versions of the nonlinear Raman spectroscopies. The heart of each FT-Raman spectrometer is an interferometer and nowadays, all commercial FT-systems are based on a Michelson interferometer (Fig. II.2.3.1).
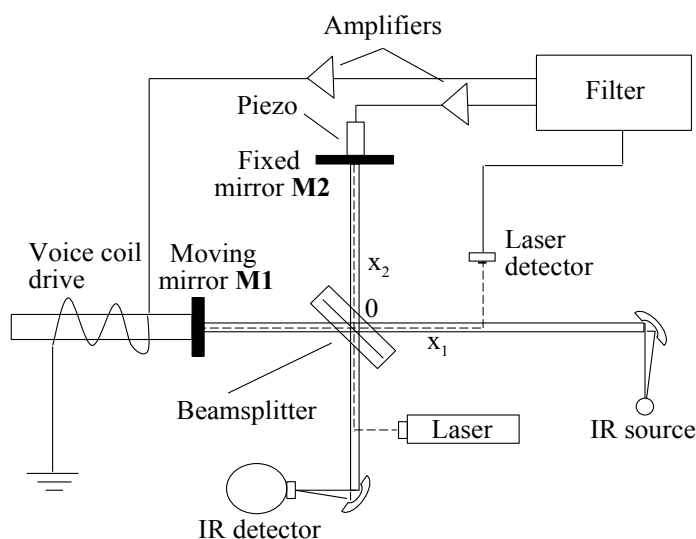
Figure II.2.3.1. An idealized Michelson interferometer.

The most common type of interferometer is by Michelson's design, shown schematically in Fig. II.2.3.1, consisting essentially of a beamsplitter, two mirrors, M1 and M2, and a means of altering the distance between one of the mirrors, M1, and the beamsplitter. Assuming a perfect beamsplitter, half of the light is transmitted to mirror M1 and half is reflected to mirror M2. After reflection at M1 and M2, the

two rays are recombined at the beamsplitter. Again, half of the light is transmitted and half is reflected. The net effect is that half of the light is returned to the source and hence lost. Therefore, only half reaches the detector. Thus, the theoretical maximum efficiency of an interferometer is 50%. In practice, no beamsplitter is perfect and losses occur every time the light is transmitted or reflected in addition to the reflection losses at the mirrors. All of these factors conspire to reduce the efficiency below 50%.

Compared to conventional spectroscopy using dispersing spectrometers, FT spectroscopy has some definite advantages:

(a) The whole spectral range $\Delta\omega$ of interest is recorded simultaneously, whereas in a conventional spectrometer each of the $M = \Delta\omega/\partial\omega$ resolved intervals $\partial\omega$ is scanned across the detector in sequence. In a conventional spectrometer the irradiance of each interval is only measured for a fraction (T/M) of the total recording time T. Since the signal is proportional to the time, the signal-to-noise ratio S/N is proportional to the $(T/M)^{1/2}$ for a dispersion spectrometer, but is $M^{1/2}$ times larger in FT spectroscopy. For $M = 1000$ times, for example, FT spectroscopy gives a thirty-three-times better signal-to-noise ratio for the same total observation time, or else gives the same S/N ratio as a conventional spectrometer in a 1000 times shorter sampling time (Fellgett's advantage)[78].

(b) The throughput of the Michelson interferometer can be much larger than that of a monochromator with comparable resolution. Diameters of 50 nm of the limiting aperture in the Michelson interferometer should be compared with the slit widths of a few μm in monochromators. Although the acceptance angle of the Michelson interferometer is smaller than for monochromators, this does not limit the output if the radiation source is sufficiently small (Jacquinot advantage)[79,80].

(c) The spectrum, calculated by a minicomputer from the recorded FT, is obtained in digital form and is therefore easy to process. Ratio spectra, scale expanded sections of the spectrum, logarithmic presentation, and other modes of processing can be readily performed by the same computer.

Because of these advantages, FT spectroscopy has rapidly developed and has become a major technique in the infrared and recently also in the visible region[63].

II.2.4 Resonance Raman spectroscopy

Raman spectroscopy is generally done in the visible region of the spectrum for which molecules have their first excited state at energies well above the energy of the exciting photons. Resonance effects manifest themselves when the energies of the exciting photons approach the energy of an (usually the lowest excited) electronic state. This resonance enhances not only the intensity of the Raman scattering but also reveals features often not observed with nonresonant excitation. These features generally have their origins in the asymmetric components of the Raman scattering tensor. In some cases the resonance or pre-resonance, is already evident with photons in the visible region. However, when the frequency of the incident light approaches that of an electronic transition or falls inside an electronic absorption band of the sample, resonances occur that may considerably enhance the intensities of certain Raman lines.

This effect is called resonance Raman scattering (RRS) and is due to the coupling of electronic and vibrational transitions.

The resonance Raman (RR) effect comes into play when the frequency of the incident radiation falls within the electronic absorption band[81-84]. The resonance condition introduces additional experimental considerations as well as changes in the selection rules and depolarization ratios. Theoretical approaches to the analysis of Raman intensities differ from those which apply in nonresonance Raman scattering. An important aspect of resonance Raman spectroscopy (RRS) is the intensity enhancement of some modes, by factors as large as 10^6, compared to Raman spectra excited off-resonance. Intensities in RRS reveal structural information about the excited electronic state.

The RR spectrum, like an ordinary Raman spectrum, is recorded as a function of the frequency shift $\Delta \nu = \nu_0 - \nu_s$ between the incident *(0)* and scattered *(s)* radiation, where peaks are observed at the vibrational frequencies of the molecule. Although the selection rules for resonance and off-resonance Raman differ, the peak frequencies in either case are those for the molecule in its ground electronic state (Fig II.2.4.1). However, the intensities of the RR-active vibrational modes depend on the nature of the resonant excited electronic state[60,62,65,85].

Excited Electronic State

Vibrational Levels Within Ground Electronic Level

Stokes   Anti-Stokes
Non-Resonance Raman Effect

Stokes   Anti-Stokes
Resonance Raman Effect
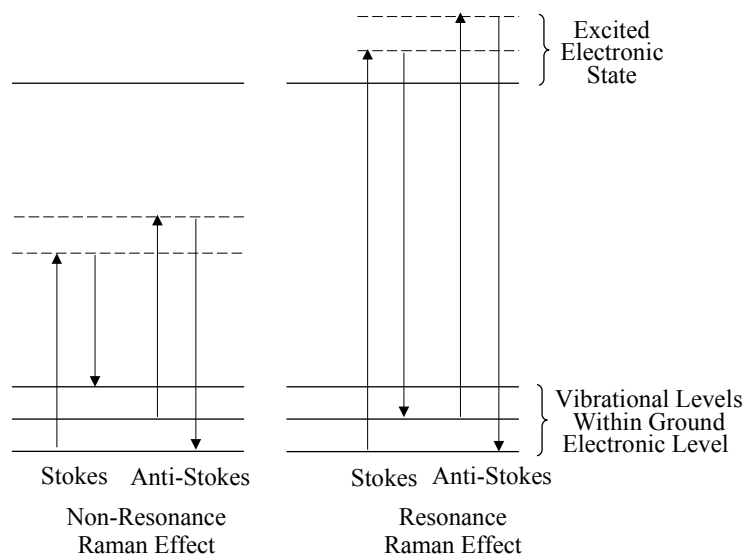
Figure II.2.4.1. Diagrams of the difference between nonresonance and resonance Raman effects.

The instrumentation for RRS is not fundamentally different to that for off-resonance Raman spectroscopy, but the frequency of the source is required to fall within the electronic absorption band. The intrinsic fluorescence of the sample may be unavoidable and require instrumental or chemical approaches to fluorescence rejection. The appropriate laser power at the sample is an important parameter in RRS because the incident radiation is absorbed, leading to sample heating and decomposition. The sample heating, without decomposition, may perturb the measured spectrum by decreasing the local concentration of the analyte in the irradiated volume. To avoid the effect of decomposition, the concentration of the sample could be monitored, by measuring the absorption spectrum, before and after the Raman spectrum acquisition. In the case of chromophores, the optimum concentration of the sample

is difficult to detect; if the sample is too dark, the incident and scattered radiation will be attenuated too strongly. Backscattering geometries permit darker samples to be employed, compared to 90° scattering, because the path distance through the sample is minimized[62,65].

RRS is considerably useful in the study of structure-function relationships of biological compounds. Because of its high intensity, RRS has found various valuable applications in different fields, such as biochemistry and medicine for identifying transition-metal-containing proteins, the study of molecular semiconductors and, for archaeological purposes, the identification of pigments and other constituents in paintings and ceramics.

II.2.5 Surface enhanced Raman spectroscopy

Surface enhanced Raman spectroscopy (SERS) was first demonstrated by Fleischmann and coworkers in 1974[86]. They used Raman spectroscopy to study the adsorption of pyridine at a silver electrode and strong Raman scattering was observed when the surface was electrochemically roughened. Jeanmaire and Van Duyne[87] and Albrecht and Creighton[88] reported in 1977 that the Raman scattering from pyridine adsorbed on a roughened metal surface was enhanced by a factor of 10^6 compared to the equivalent scattering for the same concentration of pyridine in solution[89]. All attempts to explain this effect, have so far failed to reach quantitative agreement with this enormous factor[90,91]. This enhancement phenomenon was called SERS and it depends upon the surface roughness and effective adsorption of the analyte to that surface[65]. Surface enhancement was mainly observed also on nickel[92], cadmium[93], gold and copper surfaces, although aluminium, lithium and sodium also gave enhancement to a lesser extent. The surface enhancement from other metals has been investigated[94,95].

A number of the advantages of normal Raman scattering are applicable to the SERS technique. These include molecularly specific vibrational spectra, simple versatile sampling and ready determination of analytes in air, under vacuum and in water[65]. Nevertheless, with SERS, increased sensitivity is obtained and much wider concentration ranges can be studied. Detection limits have been considerably lowered (down to 10^{-9} M) as compared to those for RR scattering[96,97]. Moreover, to provide vibrational information, electronic information is available through surface enhanced excitation profiles[98]. However, in practice the sensitivity of these experiments to interference and the requirement for adsorption to specific metal surfaces has limited the development of the technique[99-101]. Surface photolysis and fluorescence have proved to be a problem in some experiments.

Despite these difficulties, SERS has become an increasingly popular analytical tool which has been applied to numerous fields as diverse as catalysis and forensic science[65].

The SERS phenomenon arises from an interaction between an adsorbate and the surface plasmons which can be considered to be a wave of electrons present on the surface of the metal substrates[65].

Most of the theories proposed to explain the enhancement mechanism associated with SERS effect can be divided into two vast categories: *electromagnetic (EM) enhancement mechanisms*, which are based on the interaction of light with matter from a spectroscopic-physical perspective, and *chemical* or *charge transfer (CT) enhancement mechanisms* that generally propose that a chemisorbed species, either

in combination with atomically small clusters of Ag atoms or through the formation of surface complexes, scatter the incident light more efficiently than the free molecules does.

In general, EM enhancement theories predict large increases in E in the vicinity of the adsorbed molecule as a result of its proximity to a conducting surface with the "right" optical properties. Therefore, chemical enhancement theories are focused on mechanisms related to increasing the molecule's polarizability α [73]. One theory that does not fit into these broad classifications has been proposed by Cooney and coworkers[102]. They interpreted the large Raman signal from some species to be the result of surface laser damage leading to the concentration of the adsorbate at carbonized sites on the metal surface (intercalation). A theory that seeks to explain SERS must account for the wide variety of experimental observations that have been reported by various groups. The following is a partial listing of many of the major observations associated with SERS-active systems that have proven to be repeatable by several independent investigations[73].

Surface roughness. The magnitude of the surface roughness (either atomic (e.g., clusters, dislocations, steps, kink sites, and grain boundaries) scale or microscopic ($\geq 5\ nm$)) necessary to observe SERS is still undetermined. However, Raman scattering from pyridine adsorbed to either atomically flat or step-terraced single crystal Ag surface is unenhanced[103,104].

Metal specificity. By far, the largest number of SERS studies have been on Ag, and to a lesser extent, the other group IB (coinage) metals, Cu and Au. Other metals whose optical properties were used to predict enhancements that were later confirmed by experiments, are Li, Na, and K. Some reports of enhancements by Hg, Fe, Al, Ni, NiO, Pt, Pd, Rh, Ir, In, Sn, Co, Si, Ti, and TiO_2 also appeared in the literature[105,106].

Adsorbate specificity. In his publication[105], Seki lists over 130 different compounds that have been reported to exhibit enhancement at Ag electrode surfaces. However, most of the confirmed surface enhanced (resonance) Raman spectroscopy active species reported so far are nitrogen- and/or sulphur-substituted Lewis bases. Generally, specifically adsorbed surfactants, polymers, colloid peptizers (e.g., gelatin), and many inorganic ions generally do not produce high S/N SERS spectra. SERS hat seldom been reported in nonaqueous electrolytes. The SERS spectrum of H_2O has been obtained only in electrolytes with high molar concentrations of halides[107].

Wavenumbers and relative intensities. Large differences are often observed in spectral comparisons of the relative intensities of Raman bands obtained from a molecule under SERS conditions with those obtained from the same molecule in the bulk or in solution. Band-specific wavenumber shifts of about 5-20 cm^{-1} for SERS active molecules are also common, but tend to be more system-specific than differences in relative intensities.

Selection rules. It is common for spectroscopic selection rules to be relaxed by the SERS environment to the extent that bands, which are normally both Raman and IR inactive (forbidden) for the bulk species, appear unexpectedly in the SERS spectra of a molecule[99,108].

Wavelength dependence. Excitation profiles (Raman intensity of a vibrational mode versus $\hbar\omega_0$) of SERS active species increase with decreasing wavenumber. By contrast, normal Raman intensities vary with $1/\lambda^4$.

Distance dependence. Raman scattering falls off rapidly with distance from the SERS active surface ($(a/r)^{12}$, where a is the radius of curvature of the surface roughness feature and r is the distance between the molecule and the center of the radius of the curvature)[109]. Apparently, a molecule does not have to be in intimate contact with the metal surface to experience enhancement, although the greatest enhancements are observed from molecules within the first monomolecular layer of the surface[110].

Potential dependence. Both the wavenumbers and relative intensities of Raman bands from certain species adsorbed to SERS active electrode surfaces can vary with the applied potential[111]. It is common for SERS activity to be quenched when the potential of the electrode is made more negative than the point of zero charge of the electrode metal.

Laser-assisted enhancement. The SERS activity of an electrode surface that has been oxidized and reduced while illuminated with laser light is much larger than that of a similar electrode prepared in the dark[112]. Larger enhancements are also typically observed when the adsorbate molecule is present in the electrolyte solution during the oxidation-reduction cycle (ORC).

Separately, neither EM nor CT enhancement theories have been able to explain all of the experimental observations listed above. In particular, EM theories generally predict that when certain optical conditions are satisfied, all molecules at a given distance from a particular roughened metal surface should experience similar scattering enhancement resulting in a SERS spectrum resembling a normal Raman spectrum of a molecule in solution. EM theories thus fail to satisfy observations regarding *the adsorbate specificity* and *the frequency and relative intensities*, and possibly the selection rules and the potential dependence. On the other hand, CT enhancement theories cannot fully account for either the requirement for *metal roughness*, or of *the distance dependence* of SERS. As well, even under favourable conditions, CT enhancement theories by themselves can account for only a relatively small fraction of the total SERS observed.

II.2.5.1 Electromagnetic enhancement mechanism

As discussed by Metiu and Das[113], a solid conducting surface can change the spectroscopic properties of an adsorbed molecule in three ways. The first mechanism is due to the electric field enhancement, in which the EM field perturbing the molecules becomes a combination of both, the incident EM field as well as the elastically scattered field induced by EM polarization of the substrate surface. The spectroscopy of an adsorbed molecule can also be influenced by image field enhancement. The basic concept is that the conduction electrons of a metal can be polarized by the presence of adsorbed oscillating dipoles. The third mechanism consists in the lifetimes of molecular excited states of a the adsorbed molecule, which can be affected by efficient energy transfer between the adsorbed molecule and the surface[73].

According to EM theories for rough surfaces, SERS is a result of three factors. The first is that small particles plasmon resonances, which are similar to those observed in metal-sol solutions, exist on the surface of roughened metals. The second is that the dipole moment induced in the molecule is due to the EM field created by the incident light combined with the elastically scattered light resulting from resonance excitation of the metal particle surface plasmon. As a result, very high field gradients are produced when an adsorbed molecule is positioned near the tip of a surface protrusion (*lightning rod* or *antenna* effect)[114]. Third, provided the bandwidth of the optical particle resonance is wide and the Raman shift relatively small, the inelastically scattered field will be resonant or nearly resonant with the surface plasmon. Following absorption by the particle, the Raman-scattered field can then be amplified and reemitted by the oscillating particle dipole.

The classical treatment of small particle resonances developed by Kerker and coworkers[115-120] provides considerable insight into the factors that are important in designing systems tailored for SERS activity from a strictly EM perspective. The following is an overview of this treatment. The optics of very small ($\leq \lambda_L/15$) metal colloidal spheres are approximated by the expression[121]:

$$Q_s = \frac{\left(8\sigma^4\right)}{3}\left|\frac{\left(m^2 - 1\right)}{\left(m^2 + 2\right)}\right|^2 \tag{II.2.5.1.1}$$

and

$$Q_a = -4\sigma \; \mathrm{Im}\left\{\frac{\left(m^2 - 1\right)}{\left(m^2 + 2\right)}\right\} \tag{II.2.5.1.2}$$

In these expressions Q_s and Q_a represent the fraction of light that are, respectively, absorbed and scattered by the particle; σ is a size parameter equal to $2\pi\,a/\lambda$, where a is the radius of the particle and λ is the wavelength in the medium surrounding the particle; and m is the complex refractive index relative to the medium[115-121]:

$$m = n\left(1 - K_a\,i\right) \tag{II.2.5.1.3}$$

where n is is the real refractive index and K_a is the absorption coefficient. As $m \to i\sqrt{2}$, the denominators of these expressions become very small and scattering and absorption of light by the particle correspondingly become very efficient, i.e., resonance occurs. These equations are approximations of complex expressions with higher order series expansion terms that prevent the division by zero when $m^2 = -2$.

Silver is one of the few metals, along with Na, K, and Li, whose complex refractive indexes in the visible region of the EM spectrum satisfy the conditions for resonance as defined in the expressions above. At $\lambda_0 = 382\,nm$, $m_{Ag} = 0.04 - 1.40i$ in H_2O, which accounts for the bright yellow colour of colloids composed of well-dispersed small ($a \leq 10\,nm$) spherical Ag particles (i.e., the particles absorb blue light).

The modification of colloid scattering theory, which accounts for SERS, involves the effect of metal particle plasmon resonance on the emission from a molecule in the dielectric medium surrounding

the particle. Assuming a monolayer of adsorbed molecules whose oscillating dipoles are normal to the surface of small spherical particle and 90° scattering geometry, the expression for the Raman enhancement factor, $\xi_{EM} = I_R / I_R^0$, (where I_R^0 is the Raman intensity in the absence of the sphere), due to the optical properties of the metal surface is given by[115-121]:

$$\xi_{EM} = \left| \frac{(1+2g)}{(1+2g_0)} \right|^2 \qquad \text{(II.2.5.1.4)}$$

where[115-121]:

$$g = \frac{m^2 - 1}{m^2 + 2} \quad \text{and} \qquad \text{(II.2.5.1.5)}$$

$$g_0 = \frac{m_0^2 - 1}{m_0^2 + 2}. \qquad \text{(II.2.5.1.6)}$$

In calculating the enhancement factor, $g, m\ g_0$, and m_0 are evaluated at the Raman scattering (emission) frequency and at the incident (plane wave) (excitation) frequency, as indicated by the subscript. As with the isolated particle, resonance causes the scattering yield from the system to increase dramatically. However, this expression indicates that EM resonance enhancement of the Raman emission from the system can be induced by either the excitation (laser) frequency or by the Raman emission from the adsorbed molecule itself.

Blatchford and coworkers[122] demonstrated experimentally that triphenyl-phosphine and pyridine adsorbed to electrochemically roughened Ag electrodes exhibit SERS excitation profiles that maximize between $\lambda_0 = 600 - 750$ nm. Based on the description of the EM theory outlined above for small Ag particles, it might be predicted that the largest enhancement would occur near 382 nm, where $m_{Ag} \approx i\sqrt{2}$ (in H_2O). However, this prediction assumes that the particles that promote SERS activity on the roughened electrode surfaces behave as isolated small spheres of Ag. Further refinements of the EM theory take into account the effects of both size and shape of the metal particles, as well as the dielectric constant of the medium. Generally, the best agreements with experimental excitation profiles are found with nanometer-sized prolate (football-shaped) particles with high semimajor to semiminor (i.e., length to girth) axial ratios.

Systematic deviations from classical EM theory have also been observed in the excitation profiles of solutions of small metal colloid particles (sols). For sols, the peak for the maximal intensity in the SERS excitation profile is also typically red shifted relative to the λ_{max} of the sol. This behaviour has been explained by the presence of large groupings (or *aggregates*) of the smaller individual spheroid particles. While the concentration of these aggregates may be too small to produce a distinct peak in the absorption spectrum, the field between aggregated particles is predicted to be considerably larger than that at the surface of a single particle[123].

The largest EM enhancements are predicted for adsorption sites at the ends (i.e., smallest radius of curvature) of the particles. In extreme extensions of the particle shape factor, SERS enhancements as large as 10^{11} have been predicted for the tips of sharp, needlelike surface protrusions. If enhancements of

this magnitude are typical, then to account for experimentally measured enhancements of approximately 10^6, the SERS-active system must be populated with a relatively small number of "SERS-active sites".

Recent developments in SERS, among which the observation of SERS from single adsorbed molecule[124-131] have, not only reinvigorated the field, but also demonstrated once again the operation of EM mechanism. The enhancement calculated from these observations is approximatively 10^{14}. This is some three to four orders of magnitude larger than what is predicted for hot spots in the interstices of aggregates or in fractal clusters. The fact that enhancements large enough to allow single-molecule spectra to be detected have only been observed for a handful of adsorbates (generally colored molecules) and unobserved for many other molecules suggests that the extra three order of enhancement is due to some form of resonance[132].

Single molecule SERS has inspired other optical observation on silver aggregates including optical non-linear effects, which should benefit especially greatly from the inordinately high EM fields at hot spots. A report of SERS-pumping of excited vibrational states has also been reported[133]. Unfortunately, the explanation was found to be spurious[134].

II.2.5.2 Charge transfer enhancement mechanism

From the foregoing discussion of EM enhancement theory, it might be inferred that the large majority of SERS experimental observations can be satisfactorily explained by modifications of classical scattering theory to account for the effect of small particle plasmon resonances on the electric field of adsorbed molecules and vice versa. But a considerable body of experimental evidence has been acquired supporting the view that some type of chemical interaction between the adsorbed species and the SERS active surface must occur before large intensity increases in Raman scattering are observed. For example, Moskovits and DiLella[135] found that the Raman enhancement for CO adsorbed to gold-deposited Ag films was approximately 100 times more intense then that obtained for N_2 under identical conditions, even though the molecular polarizabilities of the molecules are virtually the same. While the surface Raman spectrum obtained from N_2 was relatively unchanged by adsorption, the Raman peak from CO was broadened and shifted by approximately 28 cm^{-1} from that of unbounded CO. Also, the absence of Raman activity from molar concentrations of species in which the SERS-active surface is immersed or embedded (e.g., H_2O and colloid stabilizers) has been used to challenge the universal and exclusive application of EM theory to all SERS systems. On further consideration, numerous studies have been carried out in order to establish or disqualify the existence of this mechanism[136-138]. Its supporters also use it to explain why the enhancement factor of the first adsorbate layer is much greater than those of the subsequent layers. Usually, chemical mechanisms involve the formation of a surface complex between the metallic substrate and the adsorbate. The adsorbed complex may involve adsorbed metal atoms[139] or clusters[140].

In one theory of chemical enhancement, Raman scattering enhancement is due to the resonance involving electronic transitions to eigenstates that are created when the molecule is chemisorbed[141]. Accordingly, the differences between the Raman intensities obtained from the unbound and the adsorbed molecule are due to the changes in the polarizabilities of molecular vibrational modes that occur when new bonds are formed between the molecule and the metal surface[142]. The process is analogous to

spectroscopic changes that are observed when ligands are combined with metal ions to form metal coordination complexes in solution. In support of this model, early work by Van Duyne and coworkers[87] and later, in more detailed spectroscopic evaluations by Pettinger and coworkers[143], demonstrated that many features of an SERS spectrum from the Ag/pyridine/Cl⁻ electrochemical system could be explained by formation of a complex involving a 1:2 pyridine/Cl⁻ complex with Ag.

All chemical (or CT) enhancement theories are related to changes in the polarizability α of the metal-molecule system due to the formation of chemisorptive bonds. While the general features of EM particle-plasmon theory, which largely deals with electric field (E) enhancement, can be described in classical terms, explanation of CT enhancement theories necessarily involve quantum mechanics to describe spectroscopic changes that occur as a result of chemisorption. Consequently, it is often easier to explain experimental results or to test enhancement theories within the framework of EM theory than to predict the outcome of an experiment using CT theory. Lombardi and coworkers[141,144] demonstrated that under illumination, charge can be transferred from an adsorbate (adcluster) complex to the metal or vice versa, depending on the excitation frequency and donor or acceptor level of the adsorbate relative to the metal Fermi level. An estimate of the CT enhancement contribution to SERS activity has been obtained by Persson[145] using a quantum mechanical model based on Anderson-Newns resonances. In this model, it is assumed that the energy level of the adsorbate are broadened to the extent that they overlap with the Fermi level E_F of the metal enabling charge flow from the metal into the lowest unoccupied orbital of the adsorbate. Perssons calculated the CT enhancement factor ξ_{CT} as the ratio of Raman scattering intensity of the adsorbed molecule with respect to the free molecule:

$$\xi_{CT} = \left| (ed)^2 \varepsilon'_a(0) G(\omega_L, \omega_S) / \alpha'(0) / 2 \right|^2 \qquad (II.2.5.2.1)$$

where $G(\omega_L, \omega_s)$ is associated with resonance scattering due to photon-assisted CT from the metal adsorbate ω_L is incident (laser) frequency; ω_s is the Stokes scattered frequency; $\alpha'(0)$ is the derivative of the electronic polarizability of the free molecule with respect to the normal coordinate of the vibration (normal Raman scattering); d is the distance between the "centre of charge" of orbital $|a\rangle$ of the molecule and the metal image plane; e is the charge of an electron; and $\varepsilon'_a(0)$ originates from the expansion of the energy ε_a of $|a\rangle$ in the free molecule with respect to the normal coordinate of the vibration. Using experimental values for CT resonances created by chemisorption of pyridine on Ag(111), Persson calculated a CT enhancement factor of approximately 30.

In conclusion, the EM theory predicts enhancements up to 10^{11} due to the presence of particular microscopic surface morphologies combined with the optical properties of the substrate metal, while the CT theory predicts enhancements between 10 and 10^3.[146] Alone, neither can fully account for all of the confirmed experimental idiosyncrasies inherent to SERS. Nonetheless, when taken together, EM and CT can be used with some degree of success in predicting the overall behaviour of systems that exhibit SERS activity. In this sense, it is important to understand that the total SERS enhancement is very likely a *product* of the two individual enhancement mechanisms:

$$\xi_{SERS} = \xi_{EM} \, \xi_{CT} \tag{II.2.5.2.2}$$

In theory, Raman excitation profiles can provide information on the nature of the SERS enhancement mechanism. Chemical enhancement theories predict that different Raman excitation profiles should be observed for different adsorbate molecules since the electron donor-acceptor levels of the adsorbate participate in the enhancement mechanism. Opposite, EM theories predict that the SERS excitation profiles should depend on the optical and morphological properties of the metal surface and are largely independent of the adsorbate molecule.

II.2.5.3 Surface enhanced resonance Raman scattering

The surface enhanced resonance Raman scattering (SERRS) technique is derived from SERS. It requires the analyte to be a dye, which is adsorbed on the SERS-active substrate. The laser frequency is chosen to be in resonance or close to resonance with the molecular chromophore in the dye. This provides a combination of molecular resonance from the dye and surface enhancement from the metal. The SERRS technique was originally reported by Stacy and Van Duyne in 1983[147]. In most studies the efficiency of the scattering process is improved by three or four orders of magnitude compared to that experienced in SERS, therefore an enhancement up to 10^{10} may be expected and fluorescence is quenched[148,149]. The enhancement obtained is very much greater than either RR or SERS, enabling very sensitive analysis and low detection limits to be achieved[150-153]. The fluorescence quenching properties of surface enhancement coupled with the additional sensitivity obtained from SERRS has been exploited by some groups of researchers[154-156]. The SERRS technique is sensitive, selective and produces structural information and characteristic "fingerprint" spectra. The characteristic spectra routinely observed with SERRS permits identification of mixtures without the need of preseparation. Munro and coworkers[153] have reported the analysis and characterization of 20 similar monoazo dyes, all of which produced unique characteristic spectra which in turn permitted the simultaneous analysis and detection of five dyes presented in a crude mixture. This illustrates the potential of SERRS in forensic science, where trace amounts of dyes require to be analyzed and identified. The advantages reported above have been exploited in numerous research fields.

Biology. When carefully executed, SERRS can provide a biocompatible environment for biological material. Some studies about porphyrins and their photostability[157], copper chlorophyllin[158], the identification of novel chromophores in eye lenses without preseparation of the crude mixture[159,160], and the orientation of cytochrome P450[161] by SERRS have been reported.

Medicinal chemistry. Detection of the antitumor drug mitoxantrone and its interaction with DNA in situ have been probed by SERRS. The adsorption of the drug complex onto a colloidal surface did not destroy or interfere with the native structure. Therefore, bonding information from the complex was extractable from the SERRS spectra[162].

Surface chemistry. Electrode surfaces have been examined in situ by SERRS to extract structural information and to provide quantification. The in situ SERRS detection of compounds such as 2,4,6-trinitrobenzene sulfonic acid, covalently bound to the oxide, was observed when the chemically modified surface was coated in Ag[150,163].

Analysis. Several practical examples of SERRS have been developed, in order to prepare a robust disulfide pH indicator by coupling pH-sensitive dyes, methyl red, cresol violet, and 4-pyridinethiol, to cystamine, which adsorbs strongly to the roughened metal surface forming monolayer coverage of the complex with colloidal silver and allowing strong SERRS to be recorded[164-166].

Polymers. Polymerization reaction at the metal surface have been reported by Tsai and coworkers[167]. They prepared thin films of 1,4-dinitrobenzene on silver island films and under a nitrogen atmosphere polymerization occurred which was followed by appearance, and increases in intensity, of new bands in the spectra collected.

II.2.5.4 Surface enhanced Raman scattering substrates

Since the discovery of SERS[86], numerous SERS active substrates have been explored for both theoretical insights and practical applications of the effect. The most well-documented substrates used in SERS are *roughened electrodes*, *thin metal films*, and *colloidal suspensions*.

Electrodes. Electrodes were originally used and developments within this field are continuing[168]. One of the principal advantages of the use of electrodes is that it is possible to control the surface potential. However, electrode pretreatment is crucial to obtain maximum SERS signals. An excellent discussion of the electrochemical techniques utilized in SERS may be found in the review of Chang and Laube[111]. In most cases polycrystalline Ag wires or rods are sealed into an inert holder (glass or Teflon). The surface is then polished mechanically using increasingly smaller sizes of alumina powders (to 0.5 μm). This step is sometimes followed by a chemical etching procedure. For example, a mixture of ammonia[169] or sodium cyanide[170] and hydrogen peroxide has been used. Finally, the electrode is subjected to an oxidation-reduction cycle (ORC) in an electrochemical cell. This anodization step further cleans the electrode and also produces surface roughness. The resulting surface consists of sponge-like Ag deposits in the size range 25-500 nm.

Experimental variables in the ORC include the oxidation and reduction potentials, the type of potential-time function utilized, and the amount of charge passed during the oxidation step. The oxidation potential is dictated by the electrolyte used. The amount of the charge passed during the oxidation step has an appreciable effect upon the SERS enhancement. In the case of Ag, it has been observed that the optimum SERS signals are obtained following the passage of 20-50 mC cm^{-2} charge. This is equivalent to approximately 100-200 monolayers of Ag atoms[171]. Anodization of gold electrodes requires more positive potentials multiple cycles for optimal SERS activity[172]. The cathodization is believed to cause reduction of organic materials on the electrode to hydrocarbons, which are then desorbed. Also, the presence of H$_2$ bubbles formed at the reducing potential may affect the surface morphology during the ORC of the silver surface. Secondly, it has also been observed that illumination of the electrode during anodization in the presence of halide can yield stronger SERS signals[112,173-175]. This has been attributed to partial photoreduction of the Ag$^+$ which produces microstructure on the surface. In many of the reported SERS experiments utilizing electrodes, the adsorbate was present during the anodization procedure. In some cases, it was shown that the same SERS signal intensity resulted when the adsorbate was present during anodization as when the adsorbate was added after the anodization step[111]. However, it was found that

biological samples can be very sensitive to the presence of Ag$^+$ generated in the diffusion layer during the anodization step. This can lead to cleavage bound chromophores, e.g. hemes or dissociation of non-covalently bonded substances, e.g. flavins. Protein denaturation may not be a problem if detection of a specific chromophore is the objective of the experiment. Under these conditions, enhanced sensitivity may be observed when the anodization is performed in the presence of the biomolecule. If, on the other hand, the goal is to monitor a biologically active substance, the adsorbate should be added after the anodization step. Electrochemical SERS has been extensively investigated to obtain a better understanding of the surface and of the key process, such as prevention of copper corrosion, and as a detector for chromatography[176,177]. The main disadvantage of the technique is the reproducibility of the electrode surface. It is incredibly difficult to ensure that the same degree of surface roughness and potential is achieved for each experiment. This may result in different degrees of surface enhancement. Additionally, selection rules depend upon the analyte adsorption process and orientation. Therefore the surface chemistry must be closely controlled.

Colloids. Colloidal suspensions represent another widely used class of SERS substrates. Metal colloidal particles formed upon porous membranes such as filter papers, gels, beads, polymers, etc. have been developed and investigated[178,179]. Although these adsorbed substrates are prepared easily, they are unpopular probably because they can be expensive and in some cases irreproducible. They involve more complicated preparations and are more susceptible to contamination. Chemical reduction of silver, copper, or gold salts, has been used to produce the colloidal state. Furthermore, the ability to flow the colloid through the laser beam or stir the solution is another particularly attractive feature of colloids in overcoming sample degradation that can result during static experiments at electrode surfaces because of photochemical or thermal effects. Other advantages of the colloidal suspensions (Ag or Au sols) include the ability to compare the morphology with the theory, the defined surface area, the ability to control the particle size and shape, and the ability to directly measure the extinction spectrum[73]. However, the use of colloids suffers from several disadvantages, which include instability caused by the tendency of the colloid particles to aggregate and settle out of solution, especially when an adsorbate is added. This can be avoided by adding stabilizers[180,181], by utilizing more elaborate preparation[123], or by sedimentation classification[182] schemes, which permit the preparation of smaller and more homogeneous particle sizes. Another problem is the inability to control the surface potential, which depends upon the solution potential and can vary considerably from one method to another or with time for a given method[183,184].

Several methods were suggested for the preparation of the well-known silver colloid. Each produces silver particles of different diameters and uniformities[185-187]. The Carey-Lea preparation is reported to produce particles with diameters in the range 14-22 nm[185], whereas Creighton and coworkers obtained particles with diameters of 18-22 nm[186]. However, both substrates were relatively unstable. One process that yields reproducible and reliable results is a controlled citrate reduction of silver nitrate, originally reported by Lee and Meisel[187] and modified by Munro and coworkers[188]. It produces monodispersed colloidal particles with a diameter of 28 nm. The difference in colloidal particle size may account for the varying stability of colloid preparations. There is a natural tendency for small particles to

reduce their surface area and energy in a bid to increase their stability by self-aggregating. As a Lee and Meisel colloid has a lower surface area and energy than colloids prepared by other methods, it is less likely to self-aggregate. The practicability of surface enhancement depends on effective adsorption of the analyte to the Ag surface. Positively charged analytes will adsorb readily to the colloid surface, although problems with neutral and negatively charged analytes arised. This problem may be overcome by the introduction of surface modifiers[65]. Aggregating the colloidal particles[189] can further increase the SERS enhancement. The act of aggregation forms clusters of colloid, within which are interstices. The electric field established in these regions is predicted to be very large; hence the surface enhancement experienced from this is very intense. Many different methods of aggregation have been suggested including acids, salts, and surfactants even using the analyte itself to induce aggregation[152,154,190]. This aggregation process is detected by a change in color of the colloidal suspension and a bathochromic shift of the absorbance maximum.

Metal films. The thin metal films roughened by chemical or mechanical means were also found to be sensitive[191,192]. Furthermore, the production of the films is difficult to control and hence it is difficult to obtain reproducible results[193]. Generally, the metal films are easy to prepare, compact, transportable, and stable. A further potential advantage over other types of SERS active substrates is the possibility to experimentally "tune" these SERS substrates for optimal enhancement at a desired excitation frequency by proper choice of the metal film preparation conditions[194]. The most representative of these films are the island films, the coldly deposited films in ultra high vacuum and the lithographically prepared substances, since results obtained with these systems have been extensively used in fundamental studies aimed at pointing the origins of the SERS effect.

The metal island films, which we used in our measurements, are prepared by vapor depositing 50-150 Å equivalent mass thickness of metal on a substrate (usually quartz or glass) at room temperature and under high vacuum conditions[195]. When the metal atoms hit the surface, they have sufficient mobility to nucleate and form island structure, rather than an uniform overlayer of metal atoms. The morphology and topography of evaporated metal films depend on several factors including the amount of metal deposited, type of substrate, deposition rate, temperature of the substrate, angle of incidence of the metal atoms with respect to the surface, pressure and composition of the background gas in the vacuum system. Once the film is deposited, the annealing conditions can cause the initial film structure to change dramatically[196]. Morphologies of several metal island structures have been examined by scanning electron microscopy, scanning transmission microscopy and atomic force microscopy[197-199]. The structure of the thin films was shown to vary with the deposition rate[197]. Slow rates produced more strongly aggregated films with more intense colour, whereas rapid deposition produced thinner structures that were more uniformly distributed on the substrate.

II.3 Density functional theory

"Theory:
Supposition which has scientific basis,
but not experimentally proven.
Fact:
A theory which has been proven by enough
money to pay for the experiments."
(The Wizard of ID)

II.3.1 The Kohn-Sham approach

In density functional theory (DFT)[200-203], the total energy, including electron correlation effects, is written in the form:

$$E[\rho(r)] = T[\rho(r)] + U[\rho(r)] + E_{XC}[\rho(r)].$$ (II.3.1.1)

Here, T is a kinetic energy term, U is the electrostatic interaction energy between all electrons and nuclei, and E_{XC} is the exchange-correlation energy of the system. The total electron density ρ in equation (II.3.1.1) can be related to single-particle wave functions by

$$\rho(r) = \sum_{occ} |\Psi(r)|^2,$$ (II.3.1.2)

where the summation extends over all occupied electronic levels.

Density functional theory[200-206] is based on the Hohenberg-Kohn theorem[200], which states that the total energy of a system in its ground state is a functional of that system's electronic density, $\rho(r)$, and that any density, $\rho'(r)$, other than the true density will necessarily lead to a higher energy. Therefore, the Hohenberg-Kohn theorem introduces an alternative approach to performing exact, variational, *ab initio* electronic structure calculations. In conventional *ab initio* methodology[201], Schrödinger's equation:

$$H\Psi = E\Psi$$ (II.3.1.3)

must be solved. Meanwhile, DFT requires only that we minimize the energy functional, $E[\rho(r)]$. The conceptual simplification thus offered cannot be overstated. Rather, than working with a complex 3N-dimensional wavefunction, Ψ, describing the behavior of each electron in an N-electron system, DFT allows us to work with a simple three-dimensional function, the total electronic density. Unfortunately, the exact nature of the energy functional is not known, and the total energy of a system cannot be simply output when a trial density, $\rho'(r)$, is given as input. Therefore, we must turn to approximate DFT methods, and though we will not have a wavefunction, we will ave to make use of one-electron Kohn-Sham[201] molecular orbitals, which rather closely resemble molecular orbitals from the well-known Hartree-Fock (HF) method[207,208]. Early applications of DFT tended to be within the physics community, concentrating on systems where the HF approximation is a particularly poor starting point[209]. Therefore,

the vast majority of the applications were on metallic systems, because a single determinantal approach is notoriously bad in such cases. Since DFT works with the density, and not the wavefunction, systems that would require a great number of electronic configurations to be well described by conventional *ab initio* approaches are in principle neither harder nor more expensive, for DFT than the systems that are well described by a single configuration. Correlation effects, absent within the HF approximation, are also built into the approximate energy functionals used in modern DFT applications. Therefore, DFT methods are in principle able to treat the entire periodic table with unvarying ease and accuracy.

Though the Hohenberg-Kohn theorem clearly established that one could, in principle, work directly with the density in *ab initio* calculations, it was the subsequent work of Kohn and Sham (KS)[201] that offered a practical approach to perform DFT calculations. In the KS approach, the unknown Hohenberg-Kohn functional, $E[\rho(r)]$, is partitioned as in equation (II.3.1.1). In this partitioning scheme, $U[\rho(r)]$ is simply the classical electrostatic energy, the sum of the electron-nucleus attractions and the electron-nucleus repulsions[201,205]:

$$U[\rho(r)]=\sum_A \int \frac{(-Z_A\rho(r))}{|r-R_A|}dr + \frac{1}{2}\int\int \frac{(\rho(r)\rho'(r))}{|r-r'|}dr\,dr'. \qquad \text{(II.3.1.4)}$$

The next term, $T[\rho(r)]$, is defined as the kinetic energy of a system of noninteracting electrons with the same density, $\rho(r)$, as that of the real system of interacting electrons being studied. This may seem to introduce a severe error. However, this is not the case, because the final term, $E_{XC}[\rho(r)]$, is made to contain, in addition to the exchange and correlation (XC) contributions to the energy, the difference between $T[\rho(r)]$ and the true electronic kinetic energy of the system. Following Kohn and Sham, $\rho(r)$ of an N-electron system (with N^α spin up electrons and N^β spin down electrons) is expressed as the sum of the square moduli of single occupied, orthonormal Kohn-Sham molecular orbitals[201,205],

$$\rho(r)=\rho^\alpha(r)+\rho^\beta(r)=\sum_i^{N^\alpha}|\Psi_i^\alpha(r)^2|+\sum_i^{N^\beta}|\Psi_i^\beta(r)^2|. \qquad \text{(II.3.1.5)}$$

Having done this, $T[\rho(r)]$ can be defined as[201,205]

$$T[\rho(r)]=\sum_{\sigma=\alpha,\beta}\sum_i^{N^\alpha}\int \Psi_i^\sigma(r)\frac{(-\nabla^2)}{2}\Psi_i^\sigma(r)\,dr \qquad \text{(II.3.1.6)}$$

One should note that $T[\rho(r)]$ is not a true density functional, because the KS orbitals are required. Alternate forms of $T[\rho(r)]$ that depend only on the electronic density and do not require KS orbitals have been proposed[203]. However, they are too imprecise to be of any practical use in chemistry.

Finally, recalling the fact that the energy functional is minimized by the true ground state density, $\rho(r)$, the energy $E[\rho(r)]$ must be stationary with respect to any arbitrary variation in either of the spin densities, i.e.[201,205],

$$\frac{(\delta E[\rho(r)])}{(\delta\rho^\alpha(r))}=\frac{(\delta E[\rho(r)])}{(\delta\rho^\beta(r))} \qquad \text{(II.3.1.7)}$$

This condition yields the one-electron KS equations[201,205],

$$\left\{\frac{(-\nabla^2)}{2}-\left(\sum_A \frac{(Z_A)}{|(r-R_A)|}\right)+\int \frac{(\rho(r'))}{|(r-r')|}dr'+\frac{(\delta E_{XC}[\rho(r)])}{(\delta \rho^\sigma(r))}\right\}\Psi_i^\sigma(r)=\epsilon_i\Psi_i^\sigma(r) \qquad \text{(II.3.1.8)}$$

Thus, a scheme for performing practical DFT calculations emerges. With an initial guess at the total spin densities, $\rho^\alpha(r)$ and $\rho^\beta(r)$, the KS equations are constructed and solved, and the resulting set of KS-orbitals, $\left\{\Psi_i^\sigma(r)\right\}$, are then used to generate new guess at $\rho^\alpha(r)$ and $\rho^\beta(r)$. This procedure is repeated until self-consistency is achieved, that is, the same densities and KS orbitals are regenerated.

In this preceding discussion, we avoided to deal with the precise nature of the XC energy functional, $E_{XC}[\rho(r)]$, and XC potentials, which are the functional derivatives of $E_{XC}[\rho(r)]$ with respect to $\rho^\alpha(r)$ and $\rho^\beta(r)$; $v_{XC}^\alpha[\rho(r)]$ and $v_{XC}^\beta[\rho(r)]$ are formally given by[201]:

$$v_{XC}^\sigma(r)=\frac{(\delta E_{XC}[\rho(r)])}{(\delta \rho^\sigma(r))}. \qquad \text{(II.3.1.9)}$$

If the true XC energy functional, $E_{XC}[\rho(r)]$, were known, this scheme would yield the true ground state density, and in turn, exact values for all ground state properties. Unfortunately, the precise nature of $E_{XC}[\rho(r)]$ is not known, and at the first glance, it may seem that we are no further along to performing practical DFT calculations then when we had only the Hohenberg-Kohn theorem and an unknown total energy functional, $E[\rho(r)]$. However, very simple approximations to $E_{XC}[\rho(r)]$ can, perhaps surprisingly to some, yield fairly accurate results. The KS approach is therefore of great practical importance and has become the cornerstone of all modern DFT applications.

II.3.2 Exchange and correlation energy functionals

Since the quality of any DFT calculation is limited by the quality of its approximation to the true XC energy functional, $E_{XC}[\rho(r)]$, it is not surprising that a great deal of effort has been invested in the development of ever more sophisticated XC functionals. Fortunately, one of the simplest and most popular approximations of $E_{XC}[\rho(r)]$, the Local Spin Density Approximation (LSDA)[210], is capable of yielding results that favorably compete with those obtained using HF calculations[206,211-215]. The exchange-correlation energy can be expressed in terms of LSDA as:

$$E_{XC}[\rho(r)]=\int \rho(r)\epsilon_{XC}\left(\rho^\alpha(r),\rho^\beta(r)\right)dr, \qquad \text{(II.3.2.1)}$$

where $\epsilon_{XC}\left(\rho^\alpha(r),\rho^\beta(r)\right)$ is the XC energy density at a point r in the space. Within the LSDA, ϵ_{XC} is just a function of $\rho^\alpha(r)$ and $\rho^\beta(r)$ at that specific point r in space. When $E_{XC}[\rho(r)]$ is expressed in such a fashion, the XC potential, $v_{XC}^\sigma(r)$, from equation (II.3.1.9) are given by[205,210]:

$$v_{XC}^\sigma(r)=\rho(r)\frac{\left(d \epsilon_{XC}\rho^\alpha(r),\rho^\beta(r)\right)}{\left(d \rho^\alpha(r)\right)}+\epsilon_{XC}(\rho^\alpha(r),\rho^\beta(r)),\sigma=\alpha,\beta. \qquad \text{(II.3.2.2)}$$

The heart of the LSDA is the approximation that a particular point in space of an inhomogeneous distribution of electrons with densities $\rho^\alpha(r)$ and $\rho^\beta(r)$ has the same values of the ϵ_{XC}, $\upsilon_{XC}^\alpha(r)$, and $\upsilon_{XC}^\beta(r)$ as those of any point in homogeneous distribution of electrons of the exact same densities ρ^α and ρ^β. The values of $\epsilon_{XC}(\rho^\alpha(r), \rho^\beta(r))$ has been determined for a large number of homogeneous gases of interacting electrons of varying total density, $\rho = \rho^\alpha + \rho^\beta$, and net spin density, $\rho^S = \rho^\alpha - \rho^\beta$, by means of quantum Monte Carlo methods[216,217]. The results have since been parametrized by Vosko, Wilk, and Nusair (VWN)[210] and by Perdew and Zunger (PZ)[218], in such a way that the XC potentials can be easily evaluated via equation (II.3.2.2).

Though this may seem to be a crude approximation, theoretical considerations[219] do justify the LSDA's ability to provide quantitatively accurate geometries, charge distributions, and vibrational spectra on a wide variety of systems[206,211-215]. It should be surprising to see the LSDA results surpass HF and even challenge correlated post-HF methods. One must remember that correlation effects are included within the LSDA XC functional. Systems that prove to be extremely problematic in HF theory, where correlation effects are by definition absent,are therefore not necessarily systems that offer any great challenge to the LSDA.

The most troubling aspect of the LSDA is its systematic overestimation of binding energies[215,220,221]. For general chemistry, this means that the LSDA is not particularly well suited for thermochemical applications such as computing atomization energies, heats of reaction, or activation energies. For weakly bound systems, such as hydrogen-bonded systems[222] or van der Waals complexes[223], the overestimation of the strength of certain interactions can disrupt what is often a delicate balance of forces, driving a system to a geometry that is in very poor agreement with the experiment. For a great deal of biomolecular applications this flaw is fatal.

For such applications, one must therefore go beyond the LSDA and adopt gradient-corrected XC energy functionals. The XC energy functional still has the general form of equation (II.3.2.1), but as the name suggests, the gradient of $\rho^\alpha(r)$ and $\rho^\beta(r)$ appear so that $E_{XC}[\rho(r)]$ is now given by[205]:

$$E_{XC}[\rho(r)] = \int \rho(r) \epsilon_{XC}(\rho^\alpha(r), \rho^\beta(r), \nabla \rho^\alpha(r), \nabla \rho^\beta(r)) dr. \qquad \text{(II.3.2.3)}$$

Unfortunately, once we go to gradient-corrected functionals, the conceptual simplicity of the LSDA is lost and various methods may be adopted. Consequently, many gradient-corrected XC energy functionals have been proposed[224-229].

Even though gradient-corrected XC functionals are local functionals (the values of $\epsilon_{XC}(r)$, $\upsilon_{XC}^\alpha(r)$, and $\upsilon_{XC}^\beta(r)$ at any point in space depend only on the values and derivatives of $\rho^\alpha(r)$ and $\rho^\beta(r)$ at that precise point in space), they do impose a significantly greater computational burden than the LSDA functionals do. Derivatives of $\rho^\alpha(r)$ and $\rho^\beta(r)$ must now be evaluated before $\epsilon_{XC}(r)$, $\upsilon_{XC}^\alpha(r)$, and $\upsilon_{XC}^\beta(r)$ can be synthesised. Fortunately, experience has shown that it is often not essential to include gradient corrections in the course of the self-consistent procedure[230]. In other words, The KS

equations can be iteratively solved using LSDA XC potentials. Once self-consistency is achieved, one should calculate the total energy and the forces acting on the atoms, the derivatives of the LSDA SCF density are evaluated and plugged into the gradient-corrected forms of $\epsilon_{XC}(r)$, $\upsilon_{XC}^{\alpha}(r)$, and $\upsilon_{XC}^{\beta}(r)$. Thus, gradient corrections are simply treated in a perturbative fashion. This simplification essentially renders gradient-corrected DFT calculations as inexpressive as their LSDA counterparts. It has been suggested that the LSDA's propensity for generating hydrogen bonds that are too short and therefore too strong arises from the fact that the LSDA electronic densities decay too abruptly in the outer regions[231]. However, the perturbative approach to incorporating gradient corrections does not alter the LSDA electronic structure, yet repairs the poor LSDA hydrogen bond lengths and strengths. The key would therefore seem to be the evaluation of the gradient-corrected XC functionals regarding the contribution of the tail regions to the XC energy, and not corrections to the electronic structure of the tail regions, as suggested[232]. The gradient-corrected exchange and correlation energy functionals are typically formulated so as to address either the exchange or the correlation component of $E_{XC}[\rho(r)]$. Popular gradient-corrected exchange functionals are those of Perdew and Wang[224] and Becke[226]. Perdew's gradient-corrected correlation functional[225] has been extensively used, as that of Miehlich, Savin, Stoll, and Preuss has[227], which is a reformulation of the Lee, Yang, and Parr correlation functional[232]. Since each functional addresses a specific component of $E_{XC}[\rho(r)]$, any of the exchange functionals can be coupled with any two of the correlation functionals. One of the most used functionals of this type is the coupled exchange and correlation gradient-corrected functional of Perdew and Wang[224].

Despite their often radically different forms, no particular gradient-corrected XC functional has emerged as being clearly superior. Partially, this may be due in part to the fact that the LSDA is very often a very good starting point: gradient correlations have little to correct. However, one promising example is Becke's[233,234], where the exact exchange energy, obtained in the same fashion as that of an HF calculation but with the KS orbitals replacing the HF orbitals, the LSDA XC energy, and gradient correction to the LSDA XC energy are all mixed together to create a new XC energy functional.

II.3.3 Basis set effects

A basis set is the mathematical description of the orbitals within a system used to perform theoretical calculation. Larger basis sets approximate the orbitals more accurately by imposing fewer restrictions on the location of the electrons in space. In the true quantum mechanical picture, electrons have a finite probability of existing anywhere in space. This limit corresponds to a infinite basis set expansion.

II.3.3.1 Slater and Gaussian type orbitals

There are two types of basis functions (called also *Atomic Orbitals*, AO, although in general they are not solutions to an atomic Schrödinger equation) commonly used in electronic structure calculations: *Slater Type Orbitals* (STO) and *Gaussian Type Orbitals* (GTO). The STOs have the functional form[204,235]:

$$\chi_{\zeta,n,l,m}(r,\theta,\varphi) = N\, Y_{l,m}(\theta,\varphi)\, r^{n-1} e^{-\zeta r}, \tag{II.3.3.1}$$

where N is a normalization constant and $Y_{l,m}s$ are the usual spherical functions (angular moment part). r, θ, and φ are the spherical coordinates and ζ is called the "orbital exponent". n, m, and l are the quantum numbers: principal, angular, and magnetic, respectively. The exponential dependence on the distance between the nucleus and the electron mirrors recalls the hydrogen atom orbitals. However, the STOs do not have radial nodes, nodes in the radial part are introduced by making linear contributions of STOs. The exponential dependence ensures a fairly rapid convergence with an increasing number of functions. However, the calculations of three- and four-centre two-electron integrals cannot be performed analytically. STOs are primarily used for atomic and diatomic systems where high accuracy is required, and in semi-empirical methods where all three- and four-centre integrals are neglected.

GTOs[236] can be written in terms of polar or Cartesian coordinates[204,236]:

$$\begin{aligned}
\chi_{\zeta,n,l,m}(r,\theta,\varphi) &= N\, Y_{l,m}(\theta,\varphi)\, r^{(2n-2-l)} e^{-\zeta r^2} \\
\chi_{\zeta,l_x,l_y,l_z}(x,y,z) &= N\, x^{l_x} y^{l_y} z^{l_z} e^{\zeta r^2},
\end{aligned} \tag{II.3.3.2}$$

where the sum of l_x, l_y, and l_z determines the orbital type. For example $l_x + l_y + l_z = 1$ is a p-orbital. Although a GTO appears similar in two sets of coordinates, there is a subtle difference. A d-type GTO written in terms of the spherical functions has five components $(Y_{2,2}, Y_{2,1}, Y_{2,0}, Y_{2,-1}, Y_{2,-2})$, but there appear to be six components in the Cartesian coordinates $(x^2, y^2, z^2, xy, xz, yz)$. The later six functions may be transformed to the five spherical d-functions and an additional s-function $(x^2 + y^2 + z^2)$. Similarly, there are 10 Cartesian f-functions, which may be transformed into seven spherical f-functions and one set of spherical p-functions. When only one d-function is present per atom, the saving obtained by removing the extra s-function is small, but if many d-functions and/or higher angular moment functions (f-, g-, h-, etc. functions) are present, the saving can be substantial. Furthermore, the use of only the spherical components reduces the problems of linear dependence for large basis sets.

The r^2 dependence in the exponential makes the GTO inferior to the STOs in two aspects. At the nucleus the GTO has zero slope, in contrast to the STO, which has a "cusp" (discontinuous derivative), and GTOs have problems representing the proper behavior near the nucleus. The other one problem is that the GTO falls off far from the nucleus too rapidly in comparison with a STO. Both, STOs and GTOs, can be chosen to form a complete basis, but the above considerations indicate that more GTOs are necessary for achieving a certain accuracy in comparison with STOs. Gaussian primitives are usually obtained from quantum calculations on atoms. Typically, the exponents are varied until the lowest total energy of the atom is achieved[237]. In some cases, the exponents are optimized independently, while in others, they are related to each other by an equation, and the parameters in this equation are optimized, e.g. Even-tempered or "geometrical" and well-tempered basis sets. The primitives derived this way describe isolate atoms and cannot accurately describe deformations of atomic orbitals brought by the presence of other atoms in the molecule. Basis sets for molecular calculations are therefore frequently augmented with other functions. For molecular calculations, these Gaussian primitives (PGTOs) have to

be contracted, i.e., certain linear combinations of them will be used as basis functions. The term contraction means "a linear combination of Gaussian primitives to be used as basis function"[204]:

$$\chi(CGTO) = \sum_i^k a_i \chi_i(PGTO).$$ (II.3.3.3)

Such a basis function will have its coefficients and exponents fixed. The contractions are called *Contracted Gaussian Type Orbitals* (CGTO) and they are especially useful for orbitals describing the inner (core) electrons, because they require a relatively large number of functions to represent the wave function cusp near the nucleus, and furthermore are largely independent of the environment. With the basis set contracting, always increases the energy, because it is restriction of the number of variational parameters. In this way, the basis set will be less inflexible, but the computational costs will be significantly reduced.

The *degree of contraction* is the number of PGTOs entering the CGTO, typically varying between 1 and 10. The simplification of a basis set in terms of primitive and contracted functions is given by the notation $(10s4p1d/4s1p) \rightarrow [3s2p1d/2s1p]$. The basis in parentheses is the number of primitives with heavy atoms (first row elements) before the slash and hydrogen after. The basis in the square brackets is the number of contracted functions. The previous notation will not tell how the contraction is done, it only indicates the size of the final basis (the size of the variational problem in HF calculations)[204]. The way the contractions are derived is not easy to summarize. Moreover, it depends upon the intended use for the basis functions. For some calculations, a good representation of the inner orbitals is necessary, while others require the best possible representation of valence electrons.

II.3.3.2 Pople style basis sets

6-31G. This is a split valence basis set, where the core orbitals are a contraction of six PGTOs, the inner part of the valence orbitals is a contraction of three PGTOs and the outer part of the valence represented by one PGTO[238]. The designation of the carbon/hydrogen basis is $(10s4p/4s) \rightarrow [3s2p/2s]$. In terms of contracted basis functions it contains the same number as the previous basis set (3-21G)[239], but the representation of each functions is better since more PGTOs are used.

6-311G. This is a triple split valence basis, where the core orbitals are a contraction of six PGTOs and the valence split into three functions, represented by three, one, and one PGTOs, respectively[240].

Diffuse and/or polarization functions can be added to each of the basis sets[241]. Diffuse functions are normally s- and p-functions and consequently go before the G. They are denoted + or ++, with the first + indicating one set of diffuse s- and p- functions on heavy atoms, and the second + indicating that a diffuse s- function is also added to hydrogen atoms. They allow orbitals to occupy a larger region of space. Basis sets with diffusion functions are important for systems where electrons are relatively far from nucleus: molecules with lone pair, anions, and other systems with significant negative charge, systems in their excited states, systems with low ionization potentials, descriptions of absolute acidities, and so on. Polarization functions are indicated after G, with a separate designation for heavy and hydrogen atoms. Split valence basis sets allow orbitals to change size, but not change shape. Polarized

basis sets remove this limitation by adding orbitals with angular momentum beyond what it is required for the ground state for the description of each atom.

6-31+G(d) and 6-311+G(d). They are split valence basis with one set of diffuse sp-functions on heavy atoms only and a single d-type polarization function on heavy atoms.

6-311++G**. This is the largest standard Pople basis set.

II.3.3.3 Hay-Wadt style basis sets

The Hay-Wadt LANL2DZ (Los Alamos National Laboratory 2 Double-Zeta[242-244]) basis set-relativistic *effective core potential* (ECP) combination were also used for theoretical calculations. The ECP's are derived from all-electron numerical HF atomic wavefunctions and fit to analytical representations for use in molecular calculations. *Ab initio* ECP have been generated to replace the Coulomb, exchange, and core-orthogonality effects of the chemically inert core electron in the transition metal atoms. For the second and third transition series relative ECP's have been generated, which also incorporate mass velocity and Darwin[245] relativistic effects into the potential. The *ab initio* ECP should facilitate valence electron calculations on molecules containing transition metal atoms with accuracies approaching all-electrons calculations at a fraction of the computational cost. ECP have been generated for use in molecular calculations where the outermost core orbitals are explicitly treated along with the valence orbitals.

II.3.4 Population analysis and electron densities

The probability of locating an electron at a given position r is given by the square of the wavefunction at that point[246]:

$$\rho(r) = \left| \Psi(r) \right|^2. \tag{II.3.4.1}$$

This electron density $\rho(r)$ can be expressed in terms of molecular orbitals (MO), assuming doubly occupied MOs[246]:

$$\rho(r) = 2 \sum_i^{N/2} \left| \phi_i(r) \right|^2. \tag{II.3.4.2}$$

Integration of the density over all space results in the total number of electrons in the system N [246]:

$$\int dr\, \rho(r) = 2 \sum_i^{N/2} \int dr \left| \phi_i(r) \right|^2 = N \tag{II.3.4.3}$$

The fundamental quest for the computational chemist is the extraction of chemically meaningful concepts from the wavefunction, taking into account that the electrons density ρ does not directly supply the classical chemical notions. The computational approaches to interpret the wavefunction (*population analysis*) have split along two basic approaches.

The orbital-based method. The earliest procedures were based on distributing the electrons between the atoms in a molecule based on the occupancy of the atomic orbitals.

The spatially-based method. The major alternative approach is to subdivide the physical space into regions that define the volume occupied by each atom in a molecule. Then, all electrons that are

found in this volume are assigned to that atom. One simply integrates ρ within an atomic basin. The problem is to define the extent of the atomic basin.

However, some other methods for determining the atomic charge have been developed. Neither of them makes reference either to orbitals or to the space associated with a given atom. Two of them involve the calculation of the atomic polar tensor, and the fitting of the electrostatic potential to an expansion of charges at the atomic nuclei, respectively[246].

The natural population analysis (NPA) implied in calculations, and briefly described below, is a major procedure of the orbital-based method, which was developed by Reed, Weinstock, and Weinhold[247-249], and attempts to define orbitals based on the molecular wavefunction, thereby obtaining different atomic orbital depending on the chemical environment.

The NPA method is based on occupancies of the orthonormal natural atomic orbitals, first defined by Löwdin[250], on each center. The method was illustrated with SCF-MO calculations on compounds spanning a wide range of ionic character, and with a variety of basis sets, to test the generality and stability of the calculated values. The natural charges were compared with corresponding results of Mulliken[251] population analysis, with the density integration results of Collins and Streitwieser[252], and with empirical electronegativity trends to asses their consistency with other theoretical and experimental measures of molecular charge distribution. For a supposition of a many-electron wavefunction ϕ that is composed of many Slater determinants Γ_α, the product P, which is the probability of simultaneously finding electron 1 at x_1, electron 2 at x_2, etc.[246] can be expressed as:

$$P = \phi(x_1, x_2, ..., x_N) \phi(x_1, x_2, ..., x_N) \qquad \text{(II.3.4.4)}$$

Normally, the interest is focused just on the probability of finding one electron regardless of the location of the remaining electrons. Integration over coordinates $x_2, ..., x_N$ leads to the reduced density function $P(x_1)$ [246]:

$$P(x_1) = \int dx_2, ..., x_N, \phi(x_1, x_2, ..., x_N) \phi(x_1, x_2, ..., x_N). \qquad \text{(II.3.4.5)}$$

This can be generalized to the first-order reduced density matrix $\gamma(x_1, x'_1)$ that depends on two continuous variables[207,246,253,254]:

$$\gamma(x_1, x'_1) = \int dx_2, ..., x_N, \phi(x_1, x_2, ..., x_N) \phi(x'_1, x_2, ..., x_N). \qquad \text{(II.3.4.6)}$$

The reduced density matrix can be converted into a discrete representation that involves sums over all the Slater determinants, MOs, and basis functions. This matrix will in general have many off-diagonal elements. The matrix is Hermitian, therefore it can be diagonalized. The orbitals that result from the diagonal reduced-density matrix are called natural orbitals, and the diagonal elements are the occupation number for these orbitals. The natural orbitals are orthonormal molecular orbitals having maximal occupancy. By analogy, the natural atomic orbitals are the atomic orbitals having maximal occupancy and are obtained as eigenfunctions or atomic subblocks of the density matrix, instead of the entire density matrix. The trick is to define these subblocks and then to obtain eigenfunctions that are orthonormal not only with the subblock, but with all other eigenfunctions.

Chapter III

Experimental procedures

"Knowledge is experiment's daughter."
(Leonardo Da Vinci, in "Pensieri" ca. 1492)

"All science is either physics, or stamp collecting."
(Ernest Rutherford, 1871-1937)

III.1 Chemicals and methods

"We have a habit in writing articles published in scientific journals to make the work as finished as possible, to cover up all the tracks, to not worry about the blind alleys or describe how you had the wrong idea first, and so on. So there isn't any place to publish, in a dignified manner, what you actually did in order to get to do the work."

(Richard Philips Feynman, Nobel Lecture, 1966)

III.1.1 Substrates and solutions processing

Different categories of SERS active surfaces have been prepared and used in our measurements: silver films, different classical colloids (silver and gold) and new nanostructured controlled core-shell colloids.

The *silver films*, which we used in our measurements, were prepared through thermal evaporation, and the films that were obtained have different particles roughness (1.05, 1.9, 2.9, and 14.4 Å). They were prepared in the Physics Institute of Würzburg University[194] after the procedure described in **Theoretical Background** and we possess them from **Dr. Ioana-Emilia Pavel** (Department of Chemistry and Biochemistry, University of California at Santa Barbara, Santa Barbara, USA, in **Professor Dr. Martin Moskovits**'s workgroup).

The *sodium-citrate reduced silver colloid* was prepared according to the Lee and Meisel method[187]. $AgNO_3$ (45 mg) was dissolved in 250 ml of distilled water and brought to boiling. A solution of 1% 3 sodium citrate-2 hydrate (5 ml) was added, and the mixture was kept on boiling for approximately one hour while stirring. All the time the cooling installation (water and liquid nitrogen circuits) has functioned. After boiling, the heating installation was stopped and the cooling installation has functioned yet for another two hours. The silver sol prepared in this manner was greenish yellow and had the absorption maximum at about 420 nm.

The *gold colloid* was prepared according to the method of Sutherland and Winefordner[255]. 40 ml distilled water into was added 0.1 ml of 4% (w/v) $HAuCl_4$ was stirred, then 1 ml of 1% (w/v) 3 sodium citrate-2 hydrate solution was added drop by drop, and the resulting mixture was boiled for 5 minutes without stirring. At 10 minutes after the 3 sodium citrate-2 hydrate adding, the colour of mixture developed into intensive blue, and at the end of boiling the colour was intensive red. The colloid obtained in this way had an absorption maximum about 530 nm.

The *core-shell colloids* were prepared according to the method reported by Rivas et al.[256]. There are presented different ratios of mixed core-shell colloids, but we used the mixed colloids with the

greatest reported plasmon resonance of silver and gold, respectively. The initial silver and gold colloids prepared according to the literature[187,255] were used as substrate for the core-shell colloids preparation. Additionally we have used $AgNO_3$ and $HAuCl_4$ for the initial gold and silver colloids coating. Afterwards, the corresponding volume of the citrate aqueous solution ($Na_3C_6H_5O_7$) in relation with $AgNO_3$ and $HAuCl_4$ volumes was added to induce the chemical reduction of Ag and Au and theirs deposition on Au and Ag particles, respectively.

Ag-coated Au colloid. On 100 ml gold colloid initially prepared according to the Sutherland and Winefordner method[255], was added drop-by-drop 5 ml of 10^{-3} M $AgNO_3$ aqueous solution with continuous stirring. After that, the correspondent volume of citrate aqueous solution (0.1 ml of 10^{-3} M $Na_3C_6H_5O_7$) in relation with $AgNO_3$ volume was added to produce the chemical reduction of silver and its deposition on the gold particles. The mixture was kept boiling while stirring for one hour under water and liquid nitrogen cooling. After boiling, the resulted colloid was cooled for two hours at room temperature keeping both cooling circuits functional. The silver-coated gold colloid was abbreviated $Au_{85}Ag_{15}$ and had an absorption maximum at 503 nm.

Au-coated Ag Colloid. On 50 ml silver colloid at first prepared according to the method reported by Lee and Meisel[187], was added drop-by-drop 2.5 ml $HAuCl_4$ of $3 \cdot 10^{-4}$ M aqueous solution with continuous stirring. Subsequently, the corresponding volume of citrate aqueous solution (0.06 ml of 10^{-4} M) in relation with $HAuCl_4$ volume was added to induce the chemical reduction of gold and its deposition on the silver particles. The mixture was kept boiling for 5 minutes. The notation of gold-coated silver colloid that we used in this work is $Ag_{97}Au_3$ and had an absorption maximum at 419 nm.

The solutions used in our measurements were prepared from powder dissolved in distilled water. Most of the samples employed in our studies were purchased from Aldrich, while some of them were commercially available, and others were synthesized. For the commercially available samples no analytical purity certificate was accessible, while in the case of substances purchased from Aldrich, the purity was known. The concentration ranges which we used were:

» food additives:

  (a) tartrazine (E102): 10^{-1}-10^{-8} M,

  (b) sodium benzoate (E211): 1-10^{-2} M,

  (c) erythrosine (E127): 10^{-1}-10^{-9} M,

  (d) indigo carmine (E132): 10^{-3}-10^{-9} M,

  (e) monosodium glutamate (E621): 5-10^{-2} M;

» medicines:

– anti-inflammatory drugs:

  (i) aspirin: 10^{-5} M,

  (ii) paracetamol: $3.3 \cdot 10^{-1}$-8×10^{-2} M;

– anti-malarial drugs:

  (x) mefloquine hydrochloride (MQ): 10^{-2} M,

  (xx) chloroquine diphosphate (CQ): 4×10^{-2} M;

» La, Ce, Nd complexes of:

   (^{I}) 3,5 pyrazoledicarboxylic,

   (^{II}) orotic acid,

   (^{III}) 5 aminoorotic acid,

» others

   (') tetrahydrofuran.

   Small amounts of water solution of   (a) E102 10^{-5}-10^{-8} M

   (b) E211 $2x10^{-1}$-10^{-2} M

   (c) E127 10^{-6}-10^{-9} M

   (d) E132 10^{-4}-10^{-9} M

   (e) E621 10^{-1}-10^{-2} M

   (i) aspirin 10^{-5} M

   (ii) paracetamol $8x10^{-2}$ M

   (x) MQ 10^{-2} M

   (xx) CQ $4x10^{-2}$ M

were added to   (a) and (e) 3 ml,

   (b)-(d), (i), and (ii) 3.5 ml,

   (x) and (xx) 2 ml of colloid.

NaCl solution (10^{-1} M) was also added (10:1) for producing a stabilization of the colloidal dispersion and a considerable enhancement of the SERS spectra[73]. Final concentrations of the SERS/SERRS sample were:

(a) 10^{-6}-10^{-10} M,

(b) $2.8x10^{-3}$-$2.8x10^{-4}$ M,

(c) $0.39x10^{-7}$-$0.39x10^{-10}$ M,

(d) 10^{-4}, $0.29x10^{-6}$, and $0.03x10^{-9}$ M,

(e) $9.9x10^{-4}$, $6.6x10^{-4}$, $3.3x10^{-4}$, $1.7x10^{-4}$, $1.3x10^{-4}$, $9.9x10^{-5}$, and $6.6x10^{-5}$ M

(i) $0.8x10^{-7}$ M (buffered) and $0.5x10^{-7}$ M (unbuffered),

(ii) $8x10^{-2}$ M (sinus and normal),

(x) $0.9x10^{-5}$ M,

(xx) $3.9x10^{-5}$ M.

   The HCl and NaOH solutions (10^{-1} M) were used to adjust the pH value of the solutions and pH paper and/or pH meter were employed to measure the pH values.

III.1.2 Syntheses

   The lanthanum, cerium, and neodynium complexes of 3,5-pyrazoledicarboxylic acid, orotic acid and 5-aminoorotic acid were obtained by our coworker: **Dr. Irena Kostova** (Department of Chemistry, Faculty of Pharmacy, Medical University, Sofia, Bulgaria). The method of complexes synthesis, which was employed is described below.

The compounds used for preparing the solutions were Merck products, analytically pure reagents: $La(NO_3)_3 \cdot 6H_2O$, $Ce(NO_3)_3 \cdot 6H_2O$, $Nd(NO_3)_3 \cdot 6H2O$. The complexes were synthesized by the reaction of the La(III), Ce(III), Nd(III) salts with the ligand, in amounts equal to metal: ligand molar ratio of 1: 2. The synthesis of the complexes were made in different ratio (1:1, 1:2, 1:3) but in all the cases the product was with the composition 1:2. The complexes were prepared by adding an aqueous solution of La(III), Ce(III), and Nd(III) salts to an aqueous solution of the ligand subsequently raising the pH of the mixture gradually to ca. 5.0 by adding dilute solution of sodium hydroxide. The reaction mixture was stirred with an electromagnetic stirrer at 25 °C for one hour. During the mixing of the solutions, precipitates were obtained. The precipitates were filtered (pH of the filtrate was 5.0), washed several times with water and dried in a desicator to constant weight. The obtained complexes were insoluble in water, methanol, and ethanol, but well soluble in DMSO.

The La(III), Ce(III), and Nd(III) complexes of orotic acid were obtained as previously discussed. The formation of the complex may be represented by the following equations:

$$NaOA + H_2O \leftrightarrow Na^+ + OH^- + HOA \tag{1}$$

$$[La(H_2O)_n]^{3+} + H_2O \leftrightarrow [La(OH)(H_2O)_{n-1}]^{2+} + H_3O^+ \tag{2}$$

$$[La(OH)(H_2O)_{n-1}]^{2+} + 2OA^- \rightarrow La(OA^-)_2(OH)(H_2O) + (n-2)H_2O, \tag{3}$$
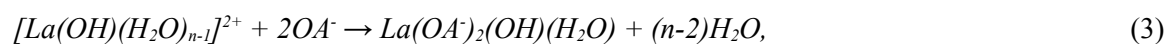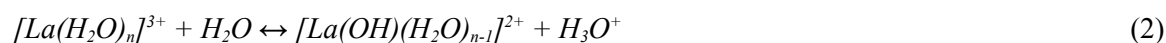
where $HOA = C_5N_2O_4H_4$ and $OA^- = C_5N_2O_4H_3^-$.

III.2 Device description

> "Scientific apparatus offers a window to knowledge, but
> as they grow more elaborate, scientists spend ever more
> time washing the windows."
>
> (Isaac Asimov)

> "Seen on the door to a light-wave lab: Do not look into
> laser with remaining good eye."
>
> (Anonymous)

> "Safety measure: Close your eyes when you see
> the laser light coming"
>
> (Anonymous)

A UV-VIS-NIR spectrophotometer (Perkin-Elmer Lambda 19) was used for recording the electronic absorption spectra of the samples with a scan speed of 240 nm min^{-1}.

The solid-state infrared spectra were recorded in KBr in the 4000-400 cm^{-1} wavenumber range using a FT-IR 113V Bruker spectrometer.
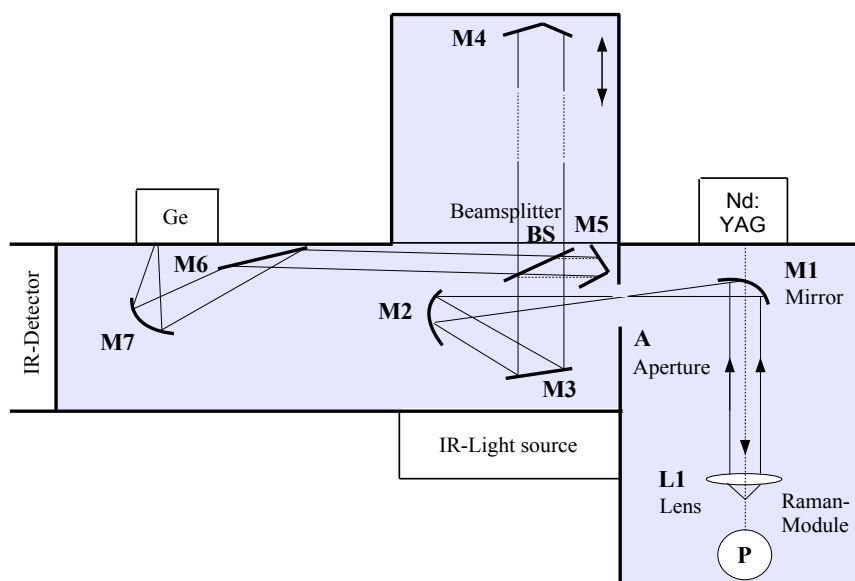
Figure III.2.1. Brief optical diagram of the Bruker IFS 120-HR spectrometer
with an integrated FRA 106 Raman module.

The FT-Raman spectra were obtained by using a Michelson interferometer (Bruker, IFS 120-HR) (Fig. III.2.1) with an integrated Raman module (Bruker, FRA106). The 1064 nm radiation from a Nd:YAG laser with an output of *ca.* 1000 mW on the sample was employed for the excitation. A Ge detector operating at liquid nitrogen temperature was used. Interferograms were recorded at a spectral resolution of 1 cm^{-1}.The spectral data were analyzed using the OPUS 2.0.5 software.
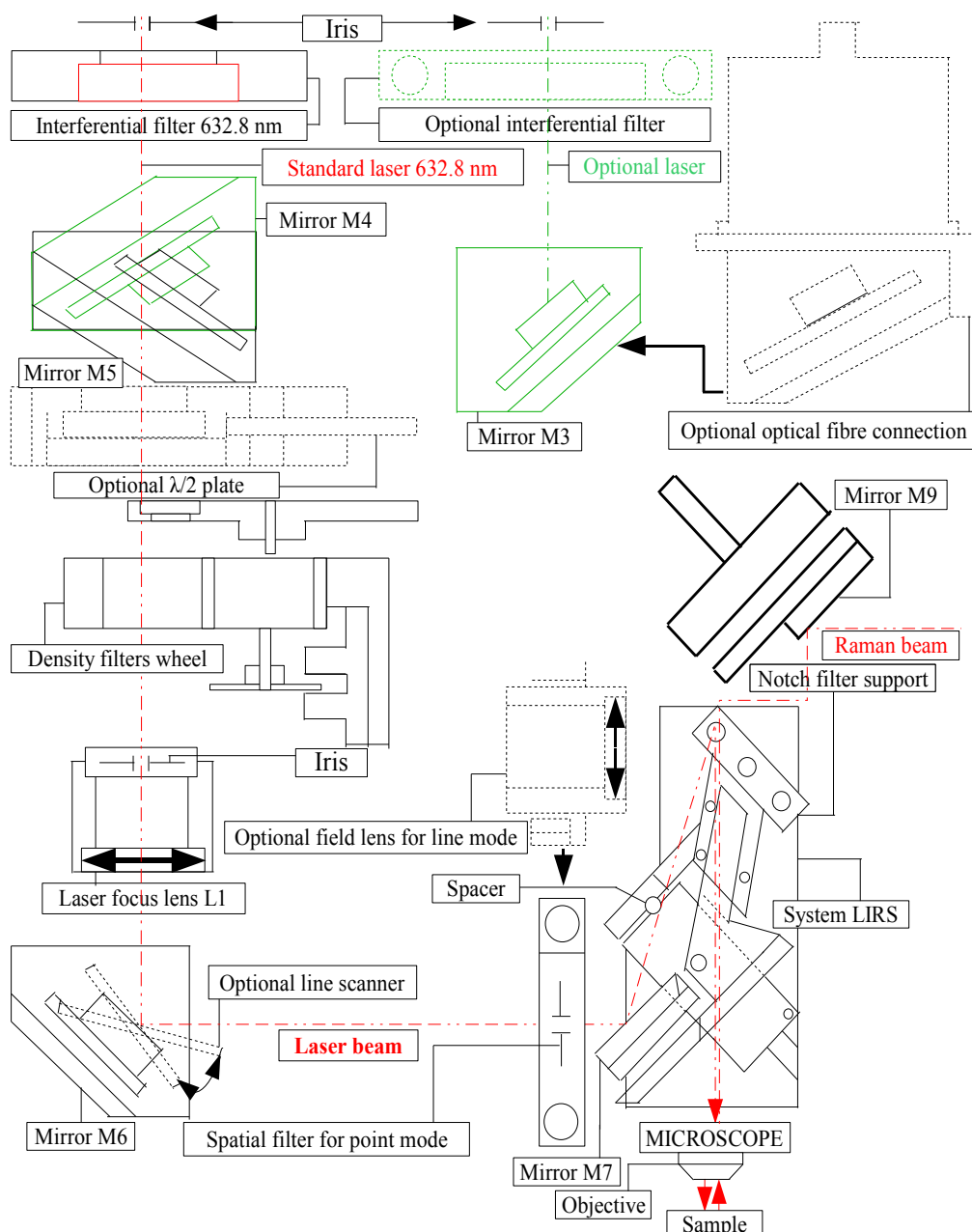
Figure III.2.2. Optical diagram of the LabRam integrated Raman system.

The micro-Raman and SERS spectra on silver colloids were recorded with a Raman microspectrometer (Horiba-Jobin-Yvon, model LabRam), which was equipped with 1800 grooves/mm holographic gratings (Fig. III.2.2). The excitation wavelength is supplied by an internal HeNe laser (632.817 nm) with an output of 3.6 mW, mounted on the back of the instrument. An entrance for another external laser beam is also placed on the back side (laser wavelength available includes virtually any laser within 440-800 nm). The external lasers which were used in our measurements are the 514.5 nm excitation line from an Ar^+ ion laser (Spectra Physics, model 2016) with an output of *ca.* 250 mW and the NIR laser diode (784.8 nm) with an output of *ca.* 35 mW. The laser is totally reflected by the notch filter towards the sample under microscope and the Raman scattering is totally transmitted through the notch filter towards the confocal hole and entrance slit spectrometer. Raman scattering can also be entered via a fiber optic probe. The fiber optic entrance is situated also on the back side of the instrument. The laser is

coupled to another fiber optic going to the probe using the objective of the microscope. The spectra were collected in the backscattering geometry using a microscope equipped with an Olympus LMPlanFL 50x or 10x objective with a spectral resolution of 4 cm^{-1}. The spectrally dispersed Raman signal was detected with a Peltier-cooled CCD camera, with 16 bit dynamic range, size 1024x256 pixel. The spectral data were analyzed using the LabSpec 4.08 software. The laser power on the sample used in our measurements is indicated for each figure caption.
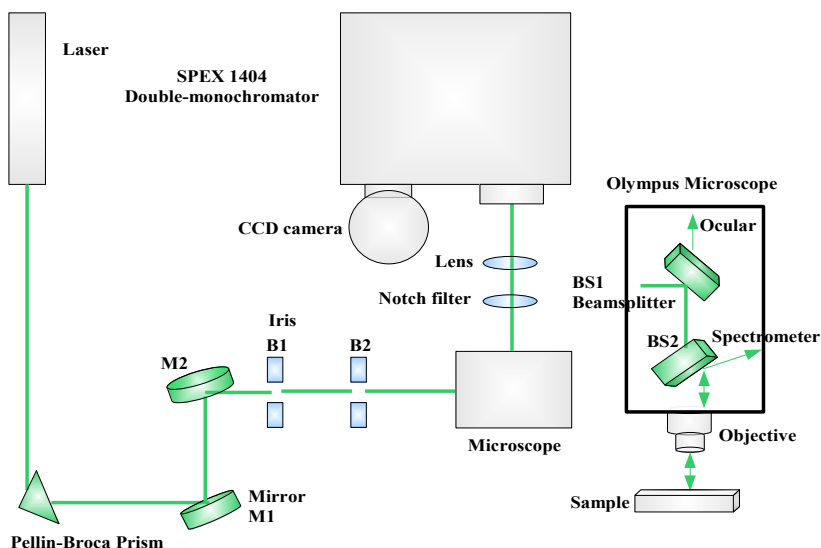
Figure III.2.3. Optical diagram of the SPEX 1404 double spectrometer.

Raman spectra were recorded by using a SPEX 1404 double monochromator (2400 grooves/mm) gratings (Fig. III.2.3) employing a scanning multichannel detection scheme. The 514.5 nm line from an Ar$^+$-Laser (Spectra Physics) was used as excitation source for recording the spectrum. The laser excitation was coupled to an optical microscope Olympus U-CMAD-2 with two objectives: DPLAN 20 160/0.17 and ULWD MS-PLAN 80/0.75. Noteworthy features of this instrumentation are a notch filter to reject the Rayleigh scattering and a liquid nitrogen-cooled charge-coupled device (Photometrics model SDS 9000 CCD camera) to provide state-of-art quantum efficiency in Raman detection. The laser power at the sample was ~300 mW and the resolution was 2 cm^{-1}. The MAPS VO 98.5 analyzing software package was used in this case for the acquisition data.

III.3 Computational details

> "Thus the partial differential equation entered theoretical physics as a handmaid, but has gradually become mistress."
>
> (Albert Einstein, 1879-1955)

The DFT calculations were performed using Gaussian 98[257] and Gaussian 03[258]. Becke's standard exchange functional (B)[259] and Becke's three-parameter hybrid exchange functional (B3)[221,259] in combination with Perdew and Wang's gradient-corrected correlation functional (PW91)[260,261] and the correlation functional of Lee, Yang and Parr (LYP)[234] were employed in the DFT calculations. Two different basis sets were used for almost all compounds: the 6-311++G** Pople split valence basis set and the LANL2DZ basis set. The LANL2DZ basis set[262] was chosen for extending the calculations at the same level of theory to molecules adsorbed on a silver surface and because of the presence of the lanthanides atoms in complexes. The 6-311+G(d) and 6-31+G(d) Pople split valence basis sets implemented in the Gaussian 98 program[257] were chosen in the geometry optimization and normal modes calculations of tartrazine (E102) and erythrosine B (E127), taking into account that results obtained with a split valence set are a significant improvement against those obtained with a minimal basis set[263]. Harmonic vibrational wavenumbers including IR and Raman intensities were calculated analytically for the fully optimized molecular geometries with or without symmetry restrictions, according to the each case. Only real harmonic vibrational wavenumbers were obtained for all structures, confirming the localization of global minima on the potential energy surfaces were obtained.

Quantum chemistry provides a concept to understand the phenomena of hydrogen bonding and its relationship to the spectral features of the molecules. The ground state geometries for THF and its hydrogen-bonded complexes, with one and two molecules of water were optimized by the gradient procedure at the second order level of closed shell Møller-Plesset (MP2) perturbation theory employing the 6-31++G(d,p) basis set. The wavenumbers for the different normal modes were also computed at the MP2/G** level of ab-initio theory[208] with Gaussian 98 program[257].

Chapter IV

Concentration dependent wavenumber shifts and linewidth changes of C_4H_8O in a binary system ($C_4H_8O+H_2O$)

Raman spectra of neat tetrahydrofuran (C_4H_8O), hereinafter, frequently referred to as THF and its binary mixtures in aqueous (H_2O) media were investigated using a rather sensitive scanning multichannel detection scheme. The spectra were recorded in the 800-1100 cm^{-1} wavenumber region for the neat liquid; THF and mixtures with varying mole fractions of THF from 0.1 to 0.9. The spectra were, however, analyzed in two different regions, 800-1000 and 975-1100 cm^{-1}. The spectra in the former region show an asymmetric peak in the neat liquid, which was deconvoluted to two Raman line profiles having peaks at ~910 cm^{-1} and at ~914 cm^{-1}, corresponding to ν(C-O) and ν(C-C) stretching modes, respectively. At other concentrations, the spectra were analyzed for three Raman line profiles and the concentration dependence of wavenumber position and the linewidth for an additional peak at ~896 cm^{-1} (at mole fraction of THF, C=0.9) exhibited a peculiar trend, which has been explained in detail by using the indirect dephasing model. The spectra in the latter region show two Raman peaks, an intense one at ~1030 cm^{-1} and a relatively less intense one at ~1071 cm^{-1} in the neat liquid. A striking feature is that their separation goes on decreasing with dilution. The optimized geometries and vibrational wavenumbers for various normal modes for neat THF as well as hydrogen bonded complexes were calculated using *ab initio* theory at the MP2 level and the results have been used to understand the changes in the spectral features with the varying concentration of the two components in the binary mixture, $C_4H_8O+H_2O$[264].

IV.1 Study presentation and motivation

The study of vibrational relaxations, such as vibrational dephasing, is one of the most powerful tools to investigate the dynamical processes in the liquid phase of the matter. It is possible to identify two principal mechanisms for interpreting the relaxation process[265]. The first process, namely population

relaxation involves a change in the quantum state of the relevant normal mode, while the second process, namely dephasing, is related to the phase decay of the vibrational wavefunction.

In the present study were chosen, the THF (C_4H_8O) molecule as the reference system, which represents the simplest model system for the vibration of the furanose ring of ribose and deoxyribose embedded in the nucleic acid backbones, and water (H_2O) as the solvent which is a much more common hydrogen donor agent involved in hydrogen bonding, especially in most of biological systems. The basic aim was to investigate the vibrational dephasing of ν(C-O) and ν(C-C) stretching modes in the hydrogen bonded species $C_4H_8O\cdots HOH$.

The two channels of relaxation, namely population relaxation and vibrational dephasing[266,267], are ultimately responsible for the spectral band shape and thereby contribute to the vibrational correlation function. In most of the cases, however, the vibrational line profiles are determined mainly by the vibrational dephasing, which takes place on a picosecond time-scale. It is also extremely sensitive to environmental changes in the vicinity of the reference molecule, which may give rise to a small wavenumber shift and linewidth change. Thus, even small changes in the spectral features of the system and the solvent may be used as a probe to investigate certain aspects of the dynamics of a reference vibrational mode. Both IR and Raman spectroscopies are the basic experimental techniques for such a study. However, the Raman study has an added advantage that through polarized Raman study, the isotropic part of Raman scattered intensity can easily be separated out, which in turn may directly be used to understand the vibrational dephasing. Hence, it is well suited for the investigation of nucleic acids also in their natural environment, i.e. aqueous solution[268].

The method of polarized Raman spectroscopy can provide information on molecular symmetry, structure and dynamics rather precisely, whereas it may be a difficult proposition to determine the structure of highly reactive molecules by standard structural tools, such as X-Ray diffraction and, in fact, many of them have been observed under special conditions such as matrix isolation. At times, microwave spectroscopy and electron diffraction are also applicable. In contrast to these, the Raman scattered intensity depends on the change in polarizability during a molecular vibration, and the slightest change in any of the six components of the polarizability tensor induces that vibrational active Raman modes allows the probing at the atomic level. The totally symmetric vibrations are essentially Raman active, but the vibrations which are non-totally symmetric, may or may not be Raman active and this sheds some light on the structure and symmetry of the molecule. An important parameter for a Raman band is its depolarization ratio, $\rho = I_\perp / I_\parallel$ ($I_\parallel$ and $I_\perp$ being parallel and perpendicular components of the Raman scattered intensity). A Raman band with $\rho = 0.75$ is said to be depolarized, for $\rho < 0.75$ is partially polarized, while for $\rho = 0$ it is completely polarized. The measurement of the depolarization ratio thus assists in the determination of symmetry of the vibrational mode.

In view of the foregoing discussions and conclusions drawn, it was thought worthwhile to study the polarized Raman spectra of THF in aqueous solutions of different concentrations and look for the environmental effects on changes in wavenumber position and linewidth of the Raman bands of THF corresponding to two prominent normal modes, namely the ν(C-O) and ν(C-C) stretchings. In order to

obtain information on structure-property correlation in aqueous solution of THF, *ab initio* calculations were also made. The geometrical structure and harmonic force fields on C_2 conformer of THF were calculated by using Hartree-Fock density functional theory and Møller-Plesset perturbation theory[208] of the second order. These scaled force fields were found to reproduce the wavenumbers within overall 1% accuracy with the B3LYP functional which are considered to yield the most accurate results[269].

IV.2 Experimental and theoretical considerations

IV.2.1 Experimental details

The sample of THF was obtained from Aldrich Co. and was used without further purification. For preparing the binary mixture, triple distilled water was used as solvent. Raman spectra were recorded by using a SPEX 1404 double monochromator employing a scanning multichannel detection scheme (Chapter III.2, Fig. III.2.3).

Since a single window covered 50 cm⁻¹, in order to cover 200 cm⁻¹ in one recording, the desired range was divided into four single windows. However, in each single window two or three overlaps were required for a good S/N ratio. The $I_\parallel$ and $I_\perp$ components were recorded separately and the isotropic part of the spectrum was obtained using the relationship $I_{iso} = I_\parallel - 4/3 I_\perp$. The polarization arrangement was adjusted by using a Glan-Taylor polarizer and double Fresnel rhomb for polarization rotation before the sample. Another Glan-Taylor polarizer was used as analyzer and was placed at the entrance slit of the spectrometer. The sample was kept in a rotating quartz cell and 90º scattering geometry was applied. All measurement were carried out at room temperature.
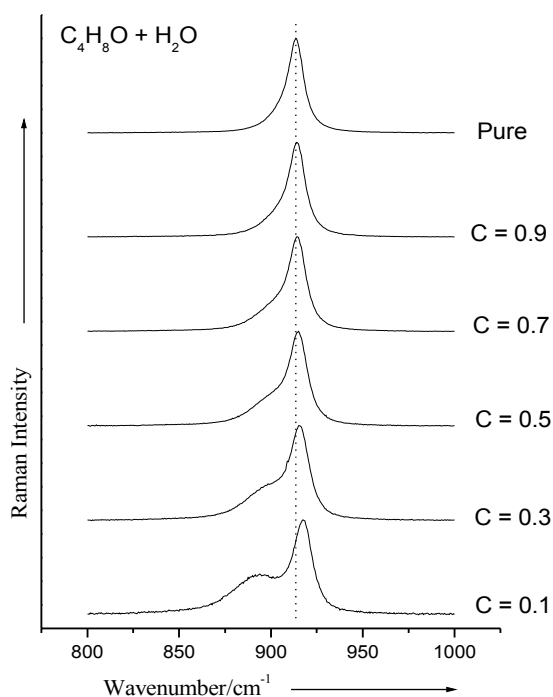
Figure IV.2.1.1. Isotropic part of the Raman spectra in the 800-1000 cm⁻¹ wavenumber region, for neat C_4H_8O and its binary mixture ($C_4H_8O+H_2O$) at five mole fractions of C_4H_8O, C=0.9, 0.7, 0.5, 0.3, and 0.1.

The entrance slit of the double monochromator was kept constant at 100 μm for all the measurements and this gives a resolution of ~1.5 cm^{-1}. It was quite evident from the quality of the spectra that the S/N ratio was reasonably good (> 40). The $I_\parallel$ and $I_\perp$ components of Raman spectra were recorded in two different regions, 800-1000 cm^{-1} and 975–1100 cm^{-1} for neat tetrahydrofuran (THF) and nine other binary mixtures (THF+H$_2$O) containing the reference system, THF with mole fractions C from 1.0 to 0.1. The isotropic part of the Raman spectra for neat THF and binary mixtures, obtained as mentioned above, in the region 800-1000 cm^{-1} are presented in Fig. IV.2.1.1. A noticeable asymmetry in the observed Raman can be ascribed to the presence of two bands separated by 5 cm^{-1}, which are obtained through a line shape analysis yielded at almost the same wavenumber positions, and linewidths within 0.1 cm^{-1}. This leaves no room for doubt that the peaks could be an artefact of the fitting procedure. The linewidth throughout the paper refer to the full width at half maximum (FWHM).

The parallel part of the Raman scattered intensity, $I_\parallel$ in the wavenumber region 975-1100 cm^{-1} for neat THF and five other mixtures with mole fractions, C=0.1, 0.3, 0.5, 0.7, and 0.9 of the reference system, THF are presented in the Fig. IV.2.1.2. In fact, $I_\perp$ in this region was too weak and too noisy and it was practically impossible to get the isotropic part I_{iso}, and hence it was considered worthwhile to analyze only $I_\parallel$ for wavenumber shift, which, in fact, gave very interesting results.
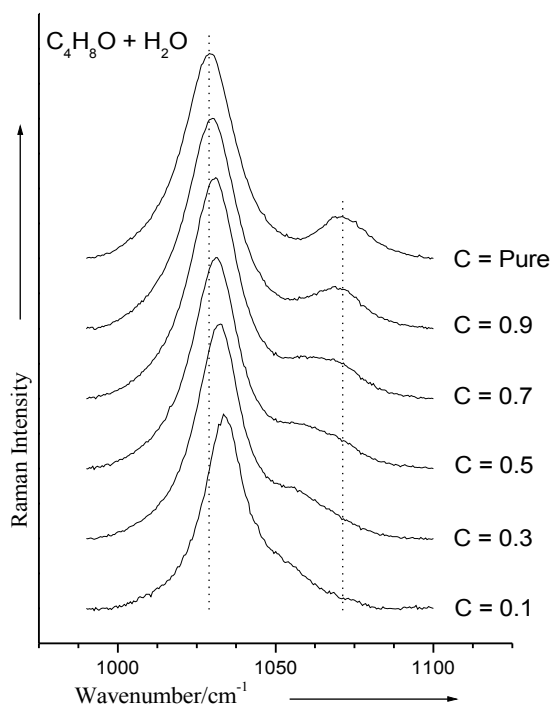
Figure IV.2.1.2. Parallel part of the Raman spectra in the 975-1100 cm^{-1} wavenumber region, for neat C$_4$H$_8$O and its binary mixture (C$_4$H$_8$O+H$_2$O) at five mole fractions of C$_4$H$_8$O, C=0.9, 0.7, 0.5, 0.3, and 0.1.

IV.2.2 Ab initio calculations of optimized geometry for THF and its complexes with water

Quantum chemistry provides a concept to understand the phenomenon of hydrogen bonding and its relationship to the observed spectral features. The ground state geometries for THF and its hydrogen

bonded complexes, with one and two molecules of water were optimized by the gradient procedure at the second order level of closed shell Møller-Plesset (MP2) perturbation theory employing the 6-31^{++}G(d,p) basis set. The wavenumbers for the different normal modes were also computed at the MP2/G** level of *ab initio* theory[208] with Gaussian 98 program[257]. The optimized geometries obtained from the *ab initio* calculations for the monomer and hydrogen bonded complexes of THF with one water molecule are shown in Fig. IV.2.2.1(a) and (b), respectively.

In the latter case, only one hydrogen bond is formed between the H atom of water molecule and the O atom of THF molecule, the hydrogen bond length in this configuration being 1.873 Å, which will be said to be a strong hydrogen bond. In another configuration, the hydrogen atoms of two water molecules form hydrogen bonds with the same O atom of the reference molecule THF as shown Fig. IV.2.2.1(c), the hydrogen bond length in this case being 1.871 and 1.878 Å. These two bond lengths are almost the same, but significantly different as compared to the case when one molecule of H_2O is attached to the reference molecule, THF (Fig. IV.2.2.1(b)). The calculation on geometry optimization and wavenumbers of the different modes of the neat THF and hydrogen bonded complexes revealed that the hydrogen bond formation causes a red shift in the ν(C-O) stretching mode, which is quite usual. On the contrary, a blue shift is observed in the ν(C-C) stretching mode. These aspects can be explained in terms of solute-solvent interaction[270,271].
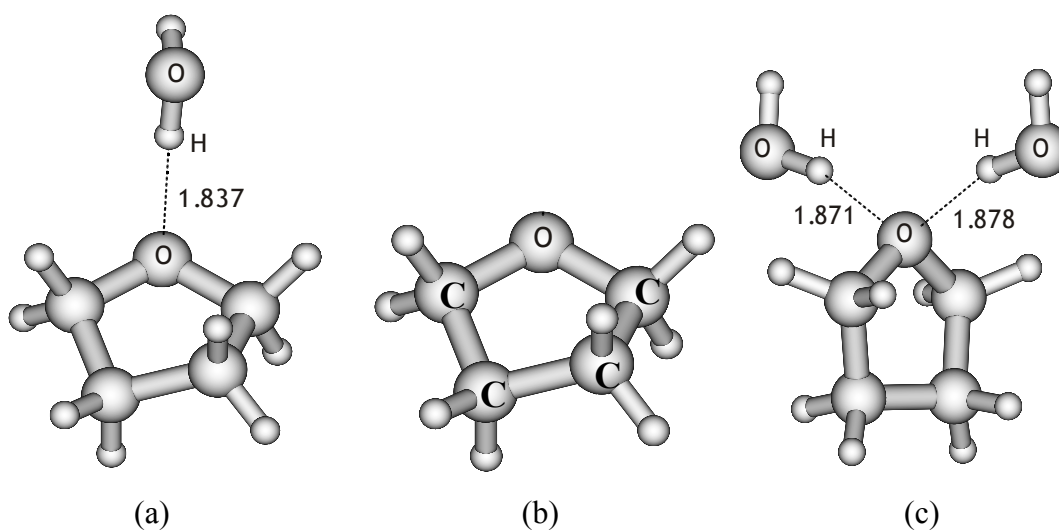
Figure IV.2.2.1. Optimized geometries obtained from ab initio calculations for: C_4H_8O (a); the complex of C_4H_8O forming one hydrogen bond with one H_2O molecule (b); the complex of C_4H_8O forming two hydrogen bonds with two H_2O molecules (c). The geometries optimization was made in **Professor Dr. B. P. Asthana'**s workgroup.

IV.2.3 Variation of peak positions with concentration for ν(C-O) and ν(C-C) modes

The variation of peak positions with concentration for the major Raman modes, namely ν(C-O) and ν(C-C) stretching modes under study, lying in the region 800-1000 cm^{-1} (as shown in Fig. IV.2.3.1) exhibit different trends when the Raman line profile is carefully analyzed. This may be characteristic of different types of intermolecular interactions and their extent in mixtures with varying mole fractions of

the reference system, C_4H_8O, as well as of the dephasing mechanisms operative for these modes. The first band at ~910 cm^{-1}, which is less intense and broad, corresponds to the ν(C-O) stretching mode in the neat liquid, while the second one at ~910 cm^{-1}, which is more intense and sharp, corresponds to the ν(C-C) stretching mode[269]. An additional band starts appearing in the ν(C-O) stretching region, when H_2O is added into the reference system, and this one may be attributed to the hydrogen bonded complex, $C_4H_8O\cdots HOH$ similar to earlier studies[272,273] on (HCONH$_2$+CH$_3$OH) and [(CH$_3$)$_2$C=O+(CD$_3$)$_2$C=O], respectively.
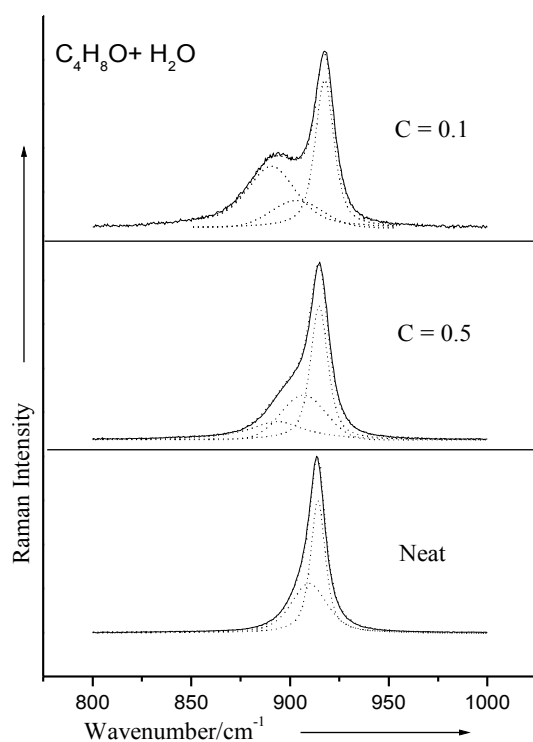
Figure IV.2.3.1. Analyzed isotropic part of Raman spectra in the 800-1000 cm^{-1} wavenumber region for the neat C_4H_8O and two other mole fractions of C_4H_8O, C=0.5 and 0.1 in the binary mixture ($C_4H_8O+H_2O$).

A rigorous line shape analysis of the Raman line profile was performed taking widely varying initial guesses, especially for the linewidths. However, even for neat liquid, each guess yields two bands at the same wavenumber positions, ~910 and ~914 cm^{-1}. During the fitting of the Raman line profile, each component was assumed to be a mixture of a Lorentzian and a Gaussian profile. In fact, an initial guess of Lorentzian to Gaussian ratio based on some standard methods[265] is given as the input parameter. The fitting procedure takes a sum of Lorentzian and Gaussian fractions (in %) and the fitting routine *Spectra Calc* has a provision to adjust this ratio to get the best fit to the experimental line profile. Thus although the fitting is made taking a sum of Lorentzian and Gaussian, a judicious mixture of the two profiles is nearly as good as a Voigt profile[265]. When the profiles for the different mixtures with varying molar ratio of C_4H_8O and H_2O were analyzed, in addition to ν(C-O) and ν(C-C) stretching modes obtained at ~910 and ~914 cm^{-1}, respectively, it was almost imperative to assume a third peak at a significantly reduced wavenumber in order to get the best fit to the experimental line profile. The new peak was separated by ~14 cm^{-1} (for C=0.9) towards the lower wavenumber side from the band at ~910 cm^{-1} corresponding to

the ν(C-O) stretching mode (Table IV.2.3.1).

Since the intensity of this new band goes on increasing with increasing solvent concentration, this could easily be explained as a Raman band caused due to the formation of a hydrogen bond between the reference molecule and the solvent molecule. The intensity ratio of the band attributed to hydrogen bond formation and the main band corresponding to ν(C-O) stretch, I_{hyb}/I_{main} is depicted in Fig. IV.2.3.2 as a function of mole fraction of the reference system. However, different complexes of C_4H_8O and H_2O molecules are possible as shown in Fig. IV.2.2.1(b) and (c).

Table IV.2.3.1. Peak positions and linewidth (FWHM) of the peaks corresponding to ν(C-C) and ν(C-O) of neat C_4H_8O as well as its hydrogen bonded complexes, as obtained from the analysis of the measured line profiles.

Mole fraction (C₄H₈O)	Peak 1		Peak 2		Peak 3	
	Peak Position (cm⁻¹)	Linewidth (FWHM)(cm⁻¹)	Peak Position (cm⁻¹)	Linewidth (FWHM)(cm⁻¹)	Peak Position (cm⁻¹)	Linewidth FHWM(cm⁻¹)
0.1	890.3	28.7	903.4	31.3	917.5	11.4
0.2	892.2	29.1	904.7	28.5	916.6	11.3
0.3	892.3	30.7	905.7	27.6	915.1	11.2
0.4	892.5	31.6	906.7	26.7	915.6	11.0
0.5	893.4	33.4	906.8	27.3	914.8	10.6
0.6	894.1	31.3	907.5	25.6	915.0	10.4
0.7	894.4	30.4	907.6	25.0	914.4	10.1
0.8	894.6	30.5	908.3	24.6	914.1	10.0
0.9	896.3	29.9	909.1	22.4	913.8	9.4
1.0			909.6	21.6	914.2	8.9
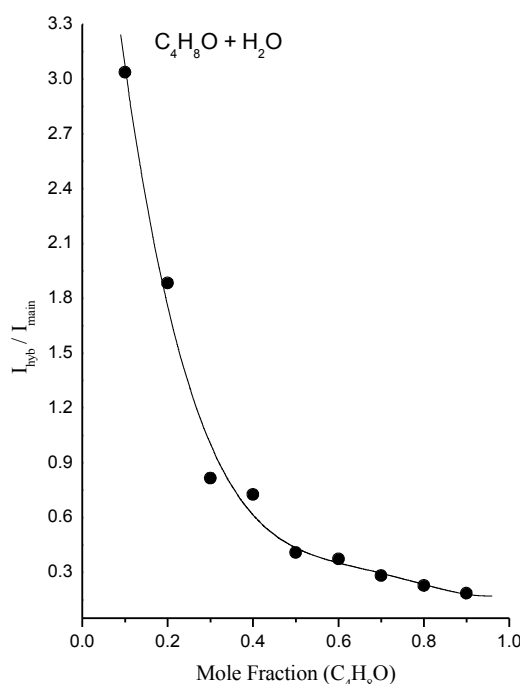
Figure IV.2.3.2. Variation of intensity ratio of the component band due to hydrogen bonding to the main Raman band due to ν(C-O) stretching. I_{hyb}/I_{main} with the mole fraction of C_4H_8O.

The variation of the ratio, I_{hyb}/I_{main} with concentration clearly proves that the additional band is due to hydrogen bonded complex. The ratio I_{hyb}/I_{main} varies slowly upon dilution up to C=0.5. On further dilution, the I_{hyb}/I_{main} ratio assumes higher values and the plot shown in Fig. IV.2.3.2 shows a

sudden rise in this ratio at high dilutions. This reveals that at higher dilutions probably all possible hydrogen bond formations shown in Fig. IV.2.2.1(b) and (c) take place, and a relatively small number of free C_4H_8O molecules are available.

The peak position of the Raman band at ~910 cm^{-1} in neat liquid, which has been assigned to ν(C-O) stretching mode, shows a downshift by ~7 cm^{-1} and the band at ~914 cm^{-1} corresponding to ν(C-C) stretching mode shows an upshift of ~3 cm^{-1} in going from mole fraction C=0.9 to 0.1, designated as Peak 2 and Peak 3, respectively, as presented in Table IV.2.3.1. In the binary mixture ($C_4H_8O+H_2O$), the O atom of the C-O group of C_4H_8O forms a hydrogen bond with the H atom of the solvent molecule H_2O (Fig. IV.2.2.1(b)), and in another optimized geometry, the O atom of the C-O group forms hydrogen bonds with the H atoms of the two H_2O molecules (Fig. IV.2.2.1(c)). The H atom of the H_2O molecules moves closer (1.837 Å) to the O atom of the C-O group of the reference molecule, THF in one configuration, while the other configuration, when the two hydrogen bonds are formed, the length of hydrogen bonds are relatively larger (1.871 and 1.878 Å) as shown in Fig. IV.2.2.1(c). The increased bond length of the two hydrogen bonds obviously means that the corresponding hydrogen bonds, O···H are slightly weaker in strength. However, the doubly hydrogen bonded species becomes more important at higher dilution, since two hydrogen bonds are formed with the same O atom leading to an obvious decrease in the C-O bond strength of the reference molecule. As a consequence of this, the wavenumber position of ν(C-O) stretching mode would decrease with dilution.

IV.2.4 Concentration dependence of wavenumber shifts in the 975-1100 cm^{-1} region

The parallel part of Raman spectra recorded in the region 975-1100 cm^{-1} shows two peaks, one intense at ~1029 cm^{-1} and another peak which is less intense at ~1070 cm^{-1} (Fig. IV.2.1.2). These two Raman bands may be assigned as the combination bands[269] of different ν(C-C) stretching and ν(C-H) bending modes. When the Raman profile is carefully analyzed for the neat as well as for the mole fractions, C=0.1, 0.3, 0.5, 0.7, and 0.9,the intense band at ~1029 cm^{-1} is blue shifted (5 cm^{-1}) and the band at ~1070 cm^{-1} is red shifted (16 cm^{-1}) upon dilution. It is evident that a blue shift will be caused owing to an increase in the corresponding force constant. This may be a consequence of transfer of electronic charge cloud to the ring. Another explanation for the blue shift in the solution may be offered in terms of solvent-solute repulsive interactions as argued by Schweitzer and Chandler[270], which shortens the bond and leads to a blue shift. A shorter bond length essentially implies an increase in the force constant too. It is also worth mentioning that such interactions cause not only a blue shift, but also a motional narrowing[270,271] in the linewidth which has also been observed for the ~1029 cm^{-1} mode (Table IV.2.4.1).

In the case of the ~1070 cm^{-1} mode, however, it is more likely that the H atom of the solute, C_4H_8O may interact with the O atom of the solvent, H_2O and this causes a downshift due to attractive interaction, which may be more pronounced leading to a large shift of 16 cm^{-1}. Further, in the latter case a line broadening will also be expected upon[270,271] dilution (Table IV.2.4.1), which has been actually observed in the present study.

Table IV.2.4.1. Peak positions and linewidths of the peaks corresponding to $\sim$1029 cm^{-1} and $\sim$1070 cm^{-1} (in neat C₄H₈O) with varying concentration of the reference system, as obtained from the analysis of the measured line profiles.

Mole fraction (C₄H₈O)	$\sim$1029 cm^{-1}		$\sim$1070 cm^{-1}	
	Peak position (cm^{-1})	Linewidth (FWHM) (cm^{-1})	Peak position (cm^{-1})	Linewidth (FWHM) (cm^{-1})
0.1	1034.2	17.0	1054.8	20.2
0.3	1031.7	18.0	1058.8	22.2
0.5	1031.1	19.0	1062.2	25.5
0.7	1030.7	19.7	1066.8	22.1
0.9	1029.7	20.0	1069.6	19.3
1.0	1029.5	20.2	1070.8	17.4

IV.2.5 Concentration dependence of wavenumber shifts and vibrational dephasing of $\sim$896 cm^{-1} mode

The peak position of the band at $\sim$896 cm^{-1} in the hydrogen bonded THF shifts towards lower wavenumber almost linearly upon dilution (Fig. IV.2.5.1), whereas the true Raman linewidth obtained after correction for the instrumental response function[274], Γ_L vs. C plot shows a maximum at C=0.5 as depicted in Fig. IV.2.5.2.
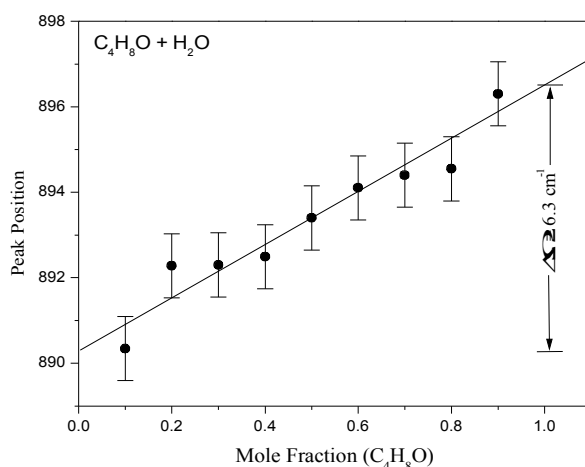
Figure IV.2.5.1. Variation of the peak position of the ν(C-O) stretching mode of hydrogen bonded C₄H₈O complex molecules presented as a function of concentration of C₄H₈O, C in mole fraction in the binary mixture (C₄H₈O+H₂O).

The wavenumber shift for this peak between the neat liquid and infinite dilution has been obtained from the plot to be $\sim$6.3 cm^{-1} by extrapolating to C=0. The concentration dependence of the wavenumber in binary liquid mixtures was explained by the Bondarev and Mardaeva[275] model. This is basically a concentration fluctuation model based on Anderson-Kubo formalism[276,277]. A linear relationship between the concentration of the reference molecule was proposed as:

$$\nu(C) = \nu_0 + C\,\Delta\Omega \qquad\qquad \text{(IV.2.5.1)}$$

where C is the concentration of the reference system expressed in mole fraction and $\Delta\Omega$ is the amplitude of the wavenumber shift between the neat liquid and infinite dilution as shown in Fig. IV.2.5.2.

It is clear from the data presented in Table IV.2.4.1 that on increasing the solvent concentration, the wavenumber of this band decreases almost linearly with concentration, which can be understood in terms of the above relationship given by the equation (IV.2.5.1). In the present case, an attractive interaction[270] causes the decrease in wavenumber with increasing concentration of solvent molecules.

Further, in accordance with this model, the random motion of the reference and solute molecules, C_4H_8O and H_2O, respectively, in the mixture, causes the concentrations in the different microvolumes to fluctuate around a mean value. These two effects together result into a Gaussian type linewidth variation peaking at C=0.5 given by the relationship:

$$\Gamma_C = 2(ln2)^{1/2} \Delta \Omega \left[\frac{(C(1-C))}{n} \right]^{1/2} \qquad (IV.2.5.2)$$

where n is the number of the neighbouring molecules influencing the reference mode. The short-range van der Waals forces alone could decide the number n appearing in the above equation, in those cases where appreciable strong association, such as hydrogen bond formation takes place when two liquids are mixed.
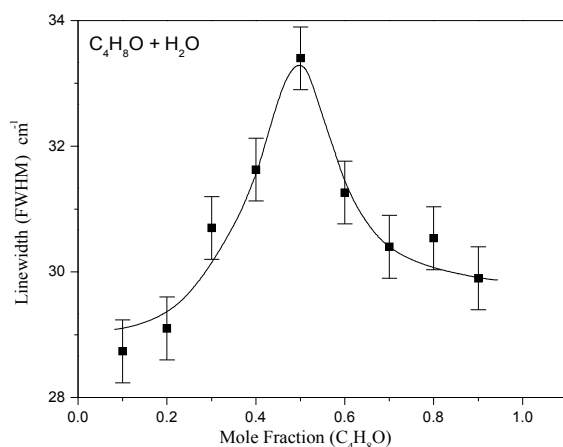
Figure IV.2.5.2. Variation of the linewidth (FWHM) of the ν(C-O) stretching mode of hydrogen bonded C_4H_8O complex molecules presented as a function of concentration of C_4H_8O, C in mole fraction in the binary mixture ($C_4H_8O+H_2O$).

The presence of the maximum in the Γ_C vs. C plot (Fig. IV.2.5.2) can be attributed to the concentration fluctuation caused by random motion in the solution. In an ideal case of uniform distribution molecules, which will obviously have the same environment and random motion as the complete volume of the mixture, due to its random motion , the number of molecules is to be different at a microvolume level. The number of molecules in these microvolumes varies on both sides of the maximum following a Gaussian distribution. In accordance with the model[275], in each microvolume, the reference molecule shall exhibit a linear concentration dependence of the wavenumber of the vibrational mode question. The contribution of concentration fluctuation in the linewidth of the ν(C-O) Raman mode in the hydrogen bonded species may be evaluated using equation (IV.2.5.2). From the linewidth and wavenumber position vs. concentration plot, the amplitude of wavenumber shift, $\Delta \Omega$ was obtained to be 6.3 cm^{-1}. By substituting this values of $\Delta \Omega$ and $n=2$ in equation (IV.2.5.2), Γ_C is calculated

to be 5.2 cm^{-1}. The number of nearest neighbors n, which influence the normal mode in question, might be taken higher (5 or 6) in such cases where no bond formation between the solute and the solvent molecules takes place and there are short-range van der Waals forces that become the deciding factor since the assumption of the first coordinate sphere may be valid. In the present case, however, one solute molecule may bind with two solvent molecules and may exchange partners due to random walk of C_4H_8O and H_2O molecules. Thus a value of $n=2$, strictly speaking between 2 and 3, may justifiably be taken. Some interesting aspects of concentration fluctuation and its influence on linewidth have been discussed by Müller et al.[278] also. However, the analysis in the present study was made taking the Bondarev and Mardaeva[275] model in conjunction with the Fischer and Laubereau[279] model, which are more handy to use.

Considering the above contribution, Γ_C to the linewidth and intrinsic linewidth to be additive, the total linewidth at concentration C, $\Gamma_C(C)$ can be expressed as:

$$\Gamma_C(C) = \Gamma_C + \Gamma_i \qquad \text{(IV.2.5.3)}$$

and the intrinsic linewidth, Γ_i is estimated to be 28.2 cm^{-1}. In order to explain the linewidth obtained after correction for the slit function[274], Γ_C directly, the Knapp and Fischer[280] model used by Asthana et al.[281], which makes use of binomial distribution and follows the approach of the Anderson-Kubo [276,277] formalism, may also be used. The Fischer and Laubereau[279] model is basically an extension of the exchange model of Anderson-Kubo[276,277]. In order to explain Γ_i obtained from equation (IV.2.5.3) this models much easier and can be applied conveniently in hydrogen bond systems[265]. According to this model[279], the excitation of low wavenumber hydrogen bonding mode, ω_2 causes a shift $\delta\omega$ in $0 \to 1$ transition of the high wavenumber reference mode, ω_1 through anharmonic coupling or, in other words, the wavenumber of combination band is not equal to the sum of the wavenumbers of the two modes $\omega_1 + \omega_2$. Using this consideration, Fischer and Laubereau[279] concluded that this model adds a contribution to the linewidth and shift of the high wavenumber mode ω_1. The shift in ω_1 mode is given by:

$$\Delta\omega_1 = \delta\omega \exp(-\beta\hbar\omega_2). \qquad \text{(IV.2.5.4)}$$

The contribution to the linewidth of the ω_1 (~896 cm^{-1}) mode coming from indirect dephasing is expressed as:

$$\Gamma = (\delta\omega)^2 T_1 \exp(-\beta\hbar\omega_2), \qquad \text{(IV.2.5.5)}$$

where, $\beta = 1/kT$, k is the Boltzmann constant, T is the absolute temperature, and T_1 is the value of the lifetime for the low wavenumber mode, ω_2 following the terminology used in Ref.[279]. By putting the value of $\delta\omega$, from equation (IV.2.5.4) in (IV.2.5.5), one can obtained:

$$\Gamma = (\Delta\omega)^2 T_1 \exp(\beta\hbar\omega_2). \qquad \text{(IV.2.5.6)}$$

The wavenumber shift $\Delta\omega_1$ in the high wavenumber mode (ω_1) between neat liquid and infinite dilution is obtained to be 6.3 cm^{-1} from the data presented in Fig. IV.2.5.1 and the low wavenumber O···H

hydrogen-bridging mode (ω_2) was taken to be ~85 cm^{-1}. The lifetime of the low wavenumber mode, T_1 may be taken to be ~7 ps and using the equation (IV.2.5.6), Γ is obtained to be ~27.9 cm^{-1}, which is in close agreement with the experimentally determined concentration independent intrinsic linewidth, Γ_i ~28.2 cm^{-1} obtained by substracting the concentration dependent part using the equation (IV.2.5.3). The value of T_1 ≈7 ps is a reasonable value in view of the fact that the entire intrinsic linewidth (FWHM) comes from the indirect dephasing. Further it is to be noted that the band at ~896 cm^{-1} is due to a hydrogen bonded species, $C_4H_8O\cdots HOH$, whereas the band at ~910 cm^{-1} is due to the non-bonded (free) C_4H_8O molecules, which will coexist even at high dilution. Thus it is not unreasonable to assume that the indirect dephasing model is operative in the entirety for the ~896 cm^{-1} band, since it involves anharmonic coupling of high wavenumber mode ω_1 with the H-bridging mode ω_2 but not for the ~910 cm^{-1} band. The value of relatively large T_1 ≈7 ps may be attributed to the constrained motion of the reference molecule due to hydrogen-bridging at two different sites and thus taking the system to a slow modulation regime.

IV.3 Conclusions

Since THF (C_4H_8O) is the simplest model compound for understanding the vibrations of the furanose ring of RNA and DNA backbones and water (H_2O) is an omnipresent solvent in biological systems, a deeper insight of the spectra-structure correlation in the ($C_4H_8O+H_2O$) mixture was a very pertinent study. Further, since THF has a peculiar behavior in a Nafion perfluorosulphonic membranes and Raman spectroscopy enables the location of the hydrophilic site of the membrane, the study of the binary mixture ($C_4H_8O+H_2O$) becomes justifiably a very relevant study. The plot of the ratio, I_{hyb}/I_{main} vs. C, as presented in Fig. IV.2.3.2 may be exploited as a Raman marker to locate the hydrophilic site of the membrane and thus, the present study has a direct biological significance. The analysis of the linewidth variation with the concentration of C_4H_8O for the band (~896 cm^{-1} at C=0.9) attributed to the hydrogen bonded complex leads to a conclusion that a slow modulation regime is operative. Although the linewidth is rather large (~33 cm^{-1}) and the difference between the smallest and the largest values of the linewidth is small (~4.7 cm^{-1}), the precision of the technique is good enough to measure this difference, thereby leading to a fairly reliable estimate of the various peak positions and linewidths. The results of *ab initio* calculations (MP2 level) coupled to the line shape analysis of the Raman bands of THF, in the fingerprint region 800-1000 cm^{-1}, to the best of our knowledge, is a first report and may probably offer a unique diagnosis tool based on a reasonably good spectra-structure correlation.

The above mentioned work has been the result of a collaboration with the research group of **Professor Dr. B. P. Asthana** from Banaras Hindu University, Varanasi, India.

Chapter V

Food additives characterization by Raman, surface-enhanced Raman spectroscopy, and theoretical studies

"In physics, you don't have to go around making trouble for yourself – nature does it for you"

(Frank Wilczek, Nobel Prize in Physics-2004)

V.1 Food additives: what are they and why are they necessary?

The use of food additives is an emotional topic which continues to provoke consumer concern. Despite modern-day associations food additives have been used for centuries. Food preservation began when man first learned to safeguard food from one harvest to the next and by the salting and smoking of meat and fish. The Egyptians used colors and flavorings, and the Romans used saltpeter (potassium nitrate), spices and colors for preservation and to improve the appearance of foods. Cooks regularly used baking powder as a raising agent, thickeners for sauces and gravies, and colors, such as cochineal, to transform good-quality raw materials into foods that were safe, wholesome and enjoyable to eat. The overall aims of traditional home cooking remain the same as those prepared and preserved by today's food manufacturing methods. Over the last 50 years, developments in food science and technology have led to the discovery of many new substances that can fulfill numerous functions in foods[282].

Food additives are any substance or mixture of substances other than the basic foodstuff which is present in food as result of any phase of production, processing, packaging, or storage. Additives perform a variety of useful functions in foods that are often taken for granted. Legally, the term "food additive" refers to "any substance with intended use which results or may reasonably be expected to result -directly or indirectly- in its becoming a component or otherwise affecting the characteristics of any food." This definition includes any substance used in the production, processing, treatment, packaging, transportation or storage of food. Many food additives are naturally occurring and some are even essential nutrients; it is the technical purpose that leads to these being classified as food additives and given an E number.

If a substance is added to a food for a specific purpose in that food, it is referred to as a direct additive. For example, the low-calorie sweetener aspartame, which is used in beverages, puddings, yoghurt, chewing gum, and other foods, is considered a direct additive. Many direct additives are identified on the ingredient label of foods.

Indirect food additives are those that become part of the food in trace amounts due to its packaging, storage or other handling. For instance, minute amounts of packaging substances may find their way into foods during storage. Food packaging manufacturers must prove to the Food and Drug Administration (FDA) that all materials coming in contact with food are safe, before they are permitted for use in such a manner.

Some additives could be eliminated if we were willing to grow the food, harvest and grind it, spend many hours cooking and canning, or accept increased risks of food spoilage. But most people today have come to rely on the many technological, aesthetic and convenience benefits that additives provide in food. Additives are used in foods for five main reasons[283]:

- To maintain product consistency. Emulsifiers give products a consistent texture and prevent them from separating. Stabilizers and thickeners give smooth uniform texture. Anti-caking agents help substances such as salt to flow freely.
- To improve or maintain nutritional value. Vitamins and minerals are added to many common foods such as milk, flour, cereal and margarine to make up for those likely to be lacking in a person's diet or lost in processing. Such fortification and enrichment has helped reduce

malnutrition among the population. All products containing added nutrients must be appropriately labeled.

● To maintain palatability and wholesomeness. Preservatives retard product spoilage caused by mold, air, bacteria, fungi or yeast. Bacterial contamination can cause foodborne illness, including life-threatening botulism. Antioxidants are preservatives that prevent fats and oils in baked goods and other foods from becoming rancid or developing an off-flavor. They also prevent cut fresh fruits such as apples from turning brown when exposed to air.

● To provide leavening or control acidity/alkalinity. Leavening agents that release acids when heated can react with baking soda to help cakes, biscuits and other baked goods to rise during baking. Other additives help modify the acidity and alkalinity of foods for proper flavor, taste and color.

● To enhance flavor or impart desired color. Many spices and natural and synthetic flavors enhance the taste of foods. Colors, likewise, enhance the appearance of certain foods to meet consumer expectations.

The food additives (E number) may be classified by numeric range[283]:

● Colorings (E100-E199) in both natural and synthetic forms are used to enhance the appearance of foods. Synthetic colors are usually used because they are more uniform and less expensive than natural colors;

● Preservatives (E200-E299) are used to reduce the growth of mold, bacteria and yeast;

● Antioxidants and acidity regulators (E300-E399) are used to prevent the chemical reactions that cause rancid fats and brown fruits;

● Thickeners, stabilizers, and emulsifiers (E400-E499) aid in maintaining smooth texture and uniform color and flavor in some foods;

● pH regulators and anti-caking agents (E500-E599);

● Flavor enhancers (E600-E699);

● Miscellaneous (E900-E999);

● Additional chemicals (E1100-E1599).

A large number of food additives are widely used in the food industry. Adverse reactions to additives seem to be rare but are likely underdiagnosed in part due to a low index of suspicion. Numerous symptoms have been attributed to food additive exposure, but the cause-effect relationship has not been well demonstrated in all. Reactions to food additives should be suspected in patients who report symptoms to multiple unrelated foods or to a certain food when commercially prepared but not when homemade and the allergy evaluation rules out a role for food protein. It is also prudent to investigate food additives in patients considered to have idiopathic reactions. There is a minor role for skin testing or in vitro testing. Oral challenge testing with common additives, preferably preceded by a trial of an additive-free diet, is the definitive procedure for detecting the offending agent. Once the specific additive is identified, management is basically avoidance of all its forms[284].

An adverse reaction to food is often mislabeled as a food allergy. Food allergy is a specific form of intolerance to a food or food component that activates the immune system. An allergen (a protein in the offending food, which in the majority of people will not produce and adverse reaction) sets of a chain of reactions in the immune system including the release of antibodies. These antibodies trigger the release of body chemicals, such as histamine, which give rise to various symptoms such as itchy skin, a runny nose, coughing or wheezing. Allergies to foods or food components are often inherited and usually

identified early in life. Food intolerance involves the body's metabolism but not the immune system. A good example is lactose intolerance, in which certain individuals lack the digestive enzyme lactose, which breaks down the milk sugar[285].

The immune system generally protects the body from harmful foreign proteins by generating a response to eliminate them. In a true allergic reaction, the body produces antibodies (a protein that specifically binds to another protein called antigen -in this case the allergen- to deactivate it and remove it from the body). The class of antibodies known as immunoglobulin E (IgE) reacts with the allergen and this in turn triggers a reaction with the mast cells (tissue cells) and basophils (a type of blood cell). Most cells are found below the surface of the skin and in the membranes lining the nose, respiratory tract, eyes and intestines. A substance called histamine or other substances such as leukotrienes and prostaglandins are released from mast cells and they cause allergic responses such as those set out in the table below. The adverse reactions are immediate and are usually localized. Some allergic reactions take several hours or even days to develop after exposure to a foreign protein. These are often called "delayed hypersensitivity reactions". Fortunately, most allergic reactions to food are relatively mild but a small number of people experience a severe and life-threatening reaction called anaphylaxis. An anaphylactic reaction can sometimes occur within a few minutes of exposure and immediate medical attention is necessary. Peanuts are well known for causing "anaphylactic shock", a serious condition in which blood pressure drops rapidly and the sufferer could die from cardiac arrest unless adrenaline is administered rapidly in order to open up the airways. The usual symptoms of allergic reactions to foods are classified as follows[286]:

- Respiratory
– runny nose or nasal congestion, sneezing, asthma (difficult breathing), coughing, wheezing, breathing difficulties.

- Skin
– swelling of the lips, mouth, tongue, face and/or throat (angioodema), urticaria (hives), rashes or redness, itching (pruritus), eczema.

- Gastrointestinal
– abdominal cramps, diarrhea, nausea, vomiting, colic, bloating.

- Systemic
– anaphylactic shock (severe generalized shock).

Food safety is only ensured by the shared responsibility of everybody involved with food from the professional to the consumer. All along the food chain, various procedures and control mechanisms are implemented to assure that the food which reaches the consumer's table is fit for consumption, that the risks of contamination are minimized, so that the population as a whole is healthier from the benefits of safe quality food. However, zero risk within food does not exist and we have to be also aware that the best legislation and control systems cannot fully protect us against those with criminal intentions. The best way to practice food safety remains to be well informed about the basic principles of food production and safe food handling at home[287].

V.2 Tartrazine (E102)

E102, a well-known food dye, could be detected in aqueous solutions by means of regular Raman and SERS at micromolar and nanomolar level, respectively. The changes observed in the profile of the band at 1365 cm^{-1}, characteristic to the υ(-N=N-) mode of the azochromophore group, allowed us to establish the present species in the Raman and SERS solutions at different concentrations or pH values. A protonation at the azo group of the molecule was detected for acidic pH values under 3. In the pH range between 3 and 8, no changes in the molecular species were observed. The DFT calculated geometries, harmonic vibrational modes and Raman scattering activities for E102 were in good agreement with the experimental data, a complete vibrational assignment being proposed. A strong chemical interaction of E102 with the colloidal particles was evidenced and an adsorbed geometry was proposed.

V.2.1 Molecule presentation

Tartrazine (E102 in Europe) is a monoazo compound, which essentially consists of 1H–pyrazole–3–carboxylic acid, 4,5–dihydro–5–oxo–1–(4–sulfophenyl)–4–[(4–sulfophenyl) azo]–trisodium salt and subsidiary color matters together with sodium chloride and/or sodium sulphate as the main uncolored components. The products that often, but not always, contain E102 are pharmaceutical drugs, foods, and cosmetics. E102 is an artificial dye, available as an orange powder. The molecular structure of E102 molecule together with its optimized geometry is presented in Fig. V.2.1.1.
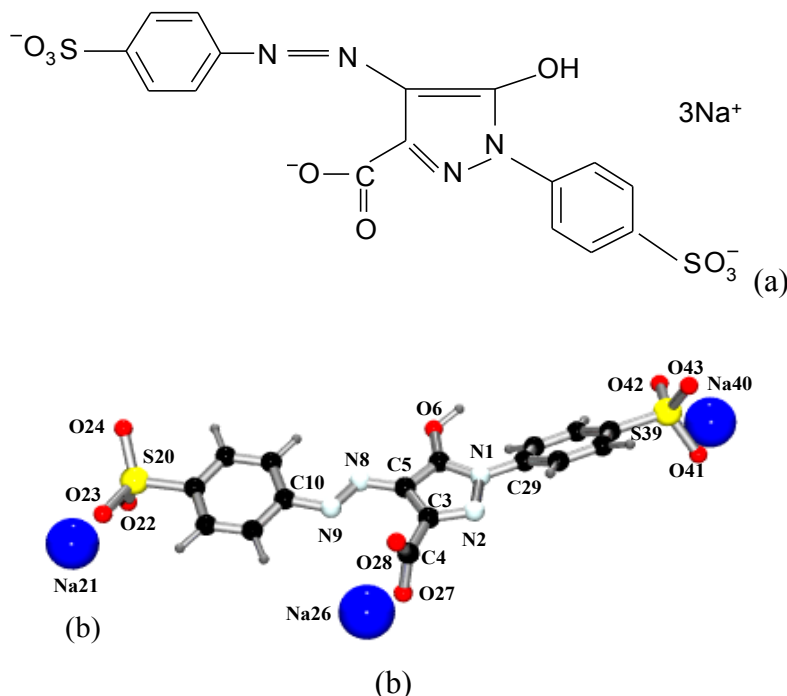
Figure V.2.1.1. Molecular structure (a) and B3PW91/LANL2DZ optimized geometry (b) of E102 molecule.

Recent studies[288,289] showed that E102 is responsible for a large number of allergic reactions including migraine, blurred vision, itching, rhinitis and skin blotching. Asthmatics and analgesics

intolerants[290] seem to be particularly at risk. The presence and/or contact of some of these dyes with drugs like aspirin[291-293], benzoic acid[294-296], or other analgesics in the human body can induce allergic and asthmatic illnesses for sensitive people. E102 is more dangerous for children because this food additive can produce hyperactivity, migraine, and behavioral problems. A *Lancet* study showed that two of the top ten causes of intractable migraine for children were due to the coal-tar dye E102 and E210 (benzoic acid preservative)[297]. After cow's milk, E102 was the second most common single cause of migraine. A study on hyperactive children found that E102 expenditure increases the excretion of zinc in the urine, lowers body zinc levels and worsens behavioral symptoms in these children[298-300].

Azo dyes can be reduced to aromatic amines[301] by the intestinal microflora. After ingering E102 a reduction of this dye in the gastrointestinal tract was observed, where the azo bond is cleaved[302,303], thus, non-sulphonated aromatic amines being broken away. As a sulphonated azo dye, it is mainly used in the food industry, in the presence of anions and other macromolecules where E102 often gives rise to a phenomenon named "metachromasia". This is a characteristic color change when certain tissue elements are stained by cationic dye[304].

The Raman spectral studies represent one of most important chapters of vibrational spectroscopy as through SERS -Surface Enhanced Raman Spectroscopy- one can eliminate the fluorescence of the biological samples. Also, vibrational spectroscopy provides important information about the structure and the properties of the biological molecules. It seems worthwhile to characterize the E102 molecule using SERS and DFT calculations.

V.2.2 Geometry optimization

Because no crystal structure data were yet reported on E102, its structure was optimized at different level of theories (BPW91/6-311+G(d), B3LYP/6-31+G(d)) and compared with those of identical or similar functional groups of E102 from literature[305-316]. The calculated structural parameters of E102 are listed in Table V.2.2.1 and the labelling of the atoms is shown in Fig. V.2.1.1b. As one can notice, there is a very good agreement between the theoretically determined parameters of E102 and the experimental values available in the literature[305-314].

The azo group of E102 makes the connection between one of the phenyl rings, and the pyrazole ring. Usually the N=N bond's length is of 125.0 pm[305,306], whereas in the E102 molecule, the average calculated N8=N9 bond length is 127.1 pm. The bond strength between the azo-N8 and the pyrazole-C4 N8-C4 is 136.5 pm, which is higher than that of the azo-N9 and the phenyl-C10 [141.7 pm][307,308]. The elongation of the bond length supports the charge delocalisation from pyrazole ring and the localization at the azo bond[309,310]. As shown in Table V.2.2.1, the calculated C4-C5 bond lengths with different methods of the E102 molecule vary from 140.2 to 140.5 pm, which is somewhere between the length of a C-C single bond (154 pm) and that of a C=C double bond (134 pm)[311]. Similarly, the C5-N1 distance of the calculated molecular structure vary from 135 pm to 137.7 pm, and are also intermediate between those for a C-N single bond (148 pm) and a C=N double bond (128 pm)[312]. Therefore, the calculated data suggest an extended π electron delocalization over the pyrazole system[313,314].

Table V.2.2.1. Selected calculated structural parameters of E102 in comparison with the available experimental data.

	Exp	Calcd			
		B3LYP		B3PW91	
		6-31+G(d)	LANL2DZ	6-31+G(d)	LANL2DZ
Bond-lengths (pm)					
S20-O22		151.8	168.2	151.1	161.8
S20-O23		147.0	168.2	146.5	167.3
S20-O24		151.7	162.5	151.0	167.1
S20-C13		180.1	186.6	179.2	185.6
C10-N9	140.4[312]/142.5[308]	142.1	143.4	141.6	142.9
N9-N8	125.0[305]	127.3	129.4	126.9	129.0
N8-C4	139.4[308]/138.6[312]	136.7	138.9	136.3	138.5
C4-C5	132.6[308,311]	140.4	140.5	140.2	140.2
C5-N1	133.5[311]	135.3	137.7	135.0	137.3
N1-N2		140.0	142.0	138.9	141.2
N2-C3	132.7[311]	131.3	133.9	131.1	133.6
C3-C4		144.5	144.7	144.1	144.3
C3-C25		150.9	150.5	150.6	150.1
C25-O27		126.4	129.6	125.7	129.5
C25-O28		126.0	129.8	126.1	129.2
C5-O6		133.9	136.8	133.3	136.2
N1-C29		141.8	142.3	141.3	141.8
C32-S39		180.4	186.6	179.4	185.6
S39-O41		151.5	167.8	150.9	167.0
S39-O42		146.9	162.5	146.4	161.8
S39-O43		151.7	168.0	151.0	167.1
Angles (°)					
O22-S20-O23		114.8	102.6	114.6	103.2
O23-S20-O24	119.6[314]	107.4	116.9	115.2	116.5
O22-S20-O24		115.0	114.3	107.6	114.3
S20-C13-C14	119.0[314]	119.3	119.1	119.0	118.6
S20-C13-C12	121.2[314]	119.8	118.0	120.2	118.6
C10-N9-N8	114.9[308]	113.6	114.0	113.5	114.0
C11-C10-N9	124.2[314]/124.5[308]	123.5	124.4	123.4	124,2
C15-C10-N9	116.8[314]	117.0	115.5	117.0	115.6
N8-C4-C5		121.5	122.1	121.6	122.2
N8-C4-C3		134.6	133.2	134.6	133.0
C5-O6-H7		110.6	113.7	110.2	113.7
C5-N1-C29		128.2	129.6	127.2	129.1
N2-N1-C29	115.7[312]	120.2	119.5	120.4	119.6
N1-C29-C34	122.0[314]	120.0	120.3	119.9	120.2
N1-C29-C30		119.3	118.8	119.4	118.8
S39-C32-C33	119.0[314]	119.0	119.4	119.0	119.1
S39-C32-C31	121.2[314]	120.0	118.0	120.1	118.3
C32-S39-O41	107.1[314]/108.3[314]	105.6	108.7	105.5	108.6
C32-S39-O42		107.3	106.1	107.2	107.4
C32-S39-O43		105.5	106.8	105.3	105.5
O41-S39-O42	119.6[314]	115.4	114.9	115.4	114.5
O41-S39-O43		107.4	102.6	107.7	103.0
O42-S39-O43	119.6[314]	114.8	117.2	114.8	117.1

X-Ray studies on diazo dyes[315] have shown that the sodium sulfonate groups lie on the opposite sides of the conjugated azo linkages. In our study, this is revealed by the C10-N9-N8 (113.6°), C11-C10-N9 (123.5°), and C15-C10-N9 (117°) calculated angles, the difference between the C10-N9 and N8-C4 bonds being a 180° rotation. The calculated bond distances from 179.2 pm to 186.6 pm for the C13-S20 bond are characteristics for intermolecular hydrogen bonds[316].

V.2.3 Vibrational spectroscopy

The UV-VIS absorption spectrum of E102 aqueous solution is presented in Fig. V.2.3.1a. As one can notice, it shows two absorption maxima, at 427 nm and 258 nm, respectively. The absorption maxima of colloid-E102 solution mixture were detected almost at the same position (Fig. V.2.3.1b). Since the resonance Raman measurements have already been reported[317,318], we have chosen the non-resonance conditions (the 514.5 nm line falls out of the absorption band) for Raman excitation.
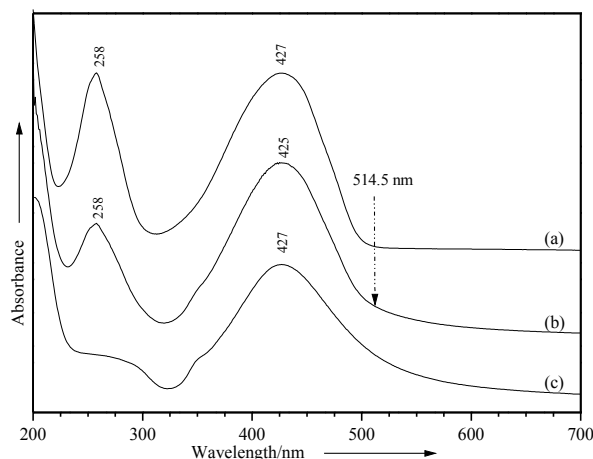
Figure V.2.3.1. Absorption UV-VIS spectra of E102 solution (a), E102 with Lee Meisel silver colloid (b), and Lee Meisel silver colloid (c).

FT-Raman spectrum of E102 solid state

The vibrational fundamentals from the FT-Raman spectrum, presented in Fig. V.2.3.2b, were analyzed by comparing these modes with those from the literature in combination with the results of our DFT calculations (i.e., harmonic vibrational wavenumbers and their Raman scattering activities). In the Table V.2.3.1 the selected calculated and experimental Raman and SERS data together with their tentative assignment are given.

In the FT-Raman spectrum (Fig. V.2.3.2b) the very strong band at 1598 cm^{-1} and the very weak peak at 1682 cm^{-1} were assigned to the C4=C5 symmetrical stretching mode of pyrazole, quadrant stretching mode of the phenyl rings contributions, and the bending mode of the OH group, respectively. The following bands (1502, 1470 and 1415 cm^{-1}) were attributed to the C4=C5 pyrazole bending contribution, the N8=N9 bending mode, and the C-H bending mode of the phenyl rings respectively, as the main contributions in the bands' shape.

The band at 1357 cm^{-1} is due to the azo group stretching mode and the symmetrical stretching mode of carboxyl group. The very weak peak at 1271 cm^{-1} was assigned to the bending mode of (-N1-N2=C3-C4-). The medium band at 1216 cm^{-1} corresponds to the C–H torsion modes of both phenyl rings, to the N2=C3-C4 bending mode, and the stretching mode of C4=C5. The medium peak at 1177 cm^{-1} was attributed to the phenyl 2 bending mode and the stretching mode of C4-N8 and C10-N9. Therefore the medium strong band at 1129 cm^{-1} corresponds to the out-of-plane C-H deformation of the phenyl rings.

The following weak band at 1093 cm^{-1} corresponds to the phenyl 2 bending mode. The band at 1046 cm^{-1} is attributed to the phenyl 1 bending mode, the N1=N2 asymmetrical stretching mode, and the (C-S20O$_3^-$ Na$^+$, C-S39O$_3^-$Na$^+$) symmetrical stretching modes. The C–H out-of-plane deformation mode of phenyl 1 was observed at 1010 cm^{-1}. The band at 880 cm^{-1} was assigned to the C–H out-of plane deformation mode of both phenyl rings. On the other hand, the very weak peak at 861 cm^{-1} corresponds to the out-of-plane deformation of both phenyl rings, and the bending modes of hydroxyl and carboxyl groups.
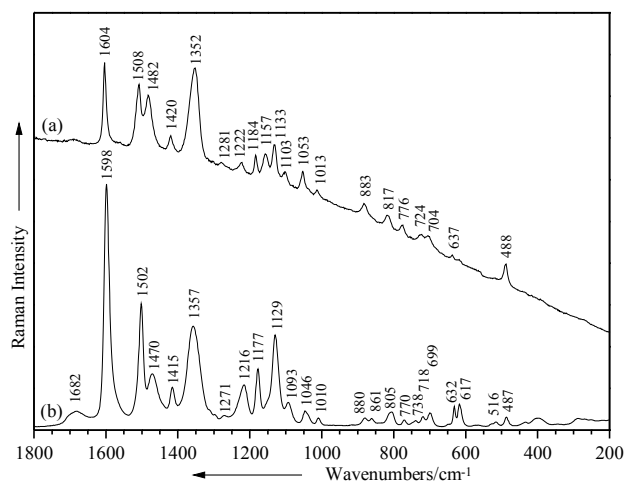
Figure V.2.3.2. Raman spectrum of the 10^{-1} M E102 solution (a), and FT-Raman spectrum of the E102 orange powder (b). Excitation: 514.5 nm, 200 mW (a); 1064 nm, 1 W (b).

Tag along bands were attributed as follows: the band at 805 cm^{-1} to the S39O$_3^-$ vibrational bending mode, the band at 770 cm^{-1} to the S39O$_3^-$ bending mode and to the C-H out-of-plane deformation for the phenyl rings. The signal at 738 cm^{-1} was assigned to the bending modes of S20O$_3^-$ and the out-of-plane C-H deformation of the phenyl 1, whereas the band at 718 cm^{-1} was considered to occur due to the bending modes of the S20O$_3^-$ and S39O$_3^-$. The weak peak at 699 cm^{-1} was assigned to the out-of-plane C-H deformation of pyrazole ring.

The signal at 632 cm^{-1} represents the out-of-plane deformation of the both phenyl rings, and the signal at 617 cm^{-1} was assigned to the pyrazole bending, and the out-of-plane C-H deformation of the phenyl rings. Further are the assignments for the peak at 516 cm^{-1}, where can be observed the S39O$_3^-$ wagging mode, and the out-of-plane C-H deformation of phenyl and pyrazole rings. The band at 487 cm^{-1} was attributed to a skeletal distorsion, and the both sulfonate groups rocking modes.

As a monoazo dye, E102 reveals the distinguishing azochromophore group –N8=N9– subject to azo hydrazone form in appropriate solutions[319,320].

Raman spectra of E102 solutions

Comparing the Raman spectra of E102 solutions with the FT-Raman spectrum of E102 orange powder (Fig. V.2.3.2), one can observe a significant background with the relative intensities of the bands slightly changed. An increased intensity for the azo and carboxyl groups (the band at 1352 cm^{-1} in the Raman spectrum of solution), and a small decrease for the bending modes of the phenyl 2 ring, for the

bending modes of the phenyl 1 ring, and for the out-of-plane C-H deformation of the phenyl groups (the peaks at 1184, 1157, and 1133 cm^{-1} in the Raman spectrum). Due to the well-known solvent effect, small blue shifts of the wavenumbers and the broadening of the bands were observed for the corresponding peaks in solution.
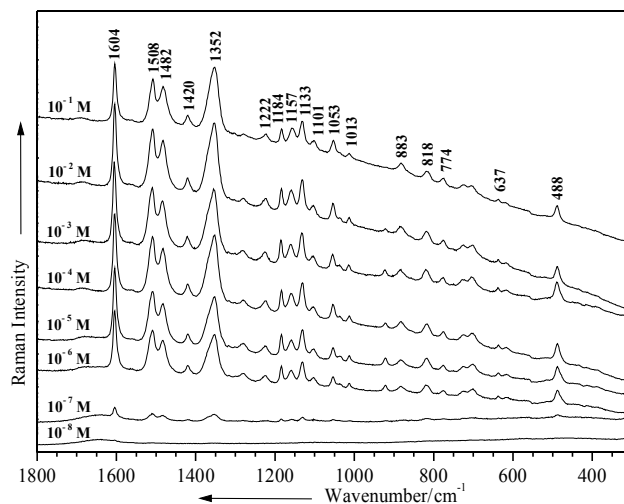
Fig. V.2.3.3. Micro-Raman spectra of E 102 aqueous solution at different concentrations.
Excitation: 514.5 nm, 200 mW.

The band at 1470 cm^{-1} from the FT-Raman spectrum becomes stronger in solution, and is importantly blue shifted (12 cm^{-1}), suggesting changes in the electron distribution over the azo bridge, a protonation of the azo group being possible. Moreover, intermolecular hydrogen bonds can contribute to this spectral change. A similar blue shift was observed for the stretching modes of the sulfonate groups at 1053 cm^{-1} shifted from 1046 cm^{-1} in the FT-Raman spectrum. The peak at 1216 cm^{-1} in the FT-Raman spectrum decreased in relative intensity and was blue shifted (6 cm^{-1}) with respect to the Raman spectrum (1222 cm^{-1}), where it was assigned to the bending mode of N2=C3-C4, and stretching mode of C4=C5.

On the other hand, the peak at 861 cm^{-1} in the FT-Raman spectrum disappears in the Raman spectrum of the solution and a new band, at 883 cm^{-1} is observed, suggesting a C–H out-of-plane deformation for both phenyl rings.

The concentration dependence Raman spectra revealed the possibility to record high quality Raman spectra of E102 aqueous solution down to the micromole concentration level[321] (Fig. V.2.3.3).

pH dependence Raman spectra

The pH dependence Raman spectra of the E 102 aqueous solution in the basic and acid pH range are presented in Figs. V.2.3.4 and V.2.3.5, respectively.

In the Raman spectra of E102 at basic pH values we can observe the significant increase in relative intensity of the 1210 cm^{-1} band, which may be assigned to the C-H bending mode, the N-H bending mode, and the pyrazole ring bending mode contributions (Fig. V.2.3.4, at pH 9), and the bands at 1168 and 1126 cm^{-1} attributed to the bending modes of the N-H and pyrazole ring. Furthermore the band at 1356 cm^{-1} as a contribution of azo and carboxyl groups is increased in relative intensity. The bands

corresponding to the phenyl 2 bending mode (1507cm^{-1}), and the azo bending mode (1482 cm^{-1}) are dramatically changed. Also, one can observe an increase in the relative intensity for the C–H out-of-plane deformation of the phenyl 2 ring (1035 cm^{-1}), by comparing it to the adjacent bands (1053, 1013 cm^{-1}) at the other pH values (Fig. V.2.3.4).
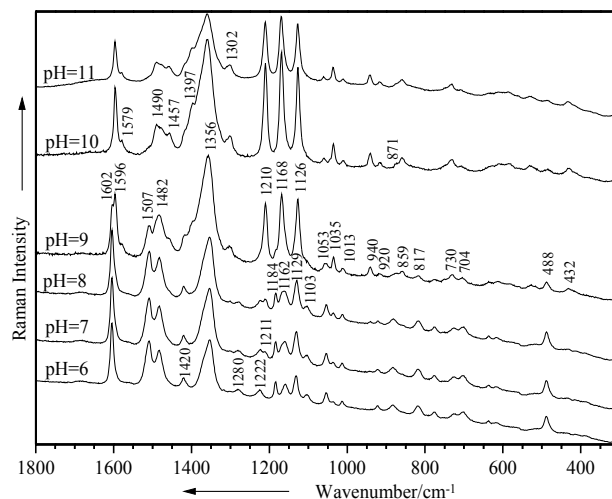
Figure V.2.3.4. Raman spectra of 10^{-4} M E102 solution at different basic pH values.
Excitation: 514.5 nm, 50 mW.

The band at 1602 cm^{-1} (Fig. V.2.3.4, at pH 6 to 9) is split into two components at 1602, 1596 cm^{-1}, with a shoulder at 1579 cm^{-1} at pH 9. By increasing the pH values, the band at 1602 cm^{-1} disappears and the new band at 1596 cm^{-1}remains. A new shoulder at 1579 cm^{-1} was also observed.

Another modification for the band intensity at 940 cm^{-1} for pH values above 9 was also observed. The signal at 488 cm^{-1} is diminished at pH values above 9. Finally, a new band at 432 cm^{-1} appearing in the Raman spectra of solutions can be observed starting from pH 9.

Comparing the Figs. V.2.3.4 and V.2.3.5, the Raman spectra of E102 solution were unchanged in the pH range from 8 to 3. Small differences could be observed in the 1360-1250 cm^{-1} spectral range at pH 2 whereas at pH 1 unresolved signal was obtained.

The aromatic moiety with sulphonic groups is the characteristic of the reactive dye. Chemical or enzymatic reduction leads to the formation of amino-sulphonic acids from the hydrolyzed derivative in the dye solution. Hydrolysis is an important degradation pathway for the reactive dyes. The important substituents in E102 are the sodium $^-$SO$_3$Na, the dye being soluble due to the presence of these groups. Since in aqueous solution the dye ionizes into sodium cations and colored sulphonate anions, sulphonic groups bonded to phenyl rings can be removed during a possible photoprocess and converted into sulphate ions[322]. This idea was applied to measure the amount of sulphanilic acid formed in the degradation of E102 in 10% sodium hydroxide solution[323].

Moreover, such a drastic photoprocess would lead to corresponding Raman changes with the appearance of the photoproducts signal, which was not observed in our spectra in basic conditions. More probably, the present modifications observed at pH values over 9, are due to the ionisation related to the

OH groups of the structure, which affects the vibrational behaviour of the O6-C5-C4-N8=N9-C involved modes[323], where the azo-hydrazone tautomers are possible.

Finally, taking into account the major changes in the band shape attributed to the azo bridge at pH 2 values, one can conclude a possible protonation of this part.

SERS spectra of E102

SERS spectrum of E 102 is presented in Fig. V.2.3.6 in comparison with the Raman spectrum of the bulk solution at micromole concentration and pH 6. Large differences in band positions and relative intensities could be observed, allowing the presumption of a chemisorbed species.
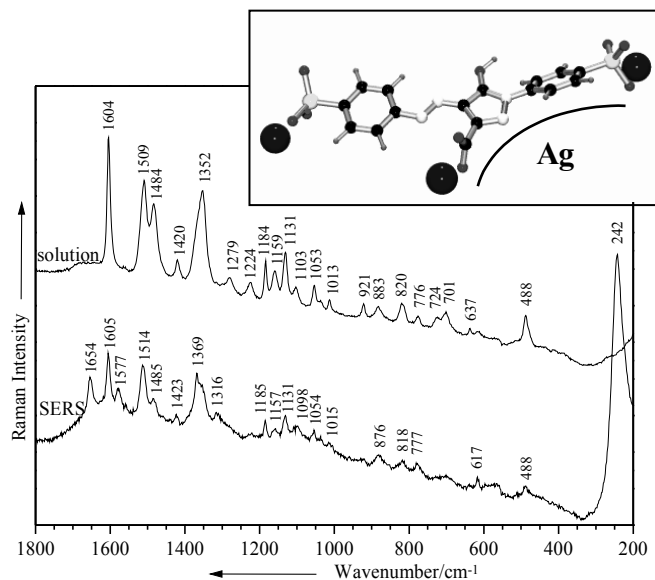
Figure V.2.3.6. Comparison between Raman and SERS spectra of E102 at the micromole concentration (10^{-6} M; pH 6), and its proposed orientation on the silver surface.

The negatively charged dye was expected to preserve the aggregation status and hence the Ag surface potential[324]. This supposition was configured by the absorption spectrum of the colloid-E102 sample (Fig. V.2.3.1).

Concentrations dependence SERS studies[321] within the concentration range between 10^{-3}–10^{-5} M reflected a most probable bulk Raman signal rather than a physisorption, since the band positions and relative intensities were unchanged, by passing from Raman to SERS.

The significant SERS signal was observed upon lowering the concentration in the 10^{-6}–10^{-10} M range, where a reorientation of the structure on the Ag colloidal particles was supposed[321] (Fig. V.2.3.7).

Since the SERS signal is concentration sensitive, in order to discuss the behavior to adsorption of the E102 on the silver particles, the SERS spectrum at micromole concentration was chosen here for the adsorption geometry proposal.

Theoretically, the E 102 molecular structure could interact with the Ag colloidal surface through more than one functional groups. Taking into account the electronegativity of the SO_3^{-} extremal functional groups, these parts would support a Coulombian repulsion due to the negative potential of the silver surface. A similar consideration could be adopted for the COO⁻ group. After considering the steric

configuration of the structure, several proper geometries for chemisorption still remain. The azo bridge C4-N8=N9-C10 could lie in the close vicinity of a bump from silver aggregate, which would lead to the torsion of the phenyl 2 or the pyrazole ring. In this case, a large enhancement of the C-N stretching modes is expected and consequently, a smaller enhancement for the mentioned rings modes.

Another possibility for E 102 to chemisorb is provided by the presence of the lone pair nitrogen atom N2 from the pyrazole ring (Fig. V.2.1.1). In this case, according to the surface selection rules[108], the stretching modes of the pyrazole ring are expected to be enhanced.
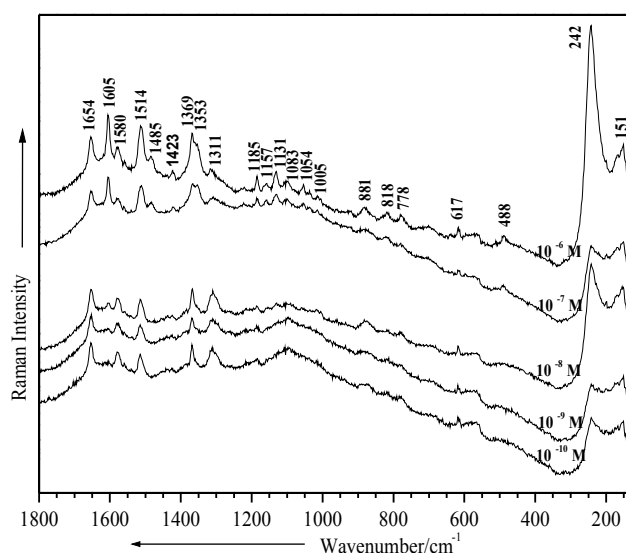
Figure V.2.3.7. SERS spectra of E 102 on Ag colloid at different concentrations. Excitation: 514.5 nm, 200 mW.

The observed bands in the SERS spectrum (Fig. V.2.3.6) support the last consideration. More specific, the very intense band at 1605 cm^{-1} assigned to the phenyl stretching modes is preponderant due to the phenyl 1 ring that is now in a close vicinity of the Ag particles with a perpendicular orientation of the skeleton ring. Moreover, the strong band observed in the SERS spectrum at 1514 cm^{-1} (blue shifted from Raman at 1509 cm^{-1}) is due to the ring stretching mode of pyrazole. Besides, this interaction generates the presence of the C3-COO^{-} functional group, negatively charged, to bend near the surface, along the C3-C bond. This contribution is supported by the 1514 cm^{-1} band shape (Fig. V.2.3.6, Table V.2.3.1).

The significantly enhanced mode at 1654 cm^{-1} is due to the ring stretching of pyrazole perpendicularly adsorbed, and its attached OH functional group. The band shape at 1369 cm^{-1} is due to the azo stretching from the bridge. Other bands with medium or weak intensities from the SERS spectrum are attributed to many bending modes of the structure. The very intense band at 242 cm^{-1} is assigned to the well-known Ag-Cl stretching mode when the chloride is present in the Ag colloid. This band completely covered the expected Ag-N (238 cm^{-1}) mode, specific for the nitrogen adsorbed molecular species. Other attempts to record SERS spectra without adding chloride ions provided poor SERS signal, where the Ag-N was however observable.

Lowering the concentration the band at 1605 cm^{-1} decreases in the SERS intensity, while the band at 1654 cm^{-1} (C=O) becomes dominant along with the azo- mode at 1369 cm^{-1}. Such chemisorption generates a reorientation of the phenyl skeletal plane with respect to the silver surface. This fact is supported by the presence of the strongly enhanced mode of phenyls at 1605 cm^{-1}, unshifted from the corresponding position in the aqueous solution Raman spectra in SERS concentrations of about 10^{-6}-10^{-7} M and its dramatically decreasing at nanomole concentrations level. The pyrazole ring bands are less representative in the SERS spectra, suggesting that this part of the molecular structure is less involved in adsorption.

V.2.4 Conclusions

Raman and SERS spectra of E102, at different concentrations, were recorded in order to use them as data bank for further applications in trace analysis of food products. The geometry of the E102 molecule was computed and optimized for the first time with the BPW91/6-311+G(d) and B3LYP/6-31+G(d) methods.

Analyzing the Raman spectra of the solutions could evidence two changes in the molecular identity of E102 on going from basic to acidic pH values. SERS spectra of E102 could be recorded even at very low concentrations with a conventional SERS setup (10^{-10} M).

A strong chemical interaction of E102 with the colloidal particles was proved where the involved in adsorption moiety is the N2-pyrazole and carboxylate. Overall, the SERS results indicate that with excitation at frequencies close to those of the Ag plasmon resonance and out of the dye resonance condition, SERS investigations are possible upon lowering concentration up to 10^{-10} M. However the SERS effect is much weaker than required for complex applications like food analysis. Therefore, for this purpose, the SERRS investigations would be more effective.

Table 2. Selected calculated and experimental Raman and SERS wavenumbers (cm^{-1}) of E102 and their tentative assignment.

FT-Raman	Calcd B3PW91 LANL2DZ	B3PW91 6-31+G(d)	B3LYP LANL2DZ	B3LYP 6-31+G(d)	Raman sol pH=6	SERS	Vibrational assignment
1682 vw	1663	1665					δ (OH); ν_s (C4=C5); δ (ph.1, ph.2)
	1657	1655	1645	1656		1654 s	δ (OH); ν_s (C4=C5); δ (ph.1, ph.2)
1598 vs		1592	1613	1629	1604 vs	1605 s	ν (ph.1, ph.2 quadrant); ip C-H def. (ph.1, ph.2); δ (OH); ν_{as} (COO$^-$)
		1581				1577 s	ph.1 and pyr. str.
1561 sh	1563	1547	1545	1562		1559 ms	ip. C-H def. (ph.1); δ (C4-C3=N2); δ (C4=C5-N1)
	1519		1515			1514 s	ip. C-H def. (ph.1); δ (COO$^-$)
1502 s	1490	1501	1507		1508 vs		δ (ph.2); δ (C4=C5)
1470 m	1478	1492	1472	1489	1482 s	1485 ms	δ (C-H) (ph.1, ph.2); δ (N8=N9-C10)
	1449	1454	1458	1454		1459 ms	ip C-H def (ph.1, ph.2); δ (C4=C5-N1)
	1442	1439	1439	1448		1436 ms	op C-H def. (ph.1, ph.2); ν_{as} (N1-N2, C4=C5, N8=N9)
	1431		1432	1429	1420 ms	1423 ms	op C-H def. (ph.1, ph.2)
1415 w	1407	1406	1414				δ (C-H)(ph.1, ph2); δ (OH); δ (N1=N2)
	1378	1389	1386	1382		1384 ms	ν_s(COO$^-$); δ (pyr.); ip. C-H def. (ph. 2)
			1379	1375		1369 s	ph.1 and ph.2 str.
1357 s	1340	1352	1362	1357	1352 vs	1353 s	ν (-C-N8=N9-C-); ν_s(COO$^-$)
	1303	1315	1327	1303		1316 s	ρ (ph.2)
1271 vw	1271	1291	1284	1284	1281 ms	1262 ms	δ (-N1-N2=C3-C4-)
1216 m	1222	1224	1219	1227	1222 ms	1215 ms	τ (C-H); δ (N2=C3-C4); ν (C4=C5)
	1218	1204	1213			1205 ms	ip C-H str. (ph.1, ph.2)
	1186			1191	1184 ms	1195 ms	δ (ph.2); ν_s (S20O$_3^-$, S39O$_3^-$)
1177 m		1169	1178	1167		1185 ms	δ (ph.2); ν (C4-N8); ν (C10-N9)
	1157	1159	1154	1159	1157 ms	1157 ms	δ (ph.1)
1129 s	1134		1132		1133 ms	1131 s	op C-H def. (ph.1, ph.2)
		1111				1109 s	δ (ph.1)
	1102	1108		1101	1103 m		δ (ph.1)
1093 w	1094		1092	1093		1098 s	δ (ph.2)
	1076	1084	1082	1072		1083 s	op C-H def. (ph.2)
1046 vw	1062	1050	1053	1048	1054 m	1053 ms	δ (ph.1); ν_{as} (N$_1$=N$_2$); ν_s (C-S20O$_3^-$Na$^+$, C-S39O$_3^-$Na$^+$)
	1031	1042	1035	1036	1037 m	1035 ms	op C-H def. (ph.2)
	1018	1014	1016	1013	1013 m	1015 ms	op C-H def. (ph.1, ph.2)
1010 vw	1010	1010	1009	1011		1005 ms	op C-H def. (ph.1)
		967				982 ms	
	956	966		940		963 ms	ν_s (S20O$_3$)
				939		936 ms	op C-H def. (ph.1)
	913	926	926	919	923 m		op. C-H def. (ph.2)
880 vw	882	881	882	886	883 m	881 ms	op C-H def (ph.1, ph.2)

							Assignment
	875	878	879	879		876 ms	op C-H def. (ph.2)
861 vw	849	860	843	862			op C-H def. (ph.1 and ph.2); δ (COO⁻)
	828	827		821	817 m	818 m	ph. 2 def.
805 vw	805	809	807	807			δ (S39O₃⁻)
		798	799	802		797 m	op pyr. def.; δ (S20O₃⁻)
	781	782		789		783 m	op C-H def. (ph.1, ph2.)
770 vw	771	766	775	773	776 m	777 m	op. C-H def. (ph.1, ph.2); δ (S39O₃⁻)
738 vw	738	741	737	736	724 w		op C-H def. (ph.1); δ (S20O₃⁻)
718 vw	702	707		706	704 w	707 m	δ (S20O₃⁻); δ (S39O₃⁻)
699 w	692	694	695	687			op. C-H def. (pyr.)
632 w/m	638	651	640	653	637 w		op. def. (ph.1, ph.2)
617 w/m	606	618	600	607	617 w	617 m	op. C-H def. (ph.1, ph.2); δ (pyr.)
	574	566	571	567		577 w	op C-H def. (ph.1, ph.2)
	558	554	555	548		565 w	op C-H def. (ph.1, ph.2)
516 vw	521	525	525	519			op C-H def. (ph.1, ph.2, pyr.); wagg. (S39O₃⁻)
	505	506	500	502		493 w	δ (S20O₃, S39O₃)
487 vw	478	480	476	479	488 w	488 w	ρ (S20O₃⁻, S39O₃⁻); op. C-H def. (ph.1, pyr.)
	467	466	465	472		466 w	op C-H def. (ph.1, ph.2)
432 vw	432	434	438	435			op C-H def. (ph.1, ph.2); ρ (S20O₃⁻, S39O₃⁻)
	421	413	422	425		415 vw	op. C-H def. (ph.1, ph.2, pyr.)
398 vw	392	392	397	395			op C-H def. (ph.1, ph.2)
343 vw	337	338	337	345			op. C-H def. (ph.1, ph.2)
	321	327	325	319		316 vw	op. C-H def. (ph.1, ph.2, pyr.).
286 vw	279	283	294	283			op def. (ph1 and ph2)
270 vw	272	270	274	272			op. C-H def. (ph.1); ρ (ph.2)
251 vw	249	251	254	249			ph.1, ph.2 def.
	239	238	239	237		242 vs	ν (Ag-Cl)
	208	200	205	210		199 s	ν (Ag-O)
	172	176	172	172		171 s	op. C-H def. (ph.1, ph.2)
	147	147	148	151		151 s	ν (Ag-O)

Abbreviation: vw – very weak; w – weak; m – medium; ms – medium strong; s – strong; vs – very strong; sh – shoulder; ν - stretching; δ - bending; ρ – rocking; τ – twisting; wagg. – wagging; pyr. – pyrazole ring; ph. – phenyl ring (1 – the ring bonding at pyrazole ring, 2 – the ring bonding at azo group); s – symmetric; as – asymmetric; def. – deformation; ip – in-plane; op – out-of-plane; str. – stretching.

V.3 Sodium benzoate (E211)

Raman spectroscopy was employed for the study of sodium benzoate, in the solid state, as well as in different acid and basic aqueous solutions. The surface-enhanced Raman scattering (SERS) spectra of sodium benzoate solutions in the 4.5–7 pH range were also recorded. Both, Raman and SERS pH dependent spectra reveal the transition of sodium benzoate from the undissociated to the anionic molecular form. The SERS spectra prove a chemical interaction of benzoate molecules with the silver colloidal particles through the lone pair electrons of the oxygen atoms of the carboxylate functional group. The orientation of the molecules on the silver surface was discussed.

V.3.1 Molecule presentation

Sodium benzoate is the sodium salt of benzoic acid (known as E 211 in Europe). The benzoic acid salts are used in low concentrations. E211 is widely used in many products, in radiator cooling system, in papers that wrapped metal for products prone corrosion, to retard the development of yeasts and molds in foods and medicinal syrups.

The aqueous solutions of sodium benzoate present a mixture of organic (benzoate anion) and inorganic (sodium cation) ions (Fig. V.3.1.1a). Only the benzoate anion can interact through hydrogen bonds with water molecules. Thus, these interactions will give an important contribution to the sum of all the interactions involving benzoate anion[325]. E211 is therapeutically used in high doses in the treatment of some rare diseases such as hyperammonemia and non-ketotic hyperglycinemia[326,327]. In most cases children affected by these inherited metabolic disorders refuse the oral uptake of E211 as a powder or in solution due to its bad taste. Therefore coated granules with lipophilic[328] and hydrophilic[329] binders have been developed.
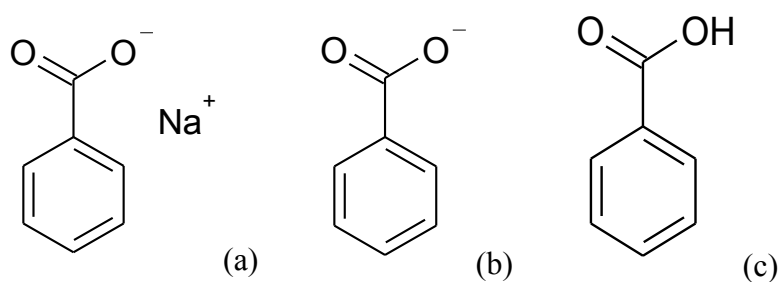
Figure V.3.1.1. Molecular structure (a), unprotonated form (b), and neutral form (c) of E211.

Benzoates, in vitro, possess antibacterial properties similar to those of fluoride and in combination with fluoride could affect caries development[330]. E211 exists in a pH-dependent equilibrium between uncharged acid molecules and charged anions. The pK$_a$ of E211 is 4.2[331,332]. Weak acid preservatives are more effective at lower pH values where solutions contain increased concentrations of undissociated acids. Optimum functionality occurs when the pH is between 2.5 and 4.0[333].

The pure and commercially available E211 was used in our measurements. On behalf of the

commercially available E211 no analytical purity certificate was accessible. In most cases, impure ingredients are used by many companies. Many times the raw materials may contain only 90% or less of the listed ingredients along with 10% or more corn starch and lactose. Lactose and corn are known allergens for some people and these items have been known to cause digestive disturbances and weaken the immune system.

V.3.2 Vibrational spectroscopy

The vibrational fundamentals from the FT-Raman (Fig. V.3.2.1a) and the micro-Raman (Fig. V.3.2.1b) spectra were analyzed by comparing the experimental vibrational modes with the previously published Raman data[334-342]. Comparing the FT-Raman spectrum (Fig. V.3.2.1a) of industrial E211 with both micro-Raman spectra of impure (industrial) (Fig. V.3.2.1b) and pure (Fig. V.3.2.1c) E211, respectively, one can observe the similarities in band positions and relative intensities.

All bands may be divided into two groups: bands connected with the carboxylate anion vibrations and bands associated with aromatic ring vibrations. The medium strong band at 1604 cm^{-1} was attributed to the asymmetrical stretching mode of the carboxylate anion – $\upsilon_a(COO^-)$, whereas the medium peak at 1415 cm^{-1} was assigned to the symmetrical stretching mode of the carboxylate anion – $\upsilon_s(COO^-)$.

The medium band at 845 cm^{-1} reveals one band resulting from the carboxylate anion symmetrical in plane deformation, while the asymmetrical in plane deformation is absent. According to the literature[334] the out of plane deformation modes of the COO$^-$ functional group exhibit a strong band in the 720-705 cm^{-1} spectral range. Examining closer this spectral region, we are able to observe that this band is missing from the FT-Raman spectrum.
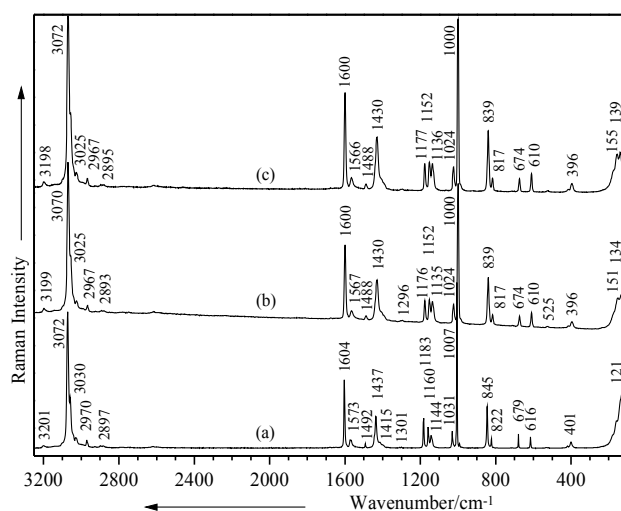
Figure V.3.2.1. FT-Raman spectrum (a) and micro-Raman spectra of industrial (b) and pure (c) sodium benzoate. Excitation: 1064 nm, 1 W (a); 514.5 nm, 25 mW (b); 514.5 nm, 100 mW (c).

One can observed that bands connected to the aromatic ring vibrations are the very weak band at 3201 cm^{-1} and the very strong band at 3072 cm^{-1}, which were attributed to the aromatic C-H stretching

modes. The following bands of the FT-Raman spectrum at 1183, 1160, 1144, and 1031 cm^{-1} are due to the in plane C-H deformation of the benzene ring. Moving forward, the very strong band at 1007 cm^{-1} can be attributed to the breathing mode of the aromatic ring[336,338]. The weak peak at 822 cm^{-1} was assigned to the in plane C-H deformation mode of the benzene ring, while the peak at 679 cm^{-1} is due to the out of plane by sextants bending mode of the benzene ring, and the band at 616 cm^{-1} is due to the in plane by quadrant bending mode of the benzene ring. The medium strong band of the spectrum, the one at 121 cm^{-1} can be assigned to the out of plane C-H deformation of the aromatic ring[340].

On passing from the FT-Raman spectrum of the powder to the micro-Raman spectrum of the E211 solution, several changes in band positions and relative intensities can be observed (Fig. V.3.2.2).

We can point out a significant background in the micro-Raman spectrum of the sodium benzoate solution (Fig. V.3.2.2b). An increased intensity for the asymmetrical stretching mode of the carboxylate anion (the band at 1598 cm^{-1} in the Raman spectrum of the solution), and an increase in relative intensity for the breathing mode of the aromatic ring (the band at 997 cm^{-1} in the Raman spectrum of solution) can be observed (Fig. V.3.2.2). Small red shifts in wavenumbers and the broadening of the bands were observed for the corresponding peaks in solution, probably due to the well-known solvent effects.
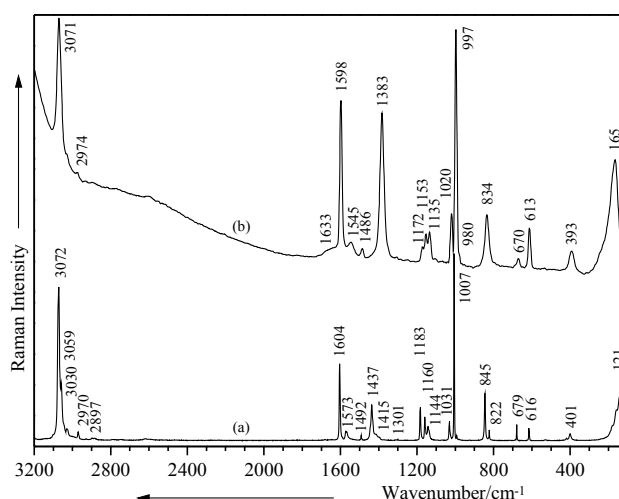
Figure V.3.2.2. FT-Raman spectrum of the E211 powder (a) and Raman spectrum of the 1 M E211 solution (b).
Excitation: 1064 nm, 1 W (a); 514.5 nm, 200 mW (b).

The band at 1415 cm^{-1} in the FT-Raman spectrum of the E211 powder becomes stronger and is importantly red shifted (32 cm^{-1}) in the Raman spectrum of solution (Fig. V.3.2.2b) suggesting changes in the electron distribution of the carboxylate anion and making possible a protonation of this group. Mainly the benzoate anion can interact through hydrogen bonds with the water molecules. As a result, these interactions will furnish an important contribution to the sum of all interactions involving the benzoate anion and can contribute to this spectral change[325]. This finding is further asserting from the band corresponding to the symmetrical in plane deformation of the carboxylate anion (845 cm^{-1} in the FT-Raman spectrum, Fig. V.3.2.2a), which slowly increases in the relative intensity and becomes broader in the Raman spectrum of solution (834 cm^{-1}) (Fig. V.3.2.2b).

Moreover, the three bands connected to the aromatic ring vibrations, namely the in plane C-H deformation modes of the aromatic ring (1183, 1160, 1144 cm^{-1} in the FT-Raman spectrum) are changed in the relative intensities' ratio in the Raman spectrum of the solution (1172, 1153, 1135 cm^{-1}). Additionally, the band correspondent to the in plane C-H deformation mode of the benzene ring (1031 cm^{-1} in the FT-Raman spectrum) increases in the relative intensity in the Raman spectrum of the solution (1020 cm^{-1}).

On the other hand the two weak peaks corresponding to the in plane and out of plane deformation through the quadrant bending mode of the benzene ring (616, 401 cm^{-1} in the FT-Raman spectrum) are importantly increased in relative intensities and become broader (613, 393 cm^{-1}) in the Raman spectrum of the solution.
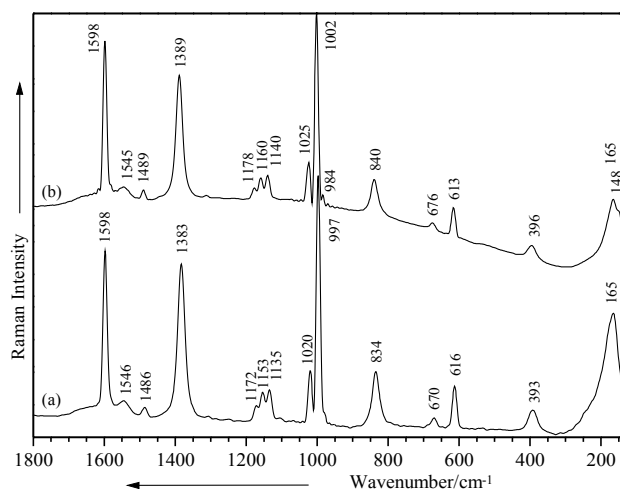
Figure V.3.2.3. Micro Raman spectra of 1 M solution of pure (a) and impure (b)
E211. Excitation: 514.5 nm, 200 mW (a), 100 mW (b).

Comparing the micro-Raman spectra of the pure and industrial sodium benzoate solutions (Fig. V.3.2.3) at the same concentration (1 M), we notice that the bands are slightly red shifted in the case of the industrial sample.

From another point of view, several bands present approximately the same relative intensities' ratio, whereas the band corresponding to the symmetrical stretching mode of the carboxylate anion (1383 cm^{-1} in the Raman spectrum of the pure E211 solution; Fig. V.3.2.3a) becomes weaker in the Raman spectrum of the industrial E211 (1389 cm^{-1}, Fig. V.3.2.3b), as well as the band assigned to the symmetrical in plane deformation of the carboxylate functional group (835 cm^{-1} in the Raman spectrum of the pure probe) and the peak attributed to the in plane by quadrant bending mode of the aromatic ring (613 cm^{-1} in the Raman spectrum of the pure E211) are also weaker (840, 613 cm^{-1}; Fig. V.3.2.3b) in the case of the impure E211 spectrum.

The Raman spectra of the E211 solution were recorded in the concentrations range from 1 to 10^{-2} M where the Raman signal becomes very weak (Fig. V.3.2.4). These differences between the Raman spectra of the pure and commercial E211 can be due to the impurities, which are present in the

commercial substance. Because of contamination in the manufacturing process, some heavy metals, most notably lead, are often found in the finished products[343]. The E211 used in the food industry can contain in small doses arsenic, lead, and mercury.
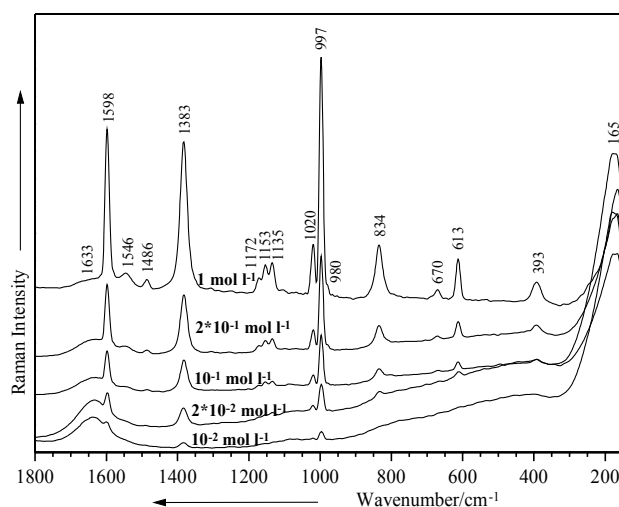
Figure V.3.2.4. Micro-Raman spectra of pure sodium benzoate solution at different concentrations.
Excitation: 514.5 nm, 200 mW.

Analyzing the micro-Raman spectra of E211 solutions at different basic (Fig. V.3.2.5) and acidic (Fig. V.3.2.6) pH values, we can figure out that this behavior shows the transition from the undissociated to the anionic molecular form of the E211 molecules.
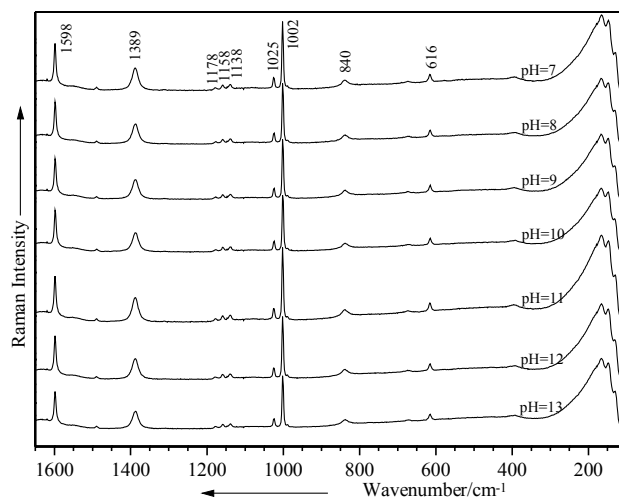
Figure V.3.2.5. Micro-Raman spectra of the 10^{-1} M E211 solution at different basic pH values.
Excitation: 514.5 nm, 100 mW.

At basic pH values no important changes can be observed in the range 7-13. The only modifications appear in the bands associated to asymmetrical and symmetrical stretching modes of the carboxylate (1598 and 1002 cm^{-1}), which decrease in relative intensities while passing to higher pH

values (Fig. V.3.2.5). The major changes in band profiles and relative intensities appear below the pH 5. On passing from neutral to acidic pH values, the bands due to the carboxylate anion stretching modes decrease in relative intensity and become broader (1598, 1387 cm^{-1}). At pH 4 appears a new band at 792 cm^{-1}, which can be due to the symmetrical out of plane deformation mode of the carboxylate anion (Fig. V.3.2.6). This band is absent in the FT-Raman spectrum of the E211 powder (Fig. V.3.2.1 a) and the Raman spectra of the E211 solution in the normal pH range (Figs. V.3.2.3 and V.3.2.4).

The Raman spectrum at pH 3 shows the undissociated molecular form of the sodium benzoate (Fig. V.3.1.1c). Characteristic for this molecular form of E211 are the benzene ring breathing vibration at 1002 cm^{-1}, the asymmetrical carboxyl stretching mode $\upsilon_a(COOH)$ at 1600 cm^{-1}, and the symmetrical carboxyl stretching mode $\upsilon_s(COOH)$ at 1387 cm^{-1}.

In the Raman spectrum at pH 5, when E211 is dissociated (Fig. V.3.1.1b), the asymmetrical carboxylate stretching mode $\upsilon_a(COO^-)$ at 1598 cm^{-1} is shifted, whereas the symmetrical carboxylate stretching mode $\upsilon_s(COO^-)$ remains at the same wavenumber, but with an increased intensity.
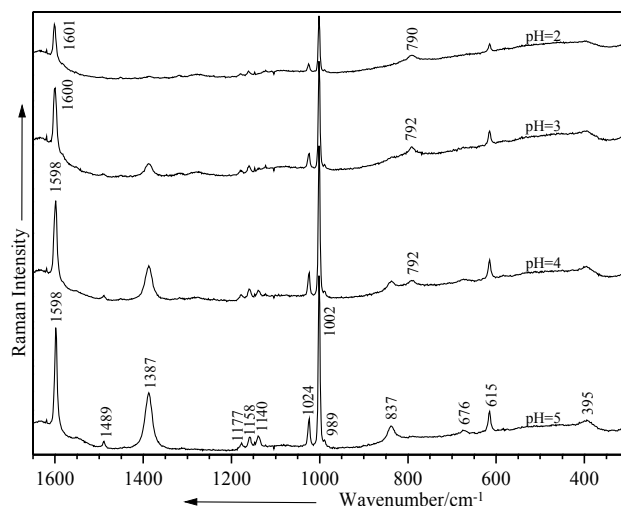
Figure V.3.2.6. Micro-Raman spectra of the 10^{-1} M E211 solution at different acidic pH values. Excitation: 514.5 nm, 100 mW.

The two distinct available forms of E211 were found to have slightly different Raman behavior. At the present stage of the work, both forms, pure and industrial E211, could be detected from the solution down to micromolar level and revealed the transition from anionic to undissociated form while passing to acidic pH values. The effectiveness of E211 as a preservative increases with decreasing pH (increasing acidity). This is because the ratio of undissociated benzoic acid to ionized benzoic acid increases as the pH decreases. The undissociated benzoic acid is the active antimicrobial agent.

The SERS spectrum of E211 is presented in Fig. V.3.2.7 in comparison with the Raman spectrum of the bulk solution at micromolar concentration and pH 7. On passing from the Raman to SERS spectra at micromolar concentrations, large differences are present both in band positions and relative intensities.

The negatively charged additive was expected to preserve the aggregation status and hence the silver surface potential[324]. Since the SERS signal is concentration sensitive, in order to discuss the

adsorption behavior of the sodium benzoate on the silver particles, the SERS spectrum at micromolar concentration was chosen here for the adsorption geometry proposal.

Theoretically, the E211 molecular structure could interact with the silver colloidal surface through the functional group, namely carboxylate or through the π electrons of the benzene ring.
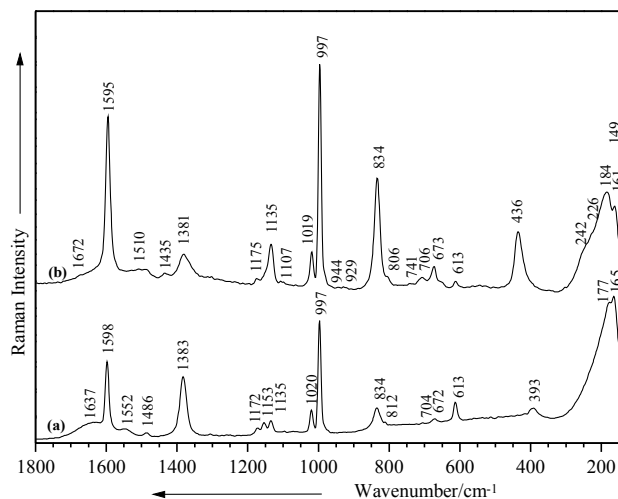
Figure V.3.2.7. Comparison between micro-Raman (2×10^{-1} M) (a) and SERS (2.8×10^{-3} M) (b) spectra of E211 (pH 7). Excitation: 514.5 nm, 200 mW (a,b).

The latter supposition is excluded because the breathing vibrational mode of the benzene ring is very high in relative intensity in the SERS spectra. Although the SERS selection rule has not been established unequivocally, the benzene ring C-H stretching vibration was demonstrated to be an unambiguous probe in the determination of surface orientation of aromatics. In accordance to the electromagnetic selection rules proposed by Creighton[108] and Moskovits and Suh[344], the C-H stretching mode should be relatively enhanced when the C-H bond is perpendicular to the surface plane as compared to the case in which the C-H bond lies parallel to the surface.

Taking into account the electronegativity of the COO⁻ extreme functional group, these parts would support a Coulombian repulsion due to the negative potential of the silver surface. The benzene ring could lie in the close vicinity of a bump from the silver aggregate. In this case, a large enhancement of the COO⁻ stretching modes is expected and consequently, a great enhancement for the mentioned ring modes.

On the other hand, the possibility for E211 to chemisorb is provided by the presence of the lone pair electrons of oxygen atom from the carboxylate (Fig. V.3.1.1). In this case, according to the surface selection rules[108] the stretching modes of the carboxylate are expected to be enhanced.

The observed bands in the SERS spectrum (Fig. V.3.2.7) support the later consideration. More specifically, the intense band at 1595 cm⁻¹ assigned to the symmetrical stretching mode of the carboxylate is in the close vicinity of the silver particles with a perpendicular orientation of the ring. The very strong band observed in the SERS spectrum at 997 cm⁻¹ is due to the phenyl ring breathing mode. This interaction generated by the presence of the COO⁻ functional group, negatively charged, leads to a

bending of the functional group near the surface through the lone pair electrons of the oxygen atom. This contribution is supported by the band at 834 cm^{-1} (Fig. V.3.2.7b), which can be assigned to the symmetrical in plane COO$^-$ deformation mode. By comparing the SERS spectrum to the Raman spectrum (Fig. V.3.2.7a), the mode at 834 cm^{-1} is significantly enhanced, which is due to the symmetrical in plane deformation of the carboxylate perpendicularly adsorbed. The new band at 436 cm^{-1} is due to the in plane bending mode of the carboxylate. Other bands with medium or weak intensities from the SERS spectrum are attributed to many bending modes of the structure.

The intense band at 184 cm^{-1} was assigned to the well-known Ag-O stretching mode[345] and the shoulder at 149 cm^{-1} can be attributed to the O-Ag-O deformation mode[346]. The structures of the carboxylate anion and aromatic ring influence each other. This might be revealed in exclusive physico-chemical or biological properties of the molecule. The metal affects the carboxylate anion as well as the aromatic ring structure. The ionic potential of the metal is the most important parameter responsible for the influence of the metal on the rest of the molecule[334,337]. The monocarboxylic acids chemisorb on silver surfaces as symmetric[335,336], bidentate carboxylate anions and both oxygen atoms of the carboxylate are symmetrically bonded to the surface[347].

Lowering the concentration (Fig. V.3.2.8) several bands decrease in the SERS intensity, while the shoulder at 806 cm^{-1} (in plane C-H wagging mode) becomes a weaker band at the concentration of 2.8 10^{-4} M. Therefore a reorientation of E211 species is not possible.
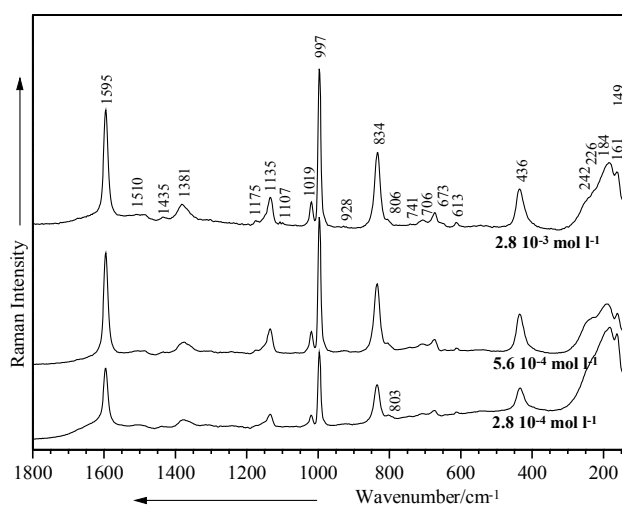
Figure V.3.2.8. SERS spectra of E211 at different concentrations. Excitation: 514.5 nm, 200 mW.

The vibrational assignment of the free species has been made using the previous data from literature[334-342] on the E211 and benzoic acid. A strong chemical interaction of sodium benzoate with the silver colloidal particles was observed at lower concentration through the carboxylate anion.

SERS spectra of the E211 at different acidic pH values (Fig. V.3.2.9) show dramatical changes in band positions and relative intensities. The SERS signal in the case of acidic pH range was recorded just for two values, namely 4.5 and 6.5. Beginning with the pH 3.5 values, the SERS signal is very weak or

absent. In the case of basic pH values, the SERS signal is very noisy (spectra not shown here).

In contrast with the normal SERS measurements (pH 7) (Fig. V.3.2.7b), beginning with the pH 6.5, the band corresponding to the COO⁻ asymmetrical stretching mode (1595 cm⁻¹ in the SERS spectrum at pH 7–Fig. V.3.2.7b) is shifted at 1603 cm⁻¹. At pH 4.5, this band is shifted at approximately the same position (1594 cm⁻¹), is decreased in relative intensity, and exhibits a weak shoulder at about 1573 cm⁻¹. Further, a new band at 1646 cm⁻¹ is present, due to the quadrant deformation mode of the benzene ring. The weak shoulder at 1573 cm⁻¹ is due to the CC aromatic bonds stretching mode. The very weak band at about 1500 cm⁻¹ in the SERS spectra at pH 7 (Fig. V.3.2.7b) and 6.5 (Fig. V.3.2.9) increases in relative intensity at pH 4.5 and was assigned to the symmetrical tangential stretching mode of the aromatic ring.

Furthermore, the symmetrical stretching mode of COO⁻ anion increases in relative intensity and is shared out into two bands at 1375 and 1359 cm⁻¹, respectively. Also the following bands at 1170, 1153, 1133, and 1022 cm⁻¹, bands corresponding to the in plane C-H deformation of the benzene ring, decrease in relative intensities. The very strong band in the SERS spectrum of E211 at pH 7 (Fig. V.3.2.7b–997 cm⁻¹) (breathing mode of the benzene ring) becomes weaker at pH 4.5. Very important to point out is the presence of the new peak at 558 cm⁻¹ (SERS spectrum at pH 4.5–Fig. V.3.2.9), which was attributed to the asymmetrical in plane deformation of the COO⁻ functional group[334].
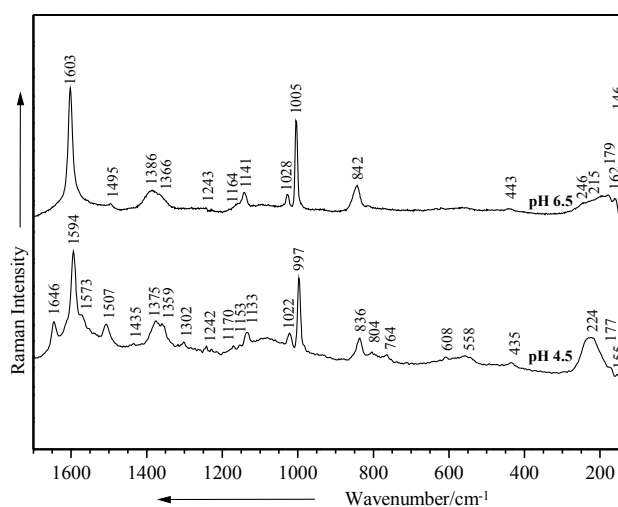
Figure V.3.2.9. SERS spectra of E211 at different acidic pH values. Excitation: 514.5 nm, 250 mW.

The acidic pH adjustment was performed with 10^{-1} M of HCl solution. The only intense band, which can be observed in the presence of Cl⁻, is the υ (Ag-Cl) stretching motion that appears at about 200 cm⁻¹ and can be very useful in the study of the adsorption of the molecule on the silver surface[348]. In our spectra, we can observe this band at 224 cm⁻¹, which increases, in relative intensity with the added quantity of HCl solution[349]. In addition to this band, other weaker bands or shoulders can be seen. These shoulders appear at 113 and 177 cm⁻¹ and are assigned to vibrations of smaller silver particles or adatoms, produced by the oxidation-reduction action of Cl⁻ on the surface of the silver colloid[140]. In the acidic pH range, the dissociated form of benzoic acid is present. We assume an adsorption geometry of the E211

molecule on silver colloidal particles in the acidic pH range through the carboxylate anion, in a perpendicular orientation.

V.3.3 Conclusions

The FT-Raman and micro-Raman spectra of the E211 powder were recorded and the marker bands of characteristic functional groups were identified. The Raman signal for the industrial E211 is weaker that than of the pure probe, probably due to the presence of heavy metals impurities.

The micro-Raman spectra of the E211 solutions could be recorded down to micromolar level. A weak fluorescence background was observed in the case of the industrial probe, possibly due to heavy metals. Analyzing the Raman spectra of E211 solutions could evidence the transition from anionic to undissociated form of the E211 the on going from basic to acidic pH values.

SERS spectra of E211 could be recorded even at low concentrations with a conventional SERS setup (2.8×10^{-4} M). The surface selection rules, along with data from literature, have reasonably explained the adsorbate structures on the metal surface at different concentrations and pH values.

A strong chemical interaction of E211 with the silver colloidal particles was observed under micromolar concentrations through the lone pair electrons of the oxygen atoms of the carboxylate anion in a perpendicular orientation. The SERS spectra of E211 at acidic pH values were recorded and revealed the same orientation through the carboxylate anion.

V.4 Erythrosine B (E127)

Erythrosine B, a very useful artificial food additive, is detectable in aqueous solutions down to micromolar level with surface-enhanced resonance Raman spectroscopy (SERRS). The presence of different species, such as protonated and unprotonated erythrosine B, is demonstrated by concentration and pH dependent SERRS experiments. In particular, the xanthene and benzene rings vibration modes and the stretching modes of the carboxylate moiety are employed as marker bands. From the measured SERRS spectra, a strong chemical interaction of erythrosine B with the silver colloidal particles is deduced and the orientation possibilities of erythrosine B adsorbed on the silver surface at different concentrations are proposed. In order to assign the observed SERRS bands, calculations employing density functional theory (DFT) were performed.

V.4.1 Molecule presentation

Erythrosine (iodoeosin, erythrosine B, or E127 in Europe) is an artificial food colorant belonging to the xanthene class and consists essentially of 2(2,4,5,7–tetraiodo–6–oxido–3–oxo–3H–xanthene–9–yl)–benzenesulfonic acid, disodium salt and subsidiary coloring matters together with water, sodium chloride and/or sodium sulfate as principal uncolored components. Erythrosine B (Ery B) appears like a dark red to brown powder[350]. Typical EryB products are milk pudding, biscuits, glace, cherries, canned

cherries and strawberries, and syrup. EryB is also used in a variety of staining procedures in histological laboratories[351].

Previously published studies have shown that consumption of EryB can increase thyroid hormone levels leading to hyperthyroidism, and can cause sensitivity to light[352]. The detection of food dyes in complex matrices such as food or pharmaceutical drugs is often performed by capillary electrophoresis[353] and spectrophotometric methods[354-356]. Several studies reported on EryB, demonstrate that its encapsulation in liosomes decreases the calcium level in plasma[357-362], that it can activate anticonvulsant drugs which reduce symptoms of painful diabetic neuropathy[363,364], and that its ability to fluorescence quench is used in protein analysis[365-368].

In vivo and *in vitro* studies show that EryB may have utility as cancer chemopreventive agent[369] but also can produce mutagenic effects[370-380]. Most commercial vitamins contain EryB and iodine as an essential nutrient[381]. Anionic xanthene dyes have been shown to exert a wide range of pharmacological effects in excitable tissues[382,383]. Therefore it has been exposed to influence the acetylcholine release, to inhibit the Na-K adenosine-triphosphatase activity, and the cardiac glycoside binding, as well as the thyroid function[384-386]. EryB is also used to reveal plaque in dental disclosing tablets[387].
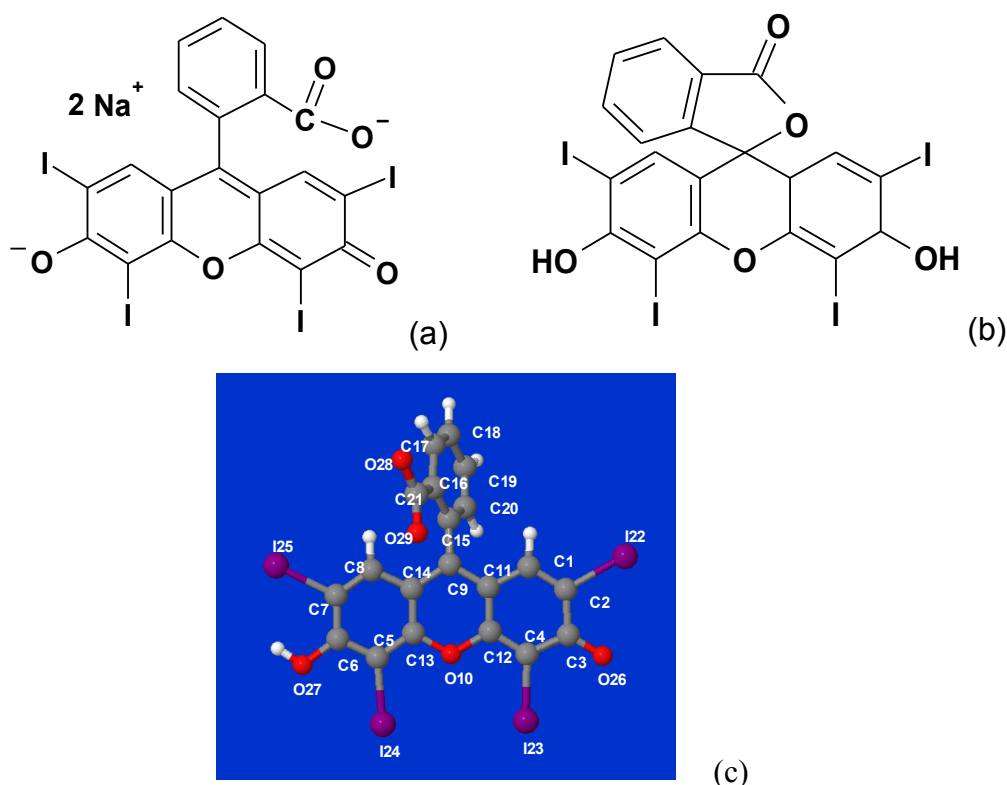
Figure V.4.1.1. Molecular structures of EryB: sodium salts (a), lactone (b) form, and B3LYP/LANL2DZ optimized geometry (c).

Vibrational spectroscopy provides important molecular information about the composition, structure and properties of biological samples. EryB can be present as sodium salts or lactone form[350] (Fig. V.4.1.1). The aim of our study is to experimentally determine the differences between its sodium salts and lactone form by SERRS.

Fluorescence of the dye, which could be produced by its anions and might be affected by its

concentration[388], was quenched by silver colloidal particles and the SERR spectra were collected by employing the 514.5 nm excitation laser line. The presence of a metal surface has the advantage that the fluorescence of dye molecules, which hampers the direct observation of the Raman spectrum, is quenched by through space, long-range energy transfer of the Perrin-Förster-type, if the dye molecules are close to a metal surface[389]. The 514.5 nm excitation laser line employed in our SERRS experiments corresponds to a resonant excitation of EryB (Fig. V.4.1.2).
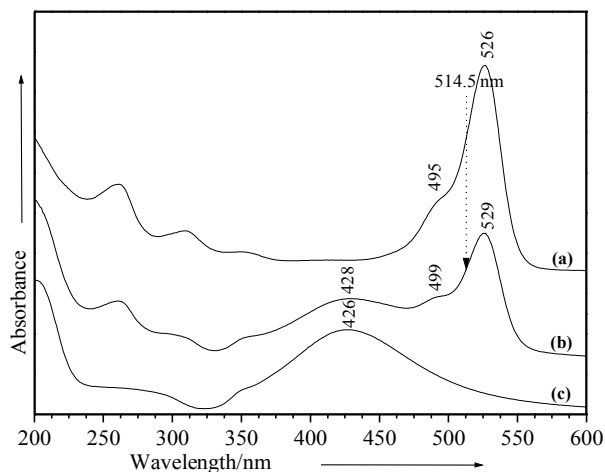
Figure V.4.1.2. UV-VIS absorption spectra of EryB (a), mixture of EryB with Lee Meisel silver colloid (b), and Lee Meisel silver colloid (c).

V.4.2 Geometry optimization

Crystal structure data reported[390] on EryB and its optimized structure at different levels of theories (BPW91/6-311+G(d), B3LYP/6-31+G(d)) were compared with those of identical or similar functional groups of EryB from literature[391-398]. The calculated structural parameters of EryB are listed in Table V.4.1.1 and the labeling of the atoms is shown in Fig. V.4.1.1c. Simultaneously we can notice that there is a very good agreement between the theoretically determined parameters of EryB and the experimental values available in the literature[391-398].

According to our DFT calculations, the molecular conformation of EryB (Fig. V.4.1.1c) is planar except for the benzoic acid, which lies nearly perpendicular to the xanthene ring with the C20-C15-C9-C14 dihedral angle of 71.8°. This angle agrees with previously X-Ray published data[390,393,399,400], and because of this value is smaller that 87.7°, we can confirm the existence of the quinoid (sodium salts) form of the EryB[401]. Also specifically for the quinoid form of EryB are that the C14-C9 and C9-C11 bond lengths are not extended (143.8 and 144.1 pm, Table V.4.1.1) and also the bonds and angles of the xanthene ring indicate normal values as a three range benzenes[401]. Usually, the cationic xanthene structures are stabilized in a quinoid form[402]. The benzene ring bearing the carboxylate group stands nearly at right angle to the xanthene part.

The carboxylate group must be towards the electrophilic central carbon so as to stabilize it until reaching an appropriate position to form the C-O bond of the lactone in the process of geometrical

distorsion[403], but in our case it is not observed. Our calculated bond lengths, angles, and dihedral angles all fall within a reasonable range expected for similar compounds. As it may be seen, the agreement between the experimental[390-406] and calculated values is fairly good (Table V.4.1.1).

The geometry of the xanthene ring system is consistent with a tautomer form in which the dye is a free acid with a keto oxygen at O26 and a hydroxyl oxygen at O27 (Fig. V.4.1.1c). The xanthene ring is nearly planar along the O15-C9 bond (the dihedral angles O10-C13-C5-I24=0.9° and O10-C12-C4-I23=0.1°) (Table V.4.1.1). The carboxylate group is nearly coplanar with the benzene ring (C15-C16-C21-O29=0.4° and C17-C16-C21-O28=2.5°) (Table V.4.1.1). The C13-O10 and C12-O10 bond lengths (139.4 pm and 141.5 pm) are similar values with the experimental data[391,396,400,404,405] and very close to a single C-O bond length (143 pm)[407,408]. The C-O bonds lengths corresponding to the carboxylate group are higher than that of a normal C=O double bond and smaller than that of a normal C-O single bond (Fig. V.4.1.1c, Table V.4.1.1), which means that the electric charge is equally distributed between both oxygen atoms[407-411].

Table V.4.1.1. Selected calculated structural parameters of EryB in comparison with the available experimental data.

	Exp.	Calcd.	
		BLYP	BPW91
		LANL2DZ	LANL2DZ
Bond-lengths (pm)			
C1-C2	133.639[1]; 138.9[401]	138.6	138.5
C2-C3	147.4[391]; 142.0[393]; 150.3[405]	146.0	145.8
C3-C4	145.5[391]; 144.3[401]	146.8	146.2
C4-C12	134.5[391]; 138.9[401]	139.0	138.7
C12-C11	145.0[391]; 133.4[400]	143.3	142.9
C5-C6	137.8[391]; 141.0[393]; 138.4[405]	141.6	141.3
C6-C7	143.0[393]; 138.1[404]; 141.5[405]	141.1	140.9
C7-C8	137.7[391]; 138.9[404]; 140.3[405]	139.5	139.2
C8-C14	143.0[393]; 147.8[400]; 139.5[404]	142.4	141.9
C14-C9	145.8[391]; 143.0[401]; 147.8[404]	143.8	143.5
C9-C11	135.7[391]; 151.6[400]	144.1	143.8
C14-C13	139.1[391]; 139.6[404]	143.3	142.9
C13-C5	138.7[391]; 149.2[400]; 138.0[404]	140.3	140.0
C11-C1	145.3[391]; 141.0[393]; 147.2[400]	142.8	142.3
C2-I22	215.0[413]; 216.7[415]	215.9	214.6
C4-I23	213.0[414]	213.7	212.6
C5-I24	212.0[414]	212.7	211.6
C7-I25	212.0[414]	216.8	215.5
C12-O10	137.2[396]; 137.5[400]; 137.4[405]	141.5	140.8
C13-O10	138.7[396]; 137.9[400]; 139.1[405]	139.4	138.7
C3-O26	121.5[391]; 120.0[405]	128.6	128.2
C6-O27	135.3[391]; 134.9[405]	140.3	139.5
C21-O28		128.5	128.4
C21-O29		129.4	129.0
C9-C15	153.6[400]; 149.9[401]; 136.2[404]	149.9	149.3
C15-C16	146.7[404]	142.5	142.2
C16-C17	133.6[404]	141.6	141.3
C17-C18	144.2[404]	140.3	140.0
C18-C19	132.6[404]	141.1	140.8
C19-C20		140.3	140.0
C20-C15		142.3	142.0
C16-C21	149.7[401]	155.5	154.9
Angles (°)			
C15-C16-C21	121.5[401]; 126.5[404]	124.5	124.3
C16-C21-O28	124.1[401]	116.5	116.4
C16-C21-O29	114.1[401]	115.3	115.3

O28-C21-O29	123.4[401]	128.2	128.2
C9-C15-C16	120.3[401]; 122.4[404]	126.1	126.0
C9-C15-C20	112.5[401]	115.7	115.7
C20-C15-C16	113.7[404]	118.2	118.3
C15-C9-C14	123.8[404]	120.9	121.0
C11-C12-O10	121.5[405]	119.5	119.7
C14-C13-O10	121.8[404]; 121.0[405]	120.9	121.0
C12-O10-C13	112.2[396]; 117.2[404]; 119.0[405]	120.7	120.7
Dihedral angles(°)			
C16-C15-C9-C11	87.5[393]; 81.4[399]; 79.6[401]	71.8	71.8
O10-C13-C5-I24		0.9	1.0
O10-C12-C4-I23		0.1	0.2
I24-C5-C6-O27		0.2	0.1
O27-C6-C7-I25		0.1	0.3
C15-C16-C21-O29		0.4	0.4
C17-C16-C21-C28		2.5	2.5

The carbon-halogen bond lengths correlate well with changes in hybridization of the carbon atom[412]. In our study, the C2-I22, C4-I23, C5-I24, and C7-I25 bond lengths (Table V.4.1.1, Fig. V.4.1.1c) vary between 211.6 pm and 216.8 pm. These values are quite similar with the normal C-I bond length (214 pm)[413-417].

Except for the benzoate moiety, the EryB molecule is planar. The mean plane defined by the atoms of the benzoate moiety is almost perpendicular (71.8°) to the xanthene ring. The hydroxyl group at C6 is not intramolecularly hydrogen bonded because the length of the [O27-H···I25=266.2 pm] bond, is longer than that of a hydrogen bond [183 pm][418].

V.4.3 Electronic spectroscopy

The absorption spectra of EryB, EryB on silver colloid, and silver colloid are presented in the Fig. V.4.1.2. The EryB absorption spectrum showed two high absorption maxima at 526 and 261 nm, respectively, and a shoulder at 495 nm. According to the literature[419], in aqueous solution, the absorbance maximum of EryB occurs at 526 nm. A possible mechanism for the EryB solution is an ionization process (proton abstraction) reaction between EryB and water[420]. The absorption maximum of EryB on silver colloid is slightly shifted to higher wavelengths (529 nm) and the band is broadened. These changes can be explained through the variation of the probe concentration[392].

Study about electron-transfer reaction between dye molecules in solution and in biological systems shows emission maxima at 550 nm and the areas under the emission curves were very similar, indicating identical fluorescence quantum yields[421]. Therefore, employing in our measurements 514.5 nm laser line for the probe excitation and the silver colloidal particles, the probe quenching was smaller and the SERRS spectra were acquired. Consequently, the charge transfer between dyes was enhanced and the fluorescence intensity decreased.

The EryB is available in two forms: the sodium salts (Fig. V.4.1.1a) and the lactone form (Fig. V.4.1.1b), which is spirit soluble. The EryB can be changed in one of the two forms depending on water addition. The increase in absorbance can be attributed to the reversible hydrolysis of the lactone group to the carboxylic acid by adding water[419,422]. The addition of considerable excesses of alkali gave no indication of further salt formation in either aqueous or alcoholic solution. If the dye (disodium salt)

contained free hydroxyl groups, further salt formation would be expected with an excess of alkali, attended by appreciable modifications in color. When an excess of acid is avoided, this transformation is attended by little or no decrease in color intensity. Further additions of acid result in a progressive transformation of the monosodium salts into the (yellow) color acid. The color and absorption of the color acid are much less intense than those of its salts. The transition between lactonoid and quinoid structure results in an extreme modification in color[350].

V.4.4 Vibrational spectroscopy

FT-Raman spectrum of solid state Ery B

The vibrational fundamentals from the FT-Raman spectrum of EryB powder, presented in the Fig. V.4.3.1 were analyzed by comparing the vibrational modes with those from the literature[359,420,424,425].

The very strong band at 1271 cm^{-1} of the FT-Raman spectrum was attributed to the asymmetrical stretching mode of C12-O10-C13 and to the C9-C15 bridge bond stretching mode. The very strong band at 1490 cm^{-1} was assigned to the in plane C-H deformation mode of the xanthene and benzene rings. The strong peak at 1344 cm^{-1} with the shoulder at 1333 cm^{-1} correspond to the in plane C-C deformation of the xanthene ring. The aromatic asymmetrical and symmetrical C-H stretching modes can be observed also at 3056 and 2886 cm^{-1}, respectively. The following strong band at 1471 cm^{-1} corresponds to the C12-O10-C13 deformation mode and to the in plane C-C and C-H deformations of the xanthene ring.
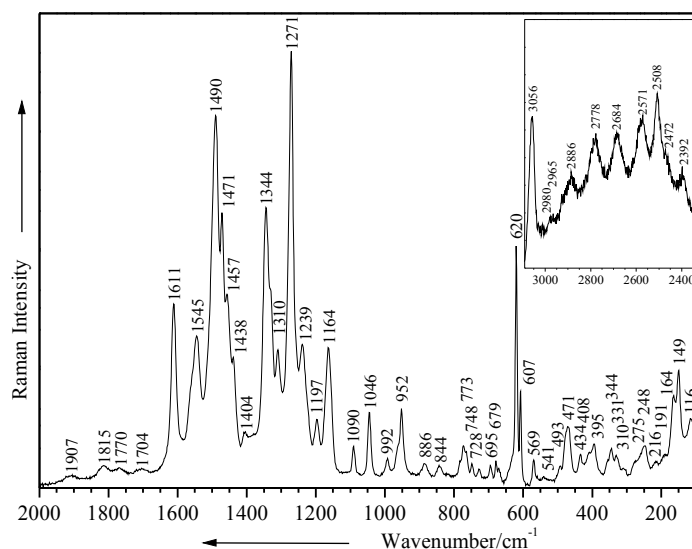
Figure V.4.3.1. FT-Raman spectrum of Ery B dark red powder.
Excitation: 1064 nm, 150 mW.

The asymmetrical COO^{-} stretching vibrational mode corresponds to the medium strong band at 1611 cm^{-1}, whereas the symmetrical stretching mode of COO^{-} functional group was found at 1457 cm^{-1}. Other bands connected with the benzene ring vibrations are the medium band at 1545 cm^{-1} that was assigned to the benzene ring doublet stretching mode and the medium peak at 1438 cm^{-1}, which was attributed to the benzene ring rocking mode. The bands at 1907 and 1770 cm^{-1} were assigned to the

C3=O26 stretching mode, whereas the alongside peak at 1704 cm^{-1} corresponds to the in plane C-C and C-H deformation modes of the xanthene ring. The very weak peak at 1404 cm^{-1} and the medium band at 1239 cm^{-1} can be assigned to the in plane C6-O27H bending mode belonging to the xanthene ring. The medium band at 1310 cm^{-1} can be due to the in plane C-H deformation mode of the benzene ring.

The weak peaks at 1197 and 1046 cm^{-1} were attributed to the symmetrical C12-O10-C13 stretching mode and to the C12-O10-C13 deformation mode, respectively. The xanthene ring breathing mode was observed at 1164 cm^{-1}, while the very weak peak at 992 cm^{-1} was attributed to the trigonal benzene ring breathing mode. Several bands from the FT-Raman spectrum are connected with the xanthene ring deformation modes (952, 844, 773, 748, 695, 679, 607 cm^{-1}) and the torsion vibrational modes of the same ring correspond to three weak peaks (344, 310, and 275 cm^{-1}), while other bands from this region are associated with the in plane C-H deformation mode of the benzene ring (1090, 728, and 620 cm^{-1}). The C-C skeletal stretching mode of the benzene ring appears at 886 cm^{-1}, whereas the skeletal deformation mode of the EryB molecule is represented by a few weak bands (471, 395, and 331 cm^{-1}).

Highly important for the FT-Raman spectrum assignment are the symmetrical C-I stretching modes, which appear in the low wavenumbers region and with low intensities (569, 541, 493, 471, 434, and 164 cm^{-1}).

Micro-Raman spectra of Ery B solutions

Comparing the micro-Raman spectrum of 10^{-1} M EryB solution with the FT-Raman spectrum of EryB powder (Fig. V.4.3.2) one can observe major differences in the band positions and relative intensities. Most noticeable differences are the increase in relative intensity for the asymmetrical stretching mode of the COO$^-$ group (1611 cm^{-1}–FT-Raman spectrum, 1621 cm^{-1}– micro-Raman spectrum; Fig. V.4.3.2), which is importantly blue shifted (10 cm^{-1}). The benzene ring doublet stretching mode present in the FT-Raman spectrum at 1545 cm^{-1} is essentially blue shifted (15 cm^{-1}) in the micro-Raman spectrum of EryB solution (1560 cm^{-1}) and becomes weaker.

The following group bands connected to the in plane C-H deformation mode of the xanthene ring (1504 cm^{-1} in the micro-Raman spectrum), the C12-O10-C13 deformation mode (1482 cm^{-1} in the micro-Raman spectrum), and the symmetrical stretching mode of the COO$^-$ group (1454 cm^{-1} in the micro-Raman spectrum) decrease in relative intensities and are also considerably blue shifted comparative with the FT-Raman spectrum (Fig. V.4.3.2). The strong peak at 1344 cm^{-1} becomes weaker and its shoulder at 1333 cm^{-1} is missing in the micro-Raman spectrum of the EryB solution (the only band at 1352 cm^{-1}). The very strong band at 1271 cm^{-1} in the FT-Raman spectrum of EryB powder corresponding to the asymmetrical C12-O10-C13 stretching mode and to the C9-C15 bridge bond stretching mode decreases in relative intensity and is 14 cm^{-1} blue shifted in the micro-Raman spectrum (1285 cm^{-1}) of EryB solution. The peak at 1164 cm^{-1} in the FT-Raman spectrum, which was assigned to the breathing mode of the xanthene ring becomes weaker in the micro-Raman spectrum of EryB solution (1163 cm^{-1}), while the very weak peak at 992 cm^{-1} in the FT-Raman spectrum that corresponds to the trigonal breathing mode of the benzene ring becomes higher in the micro-Raman spectrum of EryB solution and is 15 cm^{-1} blue shifted (1007 cm^{-1}).
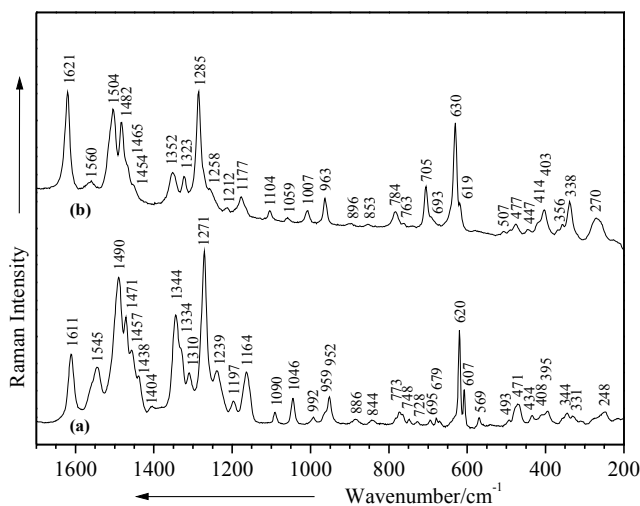
Figure V.4.3.2. FT-Raman spectrum of Ery B dark red powder (a) and micro-Raman spectrum of 10^{-1} M erythrosine solution. Excitation: 1064 nm, 150 mW (a); 632.8 nm, 3.6 mW (b).

The weak band at 952 cm^{-1} with a weak shoulder at 959 cm^{-1} in the FT-Raman spectrum of EryB powder turn out to be just one band with an increased relative intensity in the micro-Raman spectrum of solution (963 cm^{-1}). This corresponds to the xanthene ring deformation mode.
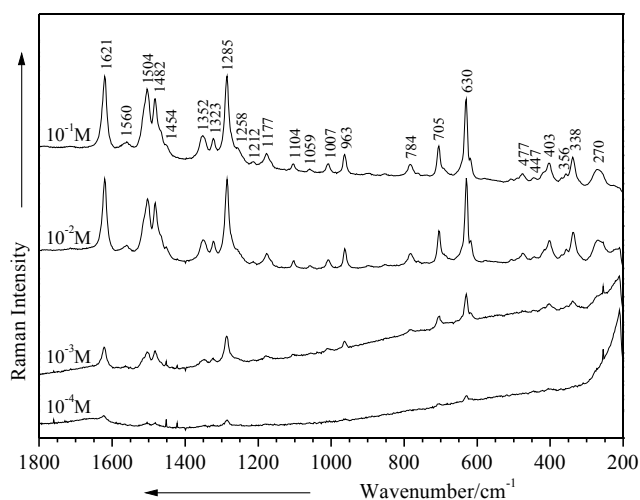
Figure. V.4.3.3. Micro-Raman spectra of Ery B solution at different concentrations.
Excitation: 632.8 nm, 3.6 mW.

Other differences between FT-Raman and micro-Raman spectra come into view the benzene ring deformations. Thus, the band at 620 cm^{-1} in the FT-Raman spectrum is 10 cm^{-1} blue shifted and increased in relative intensity in the micro-Raman spectrum of solution (630 cm^{-1}). The weak peak at 607 cm^{-1} in the FT-Raman spectrum is also blue shifted (12 cm^{-1}) in the micro-Raman spectrum and becomes weaker (619 cm^{-1}) (Fig. V.4.3.2). The bands' shifting is due, probably, to the well-known solvent effects.

At higher concentration values one can observe broadening of the bands. At lower concentrations of EryB the intermolecular interactions between ionized EryB molecules are decreased[392]. Analyzing the

concentrations dependence in the range of 10^{-1}-10^{-4} M we could observe that on going to lower concentrations the Raman signal becomes weaker and at 10^{-4} M is absent (Fig. V.4.3.3).

In the concentration dependence Raman and SERRS spectroscopy study[423] of Ery B, the FT-Raman spectrum of solid EryB was recorded, the marker bands were identified and the Raman spectra of EryB aqueous solution revealed the possibility to record high quality Raman spectra down to milimolar concentration level.

SERRS spectra of EryB

The SERRS spectrum of EryB is presented in Fig. V.4.3.4 in comparison with the micro-Raman spectrum of the bulk solution at micromolar concentration. On passing from the micro-Raman to SERRS spectra of the EryB molecule at micromolar concentrations, large differences are present either in band positions or relative intensities.

The negatively charged food additive was expected to preserve the aggregation status and hence the silver surface potential[324]. Theoretically, the EryB molecular structure could interact with the silver colloidal surface through more than one functional group.
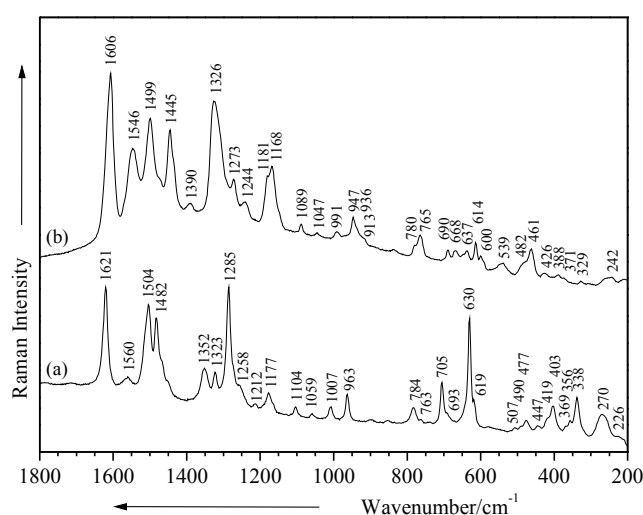
Figure V.4.3.4. Micro-Raman (10^{-1} M) (a) and SERRS (0.39 10^{-7} M) (b)
spectra of Ery B. Excitation: 623.8 nm, 3.6 mW (a); 514.5 nm, 100 mW (b).

Also, in the case of the SERRS signal, the molecular resonance has a major contribution to the overall enhancement as the spectra are dominated by the chromophore and the molecule is less pronounced. A second point regarding the SERR-activity of the respective dye is the spectral overlap of the excitation light and the absorption spectrum (Fig. V.4.1.2).

The SERS selection rule has not been established unequivocally and the benzene ring C-H stretching vibration was demonstrated to be an unambiguous probe in the determination of surface orientation of aromatics. In accordance with the electromagnetic selection rules proposed by Creighton[108] and by Moskovits and Suh[344], the C-H stretching mode should be relatively enhanced when the C-H bond is perpendicular to the surface plane rather than when the C-H bond lies parallel to the surface.

Taking into account the electronegativity of the COO⁻ extreme functional group of the benzene

ring, these parts would support a Coulombian repulsion due to the negative potential of the silver surface[426]. The benzene ring could lie in the close vicinity of a bump from silver aggregate. In this case, a large enhancement of the COO⁻ stretching modes is expected and consequently, a great enhancement for the mentioned ring modes.

On the other hand, the possibility for benzene ring to chemisorb is provided by the presence of the lone pair electrons of oxygen atom from the carboxylate (Fig. V.4.1.1). In this case, according to the surface selection rules[108] the stretching modes of the carboxylate are expected to be enhanced.

In general, SERR signals from the compound could be observed only in the presence of the citrate covering the surface of the metal particles and using the resonant excitation laser line[427]. This implies that the adsorption of this dye takes place in the electrical double layer of the colloids via interactions with the chemisorbed citrate rather than with the metal itself. This refers to both electromagnetic and chemical mechanisms, whereas the latter additionally requires the coadsorption of halide ions.

In this way, surface complexes including citrate, halide, and the dye are formed at specific sites of the metal surface where the charge transfer between the metal and the adsorbate can take place[428]. Negatively charged substituents lead to a drastic lowering of the adsorption constants. This is also true for the EryB molecule although the anionic group is remote from the surface complexes which are destabilized by repulsive interactions between the benzoate and the specifically adsorbed anions. Such interactions are only possible in a coplanar orientation of the xanthene ring system with respect to the metal surface[398]. We suppose that the EryB molecule can lie on the silver surface with the xanthene ring parallel and with the benzoate group perpendicular.

Consequently, the present red shifts seemed to be caused by the electrostatic interaction between the carboxyl group of the xanthene dyes (1621 cm⁻¹ in the micro-Raman spectrum and 1606 cm⁻¹ in the SERRS spectrum) in their excited states and the negatively charged silver surface[429]. In addition, the relative intensity was promptly increased with higher amounts of the dye. The observed bands in the SERR spectrum (Fig. V.4.3.4) support our consideration.

Specifically, the very intense band at 1606 cm⁻¹ assigned to the asymmetrical stretching mode of the carboxylate is in the close vicinity of the silver particles with a perpendicular orientation of the ring. Moreover, the shoulder at 1454 cm⁻¹ observed in the micro-Raman spectrum of EryB solution becomes a medium strong band in the SERRS spectrum at 1445 cm⁻¹ (also red shifted) and can be due to the symmetrical stretching mode of the carboxylate anion. Besides, this interaction generates the presence of the COO⁻ functional group, negatively charged, to bend near the surface through the lone pair electrons of the oxygen atom.

This contribution is supported by the medium strong band at 1546 cm⁻¹ (Fig. V.4.3.4), which is dramatically increased in relative intensity in the SERRS spectrum by comparing it with the micro-Raman spectrum (1560 cm⁻¹) and can be attributed to the stretching mode of the benzene ring doublet. This one, according to our optimized geometry of the EryB, suggests that the benzene ring is also perpendicularly oriented on the silver colloidal particles along the carboxylate group (Fig. V.4.3.5a).
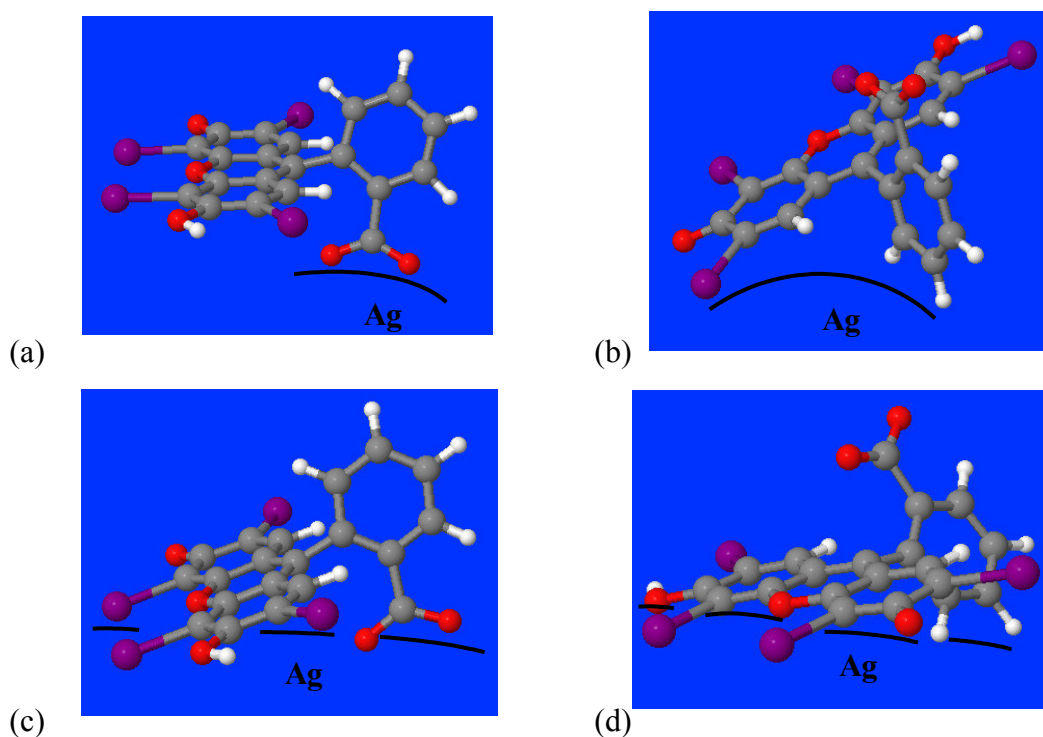
Figure V.4.3.5. Proposed orientation of EryB on the silver surface at concentration of 0.39×10^{-7} M (a); 0.39×10^{-8} M (b); 0.39×10^{-9} M (c); 0.39×10^{-10} M (d).

In comparison to the micro-Raman spectrum (Fig. V.4.3.4), the medium strong peak at 1499 cm^{-1} is slightly decreased in relative intensity and slightly red shifted, and can be due to the C-H in plane deformation mode of the xanthene and benzene rings. Furthermore, the strong band at 1482 cm^{-1} in the micro-Raman spectrum becomes a weak shoulder in the SERRS spectrum at micromolar concentration and suggests the C12-O10-C13 deformation mode. Moreover, the very strong band from the micro-Raman spectrum at 1285 cm^{-1}, which decreased in relative intensity in the SERRS spectrum and is 12 cm^{-1} red shifted (1273 cm^{-1}), can be produced by the asymmetrical stretching mode of the C12-O10-C13, while the increased peak at 1168 cm^{-1} involves probably the breathing mode of the xanthene ring. All these come to evidence that the xanthene ring lies parallel to the silver surface. The micro-Raman spectrum of EryB solution shows a very weak peak at 226 cm^{-1}. In contrast to this a slightly increased band appears at 242 cm^{-1} in the SERRS spectrum and can be due to the I$^-$ anions, which are present in the silver colloid. The frequency and the intensity of the 242 cm^{-1} band are the same for the Cl$^-$, Br$^-$, and F$^-$ containing sols. This behavior suggests that this band is independent of the anion type and therefore cannot be attributed to an Ag-I vibration. These types of vibrations could not be identified in the low frequency region[430,431]. The intense band at 197 cm^{-1} in the SERRS spectra (Fig. V.4.3.4) can be due to the well-known Ag-O stretching mode[345] and the medium peak at 143 cm^{-1} (Fig. V.4.3.4) can be attributed to the O-Ag-O deformation mode[346]. The structures of the carboxylate anion and aromatic ring influence each other. This might be revealed in exclusive physico-chemical or biological properties of the molecule. The metal affects the carboxylate anion as well as the aromatic ring structure. The ionic potential of the metal is the most important parameter responsible for the influence of the metal on the rest of the molecule[334,337]. The monocarboxylic acids chemisorb on silver surfaces as symmetric[335,336], bidentate

carboxylate anions and both oxygen atoms of the carboxylate are symmetrically bonded to the surface[347].
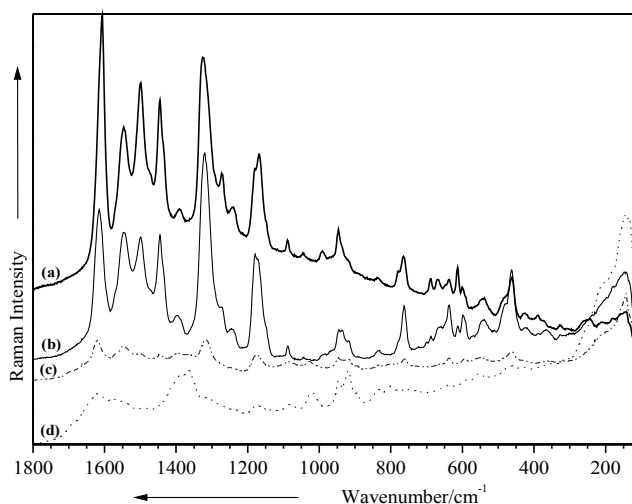
Figure V.4.3.6. SERRS spectra of EryB at different concentrations: 0.39×10^{-7} M (a); 0.39×10^{-8} M (b); 0.39×10^{-9} M (c); 0.39×10^{-10} M (d). Excitation: 514.5 nm (a-d), 100 mW (a-d).

Looking at the SERRS spectra at different concentrations (Fig. V.4.3.6a-d), we can remark that the Raman signal differs from one concentration to another which make us suppose various orientations of EryB depending on the concentration reduction. Lowering the concentration, the very strong band at 1606 cm^{-1} (Fig. V.4.3.6b, Table V.4.3.1), which was attributed to the asymmetrical stretching mode of the COO$^-$ group decreases in relative intensity, while the band at 1546 cm^{-1} that corresponds to the doublet benzene ring stretching mode slightly increases in relative intensity. The band assigned to the C-H in plane deformation of the benzene and xanthene rings (1499 cm^{-1}) decreases in relative intensity and becomes weaker than those of the doublet benzene ring stretching mode (1546 cm^{-1}) and symmetrical stretching mode of the carboxylate group (1445 cm^{-1}), which also decreases in relative intensity. The very strong band of the SERRS spectrum in the concentration range of 0.39 10^{-8} M remains the band attributed to the C-H in plane deformation mode of the benzene ring (1326 cm^{-1}). Furthermore, one can observe an increase in relative intensity for several bands: the band assigned to the bending mode of C-C-I from the the xanthene group (1179 cm^{-1}), the band which can be due to the out of plane deformation of the xanthene ring (765 cm^{-1}), and the peak at 463 cm^{-1} that was attributed to the symmetrical C-I stretching mode. Moreover, the C-I deformation mode increases in relative intensity (600 cm^{-1}).

The peak at 947 cm^{-1} splits into two weak peaks at 945 and 936 cm^{-1}, which can be assigned to the xanthene ring deformation modes. The C-C and C-H out of plane deformation modes of the benzene ring increase in relative intensity (637 cm^{-1}), whereas the xanthene ring deformation mode decreases in relative intensity (614 cm^{-1}) (Fig. V.4.3.6b).

Taking into account the vibrational modes assignment, the strong chemical interaction of EryB with the silver colloidal particles at the concentration of 0.39×10^{-8} M can be supposed through both benzene and xanthene rings. The xanthene ring lies tilted on the silver surface through the O26 and I22 atoms and the benzene ring seems to be quite perpendicularly to the silver surface. This orientation is also

supported by the Ag-O vibrational modes at 147 cm^{-1} and 119 cm^{-1}, which increase in relative intensities[432,433] (Fig. V.4.3.5b).

At the concentration of 0.39x10^{-9} M, one can observe that the symmetrical COO^{-} stretching mode becomes very weak or disappears, while the asymmetrical COO^{-} stretching mode increases in relative intensity and is 6 cm^{-1} blue shifted (Fig. V.4.3.6c). Several bands associated with the xanthene ring vibrations are increased in relative intensities as follows: the band at 1397 cm^{-1} (0.39 10^{-8} M) is split into two bands, at 1396 and 1358 cm^{-1}, which can be due to the in plane C6-O27H bending mode. Moreover, the band at 950 cm^{-1}, which was assigned to the xanthene ring deformation mode, increases in relative intensity as well as the peak at 920 cm^{-1}, which corresponds to the CC skeletal stretching mode of the benzene ring. In the low wavenumber region, the Raman signals at 637, 590, 542, and 461 cm^{-1} increase in relative intensities and are blue or red shifted in comparison to the SERR spectrum at concentration of 0.39x10^{-8} M (Table V.4.3.1). These bands are attributed to the out of plane CC, CH deformation modes of the benzene ring and to the asymmetrical and symmetrical C-I stretching modes. The most enhanced bands in this concentration range, which are due to the CH, CC deformation modes of both xanthene and benzene ring, C-I vibrations of the xanthene ring, and COO^{-} stretching modes, come to prove that the EryB molecule is adsorbed on the silver surface through the carboxylate group and the I23, I24 atoms of the xanthene ring are in a tilted orientation of the xanthene ring and a perpendicularly orientation of the benzene ring (Fig. V.4.3.5c). This orientation can be plead by the silver-halogen stretching mode at 215 cm^{-1} and both Ag-O, O-Ag-O stretching vibrations at 208 and 143 cm^{-1}, respectively[432-435].

At the concentration of 0.39x10^{-10} M (Fig. V.4.3.6d), a new shoulder at 1692 cm^{-1}, which can be due to the in plane CC, CH deformation modes of the xanthene ring, could be observed. The asymmetrical COO^{-} stretching mode decreases in relative intensity, whereas the symmetrical mode disappears. Moreover, the benzene ring doublet stretching mode becomes a shoulder (1539 cm^{-1}), the in plane C6-O27H bending mode (1388 cm^{-1}) and the C-H deformation modes of the xanthene ring (1369 cm^{-1}) increase in relative intensities (Table V.4.3.1, Fig. V.4.3.6d). In contrast to these, the in plane CH benzene deformation mode (1311 cm^{-1}) is 5 cm^{-1} red shifted and becomes weaker, while the symmetrical and asymmetrical C12-O10-C13 stretching modes disappear. The peak at 1178 cm^{-1}, which was assigned to the CC-I bending modes of the xanthene ring, becomes a weak peak and is slightly red shifted. The in plane C-H deformation modes (1078 cm^{-1}) of the benzene ring decreases in relative intensity, while the trigonal breathing mode of the benzene ring disappears.

Furthermore, the C12-O10-C13 deformation mode increases in relative intensity and is importantly (10 cm^{-1}) red shifted in comparison to the similar vibration for the concentration of 0.39x10^{-10} M (1018 cm^{-1}). The major changes in this concentration range can be observed at the xanthene ring level; the Raman bands increase in relative intensities and/or are shifted, which may suggest the arching of the xanthene ring at the silver surface. In this sense, the peak at 947 cm^{-1} becomes very strong and can be due to the xanthene ring deformation mode, while the band at 918 cm^{-1} turns out to be very strong and was attributed to the C-C skeletal stretching mode of the benzene ring[424,425].

Table V.4.3.1. Selected calculated and experimental Raman and SERRS wavenumbers (cm^{-1}) of EryB and their tentative assignment.

FT-Raman	Calc.		Raman solution	SERRS	SERRS	SERRS	SERRS	Vibrational assignment
	B3PW91	B3LYP		0.39x10^{-7}M	0.39x10^{-8} M	0.39.10^{-9} M	0.39.10^{-10} M	[51,75,77,88,92-104]
	LANL2DZ	LANL2DZ	pH 5.5					
3056 vw	3171	3153						ν_{as} (C-H) aromatic BR
2886 vw								ν_s (C-H) aromatic BR
1907 vw			1886 vw					ν_s (C3=O26)
1815 vw			1812 vw					
1770 vw			1787 vw					ν (C3=O26)
1704 vw	1650	1634	1713 vw				1692 sh	ip C-C+C-H XR def.
1611 ms	1619	1619	1621 vs	1606 vvs	1615 s	1621 vs	1621 m	ν_{as} (COO$^-$)
1545 m	1566	1546	1560 w	1546 ms	1546 ms	1552 m	1539 sh	ν (doublet BR)
1490 vs	1499	1499	1504 s	1499 s	1499 m	1499 sh		ip C-H XR+BR def
1471 s	1474	1480	1482 s	1472 sh	1472 sh			C12-O10-C13 def.; ip C-H+C-C XR def.
1457 ms	1456	1456	1454 sh	1445 s	1445 m	1448 wm		ν_s (COO$^-$)
1438 m	1439	1449						ρ (BR)
1404 w	1391	1389		1390 w	1397 w	1396 vw	1388 vs	δ^{ip} (C6-O27H)
1344 s	1360	1345	1352 m			1358 vw	1369 vs	C-H XR def.
1310 m	1321	1313	1323 w	1322 vs	1320 vvs	1316 vs	1311 w	ip C-H BR def.
1271 vvs	1285	1281	1285 vvs	1273 wm	1275 sh	1279 sh		ν_{as} (C12-O10-C13); XR def.; ν (C9-C15)
1239 m	1265	1260	1258 w	1244 vw	1244 vw	1244 sh	1236 sh	XR ip C-H def.; δ^{ip} (C6-O27H)
1197 w	1189	1221	1212 vw					ip C-H BR def; ν_s (C12-O10-C13)
1164 m		1178	1177 w	1181 sh	1179 m		1178 w	δ (C-C-I)
	1166	1163		1168 ms	1171 sh	1173 s		XR breath.
1090 w	1092	1087	1104 vw	1089 w	1089 vw	1084 m	1078 w	ip C-H BR def.
1046 w	1061	1055	1059 vw	1047 vw		1028 m	1018 ms	C12-O10-C13 def.
992 vw	1001	1000	1007 vw	991 vw				trigonal BR breath.
952 w	957	971	963 w	947 wm	945 wm	950 m	947 vs	XR def; op C-H def.
					936 wm			XR def.
886 vw	910	909	896 vw	918 sh	917 vw	920 m	918 vs	ν (C-C) skeletal BR
							894 w	
844 vw	877	877	853 vw	837 vw	838 vw	835 vw	838 w	op C-H def XR
773 w	776	789	784 w	780 sh		799 vw	799 w	XR def.
							778 vw	XR def.
748 vw	757	751	763 vw	765 wm	765 m	760 m	757 vw	op C-H XR def.
728 vw	743	738			699 sh			ip C-H BR def.
695 vw	708	703	693 sh	690 w	680 vw			XR def.

679 vw	684	679		668 w	660 sh	662 vw		XR def.
620 ms	637	634	630 vs	637 w	637 wm	637 m	634 w	op C-C, C-H BR def.
607 w	620	619	619 m	614 wm	614 w			XR def.; δ^{ip} (C-C-C)
569 vw	588	583	579 vw	600 w	600 wm	590 m	590 sh	ν (C-I)
541 vw	560	556		539 w	539 wm	542 m	557 w	ν (C-I)
493 vw	496	495	507 w					ν (C-I)
471 w	474	471	477 w	480 sh	482 sh		482 sh	ν (C-I), skeletal def.
434 vw	445	447	447 w	463 m	463 ms	461 s	461 w	ν_s (C-I)
408 vw	417	413	403 m	426 vw	426 vw			XR def.
395 w	393	391		388 vw				skeletal def.
344 vw	360	356	356 w	375 vw	366 w			τ (XR)
331 vw	333	330	338 m	329 vw				skeletal def.; ν (Ag-O)
310 vw	313	312						τ (XR)
275 vw	275	276	270 m					
248 w	258	258						
216 vw	231	231	226 w	242 w		215 sh	237 sh	ν (Ag-Cl); ν (O-Ag-O)
191 vw	206	203		197 w		208 sh	197 sh	ν (Ag-O); ν (O-Ag-O)
164 w	175	173		178 m	178 sh			ν_s (C-I) solid
149 m	151	149		143 wm	147 ms	143 vvs	143 vs	ν (Ag-O)
							134 vs	ν (Ag-O)
116 w	114	114		119 w	119 wm			ν (Ag-O)

Abbreviation: vw – very weak; w – weak; m – medium; ms – medium strong; s – strong; vs – very strong; sh – shoulder; ν - stretching; δ - bending; ρ – rocking; τ – torsion; BR – benzene ring; XR – xanthene ring; s – symmetric; as – asymmetric; breath. – breathing; def. – deformation; ip – in plane; op – out of plane.

The latter shows changes of both xanthene and benzene ring, which demonstrate that both ring are very close to the silver colloidal particles on the one side, and the difficulties to decide the molecules' orientation, on the other side. The shoulders at 237 and 197 cm^{-1} attributed to the carbon-halogen stretching vibrations[434,435] and the very strong bands of the at 143 and 134 cm^{-1} assigned to the Ag-O stretching mode[432,433], help us explain the adsorption possibility. Taking into account all these observations, we suppose a tilted orientation of the EryB molecule through π electrons of the benzene ring and the oxygens and iodine atoms of the xanthene ring (Fig. V.4.3.5d).

pH dependence SERRS spectra of EryB

In order to discuss the pH dependence SERRS spectra, one can observe in the acidic pH range (Fig. V.4.3.7a) considerable changes in band positions and relative intensities. The SERRS signal in the case of the acidic pH range was achieved beginning with pH 5 till pH 1 for a EryB concentration of 0.39 10^{-7} M, where the first SERRS signal appears.
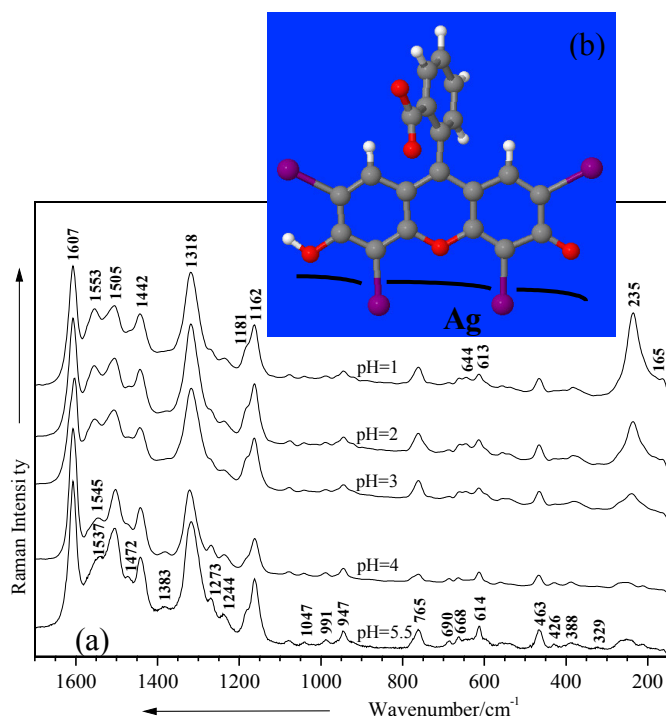
Figure V.4.3.7. SERRS spectra of EryB (0.39 10^{-7} M) at various acidic pH values (a) and its proposed orientation on silver colloidal particles (b). Excitation: 514.5 nm, 200 mW.

In contrast to the SERRS measurement at normal pH 5.5 (Fig. V.4.3.7a), beginning with the pH 4, the bands correspondent to the asymmetrical and symmetrical COO$^-$ stretching modes (1606 and 1445 cm^{-1} in the SERRS spectrum at pH 5.5) decrease in relative intensities and at pH 1 become broader and are slightly red shifted. Moreover, the shoulder at 1537 cm^{-1} (Fig. V.4.3.7a, pH 5.5), assigned to the benzene ring doublet stretching modes, becomes a broad peak beginning with pH 4 and at pH 1 gets increased in relative intensity and 8 cm^{-1} blue shifted. The shoulder at 1472 cm^{-1} in the SERR spectrum at pH 5.5, which was assigned to the C12-O10-C13 deformation mode and to the in plane C-H, C-C deformation modes of the xanthene ring, disappears on going to acidic pH values, whereas the signal at 1505 cm^{-1} (in the SERR spectrum at pH 1) assigned to the in plane C-H deformation modes of the xanthene and benzene rings, decreases in relative intensity.

The strong band at 1322 cm^{-1} from the SERR spectrum at normal pH, assigned to the in plane CH deformation modes of the benzene ring, increases in relative intensity and is 4 cm^{-1} red shifted at pH 1, whereas the two weak neighbour peaks at 1273 and 1244 cm^{-1} (in the SERR spectrum at pH 5.5) decrease in relative intensities in the acidic range and can be due to the asymmetrical C12-O10-C13 stretching mode together with the xanthene ring and C9-C15 bridge bond stretching modes and to the in plane CH deformation modes of the xanthene ring simultaneously with the in plane C6-O27H bending mode. The shoulder at 1181 cm^{-1} and the medium strong band at 1168 cm^{-1} (Fig. V.4.3.7a, pH 5.5) become broader in the acidic range and can be allocated to the CC-I bending and to the xanthene ring breathing modes. The breathing vibrational mode of the xanthene ring is slightly red shifted (1162 cm^{-1}, at pH 1). Furthermore, several bands associated with the xanthene ring deformation are broadening (947, 765, and 463 cm^{-1}), while other one decreases in relative intensity (614 cm^{-1}) (Fig. V.4.3.7a, pH 5.5). Considering the significant changes in the band positions and relative intensities of the carboxylate group and C12-O10-C13, as well as of the benzene and xanthene rings, we can assume that the protonation may occur at the carboxylate group and at O10 from the xanthene ring.

These results confirm the anion-induced charge transfer complex formation in the silver colloid. Since the charge transfer interaction is involved in SERR activity along with electromagnetic interaction, is it not plausible to apply the Creighton surface selection rule[108], which is based upon image dipole theory, to specify the exact orientation of the molecule on the silver surface. From all bands interpretation, we can suppose that the two halves of the xanthene ring may interact with the silver surface and the EryB molecule has a vertical orientation on silver colloidal particles[436,437]. This assumption can be supported through the Cl$^-$ ion coadsorption. The relationship between the build-up of a chloride layer and the adsorption of this strongly adhering dye was observed via the appearance of an intense band at 235 cm^{-1}, assigned to the silver-chloride vibration[438]. This only intense band is very useful in our study of the molecule adsorption on the silver surface[348,349]. In addition to this band, another weaker band or shoulder can be seen. This one appears at 165 cm^{-1} and was assigned to vibrations of smaller silver particles or adatoms, produced by the oxidation-reduction action of Cl$^-$ on the surface of the silver colloid[140]. We conclude that in acidic pH range, the monoanionic[391] form of the EryB molecule is present and we suppose an adsorption geometry of the EryB molecule on the silver colloidal particles through the xanthene ring, in a vertical orientation (Fig. V.4.3.7b).

On going to the basic pH values (Fig. V.4.3.8a) more differences appear in the SERR spectra, suggesting the deprotonation and reorientation of the molecule on the silver surface. The carboxyl asymmetrical stretching mode (1617 cm^{-1} in the SERR spectrum at pH 10) becomes weaker in relative intensity, broader, and is notably blue shifted (11 cm^{-1} from the position at pH 5.5) showing that the carboxyl group takes part in the deprotonation of the EryB molecule. The next bands (1548, 1496, 1438 cm^{-1} in the SERR spectrum at pH 10, Fig. V.4.3.8a), which correspond to the benzene ring doublet stretching mode, to the in plane C-H deformation of the xanthene and benzene rings, and to the symmetrical stretching mode of the carboxyl, are decreased in relative intensities and show the participation of the benzene ring to the molecule deprotonation (Fig. V.4.3.8a). The in plane C6-O27H

bending mode (1392 cm^{-1} at pH 10, Fig. V.4.3.8a) and the in plane C-H deformation mode of the benzene ring (1315 cm^{-1} at pH 10) increase in relative intensities, while the asymmetrical C12-O10-C13 stretching mode remains a weak shoulder in the acidic pH range (1270 cm^{-1}). The xanthene ring breathing mode (1168 cm^{-1} at pH 5.5) is broadened, slightly increased in relative intensity, and importantly blue shifted (11 cm^{-1}), suggesting likewise the xanthene ring's participation to the molecule deprotonation. The band at 764 cm^{-1} increases in relative intensity and can be attributed to the out of plane deformation of the xanthene ring, as well as the band at 463 cm^{-1}, also increased in relative intensity and assigned to the symmetrical C-I stretching mode.
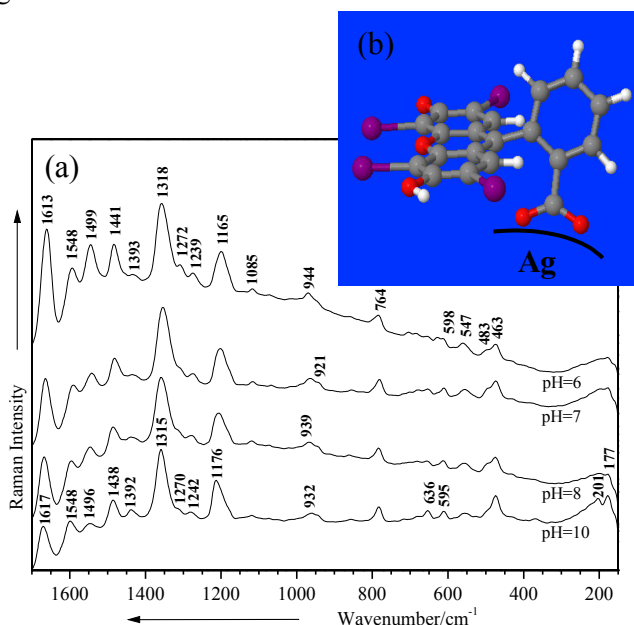
Figure V.4.3.8. SERRS spectra of EryB (0.39 10^{-7} M) at various basic pH values (a) and its proposed orientation on silver colloidal particles (b). Excitation: 514.5 nm, 200 mW.

These remarks come to demonstrate the deprotonation of the EryB molecule in the non-polar solvents and the presence of the lactone form of the EryB molecule in the basic pH range (Fig. V.4.1.1b)[395,439,440]. The molecule lies in a perpendicular orientation on the silver colloidal particles through the carboxylate moiety from the lactone structure of the molecule (Fig. V.4.3.8b).

V.4.5 Conclusions

The geometry of the EryB molecule was optimized for the first time with the Gaussian 98 program using different methods (BPW91/LANL2DZ and B3LYP/LANL2DZ).

The FT-Raman spectrum of solid EryB and the Raman spectrum of erythrosine B were recorded in aqueous solution and the marker bands were identified. EryB could be detected in aqueous solution at micromolar levels by conventional Raman and at nanomolar concentrations by SERR spectroscopy.

A strong chemical interaction of EryB with the silver colloidal particles was observed mainly at very low concentrations (0.39 10^{-7}–0.39 10^{-12} M) and revealed the reorientation possibilities while going to lower concentrations.

The surface selection rules along with data from literature and our DFT calculations have

reasonably explained the adsorbate structures on the metal surface for each concentration and for each pH range.

The pH dependence SERRS spectra of the EryB molecule demonstrate that this can be protonated on going from basic to acidic pH values, revealing the changes in the molecular identity, and the interaction possibilities with the human body.

SERRS is therefore a very effective and promising technique for detecting and monitoring the presence of synthetic additives in food at very low concentrations.

V.5 Indigo carmine (E132)

The application of resonance Raman (RR) and surface enhanced resonance Raman (SERR) spectroscopies to the qualitative and semi-quantitative analysis of the artificial dye indigo carmine has been examined using sodium citrate-reduced silver colloid and island films with various roughnesses. Additionally, the Raman spectrum of the solid state and density functional theory (DFT) calculations helped to a better understanding of the fully optimized geometry and of the vibrational wavenumbers of the dye. A strong chemical interaction of indigo carmine with the silver colloidal particles was observed mainly at very low concentration (0.03×10^{-9} M) and with silver films surfaces at concentration of 10^{-4} M.

V.5.1 Molecule presentation

Indigo carmine (E132 in Europe) is an artificial food colorant, which belongs to the indigoids class and consists in essence of disodium 5,5'–(2–(1,3–dihydro–3–oxo–2H–indazol–2–ylidene)–1,2–dihydro–3H–indol–3–one) disulphonate and appears like a dark blue powder. Its molecular structures are presented in the Fig. V.5.1.1a.

The natural dye originates from several species of plants, but, presently, nearly all indigo carmine produced is synthetic. Among other uses, it is used in the production of *denim* clothes for blue jeans[441,442]. Indigo carmine (E132) may cause nausea, vomiting, high blood pressure, skin rashes, breathing problems or allergic reactions. Typical products which contain E132 dye are: confectionery and patisserie products, and biscuits. Allergic people should avoid this dye.

The E132 dye determination in complex matrices like food and pharmaceutical drugs was reported using capillary electrophoresis[353], while its behavior in different environments was achieved with spectrophotometric methods[354-356]. *In vivo* and *in vitro* studies show that E132 may have utility as cancer chemopreventive agent[369], but at the same time it can produce mutagenic effects[370-372]. E132 was found to be non-toxic for the human luteal cells *in vitro*[443], which gave reasons for its employment to the tumor identification by staining[444,445]. It can be used, also, as radiographic agent[446] and to check with NMR techniques the nucleotide conformational changes[447].

Anionic dyes like E132, which have more than one -SO₃H group, exhibit high water solubility which corresponds to the ability of cithosan to protonate in the aqueous medium[359]. Arterial blood saturation (SpO₂) is one of the most important parameters in monitoring patients while they are receiving

anesthesia. E132, after intra-arterial injection, has been reported to interfere with arterial blood saturation readings[448,449].

(a)

(b)
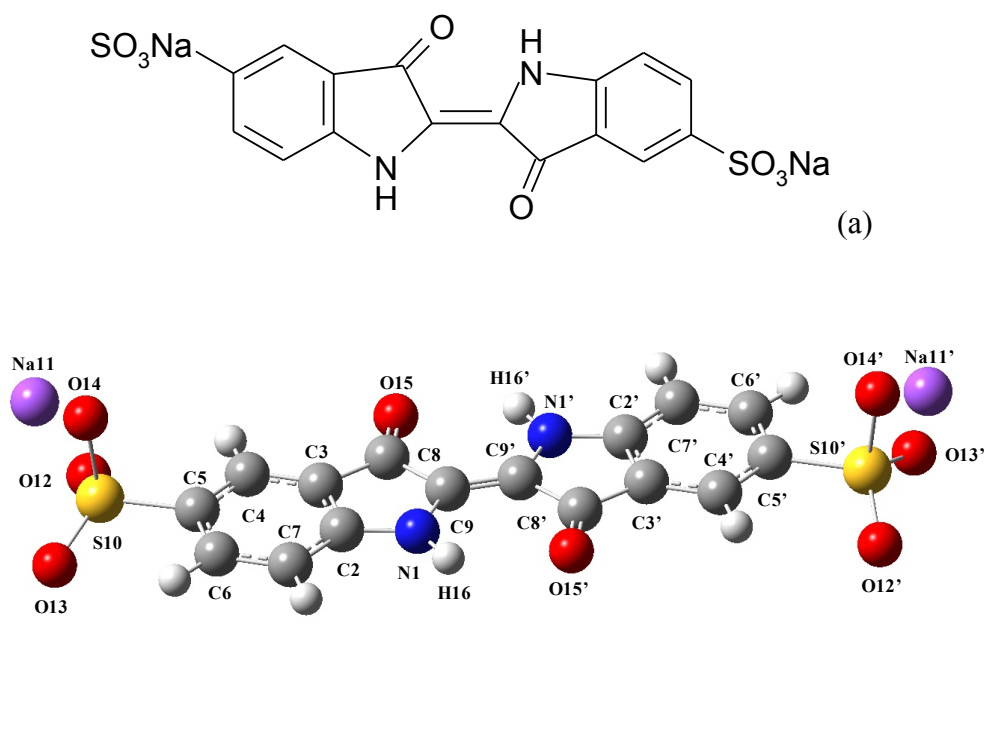
Figure V.5.1.1. Molecular structure (a) and B3LYP/LANL2DZ
optimized geometry (b) of E132.

E132 can generate brain tumors and combined with other dyes, like erythrosine (E127), can produces bronchoconstriction. It is the most commonly used contrast-staining agent for the enhancement of the superficial structures of the intestinal mucous membrane[450]. In this case, the E132 can be used for adenomas detection[451], and for antipsychotic drugs determination[452]. Several colorimetric studies show that E132 can be used as reagent to measure the ozone concentration[453,454].

Vibrational spectroscopy is one of the most powerful and widely used tools in modern materials research.. Quantum chemical calculations predicting harmonic wavenumbers and spectral intensities are essential when interpreting experimental spectra, particularly for large molecules where the high density of states results in spectral complexity. Accurate vibrational assignments for such systems are necessary for materials characterization purposes. Assignments for complex systems can be proposed on the basis of wavenumber agreement between the computed harmonics and the observed fundamentals.

Considering all these, together with the positive and negative effects of E132 in humans and animals, we propose in the present work its characterization in the solid state, in different concentrations range, free and adsorbed on silver colloidal particles using RR and SERR spectroscopies.

V.5.2 Geometry optimization

In order to establish the orientation of E132 on silver surface and the changes in molecular identity, it is necessary to known very well its structure. Unfortunately, no crystal data were so far reported on E132. Therefore, its geometry was optimized for the first time at different level of theories

(BPW91/6-311++G**, B3PW91/LANL2DZ, B3LYP/6-311++G**, and B3LYP/LANL2DZ) with the Gaussian 03 program and compared with those of identical or similar functional groups of E132 from literature[311,312,314,455-479]. The calculated structural parameters of E132 are listed in Table V.5.2.1 and the labeling of the atoms is shown in Fig. V.5.1.1b. As one can notice, there is a very good agreement between the theoretically determined parameters of E132 and the experimental values available in the literature[311,312,314,455-479].

The E132 molecule is quite planar except for both sulphonic groups, with a symmetry center placed at the C9=C9' bridge bond level (Fig. V.5.1.1b). Both N-H and both C=O bonds lie in opposite direction regarding to the C9=C9' bridge bond. The molecule planarity can be demonstrated by a few torsion angles: N1-C9=C9'-C8' (0.0°), N1'-C9'=C9-C8 (0.0°), O15-C8-C9=C9' (-0.1°), O15'-C8'-C9'=C9 (-0.1°), O15-C8-C3-C4 (-0.1°), O15'-C8'-C3'-C4' (-0.1°) and three dihedral angles that have the calculated average at about 180° (N1-C9-C8-O15, N1'-C9'-C8'-O15', N1-C9=C9'-N1') (Fig. V.5.1.1b, Table V.5.2.1). Both sulphonic groups exhibit trigonal pyramid symmetry[455], the calculated average angles for O12-S10-O14 and O13-S10-O14 are 108.1°, while for O12'-S10'-O14' and O13'-S10'-O14' the angles are 108.2°, on the one side and the calculated average angle for O12-S10-O13 angle is 120.8°, whereas for the O12'-S10'-O13' is 120.8°, on the other side (Table V.5.2.1). The position of the sulphonic groups is on both sides of the symmetry bridge bond, with both doubly bonded oxygen atoms in opposite direction (Fig. V.5.1.1b, Table V.5.2.1). Both sulphonic groups are rotated by 97.2° (calculated average) from the molecular plane (Table V.5.2.1).

The calculated average bond lengths of N1-C2/N1'-C2'and C9-N1/C9'-N1' by using different calculation methods produce an estimate of 138.8 pm, which is smaller than the length of a C-N single bond (148 pm), longer than that of a C=N double bond (128 pm)[312], and around the C-N single bond length in the ground state (137.6 pm)[456]. Taken into consideration these literature data[312,456], we can assume that with these calculated values of the N1-C2/N1'-C2' and C9-N1/C9'N1' bond lengths, the N-H bond exists in the transition–state structure and can be valuable to explain the protonation of E132 molecule and the connection with the water molecule[457]. Besides the calculated values, which demonstrate the transition–state[458], the proton transfer from the H_2O to the N-H is expected[459,460].

The C-N distances of the calculated molecular structure vary from 138.1 pm to 139.7 pm and are shorter than that of the C-N single bond (147 pm)[312]. These molecular distances imply a non–negligible polarization of the neutral system towards the metal cation in the case of SERRS. The polarization is transmitted to the C-N bond, inducing a greater participation of the nitrogen lone pairs in the C-N bond, which results in a shortening of the bond length[460]. Our calculated C-N bond lengths suggest the transition state of the molecule and the possible protonation of the nitrogen atom[461].

The C5-S10 (181.9 pm) and C5'-S10' (181.9 pm) are similar to the C-S single bond (182 pm)[314,462,463]. Since donor and acceptor groups are in each chromophore, conjugated effects are observed in all molecules, which have smaller C-N, C-O, C-S, and C-C bond lengths than those of the standard bond lengths[464] and longer C=C bond length than that of the standard bond length. Compared with known indigoide compounds, the molecular structures of chromophores and indigoide dyes are different, because

of the lack of five-memebered and phenyl rings in the chromphores[465,466]. In this way, the calculated average of the C2-C3/C2'-C3', C3-C4/C3'-C4', C4-C5/4'-C5', C5-C6/C5'-C6', C6-C7/C6'-C7', and C7-C2/C7'-C2' bond lengths, which belong to the phenyl rings, are situated between 143.3 and 139.7 pm (Table V.5.2.1). These distances are specific for the phenyl rings[311,463]. In a different manner, the C-C bond lengths of five-memebered rings, which are longer than those of both phenyl rings, have the calculated average between 147.3 and 149.2 pm (Table V.5.2.1), values that have been given for rings containing nitrogen atoms[467,468].

Table V.5.2.1. Selected calculated structural parameters of E132 in comparison with the available experimental data.

	Exp.		Calcd.			
			B3LYP		B3PW91	
			6-311++G**	LANL2DZ	6-311++G**	LANL2DZ
Bond-lengths (pm)						
N1-C2			138.2	139.7	137.7	139.2
N1'-C2'			138.2	139.7	137.7	139.2
C2-C3			141.4	142.9	141.2	142.5
C2'-C3'			141.5	142.9	141.2	142.5
C3-C4			138.9	139.9	138.7	139.5
C3'-C4'			138.9	139.9	138.7	139.5
C4-C5	150.9[468]		139.1	139.8	138.8	139.5
C4'-C5'	150.9[468]		139.1	139.8	138.8	139.5
C5-C6	153.6[468]		140.4	141.0	140.2	140.6
C5'-C6'	153.6[468]		140.4	141.0	140.2	140.6
C6-C7	152.7[468]		138.8	140.3	138.6	139.9
C6'-C7'	152.7[468]		138.9	140.3	138.6	139.9
C7-C2	151.0[468]		139.6	140.5	139.4	140.2
C7'-C2'	151.0[468]		139.6	140.5	139.4	140.2
C3-C8	150.4[468]		147.1	147.4	146.7	147.0
C3'-C8'	150.4[468]		147.1	147.4	146.7	147.0
C8-C9			149.3	149.4	148.9	148.9
C8'-C9'			149.3	149.4	148.9	148.9
C9-N1			138.1	139.5	137.6	139.0
C9'-N1'			138.1	139.5	137.6	139.0
C9-C9'			135.7	136.8	135.6	136.6
C8-O15			122.4	126.2	122.2	125.8
C8'-O15'			122.4	126.2	122.2	125.8
N1-H16			101.2	101.6	101.1	101.5
N1'-H16'			101.2	101.6	101.1	101.5
C5-S10	177.8[468];		177.9	184.4	176.9	183.4
C5'-S10'	177.8[468]		177.9	184.4	176.9	183.4
S10-O12	144.5[478]; 148.3[477]; 148.3[468]; 149.1[476]		145.4	161.8	144.8	161.1
S10'-O12'	144.5[478]; 148.3[477]; 148.3[468]; 149.1[476]		145.4	161.8	144.8	161.1
S10-O13	144.5[478]; 164.7[477]; 148.3[468]; 146.5[476]		145.6	161.8	145.2	161.2
S10'-O13'	144.5[478]; 164.7[477]; 148.3[468]; 146.5[476]		145.5	161.8	145.2	161.2
S10-O14	158.8[478]; 173.1[477]; 149.0[468]; 151.9[476]		165.4	181.1	164.1	179.8
S10'-O14'	158.8[478]; 173.1[477]; 149.0[468]; 151.9[476]		165.4	181.1	164.1	179.8
O14-Na11	98.3[478]		97.1	99.1	96.9	98.8
O14'-Na11'	98.3[478]		97.1	99.1	96.9	98.8
N1'-H16'⋯O15	197.1[472]		228.4	227.6	227.1	226.9
N1-H16⋯O15'	198.3[472]		228.5	227.6	227.1	226.9
Angles (°)						
C2-C3-C8	113.6[468]		107.6	107.7	107.5	107.6
C2'-C3'-C8'	113.6[468]		107.6	107.7	107.5	107.6
C3-C8-C9	112.0[468]		104.1	104.6	104.0	104.5
C3'-C8'-C9'	112.0[468]		104.1	104.6	104.0	104.5
C3-C4-C5	114.7[468]		117.3	116.2	117.3	116.2
C3'-C4'-C5'	114.7[468]		117.3	116.2	117.3	116.2
C4-C5-S10	111.4[468]		119.0	118.3	119.0	118.3
C4'-C5'-S10'	111.4[468]		119.0	118.3	119.0	118.3
C6-C5-S10	109.8[468]		118.9	117.8	118.9	117.8
C6'-C5'-S10'	109.8[468]		118.9	117.8	118.9	117.8
C5-S10-O12	112.1[478]; 107.1[468]		109.8	110.2	109.4	110.3
C5'-S10'-O12'	112.1[478]; 107.1[468]		110.0	110.2	109.4	110.3
C5-S10-O13	109.0[478]; 106.4[468]		110.2	109.9	110.3	110.0
C5'-S10'-O13'	109.0[478]; 106.4[468]		110.0	109.9	110.3	110.0
C5-S10-O14	97.7[468]		97.9	96.8	98.4	96.9
C5'-S10'-O14'	97.7[468]		97.9	96.8	98.4	96.9
O12-S10-O14			108.4	108.1	108.7	108.1
O12'-S10'-O14'			108.2	108.1	108.7	108.1
O13-S10-O14			107.6	108.1	107.2	108.0
O13'-S10'-O14'			108.0	108.1	107.2	108.0
O12-S10-O13	121.2[478]		120.5	121.0	120.6	120.8
O12'-S10'-O13'	121.2[478]		120.5	121.0	120.6	120.8
S10-O14-Na11	105.0[478]		108.5	109.8	108.1	109.9
S10'-O14'-Na11'	105.0[478]		108.6	109.8	108.1	109.9
Dihedral angles (°)						
N1-C9-C9'-C8'			0.0	0.0	0.0	0.0
N1'-C9'-C9-C8			0.0	0.0	0.0	0.0

O15-C8-C9-C9'	-0.1	-0.1	0.0	-0.1
O15'-C8'-C9'-C9	-0.1	-0.1	0.0	-0.1
N1-C9-C8-O15	180.0	179.9	180.0	179.9
N1'-C9'-C8'-O15'	180.0	179.9	180.0	179.9
N1-C9-C9'-N1'	179.9	-180.0	179.9	-180.0
O15-C8-C3-C4	0.1	-0.1	0.1	-0.1
O15'-C8'-C3'-C4'	0.1	-0.1	0.1	-0.1
Na11-O14-S10-C5	-179.1	178.6	-178.9	178.8
Na11'-O14'-S10'-C5'	-179.3	178.6	-178.9	178.7

The N-H proton is much tightly bound than the carbonyl proton[469] and can, consequently, form hydrogen bonding. Hydrogen bonds in the excited state are known to mediate not only the proton transfer but also the electron transfer. E132 is a *trans*-indigo derivative, which can form intramolecular double hydrogen bonds[470].

From our DFT calculations, we can deduce that the molecule exhibits a preference for the *trans* conformer (Fig. V.5.1.1b) and in this case, hydrogen bonding can take place between the hydrogen atom of the N-H bonds and the oxygen atom of the C=O bonds. The N-H···O and C-H···O hydrogen bonds can stabilize the different conformers of the molecules[471]. E132 molecule presents *trans* conformation, which makes possible two hydrogen bond interactions, between H16 of the N1-H16 bond and the doubly bonded O15' of the C8'=O15' bond (N1-H16···O15'=227.6 pm), and between H16' of the N1'-H16' and the doubly bonded O15 of the C8-O15 (N1'-H16'···O15=227.7 pm) (Table V.5.2.1, Fig. V.5.1.1b). The stable protonated structures of E132 are characterized by these two slightly strong N^+-H···O=C hydrogen bonds[469,472], which restrict the accessible conformational space. The intramolecular hydrogen bonds of E132 that are approximately 227 pm, are in competition with its intermolecular packing through the π-π stacks that are held together by intermolecular hydrogen bonds[473].

Two types of S-O bonds can be observed in the E132 molecule: bonds with the length situated between 145.4 and 161.8 pm, and bonds that have the length between 165.4 and 181.1 pm. The first type of S-O bonds have the length similar to the distance of the free SO_3 molecule (147-158 pm)[474] and the other bond type corresponds to the $-SO_3^-$ molecule bonded to metallic surfaces (181 pm)[474-478]. Taking into consideration these discussions and in accordance with our theoretical values (Table V.5.2.1, Fig. V.5.1.1b), the SO_3 groups are bonded with the Na atoms throughout S10-O14···Na11 and S10'-O14'···Na11'. The binding in the E132 molecule of the $-SO_3^-$ groups to Na atoms means that all bond lengths become shorter than in the free SO_3 molecule (Table V.5.2.1, Fig. V.5.1.1b)[479].

V.5.3 Electronic Spectroscopy

The UV–VIS absorption spectrum of E132 aqueous solution is presented in Fig. V.5.3.1a. As one can notice, it shows four absorption maxima at 610, 336, 287, and 252 nm, respectively. The absorption maxima of the colloid–E132 solution mixture were detected almost at the same position (Fig. V.5.3.1b).

Since some RR measurements have already been reported[480,481] and taking into account the great fluorescence of the substance, we tried to excite it using resonance conditions in order to explain the adsorption type of the molecule on the metallic surfaces.

The UV-VIS absorption spectra of island films are displayed in Fig. V.5.3.2. In spite of the absorption spectra we can mention that the absorption maxima of the presented four island films are shifted depending on the particles roughness and film thickness.
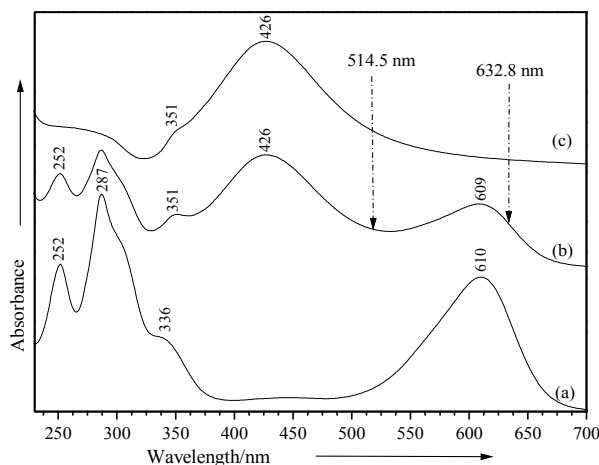
Figure V.5.3.1. UV-VIS absorption spectra of E132 solution (a), E132 with Lee Meisel silver colloid (b), and Lee Meisel silver colloid (c).
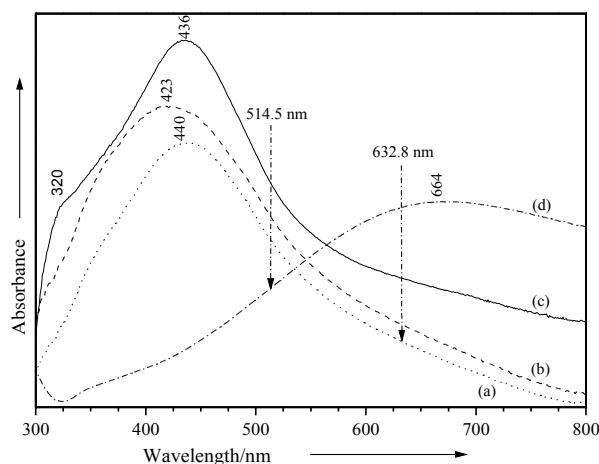
Figure V.5.3.2. UV-VIS absorption spectra of island films with different thicknesses: 1.9 Å (a), 2.9 Å (b), 14.4 Å (c), and 1.05 Å (d).

V.5.4 Raman spectroscopies

Resonance Raman spectra of E132 in the solid state and solution

The vibrational fundamentals from the Raman spectrum of the solid state (Fig. V.5.4.1) were analyzed by comparing these modes with those from the literature[461,463,477-491] in combination with the results of our DFT calculations. In Table V.5.4.1 the selected calculated and experimental RR and SERRS data, together with their attempted assignment are given. Wavenumbers corresponding to the stretching vibrations of the C8=O15 and C8'=O15' bonds of both pyrrolidone rings are observed in the Raman spectrum of the solid state through the very weak peak at 1738 cm^{-1} and the medium strong band at 1698 cm^{-1}. Both wavenumbers can be also assigned to the different C=C bond stretching modes (C9=C9' bridge bond at 1738 cm^{-1}, C=C double bond of both phenyl rings at 1698 cm^{-1})[481,482]. The distinction between those two double bonds is established from the calculated Raman vibrational modes.

In the RR spectrum of the solution only the second band at 1702 cm^{-1} can be detected, which is a

slightly blue shifted (4 cm^{-1}). The medium strong band at 1623 cm^{-1} in the Raman spectrum of the solid state (Fig. V.5.4.1a) is assigned to both C=C and C=O stretching modes of pyrrolidone rings and to the in plane C-H bending modes of the phenyl rings[485-487]; in contrast, in the RR spectrum of the solution, this band is 9 cm^{-1} blue shifted (1632 cm^{-1}) and slightly increased in relative intensity (Fig. V.5.4.1b). In the Raman spectrum the very strong band at 1576 cm^{-1} is assigned to the C3=C2/C3'=C2' asymmetrical stretching modes of both pyrrolidone rings (Fig. V.5.4.1a), while the shoulder at 1539 cm^{-1} together with the weak band at 1517 cm^{-1} are attributed to the C3=C2/C3'=C2' symmetrical stretching modes, in combination with both phenyl rings stretching modes[487-489]. As opposed to the Raman spectrum of the solid state, in the RR spectrum of the solution both bands are significantly blue shifted (1581 and 1531 cm^{-1}) and the shoulder disappears (Fig. V.5.4.1b).

The medium band at 1472 cm^{-1} in the Raman spectrum of the solid, which is only 4 cm^{-1} blue shifted (1476 cm^{-1}, Fig. V.5.4.1) in the RR spectrum of the solution and which decreases in relative intensity, is attributed to the N-C stretching and to the in plane C-H bending modes[488,489]. The weak peak at 1444 cm^{-1} is attributed to the C-C and N-C=C-N stretching contributions, to the in plane N-H bending mode, and to the in plane C-H bending mode of the phenyl rings, as the main contributions in the bands' shape. In the RR spectrum of the solution, this band has almost the same position and relative intensity (Fig. V.5.4.1b). The weak band at 1415 cm^{-1} in the Raman spectrum of the solid state, which becomes a shoulder and is considerably blue shifted (15 cm^{-1}, Fig. V.5.4.1b) in the RR spectrum of the solution, can be due to the symmetrical C8=O15 and C8'=O15' stretching modes and to the in plane C-H and N-H bending modes (Fig. V.5.4.1b, Table V.5.4.1).
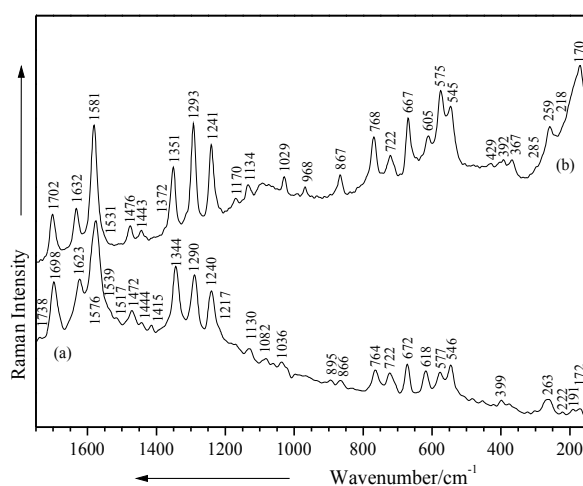
Figure V.5.4.1. Raman spectrum of E132 in solid state (a) and resonance Raman spectrum of its 10^{-3} M solution (b). Excitation: 514.5 nm (a,b), 200 mW (a,b).

One of the stronger bands in the Raman spectrum of the solid state at 1344 cm^{-1} is due to the in plane C-H and N-H bending modes[485,487] and to the O12S10O13/O12'S10'O13' stretching contributions[476]; in the RR spectrum of the solution this band is observed at 1351 cm^{-1}, is slightly blue shifted (7 cm^{-1}, Fig. V.5.4.1b) and highly increased in relative intensity. The strong peak at 1290 cm^{-1} is

assigned to the stretching modes of N1-C2/N1'-C2' and to the C-C bending mode[485-487].

Taking into account the literature data[477,481] and according to our calculated Raman wavenumbers, this band has a $-SO_3^-$ symmetrical stretching contribution. In solution, this band is highly increased in relative intensity and somewhat shifted (Fig. V.5.4.1b, Table V.5.4.1). The medium strong band at 1240 cm^{-1} (Raman spectrum of the solid, Fig. V.5.4.1a) corresponds to the in plane C–H and C=O bending modes, while the shoulder at 1217 cm^{-1} is attributed to the phenyl rings breathing modes. In the RR spectrum of the solution, one can observe only one strong band at 1241 cm^{-1} (Fig. V.5.4.1b).

The weak peak at 1185 cm^{-1} in the Raman spectrum of the solid state which is absent in the RR spectrum of the solution was attributed to both N1-C2/N1'-C2' and C9=C9' bridge bond stretching modes. Therefore the weak band at 1172 cm^{-1} (1170 cm^{-1} in the solution) corresponds to the asymmetrical O12S10O13/O12'S10'O13' stretching modes and to the in plane C-C bending modes of the phenyl rings. The symmetrical O12S10O13/O12'S10'O13' stretching contributions are observed at 1130 cm^{-1} in the solid state and at 1134 cm^{-1} in the solution (Table V.5.4.1, Fig. V.5.4.1). The following weak signals at 1082 and 1062 cm^{-1} in the Raman spectrum of the solid state (1091 cm^{-1} and 1074 cm^{-1} in the solution) correspond to the out of plane bending modes of both O14-Na11/14'-Na11' bonds and to the in plane C-H bending modes (Fig. V.5.4.1)[463,487,488]. The out of plane C–H deformation mode of the phenyl rings is observed in the solid state at 1036/997 cm^{-1} and at 1029/990 cm^{-1} in the solution. The very weak band at 967 cm^{-1} in the Raman spectrum of the solid state (968 cm^{-1} in the solution) is assigned to the out of plane C–H bending mode and to the O12S10O13/O12'S10'O13' deformation modes. On the other hand, the very weak peak at 895 cm^{-1} (solid state) and 896 cm^{-1} (solution) corresponds to the symmetrical C2-N1-C9/C2'-N1'-C9' stretching modes[488].

The next bands in the Raman spectrum of solid state E132 are attributed as follows: the weak peak at 833 cm^{-1} (839 cm^{-1} in the solution) to the C5-S10/C5'-O10' stretching modes[461] and to the CC out of plane bending mode of the five-membered rings; the band at 764 cm^{-1} (768 cm^{-1} in the solution) to the pyrrolidone rings breathing mode and to the out of plane CH and CC bending modes; the peak at 722 cm^{-1} (increased in the RR spectrum of the solution) to the C2-N1-C9/C2'-N1'-C9' bending modes. The weak peak at 672 cm^{-1} in the Raman spectrum of the solid state, which is slightly blue shifted in the RR spectrum of the solution (667 cm^{-1}) and highly increased in relative intensity is assigned to the out of plane N-H and CC bending modes of both pyrrolidone rings. The signal at 618 cm^{-1} in the Raman spectrum of the solid state (605 cm^{-1} in the solution) is assigned to the out of plane CH/N-H bending modes and to both -SO$_3^-$ groups bending modes. The very weak signals at 577 and 546 cm^{-1} in the Raman spectrum of the solid state are assigned to the C2=C3-C8O15-C9/C2'=C3'-C8'O15'-C9' bending modes. These bands are shifted in the RR spectrum of the solution and highly increased in relative intensity (572 cm^{-1} and 546 cm^{-1}). The shoulder at 511 cm^{-1} in the solid state (506 cm^{-1} in the solution) can be assigned to the out of plane CCC and O=CC bending modes, whereas the weak band at 483 cm^{-1} in the solid state (481 cm^{-1} in the solution) is attributed to the skeletal distorsion and to both sulfonate groups rocking modes[472,489,491].

In the lower wavenumber region skeletal deformation and sulfonate groups vibrations are

observed (Table V.5.4.1, Fig. V.5.4.1). The concentration dependent RR spectra revealed the possibility to record high quality RR spectra of E132 aqueous solution down to the micromolar concentration level (Fig. V.5.4.2).
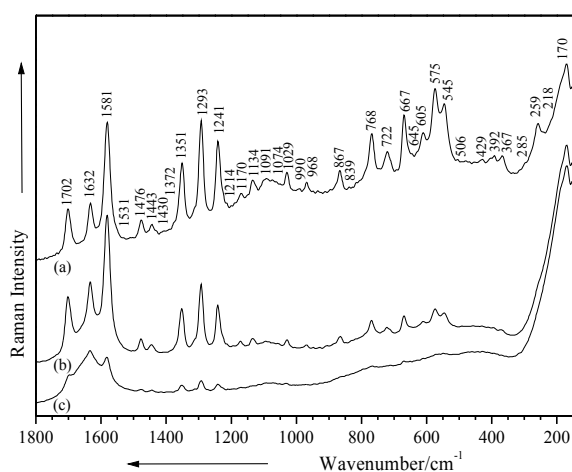
Figure V.5.4.2. Resonance Raman spectra of E132 solutions at different concentrations: 10^{-3} M (a), 10^{-4} M (b), 10^{-5} M (c). Excitation: 514.5 nm, 200 mW.

SERR spectra of E132

SERR spectra of E132 (0.29 10^{-6} M and 0.03 10^{-9} M) on silver colloidal particles are presented in Fig. V.5.4.3 together with the RR spectrum of the bulk solution (10^{-4} M). SERR spectrum on silver colloid of this compound for the 0.29 10^{-6} M concentration (Fig. V.5.4.3b) presents almost similar band positions and relative intensities as the aqueous solution's RR spectrum (Fig. V.5.4.3a), reflecting a most probably bulk Raman signal rather than the physisorption of the molecular species on the nanoparticles surface. The electronic absorption bands of E132 and silver colloid present different positions at 610 and 426 nm, respectively (Figs. V.5.3.2a,c). Moreover, adding the E132 solution into the silver colloid, the plasmon resonance remains unchanged (Fig. V.5.3.2b). This fact reflects that the modification in the aggregation state of silver particles with the adsorbed molecules is unchanged. Being a large size molecular species, E132 could easily cover the active sites of the aggregated silver particles when the molecular concentration exceeds the adsorption available silver particles. When some amount of E132 molecular species is added into the silver colloid, theoretically, chemisorption (or physisorption) and aggregation may occur simultaneously. Both effects may be associated with a new absorption band of the SERRS system[492]. This expected electronic band was not observed here, suggesting that the E132 does not contribute to a supplementary aggregation of the silver particles.

Moreover, either the E132 molecular species or the silver colloid exhibit different absorption maxima at 426 and 610 nm. The chemisorption in the SERRS system at micromolar concentration is also excluded since the SERRS signal is similar to the Raman one from the bulk solution (Fig. V.5.4.3).

Otherwise, if the mixture of silver colloid with E132 solution at nanomolar level is measured after 12 hours from the mixture throughput, the aggregation state seems to occur. The SERRS signal is dramatically changed in band positions and relative intensities (Fig. V.5.4.3c). In this case we can discuss

about chemisorption of E132 on silver colloidal particles. Because the chemisorption effect is very difficult to observe, we tried also SERRS on island films with different roughnesses, their efficiency being previously discussed[493]. The negatively charged dye was expected to preserve the aggregation state and hence the silver surface potential[324]. Since the SERRS signal is concentration sensitive, in order to discuss the behaviour to adsorption of E132 on the metallic surfaces, the SERRS spectrum at nanomolar concentration was chosen here for the adsorption geometry proposal. Theoretically, E132 can interact with the silver surface *via* several functional groups. The negative charge of the $-SO^{3-}$ groups, however, leads to a Coulombian repulsion due to the negative potential of the silver surface. After considering the steric configuration of the structure, several other potential geometries for chemisorption still remain. Another possibility for indigo carmine to chemisorb is provided by the presence of the lone pair nitrogen, oxygen atoms from the pyrrolidone rings and also by the presence of π electrons distribution over the phenyl and pyrrolidone rings (Fig. V.5.1.1b). In this case, according to the surface selection rules[108], the stretching modes of the rings are expected to be enhanced.

The observed bands in the SERRS spectrum (Fig. V.5.4.3c) support the consideration, which reveals the participation of $-SO_3^-$ groups in the molecule adsorption. More specifically, the very intense band at 1350 cm^{-1} assigned to the O12SO13/O12'S'O13' stretching modes and to the C-H/N-H bending modes is preponderantly due to the SO_2 groups that are now in a close vicinity of the silver particles with a bidentate binding mode. Moreover, the strong band observed in the SERRS spectrum at 1159 cm^{-1} (blue shifted from RR at 1134 cm^{-1}) is due to the symmetrical SO_2 stretching mode[477,481]. Besides, this interaction generates the presence of the O12SO13 functional group to bend near the surface, along with the S-O bonds. This contribution is supported by the 1159 cm^{-1} band shape (Fig. V.5.4.3, Table V.5.4.1).
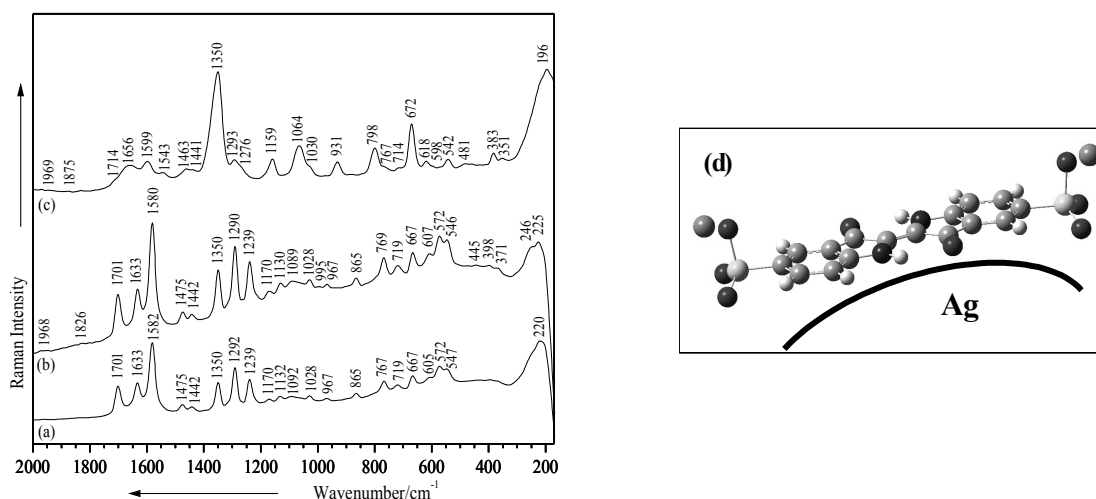
Figure V.5.4.3. Comparison between the resonance Raman (10^{-4} M) (a) and SERRS on silver colloid: 0.29 10^{-6} M (b) and 0.03 10^{-9} M(c), spectra of E132. Excitation: 514.5 nm (a,b,c), 200 mW (a,b,c). Proposed orientation of E132 on silver colloidal particles (d).

The significantly enhanced mode at 1064 cm^{-1} is due to the in plane C-H and out of plane O14-Na bending modes, which suggests that the rings are located very close to the silver surface.

Table V.5.4.1. Selected calculated and experimental RR and SERRS wavenumbers (cm^{-1}) of E132 and their tentative assignment.

Raman solid	Calcd. (Raman)				RR solution	SERRS colloid	SERRS films	SERRS films	Vibrational assignment
	B3PW91		B3LYP						
514.5 nm	LANL2DZ	6-311++G**	LANL2DZ	6-311++G**	514.5 nm	514.5 nm	514.5 nm	632.8 nm	
1738 vw	1768	1785	1750	1767				1744 sh	ν_{as} (C9-C9'); ν_{as} (C=O)[488]
1698 ms	1687	1701	1669	1681	1702 m	1714 sh	1702 vs	1702 w	ν_s (C9=C9'); ν (C=C)$_{ph}$[483]; ν_s (C=O)[481,482,487,489]
	1655	1653	1661	1642		1656 w	1650 sh	1652 w	ν (C=O)[483,488]; ν (CC)$_{ph}$[488]
1623 ms	1640	1632	1635	1616	1632 m		1630 s	1629 wm	ν (C=O)[484,490], ν (C=C); δ_{ip} (C-H)[481,485-487]
1576 vvs	1511				1581 vvs	1599 wm	1581 vs	1582 vvs	ν_{as} (C=C)$_{pr}$[481,485,487-489]; ν (C=O)[485-487]; Є (C=N)[461]
1539 sh	1508	1509	1497	1498	1531 sh	1543 vw		1527 sh	ν (ph, pr); ν_s (C=C)$_{pr}$[489]
1472 m	1495	1486	1482	1482	1476 w	1463 vw	1475 m	1479 vw	ν (ph, pr)[484]; δ_{ip} (C-H)[485,487-489]; ν (N=C)[488]
1444 w	1466		1451	1473	1443vw	1441 vw	1444 w	1447 w	ν (N-C=C-N, C-C); δ_{ip} (C-H)[485,487,488], δ_{ip} (N-H)[489,490]
1415 w	1449	1447	1432	1437	1430 sh				ν_s (C=O); δ_{ip} (C-H, N-H)
	1407	1396	1390	1411	1372 sh		1396 vw		ν (N1C9-C9'N1'); ω (N-H)[488]
1344 s	1357	1348	1343	1352	1351 ms	1350 vvs	1350 vvs	1353 wm	δ (C-H, N-H)[485,487], ν (ph, pr); ν (SO$_2$)[477]
	1310	1305	1306	1314			1317 sh	1320 sh	δ (N-H)[482]
1290 s	1288	1280	1288	1296	1293 vs	1293 w	1293 vs	1296 s	ν_s (-SO$_3^-$)[481]; δ (C-C)[485-487], ν (N1-C2)
1240 ms	1239	1243	1265	1244	1241 s	1276 sh	1245 s	1248 wm	δ (C-H, C=O)[485-487]
1217 sh	1205	1210		1200				1227 wm	ph breath
1185 w		1197	1196	1187			1188 vw		ν (NC)[488,489], ν (C9-C9')[485,487,488]
1172 w	1167	1173	1160	1173	1170 w			1178 vw	ν_{as} (SO$_2$); δ_{ip} (C-C)[487,488]
1130 w	1164	1152	1157	1139	1134 w	1159 m	1130 wm	1136 vw	ν_s (SO$_2$)[477]; ν (C-C)[485,487]
1082 vw	1083	1108	1101	1090	1091 w		1090 w		δ_{op} (O14-Na); δ_{ip} (C-H)[485,487,488]; δ_{ip} (C-C)[487,488]
1062 vw	1082	1074	1072	1071	1074 w	1064 m		1059 vw	δ_{ip} (C-H); δ_{op} (O14-Na)
1036 vw	1022		1023	1068	1029 m	1030 sh	1037 w	1041 w	δ_{op} (C-H)[485-487]
997 vw	999	988	989	984	990 w				δ_{op} (C-H)
967 vw	978	979	970	982	968 w	931 m	966 w		δ_{ip} (C=O); δ_{op} (C-H)[485,487], O12SO13 def[480]
895 vw	904	913	897	910	896 vw		896 vw		ν_s (C4C5C6, C-N-C)[488]
866 vw	859	883	870	879	867 w		866 w	868 wm	δ_{ip} (N-H); ν (C-N)[485,487,488]
833 vw	840	832	837	834	839 vw			819 sh	skeletal str.[491], δ_{op} (C-C)$_{pr}$[487,488]; δ_{op} (C=O); ν (C-S)[461]
	786	795	795	796		798 ms			δ_{ip} (C8C9C9'C8')[488]
764 w	778	766	773	784	768 ms	767 sh	769 m	768 s	δ_{op} (C-C, C-H); pr breath.
722 w	738	734	734	727	722 m	714 vw	722 ms	723 wm	ph, pr def.; δ (C-N-C)[485,487,491]
672 w	680	676	671	676	667 ms	672 s	673 ms	673 vs	δ_{op} (N-H, C-C)[485,487]
	657	658	648	653	645 sh				ν (C-S)
618 w	628	605	619	606	605 m	618 w	618 m	618 m	δ (-SO$_3^-$)[481], δ_{op} (N-H, CH$_{ph}$)[485]
577 w	573	574	571	574	575 s	598 sh	574 m	576 ms	δ (C=C-CO-C)[481]; δ (C=O, C-H, C-NH-C)[485,487,488]
546 w	555	560	551	555	545 ms	542 w	547 ms	548 s	δ (C=C-CO-C)[481,485,487]
511 sh	504	525	501	515	506 vw				δ_{op} (CCC, O=CC)[488]
483 vw	458	477		484	481 vw	481 vw			ρ (SO$_3$)[463]; skeletal def.
455 vw	455	463	455	464	469 vw		466 vw		skeletal def.[489,491]; δ_{op} (C9=C9', C-H)[485]
421 vw	427	434	427	435	429 vw			430 w	skeletal def.[489,491]
399 vw	401	411	402	413	402 sh				δ_{ip} (O12-S-O13); op def. (ph, pr)
378 vw	395	400	390	396	392 vw	383 wm	399 w	398 wm	δ_{ip} (C-S, C-O15)
	373	378	369	365	367 vw		373 w		δ_{op} (N1-C9-C9'-N1', O12-S-O13); ν (Ag-N)[495]
322 vw	329	344	323	346		351 vw			skeletal def.; δ_{op} (O12-S-O13)
302 vw	313	287	308	286	285 sh		293 sh	306 wm	δ (O14-Na)
264 w	264	271	264	271	259 m		268 wm	263 s	skeletal def.[491]; ν (Ag-O)[494]
222 w	226	224	225	221	225 m				δ (SO$_3$)
191 vw	208		207		218 sh	196 vvs			op skeletal def.; ν (Ag-O)[494]
172 vw	181	162	179	162	170 vs				ν (O-Ag-O)[494]

Abbreviation: vw – very weak; w – weak; wm – weak medium; m – medium; ms – medium strong; s – strong; vs – very strong; sh – shoulder; ν - stretching; δ - bending; pr – pyrrolidone ring; ph – phenyl ring; s – symmetric; as – asymmetric; def. – deformation; ip – in plane; op – out of plane; breath. – breathing; str. – stretching; Є – existence.

The band shape at 931 cm^{-1} is assigned to the out of plane C-H bending mode and to the O12SO13/O12'S'O13' deformation modes[480,485,487]. The new medium band at 798 cm^{-1} can be due to the in plane C8-C9=C9'-C8 bending mode, while other bands with medium or weak intensities in the SERRS spectrum are attributed to many bending modes of the structure. The E132 molecule binds to the silver colloidal surface through the lone pair electrons of two oxygen atoms of the -SO$_3^-$ groups, symmetric bidentate (Fig. V.5.4.3d). This assumption is supported by the Ag-O stretching modes[494], which can be detected as a very strong band at 196 cm^{-1}.

To obtain the SERR spectra on island films, the E132 moecule was excited with both 514.5 and 632.8 nm laser lines. The spectra present substantial dissimilarities in band positions and relative intensities, allowing the assumption of a chemisorbed species (Figs. V.5.4.4 and V.5.4.5). The observed bands in the SERR spectra of E132 (Fig. V.5.4.4), recorded with the 514.5 nm laser line, support the consideration that the most increased bands may be attributed to the main functional group, which is implied in the chemisorption effect. More specifically, the very intense band at 1350 cm^{-1} (increased in relative intensity as compared to the band at 1351 cm^{-1} in the RR spectrum of the solution) can be attributed to the O12SO13/O12'S'O13' stretching modes and to the C-H/N-H bending modes. The very strong band observed in the SERR spectrum at 1581 cm^{-1} (at the same position in the RR spectrum of the solution) decreases in relative intensity and is due to the C=O and C=C stretching modes belonging to the pyrrolidone groups.
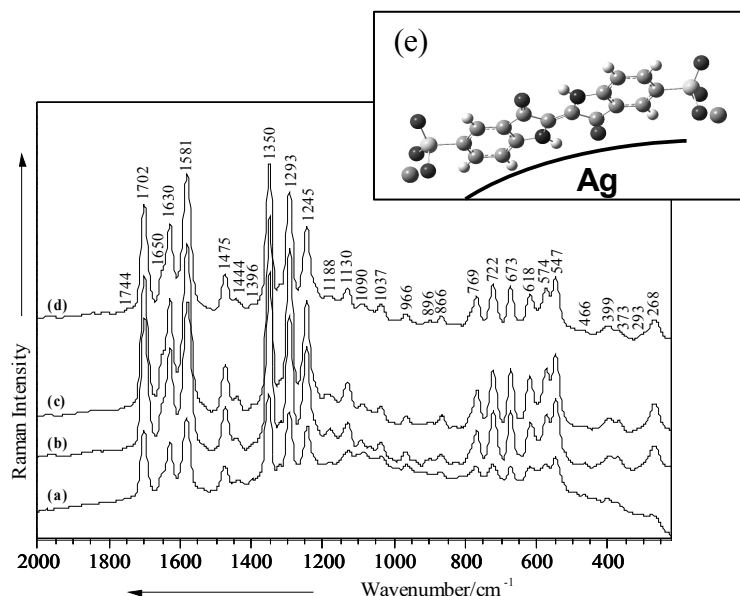
Figure V.5.4.4. SERR spectra of 10^{-4} M E132 on island films with different roughnesses: (a) 14.4 Å, (b) 2.9 Å, (c) 1.9 Å, (d) 1.05 Å. Excitation: 514.5 nm, 200 mW. Proposed orientation of E132 on silver films (e).

The strong band at 1702 cm^{-1} becomes very strong through comparison to the RR spectrum of the solution and is attributed to the symmetrical C9=C9' bridge bond stretching contribution and to the symmetrical C=O stretching modes, although the very strong peak at 1293 cm^{-1} has the same position and relative intensity as in the solution and can be due to the symmetrical –SO$_3^-$ stretching modes and to the C-C bending mode[481,485-487]. The strong band at 1630 cm^{-1} (slightly red shifted from the RR spectrum of the solution, 1632 cm^{-1}) and its neighbour shoulder at 1650 cm^{-1}, which is absent in the solution, are

assigned to the C=C/C=O stretching modes and to the in plane C-H bending mode, whereas the strong signal at 1245 cm^{-1} (slightly blue shifted from the solution, 1241 cm^{-1}) can be seen as C-H/C=O bending contributions. The peak at 1475 cm^{-1} increases in relative intensity as compared to the solution and can be due to the phenyl and pyrrolidone rings stretching modes[484], while the new weak peak at 1188 cm^{-1} appears as a stretching contribution of the NC bonds[488,489] and of the C9=C9' bridge bond[485,487]. In the low wavenumber region of the SERRS spectra (Fig. V.5.4.4), some bands (769, 722, 673 cm^{-1}) are significantly increased in relative intensities and appear as phenyl and pyrrolidone rings contributions[485,487,491]. The next three peaks at 618, 574, and 547 cm^{-1} in the SERR spectrum of E132 are rather blue shifted in comparison with the RR spectrum of the solution and can be assigned to the –SO$_3^-$ groups bending modes, to the C=O, C-H, C-NH-C bending modes, and to the C=C-CO-C bending mode, respectively[481,485-497].

Moreover, this interaction leads for the negatively charged SO$_3^-$ functional group to bend near the surface, along the S-O14, S-O13, S'-O14', S-O12' bonds. Taking into account the increases in relative intensities of some bands corresponding to the N-H and C=O vibrations and the appearance of the weak band at 1188 cm^{-1} as a contribution of N-C and C9=C9' stretching modes, we can suggest a tilted orientation of E132 on the silver surface, through the S-O13, S-O14, S'-O12', S'-O14' bonds, and through the lone pair electrons of the nitrogen and oxygen atoms situated on the one side of pyrrolidone groups (Fig. V.5.4.4e). This contribution is supported by the shoulder at 373 cm^{-1} and the medium band at 268 cm^{-1}, which were attributed to the Ag-N[495] and Ag-O[494] stretching vibrations, respectively.
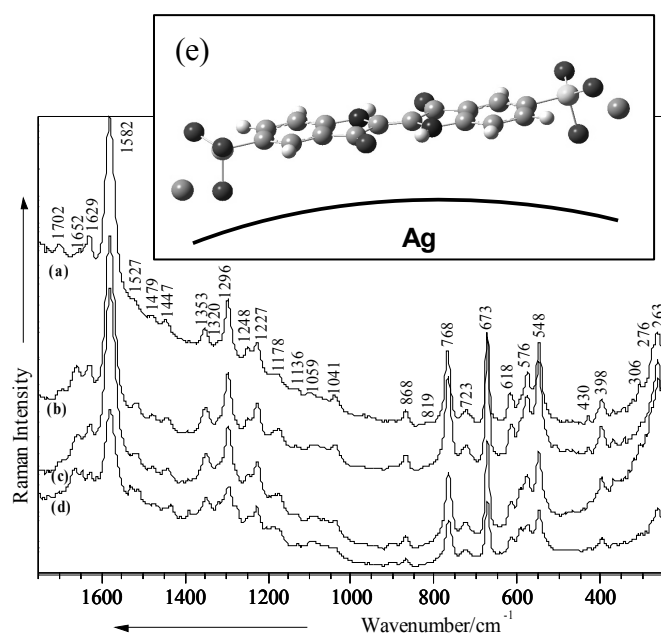
Figure V.5.4.5. SERR spectra of 10^{-4} M E132 on island films with different roughnesses: (a) 14.4 Å, (b) 2.9 Å, (c) 1.9 Å, (d) 1.05 Å. Excitation: 632.8 nm, 3.6 mW. Proposed orientation of E132 on silver films (e).

In the SERR spectra recorded with the red laser line, we can observe also more changes in the band positions and relative intensities, assuming the presence of chemisorbed species of E132. The very strong band in the SERR spectra at 1582 cm^{-1} is attributed to the asymmetrical stretching contribution of C=C bonds belonging to the pyrrolidone rings and to the C=O stretching modes. The band at 1353 cm^{-1}

(very strong in the RR spectra of the solution) becomes weaker and can be due to the C-H/N-H stretching modes, and to the SO_2 groups stretching mode (Fig. V.5.4.5). The band at 1248 cm^{-1} together with the new peak at 1227 cm^{-1} correspond to the C-H/C=O bending modes and to the breathing mode of the phenyl groups, respectively[485-487]. The band at 868 cm^{-1} increases in relative intensity as compared to the RR spectrum of the solution and appears as a C-N stretching contribution[487,488]. In the same way, the band at 768 cm^{-1} can be due to the out of plane C-C/C-H bending modes and to the pyrrolidone rings breathing modes. The very weak peak at 667 cm^{-1} in the solution becomes very strong in the SERR spectra (Fig. V.5.4.5, 673 cm^{-1}), and can be assigned to the out of plane N-H/C-C bending modes, whereas the great increase in relative intensity of the band at 548 cm^{-1} in the SERR spectra is due to the C=C-CO-C bending modes[481,485,487]. From all these observations we can suppose that E132 molecule interacts with the silver surface through the π electrons distributed over the phenyl and pyrrolidone rings. The weak/medium band at 398 cm^{-1}, which is slightly red shifted and increased in relative intensity as compared to the solution (392 cm^{-1}) is assigned to the in plane C-S/C=O bending modes, while the new weak/medium peak at 306 cm^{-1} can be due to the O14-Na/O14'-Na' bending modes. The strong signal at 263 cm^{-1} together with its shoulder at 276 cm^{-1} are due to the well known Ag-O stretching modes. The assumption that E132 binds to the silver surface through the π electrons of the phenyl and pyrrolidone rings is now associated with the binding through the O14 and O14' (Fig. V.5.4.5e).

V.5.5 Conclusions

The geometry of E132 was computed and optimized with B3PW91/6-311++G**, B3PW91/LANL2DZ, B3LYP/6-311++G**, and B3LYP/LANL2DZ methods of the Gaussian 03 program.

The Raman spectrum of E132 in solid state and the RR spectra in aqueous solution were recorded and the marker bands were identified. E132 could be detected in aqueous solution down to micromolar levels with RR, at nanomolar concentrations with SERR spectroscopy on sodium citrate-reduced silver colloid, and down to micromolar levels with SERR spectroscopy on island films with various roughnesses.

The surface selection rules together with the data from literature can explain the adsorbate structures on the metal surfaces. A strong chemical interaction of E132 with the silver colloidal particles is observed at nanomolar concentrations after 12 hours from the aggregation; the interaction taking place through the lone pair electrons of the two oxygen atoms of the -SO_3^- groups, symmetric bidentate.

The chemical interaction of E132 with the island films is observed down to micromolar concentrations and the binding modes on the metallic surface are different; when the molecule is excited with the green laser line, the interaction taking place through the lone pair electrons of two oxygen atoms of the -SO_3^- groups, one oxygen atom and one nitrogen atom of the pyrrolidone ring, in a tilted orientation; when the molecule is excited with the red laser line, the molecule binds to the silver surface through the π electrons distributed over the pyrrolidone and phenyl rings and through the negative oxygen ions of both –SO_3^- groups, in a perpendicular orientation.

V.6 Monosodium glutamate (E621)

Monosodium glutamate (MSG), a common flavor enhancer, is detected in aqueous solutions by Raman and surface-enhanced Raman (SERS) spectroscopies at the micromolar level. The presence of different species, such as protonated and unprotonated MSG, is demonstrated by concentration and pH dependent Raman and SERS experiments. In particular, the symmetric bending modes of the amino group and the stretching modes of the carboxy moiety are employed as marker bands. The protonation of the NH_2 group at acidic pH values, for example, is detected in the Raman spectra. From the measured SERS spectra, a strong chemical interaction of MSG with the colloidal particles is deduced and a geometry of MSG adsorbed on the silver surface is proposed. In order to assign the observed Raman bands, calculations employing density functional theory (DFT) were performed. The set of theoretical data enables a complete vibrational assignment of the experimentally detected Raman spectra and the differentiation between the anhydrous and monohydrate forms of MSG.

V.6.1 Molecule presentation

MSG has been a common flavor enhancer for nearly a century. Its principal component is the amino acid glutamic acid or glutamate. Glutamate is found naturally in protein–containing foods such as meat, vegetables, poultry, and milk. The human body also produces glutamate in large amounts. Muscles, brain, and other organs contain about four pounds of glutamate, which is found in two forms: "free" from of glutamate and "bound" glutamate, i.e. glutamate linked to other amino acids in proteins; only the "free" glutamate is effective in enhancing the flavor of food. Foods often used because of their flavoring qualities, such as tomatoes and mushrooms, contain high levels of naturally occurring "free" glutamate.

MSG or E621, the sodium salt of glutamic acid, is probably the most common food additive used in many packaged and prepared foods. Other synonyms of MSG are: L-glutamic acid monosodium salt, hydrolyzed vegetable protein, autolyzed yeast, and whey protein. It is a white crystalline powder commercially produced by the fermentation of molasses, which exists in many products made from fermented proteins, such as soy sauce and hydrolyzed vegetable protein.

MSG is a neurotoxin and is employed to give a "meaty", "savory", or "brothy" taste to foods by stimulating the glutamate receptors on the tongue. It causes the taste of *umami*, one of the five basic flavors besides salts, sweet, bitter, and sour. Additionally, it has been associated with a conjunction of symptoms in susceptible individuals, such as severe chest and/or facial pressure and overall burning sensations, similar to the feeling of experiencing a heart attack[497]. MSG has been also found to precipitate a severe headache and/or asthma in individuals[498,499]. In susceptible children, MSG has been linked with epilepsy–type "shudder" attacks[500].

In animal studies, it caused damages to the brains of young rodents[497]. MSG food additives have been found to be even teratogenic when tested on animals[501-503]. Such experiments on animals are conducted on healthy species fed on a nutritious diet[504], not on malnourished, elderly or sick animals. It

also has to be considered that only one agent is tested at a time, whereas humans usually consume 12 to 60 different food additives in the course of a single meal[502,505].
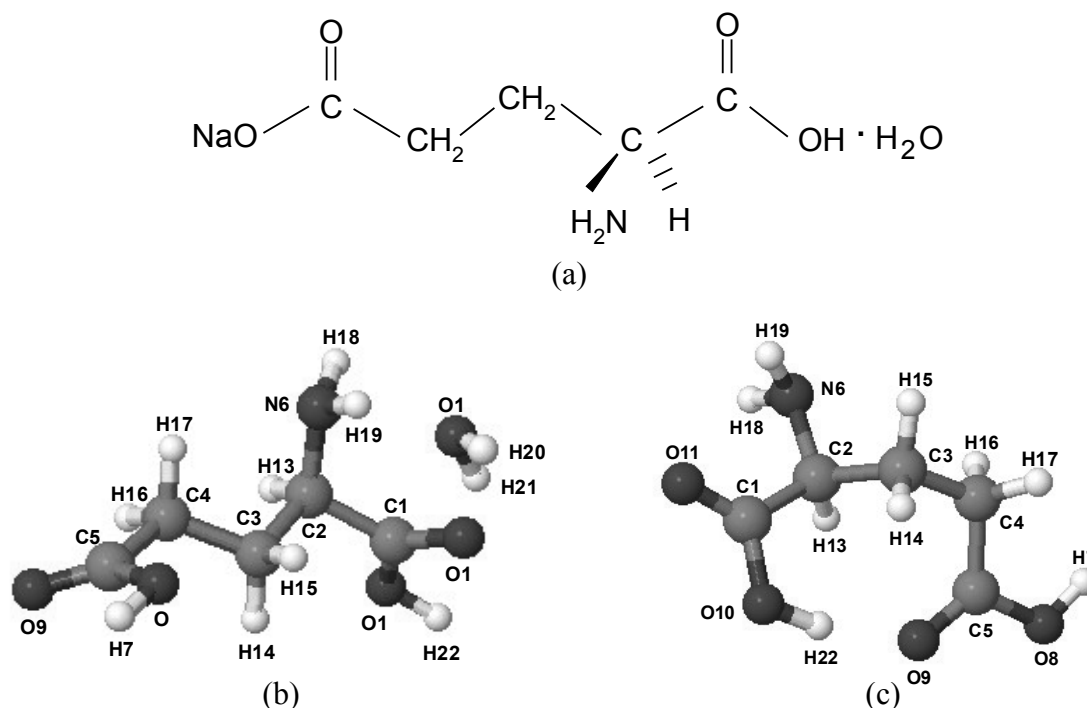
Figure V.6.1.1. Molecular stucture (a), B3LYP/LANL2DZ optimized geometry of MSG monohydrate (b), and anhydrous MSG (c).

It can be difficult to pinpoint MSG in many foods because it can be "hidden". Food processing companies disguise it with many names, which are permitted in the US by the Food and Drug Administration (FDA). Persons sensitive to MSG try to avoid foods with MSG on the label, but they are often unaware of the additional names that MSG goes by. Patients may also believe that the observed symptoms are due to an allergic reaction to the product, but they are experiencing signs of toxic poisoning. The toxicity of MSG produces cardiac, circulatory, muscular, gastrointestinal, visual, and neurological effects[506-510].

MSG can be present in its monohydrate and anhydrous form. Crystallization measurements of MSG using ATR/FT-IR spectroscopy were accomplished and its particle size and crystallographic form were determined[511,512]. In the time–resolved X–ray diffraction patterns of crystallization experiments, however, no obvious phase transformation between the two forms was observed[513]. The aim of our study is to experimentally determine the differences between the monohydrate and anhydrous form by Raman and surface–enhanced Raman spectroscopies. In addition to the spectroscopic experiments, calculations based on density functional theory (DFT) on both forms are performed for obtaining reliable vibrational assignments. The molecular structure of MSG is presented in the Fig. V.6.1.1a.

Commercially available MSG was used in our measurements, for which no analytical purity certificate was accessible. Although impure ingredients are often used by many companies, MSG is used extensively in many parts of the world in powder or crystal form as a flavoring agent in foods such as meats, vegetables, sauces and gravies. Cassava starch and molasses are the major raw materials used in the manufacture of MSG. The starch is usually hydrolyzed into glucose by boiling with hydrochloric or

sulfuric acid solutions in closed converters under pressure. The glucose is filtered and converted into glutamic acid by bacterial fermentation. The resulting glutamic acid is refined, filtered and treated with caustic soda to produce MSG, which is then centrifuged and dried in drum driers. The finished product is usually at least 99 % pure[514].

V.6.2 Geometry optimization

Because no crystal structure data are available for MSG in both its anhydrous and monohydrate form, their structures were optimized at different levels of theory (BPW91/6-311++G**, B3PW91/LANL2DZ, B3LYP/6-311++G**, B3LYP/LANL2DZ) and compared with literature data for compounds containing identical or similar functional groups[311,312,456-461,471,515-525].

Monohydrate form of MSG

The calculated structural parameters of monohydrated MSG are listed in Table V.6.2.1 and the labeling of the atoms is shown in Fig. V.6.1.1b. As one can notice, the agreement between the theoretically determined parameters of MSG and the experimental values available in the literature is very good[311,312,410,456-461,471,515-525].

For α,ω-alkanedicarboxylic acids, two different trends for the C-C bond lengths along the carbon chain are observable: for diacids with an odd number of carbon atoms the distribution is uniform, whereas even members exhibit an alternating distribution of long and short distances[515,516]. This finding is in a good agreement with our calculations on MSG, where the C-C bond lengths of the carbon atoms of the chain are in the range of 150.3 pm to 155.8 pm (Table V.6.2.1) for all levels of theory employed.

A common phenomenon among odd diacids is the dimorphism, which is a disturbing phenomenon for any study that relates crystal structure of a compound to its properties[515,516]. Odd members crystallize in two modifications generally termed α and β[516,517] and possess a twisted molecular conformation in the crystal structure as opposed to the extended conformation seen in even diacids. The two carboxyl groups of MSG twist to an equal but opposite extent with respect to the carbon chain. In our theoretical data, this is disclosed by the bond angles of 112.4° for O10-C1-C2 and of 112.5° for O8-C5-C4, the difference between C5-O8 and C1-O10 bonds is approximately 60° rotation by dihedral angle of 52.8° for C3-C4-C5-O8. This conformation is specific to the β form of the odd diacids[515,516].

The geometric features of MSG and the transition state of the NH_2 rotation are very similar and, as shown in Table V.6.2.1, the average C2-N6 bond length calculated with different methods is 144.9 pm; this value is slightly smaller than the length of a C-N single bond (148 pm), higher that of a C=N double bond (128 pm)[312], and also higher than the C-N single bond length in the electronic ground state (137.6 pm)[456]. From all these literature data[312,456], we can comment that with this calculated value of the C2-N6 bond length, the NH_2 group exists in the transition–state structure and can be valuable to explain the protonation of the MSG molecule and the association with water molecule[457,458]. Besides the calculated value, which demonstrates the presence of the transition–state[458], a proton transfer from H_2O to the NH_2 moiety is expected[459,460].

As shown in Table V.6.2.1, the calculated C-O bond lengths of the carboxyl groups vary from

134.4 to 139.4 pm, which is shorter than the length of a C-O single bond (143 pm)[311]; the calculated C=O bond lengths are between 120.5 pm and 124.8 pm, which is larger than a regular C=O bond length (120 pm)[311]. Both bond length characteristics are due to the charge delocalization in the corresponding carboxyl moiety[518]. The impact of charge delocalization on the adjacent NH_2 group is also evident: the C2-N6 distance of the calculated molecular structure is in the range 144.3 pm to 145.6 pm, which is shorter than a C-N single bond (147 pm)[312]. This implies a non–negligible polarization of the neutral system towards the metal cation in the case of SERS. The polarization is transmitted to the C2-N6 bond, inducing a greater participation of the nitrogen lone pairs in the C2-N6 bond, which results in a shortening of the bond length[460]. The interatomic calculated distance N6-H19···O12 between H19 of the NH_2 group and O12 of the water molecule is between 192.0 pm and 212.9 pm (Table V.6.2.1), whereas the stronger hydrogen bond is significantly shorter (189.8 pm to 172.4 pm)[519]. Our calculated value shows a non–stronger hydrogen bond. The calculated C2-N6 bond length suggests the transition state of the molecule and the possible protonation of the nitrogen atom[461].

Hydrogen bonding can occur between O12 of the water molecule of the monohydrate form of MSG and the H19 of the NH_2 group (N6-H19···O12); the distance varies from 192 pm for the LANL2DZ basis up to 212.9 pm for the 6-311++G** basis set (Table V.6.2.1). Another possible hydrogen bond can occur between water and O11 of the one of carboxyl groups (C1-O11···H20); in this case, the hydrogen bond length is in the range 181.0 pm to 194.6 pm (Table V.6.2.1). Together these two hydrogen bonds can demonstrate the double proton transfer and the glutamate protonation[520].

Table V.6.2.1. Selected calculated structural parameters of monohydrate MSG in comparison with the available experimental data.

| | Exp. | Calcd. | | | |
| | | B3LYP | | B3PW91 | |
		6-311++G**	LANL2DZ	6-311++G**	LANL2DZ
Bond lengths (pm)					
C1-C2		153.3	154.1	152.7	153.5
C2-C3		154.7	155.8	154.1	150.0
C3-C4		153.6	154.4	152.9	153.7
C4-C5		150.8	151.0	150.3	150.4
C2-N6	147.6[460], 144.2[311], 145.9[520]	144.9	145.6	144.3	144.9
N6-H18	101.9-102.2[525]	101.3	101.5	101.3	101.3
N6-H19	101.9-102.2[525]	101.8	102.5	101.8	102.4
C1-O10	135.2[519]	134.9	138.0	134.4	137.4
C1-O11	124.7[519]	121.2	124.8	121.0	124.6
C5-O8		135.9	139.4	135.3	138.8
C5-O9		120.6	124.1	120.5	123.9
N6-H19···O12	205.6[519], 214.1[521]	212.9	192.6	212.9	192.0
O12-H20	98.0[519]	97.1	98.8	96.9	98.7
O12-H21	96.3[519]	96.1	97.3	95.9	97.1
C1-O11···H20		194.6	182.0	193.5	181.0
Angles (°)					
C1-C2-C3		107.9	107.5	107.9	107.5
C2-C3-C4		111.4	110.1	111.2	109.9
C3-C4-C5		113.8	114.2	114.2	114.3
C1-C2-N6		115.0	114.2	115.1	114.3
C2-C1-O11		126.4	126.9	126.3	126.8
C2-C1-O10		111.9	112.4	112.0	112.4
O10-C1-O11		121.7	120.8	121.7	120.8
C1-O10-H22	110.5[519]	107.8	111.6	107.5	111.6
O11-H20-O12		155.2	154.4	157.0	155.3
H20-O12-H21		106.5	113.1	106.1	113.1
H18-N6-H19	117.4[519]	107.9	114.1	107.7	114.0
C4-C5-O8		112.2	112.5	112.3	112.5
O8-C5-O9		122.0	121.1	122.0	126.4
C5-O8-H7	106.4[519]	107.0	110.3	106.6	110.3
H14-C3-H15		107.5	108.1	107.5	108.1
Dihedral angles (°)					
C1-C2-C3-C4	-171.9[524]	-170.8	-171.3	-171.3	-171.8
C2-C3-C4-C5	-173.7[524]	-177.1	-174.7	-175.4	-173.9
N6-C2-C3-C4	68.8[524]	62.6	63.3	62.1	62.7
N6-C2-C1-O11		28.4	38.2	26.6	35.8
N6-C2-C1-O10		-152.6	-142.7	-154.4	-145.2

C1-O11-H20-O12	-11.6	-5.2	-9.5	-4.6
C3-C4-C5-O8	52.8	45.5	50.0	44.8
C3-C4-C5-O9	-128.1	-135.7	-131.1	-136.4

Anhydrous form of MSG

In the case of the anhydrous form of MSG, the distribution of the C-C bond lengths along the carbon chain is alternating, long and short bond lengths[515,516], and this can be pointed out by our calculations, where the C-C bond lengths of the carbon chain are in the range of 151.5 pm to 155.9 pm (Table V.6.2.2).

Anhydrous MSG is arched and two hydrogen bond interactions are possible: between H19 of the NH$_2$ group and O11 of the carboxyl group (C1-O11···H19=267.1 pm), and between H22 of a carboxyl group and O9 of the other carboxyl group (C5-O9···H22=179.2 pm). The stable protonated structures of the anhydrous MSG are characterized by one slightly strong N$^+$-H···O=C hydrogen bond, which restricts the accessible conformational space. Taking this into account, we can observe that the stable form of anhydrous MSG corresponds to the protonated form[521,522].

The C2-N6 calculated bond length are in the range 145.0 pm to 146.5 pm. In this anhydrous form like in the case of monohydrate form this is shorter that the normal C-N single bond (147 pm)[312] and comes to demonstrate the possibility of the MSG molecule protonation[460,521]. The two carboxyl groups are not equally twisted and are not in opposite direction with respect to the carbon chain. In our study, this is revealed by the calculated angles O10-C1-C2 (114.5°), O8-C5-C4 (116.5°), (Fig. V.6.1.1c, Table V.6.2.2). This conformation is characteristic of the α form of odd diacids, although the two carboxyl groups turn in opposite directions and one of the carboxyl group twists to a greater extent than the other. The mutual inclination between the two carboxyl planes is similar as in the β form (60°)[515,516]. The two carbon-oxygen bonds for each carboxyl group differ in bond length values (Tables V.6.2.1, V.6.2.2) suggesting that the C-O single bond length is coordinated[410].

The N-H···O and C-H···O hydrogen bonds can stabilize the different conformers of the molecules[471]. In accordance with IUPAC-IUB[523,524] recommendations, dihedral or torsional angles were specified within -180° and 180° for the side–chain (C1-C2-C3-C4, C2-C3-C4-C5, N6-C2-C3-C4) of both conformations and the corresponding torsional angles were optimized at about 180° (Tables V.6.2.1, V.6.2.2). The calculated N-H bond lengths, which are somewhere between 101.3 pm and 102.4 pm for the monohydrate form of MSG and between 101.5 pm and 102.0 for the anhydrous form of MSG, are in good agreement with the literature[525,526].

The both forms of MSG have two different geometries, which are explained by the various possibilities of the molecule protonation.

Table V.6.2.2. Selected calculated structural parameters of anhydrous MSG in comparison with the available experimental data.

	Exp.	Calcd.			
		B3LYP		B3PW91	
		6-311++G**	LANL2DZ	6-311++G**	LANL2DZ
Bond lengths (pm)					
C1-C2		154.2	155.4	153.7	154.8
C2-C3		155.4	156.5	154.8	155.9
C3-C4		152.8	153.8	152.2	153.2
C4-C5		152.1	152.8	151.5	152.2
C2-N6	147.6[460], 144.2[311], 145.9[520]	145.6	146.5	145.0	145.8
N6-H19	101.9-102.2[525]	101.7	102.0	101.7	101.9
N6-H18	101.9-102.2[525]	101.5	101.9	101.5	101.7
C1-O10	135.2[519]	135.0	137.6	134.0	137.0

C1-O11	124.7[519]	120.8	123.6	120.2	123.4
C5-O8		134.6	138.1	134.4	137.4
C5-O9		120.3	123.9	120.7	123.8
Angles (°)					
C1-C2-C3		109.9	109.4	109.8	109.3
C2-C3-C4		112.9	112.5	112.7	112.4
C3-C4-C5		112.4	111.8	112.1	111.7
C1-C2-N6		114.6	114.2	114.6	114.3
C2-C1-O11		123.4	123.7	123.3	123.7
C2-C1-O10		115.1	114.5	114.9	114.3
O10-C1-O11		121.5	121.8	121.8	122.0
C1-O10-H22	110.5[519]	111.1	113.6	110.6	113.4
H19-N6-H18	117.4[519]	105.6	109.9	105.4	110.0
C4-C5-O8		116.3	116.5	116.3	116.5
O8-C5-O9		119.1	118.7	119.1	118.7
C4-C5-O9	106.4[519]	124.6	124.8	124.5	124.7
C5-O8-H7		110.9	113.8	110.5	113.9
Dihedral angles (°)					
C1-C2-C3-C4	-171.9[524]	135.5	133.7	136.1	134.1
C2-C3-C4-C5	-173.7[519]	-69.0	-69.1	-69.1	-69.2
N6-C2-C3-C4	68.8[519]	-97.4	-99.8	-96.7	-99.4
N6-C2-C1-O11		-12.0	-12.0	-11.2	-11.5
N6-C2-C1-O10		168.4	168.6	169.1	169.1
C3-C4-C5-O8		-178.4	-176.0	-179.1	-176.6
C3-C4-C5-O9		1.7	4.2	0.8	3.5

V.6.3 Raman spectroscopies

FT-Raman spectroscopy of solid MSG

The FT-Raman spectrum of solid MSG presented in Fig. V.6.3.1 was analyzed by comparing the observed bands with those of similar molecules reported in the literature[39,40,108,324,494-496,527-541] and by comparing the experimental spectrum with the harmonic vibrational wavenumbers and Raman scattering activities obtained in our DFT calculations.
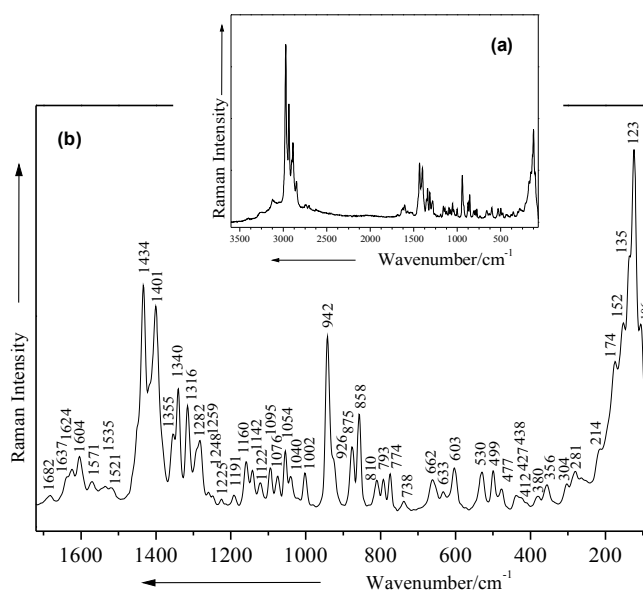
Fig. V.6.3.1. FT-Raman spectrum of MSG: 3600-68 cm^{-1} (a) and 1700-100 cm^{-1} (b) spectral regions. Excitation: 1064 nm, 1000 mW.

In Table V.6.3.1 selected calculated and experimental Raman and SERS data together with their tentative assignment are listed. Because of the basic amino group of MSG and the two carboxyl groups, one of the carboxyl group may bind to itself or may form an internal salt with the amine (zwitterion) as in amino acids. In this case, the Raman spectrum exhibits bands in the regions 3100-2600 cm^{-1} (NH_3^+ stretch), 1665-1585 cm^{-1} (NH_3^+ asymmetrical deformation), 1605-1555 cm^{-1} (COO^- asymmetrical stretch), 1530-1490 cm^{-1} (NH_3^+ symmetrical deformation), and 1340-1315 cm^{-1} (CH deformation)[39,527,528]. In the

zwitterionic form contributions from both the ionized (carboxylate) and the non–ionized carboxylic groups are expected.

In the FT-Raman spectrum (Fig. V.6.3.1a) the extremely strong band at 2971 cm^{-1} and the very strong peak at 2936 cm^{-1} are assigned to the asymmetrical and symmetrical CH$_2$ stretching modes[529]. The very weak band at 3399 cm^{-1} and the shoulder at 3183 cm^{-1} correspond to the asymmetrical and symmetrical N-H stretching modes, while the weak peak at 3121 cm^{-1} is attributed to the NH$_3^+$ asymmetrical stretching mode. The very strong band at 2889 cm^{-1} is assigned to the CH$_2$ stretching mode[530]. Figure V.6.3.1b displays the fingerprint region from 1700-150 cm^{-1}. The most characteristic band for carboxylic acid dimers 960-875 cm^{-1} is due to the in–plane and out–of–plane OH···O wagging modes[531]. Also, a prominent band appears at 1315-1200[532] cm^{-1}. A narrower region, 1315-1280 cm^{-1}, has been assigned to dimers and a somewhat weaker band is observed at 1440-1395[531] cm^{-1}. These two bands near 1290 and 1410 cm^{-1} both involve interacting C-O stretching and C-O-H in plane bending modes. As it can be seen, the carboxylic acid dimer is best characterized by the Raman band at 1680-1640[533] cm^{-1}. The very weak peak at 1682 cm^{-1} is due to the stretching mode of C=O bond of the carboxyl groups. The weak band at 1637 cm^{-1} is assigned to the asymmetrical bending mode of the NH$_3^+$ group, whereas the weak peak at 1624 cm^{-1} corresponds to the asymmetrical stretching mode of the COO$^-$ groups. The adjacent weak peak at 1604 cm^{-1} is attributed to the NH$_3^+$ deformation mode whilethe other one at 1571 cm^{-1} to the COO$^-$Na$^+$ stretching mode. The symmetrical bending mode of the NH$_3^+$ group appears at 1521 cm^{-1}, while the symmetrical COO$^-$ stretching mode is represented by the medium strong band at 1401[534] cm^{-1}. The bands at 1434 and 1355 cm^{-1} are due to the CH$_2$ scissoring and wagging modes. The medium and weak bands at 1340, 1316, 1291, 1282, and 1259 cm^{-1} are assigned to the deformation modes of CH$_2$, i.e. twisting and wagging. The band at 1122 cm^{-1} is assigned to the NH$_2$ twisting and NH$_3^+$ rocking modes. The nearby medium band at 1095 cm^{-1} corresponds to the CH$_2$ rocking mode, while the medium band at 1076 cm^{-1} is assigned to the NH$_3^+$ rocking mode and to the C-N stretching mode. The medium band at 1054 cm^{-1} and the weak peak at 1040 cm^{-1} are assigned to the CH$_2$ rocking mode and to the C-C stretching mode of the carbon chain. The C–C stretching modes are also observed at 1002 and 942 cm^{-1} and suggest the completely ionized form of MSG as well as the all band positions[40]. The medium intense band at 875 cm^{-1} is assigned to the CH$_2$ rocking mode, whereas the medium peak at 858 cm^{-1} is attributed to the COOH deformation modes. On the other hand, the weak and very weak peaks at 774 and 738 cm^{-1}, respectively, correspond to the COO$^-$ bending modes, while the very weak and the medium bands at 633 and 603 cm^{-1} are assigned to the COO$^-$ scissoring and wagging modes, respectively.

Low wavenumber bands are assigned as follows: the band at 530 cm^{-1} to the deformation mode of the C2-C1-O10-H22, the medium band at 499 cm^{-1} to the COO$^-$ rocking and to the NH$_3^+$ torsion modes, and the weak peak at 477 cm^{-1} to the NH$_3^+$ torsion mode. The contributions at 412, 380, 281, 214 cm^{-1} are due to the skeletal deformation modes. Thus, our results are consistent with the presence of a zwitterionic structure of MSG in the solid state.

Raman spectroscopy of MSG solutions

Comparing the Raman spectra of MSG in solution (1M, Fig. Fig. V.6.3.2) with the FT-Raman

spectrum of MSG in the solid state (Fig. V.6.3.1), one can observe a weaker background with the relative intensities of the bands slightly changed. An increased intensity for the symmetrical stretching mode of the COO$^-$ groups (the band at 1407 cm^{-1} in the Raman spectrum of the solution), and a decreased one for the bending modes of CH$_2$ (the peak at 1439 cm^{-1} in the Raman spectrum of the solution). Due to the well–known solvent effect, small blue shifts of the wavenumbers and the broadening of the bands were observed for the corresponding peaks in the Raman spectrum of solution. The main bands of the micro-Raman spectrum of MSG solution were acquired and identified[535].

The band at 1624 cm^{-1} in the FT-Raman spectrum becomes smaller and broader in solution (1620 cm^{-1}) and is due to the asymmetrical COO$^-$Na$^+$ stretching mode. The broadening of the peak at 1620 cm^{-1} is due to the presence of the water[536]. The weak peak at 1571 cm^{-1} in the FT-Raman spectrum of the MSG powder becomes a weak shoulder in the Raman spectrum of solution (1555 cm^{-1}) and is significantly red shifted (16 cm^{-1}), suggesting changes in the electron distribution of the carboxylate group (COO$^-$Na$^+$) and the presence of the zwitterion form of the probe. Other spectra–structure correlations include the strong band at 1341 cm^{-1} and the shoulder at 1317 cm^{-1}, which correspond to the CH$_2$ deformation and twisting modes, respectively. The next bands at 1282 and 1138 cm^{-1} become relatively smaller as compared to the FT-Raman spectrum and are attributed to the CH$_2$ wagging and twisting modes.
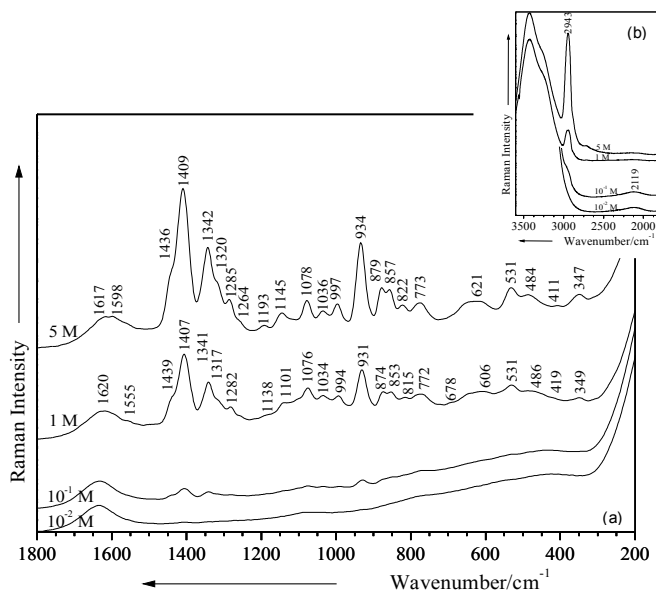
Figure V.6.3.2. Raman spectra of MSG solution at different concentrations in lower (a) and higher (b) wavenumber regions. Excitation: 514 nm, 200 mW.

The medium intense band at 1095 cm^{-1} in the FT-Raman spectrum of the solid state, which is assigned to the CH$_2$ rocking mode, decreases in relative intensity and is 6 cm^{-1} red shifted in the Raman spectrum of the solution (1101 cm^{-1}), while the medium band at 1076 cm^{-1} in the FT-Raman spectrum that corresponds to the NH$_3^+$ rocking mode, increases in relative intensity, becomes broader and has the same position (1076 cm^{-1}) as in the Raman spectrum of the solution. At the same time, the CH$_2$ rocking mode at 1040 cm^{-1} in the FT-Raman spectrum is increased in relative intensity and 6 cm^{-1} red shifted in solution. The C–C stretching modes observed at 1002 and 942 cm^{-1} in the FT-Raman spectrum of the MSG solid state, suggesting the presence of the completely ionized form of MSG[40], merge to a single broad band in

solution (931 cm^{-1}) with the same assignment[537]. The "sensitive" region between 1000 and 700 cm^{-1} is practically representative for all studied amino acids. The wavenumber values are increased by 20-50 cm^{-1} upon protonation of the carboxyl group. Moreover, intermolecular hydrogen bonds can contribute to this spectral change. The bands at 875 and 858 cm^{-1} in the FT-Raman spectrum are less blue shifted with respect to the Raman spectrum of the solution (874 and 853 cm^{-1}), where they were assigned to the CH$_2$ rocking mode, and to the deformation mode of COOH group.

On the other hand, the peak at 633 cm^{-1} in the FT-Raman spectrum disappears in the Raman spectrum of the solution, whereas the band at 603 cm^{-1} becomes weaker, suggesting a COO$^-$ wagging mode. Bands at lower wavenumbers are due to the skeletal bending modes; the positions of the Raman bands occurring below 600 cm^{-1} remain essentially unaffected by protonation of MSG.

As shown in Fig. V.6.3.2b, we can show that the concentration dependent Raman spectra demonstrate the possibility to record high quality Raman spectra of MSG aqueous solution at relatively high concentration levels down to 10^{-2} M. One also observes that by lowering the concentration, the very strong band at 2943 cm^{-1} of the symmetrical CH$_2$ stretching mode, disappears and a new broader band at 2119 cm^{-1} appears; this is attributed to the increased water concentration and its solvent effect. The CH$_2$ stretching mode is more intense in the solid state compared with the situation in solution or at low concentration levels[538].

pH dependent Raman spectra

The pH dependence of Raman spectra of MSG aqueous solutions in the basic and acidic pH range is presented in Figs. V.6.3.3 and V.6.3.4, respectively. The wavenumber of the carbonyl band, between 1700-1750 cm^{-1} (Table V.6.3.1, 1739 cm^{-1} for the FT-Raman spectrum) is found invariable in neutral carboxylic acids, and invariably vanishes on complete ionization of the carboxyl group[536,537].
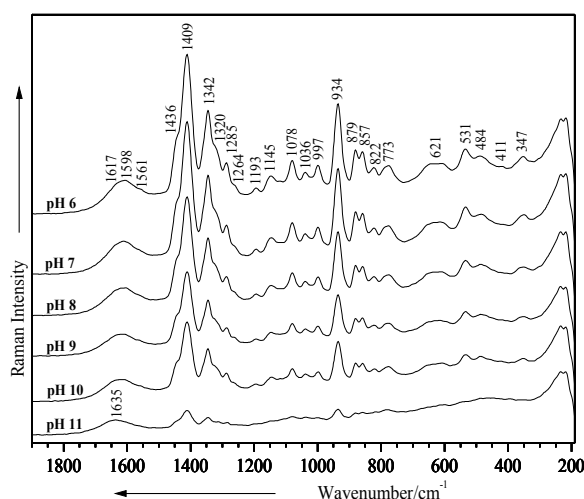
Figure V.6.3.3. Raman spectra of 5 M MSG solution at different basic pH values.
Excitation: 514.5 nm, 200 mW.

The presence of one or more strong Raman bands near 1400 cm^{-1} is apparently characteristic of the ionized carboxyl group. The influence of an adjoining carboxyl group, like that of a charged NH$_3^+$ group, is thus to increase the C=O wavenumber. The effect of ionization is always shown by a great

increase of intensity and a wavenumber shift of one or more bands near 1400 cm^{-1}. In the Raman spectra of MSG at basic pH values a significant broadening of the band at 1635 cm^{-1} is observable, which may be assigned to the asymmetrical COO$^-$ stretching mode (Fig. V.6.3.3, pH 11); the shoulder at 1561 cm^{-1}, attributed to the stretching mode of COO$^-$Na$^+$, disappears with increasing pH. The moderately intense band near 1580 cm^{-1} is specific for ionized carboxylic acids[537].

Furthermore, the band at 1409 cm^{-1} as a contribution of the symmetrical COO$^-$ stretching mode becomes broader and decreases in relative intensity in the basic range, while the shoulder at 1436 cm^{-1} is slightly increased in relative intensity and appears as a weak peak. The bands corresponding to the CH$_2$ deformation modes (1342, 1320, and 1285 cm^{-1}) decrease in relative intensity, whereas the band corresponding to another CH$_2$ deformation mode (1193 cm^{-1}) disappears in the basic pH range. With increasing pH, one can also observe first a broadening and then the disappearance of the CH$_2$ twisting mode (1145 cm^{-1}), by comparing it to the adjacent bands (1078, 1036 cm^{-1}) assigned to the rocking modes of NH$_3^+$ and CH$_2$, which remain approximately constant in relative intensity in the basic pH range (Fig. V.6.3.3). The band at 997 cm^{-1} (Fig. V.6.3.3, at pH 6 to 10) is slightly decreased in relative intensity; it is attributed to the completely ionized form of MSG and it becomes weaker with increasing pH until it disappears at pH 11. The strong band at 934 cm^{-1}, which corresponds to the completely ionized form of MSG, is slightly decreased in intensity and broader in the basic pH range. In general, all bands, due to the ionized form of MSG become weaker or even disappear; this already suggests deprotonation of MSG in the basic pH range.
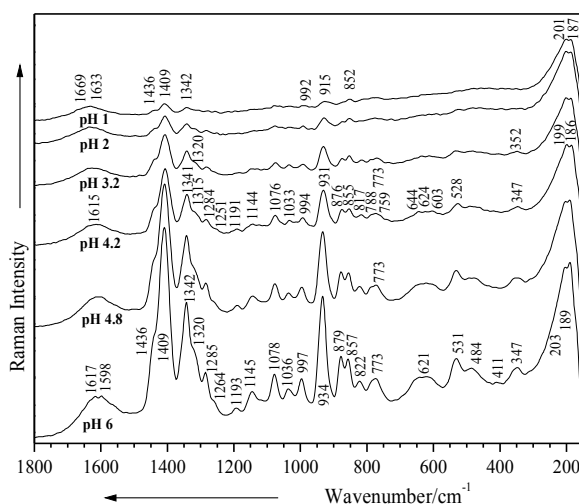
Figure V.6.3.4. Raman spectra of 5 M MSG solution at different acidic pH values.
Excitation: 514.5 nm, 200 mW.

Comparing Figs. V.6.3.3 and V.6.3.4, the Raman spectra of MSG solutions remain mainly unchanged in the pH range from 6 to 3. Small differences can be observed in the 1800-1400 cm^{-1} wavenumber region at pH 2, whereas at pH 1 a broad, unresolved signal was observed. Moreover in the 1500-1650 cm^{-1} region more bands appear at low pH compared with the basic pH range. One can perceive that the asymmetrical stretching mode of NH$_3^+$ group is represented by two weak peaks on going to acidic

pH values (1669 and 1633 cm^{-1}) (Fig. V.6.3.4). The band at 1078 cm^{-1} that corresponds to the NH$_3^+$ rocking mode, becomes broader and decreases in relative intensity in the acidic pH range, whereas the bands, which are due to the completely ionized form of MSG are shifted to lower wavenumbers (992 and 915 cm^{-1} at pH1). On the other hand, the band at 773 cm^{-1} at pH 6 (Fig. V.6.3.4) is split in the acidic range in three weak peaks, which are due to the COO$^-$ deformation modes. In the low wavenumber region, the band at 347 cm^{-1} is changed in shape, relative intensity and is 5 cm^{-1} shifted to higher wavenumbers (352 cm^{-1} at pH 3.2, (Fig. V.6.3.4)), and may be due to the COO$^-$Na$^+$ rocking mode and NH$_3^+$ torsion mode. The total pairwise interaction energy between Na$^+$ and glutamate is attractive and one can expect a dominant Coulombian interaction[539].

Thus, the fully protonated MSG molecule predominates at low pH values. Finally, taking into account the major changes in the band shape attributed to both NH$_3^+$ and COO$^-$ Raman bands at acidic pH values, a protonation of the NH$_2$ group is very likely.

SERS spectra of MSG

A SERS spectrum of MSG (9.9 10^{-4} M) is presented in Fig. V.6.3.5 in comparison with the Raman spectrum of the bulk solution (1 M) at pH 6. Large differences in band positions and relative intensities are observed, allowing the presumption of a chemisorbed species. The negatively charged food additive was expected to preserve the aggregation status and hence the Ag surface potential[324]. The significant SERS signal of MSG molecule was observed at micromolar concentration range, where a reorientation of the structure on the Ag colloidal particles is possible. Since the SERS signal is concentration sensitive, in order to discuss the behavior in adsorption of the MSG on the silver particles, the SERS spectrum at micromole concentration was chosen here for the adsorption geometry proposal.

Theoretically, MSG can interact with the Ag colloidal surface *via* several functional groups. The negative charge of the COO$^-$ moiety, however, leads to a Coulombian repulsion[539,540] due to the negative potential of the Ag surface. After considering the steric configuration of the structure, several other potential geometries for chemisorption still remain. One possibility for MSG to chemisorb is provided by the presence of the lone pair nitrogen atom N6 of the NH$_2$ group (Fig. V.6.1.1). In this case, according to the surface selection rules[108], the stretching modes of the NH$_2$ group are expected to be enhanced. The observed bands in the SERS spectrum (Fig. V.6.3.5) support this consideration. More specifically, the very intense band at 1393 cm^{-1} (red shifted relative to the position of 1407 cm^{-1} in the Raman spectrum) assigned to the NH$_3^+$ asymmetrical stretching mode is preponderant due to the NH$_2$ group that is now in a close vicinity of the Ag particles with a perpendicular orientation of the skeleton ring (Fig. V.6.3.5c). Moreover, the medium band observed in the SERS spectrum at 1643 cm^{-1} (absent in the Raman spectrum of the solution) is due to the asymmetrical bending mode of the NH$_3^+$ group.

The shoulder at 1555 cm^{-1} in the Raman spectrum of the solution is considerably blue shifted (20 cm^{-1}) in the SERS spectrum (1575 cm^{-1}), increased in relative intensity, and can be due to the C5OO$^-$Na$^+$ stretching mode. Besides, this interaction generates the presence of the C5OO$^-$ functional group, negatively charged, to bend near the surface, along the C4-C5 bond. This contribution is supported by the disappearance of the bands at 1341 and 1317 cm^{-1}, by the increase in relative intensity of the band at 1284

cm^{-1}, which was attributed to the wagging mode of the CH$_2$ group, and by the appearance of the weak band at 1229 cm^{-1} that can correspond to the stretching mode of C-O bond belongs to the carboxylate group (Fig. V.6.3.5b, Table V.6.3.1). The appearance of the weak peak at 1127 cm^{-1} is due to the NH$_3^+$ rocking mode, whereas the medium strong band at 1076 cm^{-1} in the Raman spectrum of the solution disappears in the SERS spectrum. The significantly enhanced bands at 1012, 975, 928 cm^{-1} are due to the completely ionized form of MSG, which is perpendicularly adsorbed *via* the amino group. The new band shape at 904 cm^{-1} is due to the C1-C2-N6 stretching mode. Other bands with medium or weak intensities in the SERS spectrum are attributed to various bending modes.

The very intense band at 223 cm^{-1} is assigned to the Ag-N stretching mode. The interaction of the metals with amino acids can occur *via* two different orientations when binding to the carboxylate anion: unidentate and bidentate[541]. In general, the Ag$^+$ affinity of an amino acid depends to a large extent on the interaction of the Ag$^+$ ion with the side chain. This interaction is dictated by two factors: the intrinsic Lewis acid strength of the substituent and the amount of steric strain introduced by forming the rings[494]. Alkyl groups stabilize positive charges inductively and not by direct coordination. This results in small increases in Ag$^+$ affinities, with the stabilization increasing with the size of the alkyl group. The MSG molecule binds to the silver colloidal surface through the lone pair electrons of the nitrogen atom and the oxygen of the carboxyl group (Fig. V.6.3.5c). This assumption is supported by the Ag-O[494] and Ag-N[496] stretching modes, which can be detected at 223 and 350 cm^{-1}, respectively.
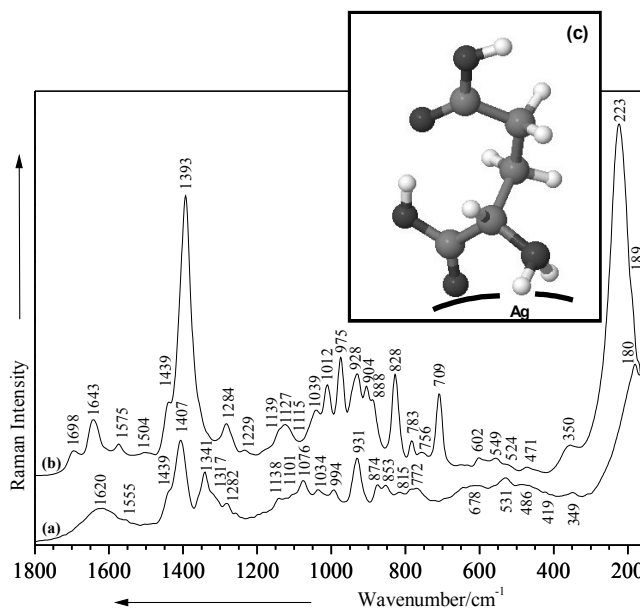
Figure V.6.3.5. Comparison between Raman (a) and SERS (b) spectra of MSG (pH 6), and its proposed orientation on the silver surface (c). Excitation: 514.5 nm, 200 mW.

Looking at the concentration dependent SERS spectra of MSG (Fig. V.6.3.6a), considerable changes in the SERS signal, can be observed beginning with a concentration of 1.7 10^{-4} M. The shoulder at 1439 cm^{-1}, which is due to the CH$_2$ bending mode, becomes weaker and disappears at lower concentration, while the very strong band at 1393 cm^{-1}, attributed to the symmetrical COO$^-$ stretching

mode, remains at the same position on going to the lower concentration and becomes broader. The signal at 1284 cm^{-1} is slightly increased in relative intensity and can be due to the of CH$_2$ wagging mode, whereas the weak peak at 1229 cm^{-1}, attributed to the C-O stretching mode, decreases in relative intensity till disappearance in the lower concentration range. Moreover, a new weak band can be observed at 1176 cm^{-1} (Fig. V.6.3.6a) that can be assigned to the CH$_2$ deformation mode, while the two neighboring shoulders (1139 and 1115 cm^{-1}) of the weak peak at 1127 cm^{-1} disappear on going to the lower concentrations and one weak band at 1129 cm^{-1}, corresponding to the NH$_2$ twisting and the NH$_3^+$ rocking mode, can be observed. Therefore, the weak signal at 1039 cm^{-1} is slightly red shifted (8 cm^{-1}) and becomes a shoulder in the lower concentrations range (Fig. V.6.3.6a).

Two of the bands corresponding to the completely ionized form of MSG increase in relative intensities (1012, 931 cm^{-1}), while the middle one (975 cm^{-1}) decreases in relative intensity. The next bands are changed as follows: the medium peak at 904 cm^{-1} disappears beginning with the concentration of 1.7x10^{-4} M; the medium signal at 888 cm^{-1} becomes a shoulder, which is 4 cm^{-1} red shifted and can be due to the CH$_2$ rocking mode; the medium strong band at 828 cm^{-1} corresponding to the CO and NH deformation modes, decreases in relative intensity while going to the lower concentration.

Taking into account these changes in the micromolar concentration range, we can suppose a reorientation of the MSG on the silver surface through the lone pair electrons of the nitrogen atom and the O$^-$ of the other carboxyl group in a flat orientation (Fig. V.6.3.6b). This assumption is emphasized by the Ag-O[494] and Ag-N[496] stretching modes, which can be observed at 213 and 278 cm^{-1}, respectively.
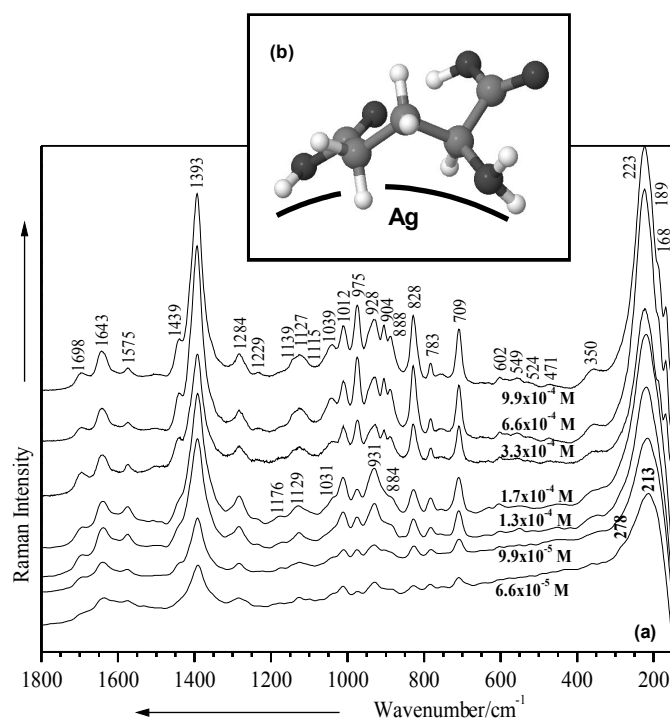
Figure V.6.3.6. SERS spectra of MSG at different concentrations (a) and its proposed orientation in the lower concentrations range (b). Excitation: 514.5 nm, 200 mW.

pH dependent SERS spectra

The pH dependent SERS spectra of MSG in the basic range are presented in Fig. 8. The weak peak at 1698 cm^{-1} that can be due to the carbonyl stretching mode (Table V.6.3.1, Fig. V.6.3.7) confirms the presence of the unionized form of the molecule[536,537], and invariably vanishes on complete ionization of the carboxyl group.

This weak peak becomes a shoulder (pH 9), and can contribute to demonstrate the MSG molecule deprotonation. The next medium band at 1643 cm^{-1}, which is due to the asymmetrical bending mode of the NH$_3^+$ group, increases in relative intensity on going to basic pH values, as well as the weak band at 1575 cm^{-1}, which was attributed to the COO$^-$Na$^+$ stretching mode. The strong band at 1393 cm^{-1} is also increased in relative intensity at basic pH and can be due to the symmetrical COO$^-$ stretching mode, while the weak shoulder at 1441 cm^{-1} is slightly red shifted and becomes smaller (1436 cm^{-1} at pH 11, Fig. V.6.3.7). The weak band at 1284 cm^{-1}, which increases in relative intensity in the basic pH range is assigned to the CH$_2$ wagging mode, while the very weak peak at 1234 cm^{-1} at pH 6 becomes more intense at pH 11 and corresponds to the C-O stretching and OH bending modes. The presence of the weak band at 1127 cm^{-1} at pH 6 that corresponds to the NH$_3^+$ rocking mode is changed beginning with pH 9, where it becomes smaller and two new shoulders at 1175 and 1113 cm^{-1}, which can be due to the CH$_2$ deformation modes, appear beginning with pH 9 and 11, respectively; the profiles and relative intensities of the bands at 1011, 975, and 929 cm^{-1} are changed, suggesting the deprotonation of the molecule.
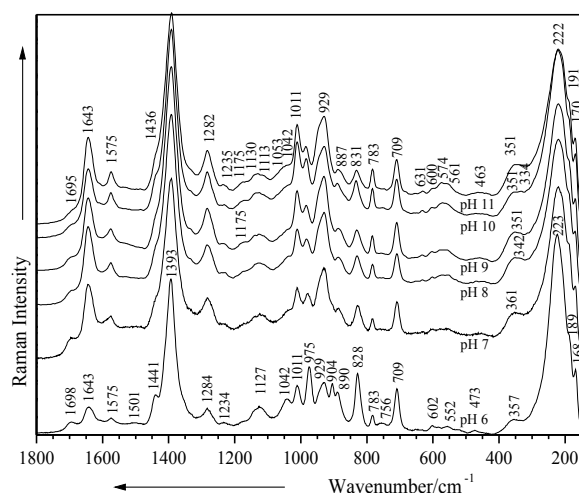
Figure V.6.3.7. SERS spectra of MSG at different basic pH values.
Excitation: 514.5 nm, 200 mW.

In the SERS spectrum of MSG at pH 7, one can observe the disappearance of the signal at 904 cm^{-1}, which may be assigned to the asymmetrical C-C-N stretching mode (Fig. V.6.3.7); the weak peak at 890 cm^{-1} attributed to the rocking mode of the CH$_2$ becomes broader and weaker with increasing pH. The very intense band at 828 cm^{-1} (Fig. V.6.3.7, pH 6) can be specific for the ionized MSG form[495,496]. Furthermore, this band, as a contribution of C-O and N-H deformation modes, becomes broader and decreases in relative intensity in the basic range (see Fig. V.6.3.7, pH11), while the weak band at 783 cm^{-1} is slightly increased in relative intensity and unshifted.

The strong band at 709 cm^{-1}, which corresponds to the COO$^-$ deformation mode and to the ionized form of the MSG is less decreased in relative intensity in the basic pH range. Another intense band from the Raman spectra of the solution in the basic pH range remains the band at 223 cm^{-1}, which corresponds to the carboxyl torsion mode and to the Ag-O stretching mode[495,496]; in contrast, the weak band at 350 cm^{-1} that corresponds to the Ag-N stretching mode becomes a shoulder.

As an outcome of this analysis, we conclude that the deprotonated form of MSG exists in the basic pH range and that the orientation of the molecule is as in the micromolar concentration range (Fig. V.6.3.6b).

Adding HCl solution, the only observable band occurs at 239 cm^{-1} (spectrum not shown), which can be due to the Ag-Cl stretching mode. Finally, taking into account the absence of the Raman signal, we can deduce that in the acidic range the molecule cannot be adsorbed on the silver surface.

V.6.4 Conclusions

Raman and SERS spectra of MSG were recorded at different concentrations. This study may serve as a reference for further Raman spectroscopic applications in trace analysis of food products.

The geometry of MSG was computed and optimized for the first time with the BPW91/6-311++G**, BPW91/LANL2DZ, B3LYP/6-311++G**, and B3LYP/LANL2DZ methods. We demonstrated that both forms of MSG possess different geometries that can be explained by the molecule protonation possibilities. The results from the FT-Raman spectrum are consistent with the zwitterionic structure of MSG in the solid state.

Analyzing the Raman spectra of the solutions could evidence two changes in the molecular identity of MSG on going from basic to acidic pH values. The quantitatively protonated form of MSG dominates at low pH values.

SERS spectra of MSG were recorded even at very low concentrations down to 10^{-5} M. A strong chemical interaction of MSG with the colloidal particles was observed, involving an adsorption *via* the lone pairs of the nitrogen atom and the oxygen atoms of the carboxyl group. The surface selection rules along with our theoretical results are subject to explain the adsorbate structure on the metal surface at different concentrations and pH values.

The above mentioned work has been the result of a collaboration with **Lect. Dr. N. Leopold** and **MSc. C. Lehene** from Babes-Bolyai University, Cluj-Napoca, Romania.

Table V.6.3.1. Selected calculated and experimental Raman and SERS wavenumbers (cm^{-1}) of MSG and their tentative assignment.

FT-Raman	Calcd.				Raman solution	SERS	Vibrational assignment
	B3PW91		B3LYP				
	LANL2DZ	6-311++G**	LANL2DZ	6-311++G**			
3399 vw							ν_{asym} (N-H)
3265 sh					3254 sh		ν (N-H)
3183 sh							ν_{sym} (N-H)
3121 w	3114	3127	3132	3113			ν_{asym} (NH$_3^+$)
3050 vw							ν (OH)[5]
2971 vvs							ν_{asym} (CH$_2$)
2936 vs					2943 vs	2932 s	ν_{sym} (CH$_2$)
2889 vs							ν (CH$_2$)
2627 w							ν_{sym} (NH$_3^+$)
1739 vvw						1698 w	ν (C=O) hydrogen bonded
1682 vw	1699	1679	1682	1683			δ (HOH); ν (C=O)
1637 w						1643 w/m	δ_{asym} (NH$_3^+$)
1624 w					1620 m		ν_{asym} (COO$^-$)
1604 w		1613		1608			NH$_3^+$ def.
1571 w	1597		1588		1555 sh	1575 w	ν (COO$^-$Na$^+$)
1535 vw							τ (CH$_2$)
1521 vw	1522		1521			1504 vw	δ_{sym} (NH$_3^+$)
1434 ms	1424	1421	1418	1421	1439 sh	1439 sh	δ (CH$_2$)
1401 ms	1400	1383	1397	1386	1407 vs	1393 vs	ν_{sym} (COO$^-$)
1355 m	1363/1366	1367	1355/1361	1353/1359			ω (CH$_2$)
1340 m	1344	1355	1335	1335	1341 s		CH$_2$ def.
1316 m	1326	1338	1321	1313	1317 sh		τ (CH$_2$)
1291 sh							τ (CH$_2$)
1282 m	1283	1308	1281	1276	1282 m	1284 w/m	ω (CH$_2$)
1259 vw	1279	1272	1275	1259			ω (CH$_2$)
1248 vw		1249					ν (C-N)
1225 vw		1214		1211		1229 vw	ν (C-O); δ (OH)
1191 w	1195		1192				CH$_2$ def.
1160 m	1181	1180	1163	1166			CH$_2$ def.
1142 m		1150		1133	1138 sh	1139 sh	τ (CH$_2$)
1122 w/m	1118	1120	1110	1118		1127 w	τ (NH$_2$), ρ (NH$_3^+$)
1095 m	1090		1097		1101 sh	1115 sh	ρ (CH$_2$)
1076 m		1072	1076		1076 ms		ρ (NH$_3^+$); ν (C-N)
1054 m				1058			ρ (CH$_2$); ν (CC)
1040 w	1044		1038		1034 m	1039 w	ρ (CH$_2$)
1002 m		1022		1021	994 m	1012 m	Completely ionized form
942 ms	967	958	955	949		975 ms	Completely ionized form; ν (M=O); COO$^-$ def.
926 sh				931	931 s	928 m	Completely ionized form
	915		904			904 m	ν (C-C-N)
875 m		888		880	874 m	888 m	ρ (CH$_2$)
858 m	863		860		853 m		ν (O-O); COOH def.

810 w	840	849	828	839	815 w	828 ms	(CO) def.; (N-H) def.
793 w	809	788	805	790		783 w/m	δ (NH$_2$)
774 w	759	776	753	773	772 m	756 vw	(COO$^-$) def.
738 vw		705		703			δ (COO$^-$)
662 m	684	676	672	673	678 w	709 ms	ν_{asym} [O-Ag-O]
633 vw	632/647	623	628/641	620			COO$^-$ sciss.
603 m	599	611	596	608	606 w	602 vw	ω (COO$^-$)
530 m	555	560	551	551	531 m	549 vw	(HOCC) def.
499 m	521	517	519	516		524 vw	ρ (COO$^-$), τ (NH$_3^+$)
477 w					486 w	471 vw	τ (NH$_3^+$); ν (Ag-N)
438 vw	452	441	450	439			δ (OH, CH)
427 vw	430		427				δ (OH, CH)
412 vw					419 vw		τ (skel.)
380 vw	386	397	387	398			δ (skel.)
356 w	365	378	361	376	349 vw	350 w	ν (COO$^-$Ag$^+$), ν (Ag-NH$_2$)
304 w	305	305	305	305			skel. def.
281 w	256	255	256	296			δ (skel.)
214 sh	232	232	232	233		223 vvs	δ (skel.); Ag-O
174 ms	170/189	169	173	174	180 vvs	189 sh	τ (COO$^-$)
152 ms		153		156		168 ms	ν (O-Ag-O)

Abbreviation: vw – very weak; w – weak; m – medium; ms – medium strong; s – strong; vs – very strong; sh – shoulder; υ - stretching; δ - bending; ρ – rocking; τ – twisting; ω – wagging; sciss. – scissoring; skel. – skeletal; sym – symmetric; asym – asymmetric; def. – deformation.

Chapter VI

Medicines monitored by Raman and surface-enhanced Raman spectroscopy

---

"Medicine makes people ill, mathematics makes them sad,
and technology makes them sinful."
(Martin Luther, German Priest 1483-1546)

"By medicine life may be prolonged, yet death will seize the
doctor too."
(William Shakespeare 1564-1616)

VI.1 Anti-inflammatory drugs: what are they for?

Non-steroidal anti-inflammatory drugs are drugs with analgesic, antipyretic and anti-inflammatory effects. Consequently, they reduce pain, fever and inflammation. The most popular members of this group of drugs are aspirin and paracetamol.

They work by blocking the production of chemicals in the body known as *prostaglandins*. These chemicals are produced as a normal body function and are involved in pain transmission, inflammation and tissue damage.

VI.1.1 Aspirin

Aspirin, pharmaceutically available in two forms, buffered and unbuffered, was found to be detectable by the micro-Raman spectroscopy of the tablet, in spite of the different excipients, which are used in drugs preparation. A strong chemical interaction of the both aspirin species with the silver colloidal particles was observed at micromole concentrations. Different adsorption behaviors of these molecular species are discussed.

Introduction

Aspirin, as well as related derivatives of salicylic acid belongs to the analgesics class, being frequently used on top of non-steroidal anti-inflammatory drugs. Belonging to the peripheral analgesics class, aspirin like other non-steroidal anti-inflammatory drugs acts for reducing inflammation caused by injury or arthritis. Aspirin presents low acidity (pKa 3) and by oral administrating, almost all salicylate is found in the unionized form in the stomach[542]. This is poorly soluble in the acid media of the stomach and the precipitate products concentrate, thereby delaying its absorption up to 24 hours. However, aspirin absorption following overdose commonly occurs more slowly in the blood concentrations, which continue to rise for up to 24 hours after ingestion[543]. Absorption of salicylate can be further delayed if an enteric-coated preparation has been ingested[544].

In spite of its largely pharmaceutical and medical interest, the spectroscopic data available are limited to recent theoretical and experimental IR and Raman data[545], where the differences between the calculated and experimental wavenumbers are partly due to anharmonicity and to the intermolecular interactions and also correlation effects[545]. In addition, previous IR and *ab initio* studies were reported by Binev et al.[546], and the interaction of aspirin with RNA[547] or DNA[548] was studied using FTIR and laser Raman difference spectroscopy, respectively.

The potential polymorph of aspirin were also reported[549], an exploration of the potential conformers being presented. Further, a direct assay and monitoring of aspirin tablets using Raman spectroscopy was reported[550]. As a basis for assaying aspirin and analysis of the major degradation products, salicylic acid, the Raman technique was highlighted being feasible[550].

Moreover, the Raman and SERS spectra of aspirin were reported[551], where the adsorption was promoted by mixing aspirin/chloroform solution with silver sol. It was supposed that the aspirin species,

like salicylic acid, adsorbs on silver particles via the carboxylate group. Having a larger substitution group than salicylic acid, at the ortho-position of carboxylate group, the surface adsorption was qualitatively appreciated as being not as easy as for the salicylic acid[551].

In the present study, we report the vibrational Raman characterization of buffered (ASA) and unbuffered aspirin (ANT) in order to get insight into their adsorption behavior on a given surface, and to check the possibility to monitor the both pharmaceutical species using SERS spectroscopy.

Results and discussions

The vibrational fundamentals from the micro-Raman spectra, presented in the Fig. VI.1.1.1 for unbuffered and buffered aspirin were analyzed by comparing the experimental vibrational modes with the previous published Raman data[545-551]. Comparing micro-Raman spectra of ASA and ANT (Fig. VI.1.1.1), we can observe many differences in band position and relative intensities.
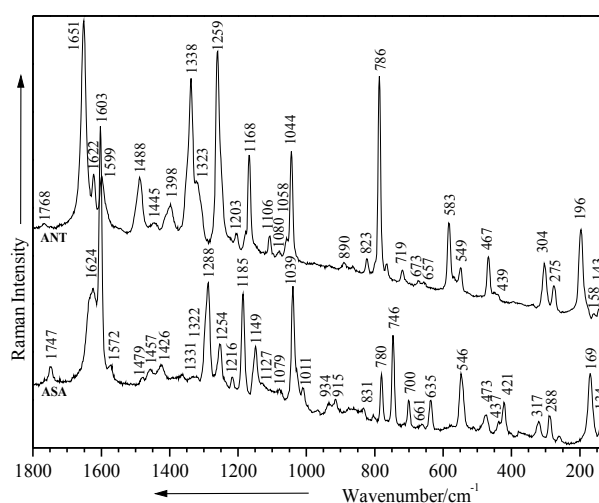
Figure VI.1.1.1. Micro-Raman spectra of ASA and ANT. (Excitation 514.5 nm, 150 mW).

Our Raman spectrum of ASA species is very similar with that reported by Wang et. al.[551]. Moreover, this similarity was found also by comparison with the Raman spectrum of pure aspirin from Sigma Aldrich (spectrum not given here). Distinctly from ASA, strong bands were observed for ANT at 1651, 1488, 1338, and 583 cm^{-1}, whereas other bands from ASA (1288, 1185, 1149, 746 cm^{-1}) are absent in the spectrum of ANT. Rather similar behavior of the υ(C=O) at 1622-1624 cm^{-1} was observed for both species, whereas the υ_s(COO$^-$) spectral region is very different. According to the literature[40], the characteristic υ_s(COO$^-$) mode could be present in the 1380-1420 cm^{-1} spectral range, whereas the asymmetric mode of the COO$^-$ could exhibit a weak Raman band in the 1561-1552 cm^{-1} spectral range. Taking a closer examination of these spectral regions, one can observe weak to medium different bands in the spectra of ANT and ASA. These differences could be tentatively explained by the presence of the buffering agent, responsible for the given acidity of the species.

They could be also responsible for the supplementary observed bands of ASA (1288, 1185 and 1149 cm^{-1}). Further on, the deformation modes of the COO$^-$ group were also found at different positions (786 and 780 cm^{-1} for ANT and ASA, respectively). The ester C=O stretching mode was observed in both

species at 1747 cm^{-1} for ASA and 1768 cm^{-1} for ANT, respectively.

On passing from Raman to SERS spectra of each corresponding species, large differences in band positions and relative intensities can be observed (Fig. VI.1.1.2), allowing the supposition of chemisorbed species[552].

The strongest SERS bands of ANT are observed at 1387, 1635, 1262, 825, and 239 cm^{-1}, whereas for the ASA, the main bands are located at 1614, 1367, 1302, 1239, 1026, 802, and 218 cm^{-1}, respectively. According to the surface selection rules[108] the vibrational modes that are preponderantly enhanced should have such an orientation on the metal surface for which the polarizability Raman tensor component has a perpendicular orientation with respect to the surface. Based on the previous Raman assignments the bands at 1387 cm^{-1} (for ANT) and at 1367 cm^{-1} (for ASA) are due to the enhanced symmetrical stretching mode of COO$^-$ group.
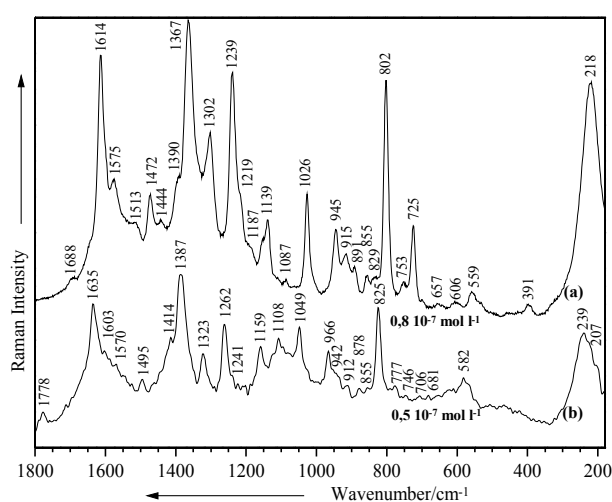
Figure VI.1.1.2. SERS spectra of ASA (a) and ANT (b). (Excitation: 514.5 nm, 200 mW).

Moreover the close presence of this group with respect to the surface provides the specific enhancement of the C=O mode observed at 1635 cm^{-1} (for ANT) and 1614 cm^{-1} (for ASA), respectively, both of them being shifted from their Raman corresponding positions due to the interaction with the metal surface. However the manner of interaction seems to be different since in the low wavenumber spectral region different strong bands assigned to ASA-Ag and ANT-Ag modes were observed in both cases. These differences suggest a double interaction in the case of ANT through both C=O functional groups, one from the carboxylate and the other from the ester, whereas in the case of ASA an interaction through only one of these functional would be more probable since only one well resolved band was observed at 218 cm^{-1} (Fig VI.1.1.2a), assigned to the Ag-O stretching mode[345]. This supposition was further confirmed by the presence of the 1778 cm^{-1} SERS band of ANT.

Conclusions

The Raman spectra of the different aspirin tablets can be employed for differentiating the buffered and unbuffered pharmaceutical species.

The two distinct species of aspirin, buffered and unbuffered were found to be slightly different

chemisorbed on the silver surface. At the present stage of the work both pharmaceutical compounds, buffered and unbuffered aspirin, could be detected from powder tablets up to micromolar level.

VI.1.2 Paracetamol

The commercial normal and sinus paracetamol drugs were investigated with Raman spectroscopies to stand out the presence of monoclinic and orthorhombic forms of paracetamol in the solid state, in aqueous solution, and on the glass surfaces after recrystallization.

In the SERS experiments on island film surfaces with different roughnesses, a strong chemical interaction of paracetamol on them is observed at concentration of $8x10^{-2}$ M. Because of the enhancement of selected Raman bands, we propose that the paracetamol binds to the silver metallic surfaces through the lone pair electrons of nitrogen and oxygen atoms of the amide group and π electrons of the phenyl rings in a flat orientation.

Introduction

Paracetamol (N-acetyl-p-aminophenol, 4-hydroxyacetanilide) is a long-established pharmaceutical with analgesic, antipyretic, and weak anti-inflammatory activities[553,554]. The biological activity and the pharmaceutical properties of drugs are strongly dependent on their structure. Upon overdosing, the paracetamol can cause hepatic necrosis in humans and experimental animals[555,556]. Furthermore, it is known that alcohol may predispose to liver damage caused by therapeutic doses of paracetamol[557]. Because of these toxic side effects, the paracetamol has been subject to many toxicological studies[558,559]. Previous studies have shown that long-term, daily use of paracetamol is associated independently with an increased risk of renal disease[560] and causes an immediate and highly specific inhibition of replicative DNA synthesis[561].

Paracetamol can crystallize in three different polymorphic forms known as form I, II, and III[562-567]. The monoclinic form (form I) is the normal commercial form[568,569], the form II was identified by recrystallization from an ethanolic solution and corresponds to an orthorhombic form[569,570], and the form III was mentioned as a very unstable form[562-566], which cannot be studied due to its instability. The metastable polimorphs of paracetamol are of particular industrial interest because the commercial form I requires binders for tablet formation[571,572]. The form I of paracetamol is stable at ambient temperature and pressure[573,574], while the orthorhombic form of paracetamol is suitable for direct compression tableting and may also be slightly more soluble and may crystallize only in small quantities[569,575-577].

The consideration of excipients generally regarded as "inert" substances employed to prepare drug products with suitable technological and biopharmaceutical features has been gradually changed to a more adequate concept of physically, chemically, and also biopharmaceutically "active" components. The paracetamol tablets contain some excipients, which can differ from country to country and from type to type of paracetamol tablets. As previously described[567,578], the most employed excipient in the paracetamol processing are: maize starch, avicel, cellulose, magnesium stearate, potassium sorbate, stearic acid, sodium bicarbonate, and talc. The risks for bioinequivalence caused by excipients are reflected in the absorption rate, differences between brands and test formulations, as in the case of the tablets containing

high amounts of sodium bicarbonate.

Numerous IR[579-595] and Raman[565,566,596-602] studies are already recorded in order to characterize and identify the three metastable forms of paracetamol, the transition between them, and the comparison between tablets and solutions.

In the present work, we propose the vibrational Raman characterization of two different commercial paracetamol tablets (normal and sinus), in order to distinguish the various action mode in terms of pH value, the adsorption manner to the silver metallic surfaces, and to check the possibility to monitor the both pharmaceutical species using SERS spectroscopy.

FT-Raman and Raman spectra of the paracetamol tablets

The vibrational fundamentals from the FT- and micro-Raman spectra, presented in Fig. VI.1.2.1, were analyzed by comparing these vibrational modes with those from the literature[565-602]. The optimized geometry of paracetamol is presented in Fig. VI.1.2.2a.
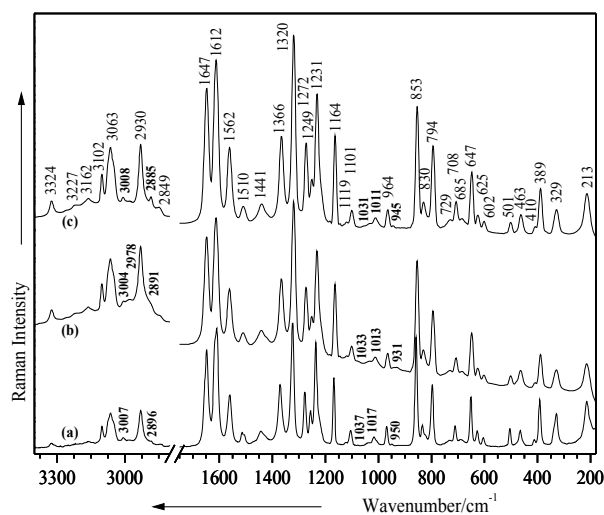
Figure VI.1.2.1. FT-Raman (a) and micro-Raman (b,c) spectra of normal (a,b) and sinus (c) tablets of paracetamol. Excitation: 1064 nm, 390 mW (a); 514.5 nm, 100 mW (b,c).

The FT- and micro-Raman spectra of both types of paracetamol tablets (Fig. VI.1.2.1), exhibit in general the same band positions and relative intensities with minor differences regarding some band shiftings. Furthermore the peaks at 1562 and 1510 cm^{-1} were assigned to the C-N amide stretching modes, while the bands at 1612 and 1441 cm^{-1} were attributed to the C-C aromatic stretching modes. These bands together with their assignment are specific for the monoclinic form I of the paracetamol[579,580,602]. For this form some particular peaks are present at 1231, 794, and 708 cm^{-1}, peaks which correspond to the phenyl-N stretching mode, to the out of plane deformation mode of p-substituted aromatic system, and to the out of plane CN-H and phenyl deformation modes, respectively[579,589,598,603]. Other characteristic frequencies of the form I of paracetamol, which can be seen in the FT- and micro-Raman spectra of the solid state, are the medium band at 1272 cm^{-1}, which was assigned to the C-O stretching mode[584,601] and the weak medium peak at 463 cm^{-1} that can be attributed to the skeletal bending mode[579].

For the quantitative determination, the peak at 463 cm^{-1} is typical of the monoclinic form of

paracetamol because of its medium relative intensity, while in the case of orthorhombic form this is only a shoulder[598]. Different polymorphs of the same molecule have different molecular structures and hence unique Raman spectra. Form I of paracetamol has Raman bands at 1272, 1231, 708, 463, and 213 cm^{-1}, which are not present in the spectrum of the form II. On the other hand, the spectrum of the form II exhibits bands at 1185, 454, and 201 cm^{-1}, which are not present in the spectrum of the form I[566]. Taking into account all these characteristic Raman bands, we can figure out the presence of the monoclinic form in both, normal and sinus, paracetamol tablets. When one tablet of each paracetamol type was dissolved in 10 ml distilled water and after that one drop of the solution was left to dry on the glass, the paracetamol recrystallizes (Fig. VI.1.2.2b,c) and the Raman spectra of both paracetamol forms look quite different (Fig. VI.1.2.3a,b). The weak medium peak detected at 3324 cm^{-1} in the solid state is now slightly shifted at 3325 cm^{-1} for the normal paracetamol, and at 3323 cm^{-1} for the paracetamol sinus. This weak difference (1 cm^{-1}) is enough to assert, that the band at 3325 cm^{-1} is specific to the orthorhombic form of the paracetamol[596]. In the same case, the bands at 1559, 1099, 725, and 622 cm^{-1} (Fig. VI.1.2.3a) are typical for the orthorhombic form of paracetamol, whereas the peaks at 1562, 1101, 730, and 623 cm^{-1} (Fig VI.1.2.3b) are more specific for the monoclinic form of the paracetamol[589,596]. Other remaining bands of the spectra are, as previously discussed, attributed to the monoclinic form of the paracetamol. In this case, one can assume that after recrystallization, the normal paracetamol includes a mixture between monoclinic and orthorhombic forms.
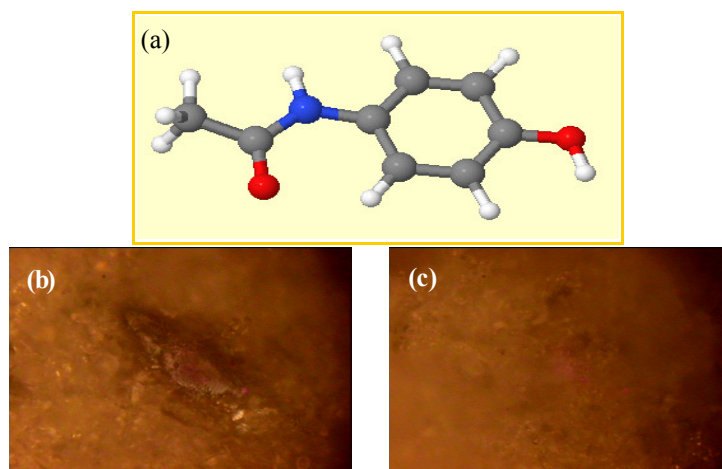
Figure VI.1.2.2. B3LYP/6-31+G* optimized geometry of the paracetamol (a); microscopical images of its normal (b) and sinus (c) commercial types (1 tablet dissolved in 10 ml distilled water) after drying on the glass surfaces.

Apart from the active ingredient, 4-hydroxyacetanilide, the paracetamol contains other inactive substances generically entitled, "excipients"[604,605]. The paracetamol tablet is an active substance (4-hydroxyacetanilide) mixed with binders powders and pressed into a tablet form. Normally, an inactive ingredient denominated "binder" is added to help hold the tablet together and give it strength. The common ones including lactose powder, maize starch, and microcrystalline cellulose. Starch is also generally used as an ingredient that dissolves readily in water to help the tablet disperse once swallowed. In this case, the maize starch is an excellent disintegrant[604]. Small amounts of lubricants are usually added, as well. The most common lubricants are the stearic acid and the magnesium stearate[605]. They help the tablets, once pressed, to be more easily ejected out of the matrix. The inactive ingredients can give

additional Raman bands or can amplify and/or shift some bands from the drug spectra.

Looking at the Raman spectra of normal and sinus paracetamol on the glass surfaces after recrystallization (Fig. VI.1.2.3), one can observe the enhancement of some bands in comparison with the Raman spectra of the tablets, where the Raman signal seems to be quite similar between both types of paracetamol. The enhancement of the band at 2883 cm^{-1} (paracetamol sinus, Fig. VI.1.2.3b) can be due to the presence of the cellulose, lactose, talc, stearic acid, and magnesiun stearate, which normally have very strong bands in the 2870-2895 cm^{-1} spectral range[63-71]. The peaks at 708 and 388 cm^{-1} from the same spectrum, (Fig. VI.1.2.3b) increase in relative intensity compared to the spectrum of the normal paracetamol (Fig. VI.1.2.3a) and to the spectra of the tablets (Fig. VI.1.2.1). These increases can be produced as a result of lactose, which has strong peaks in the range of 864-698 cm^{-1} and 357-377 cm^{-1}, because of the cellulose that presents substantial bands around 382 cm^{-1}, and because of the maize starch, which gives a superior band near to 360 cm^{-1} [604,607-611].
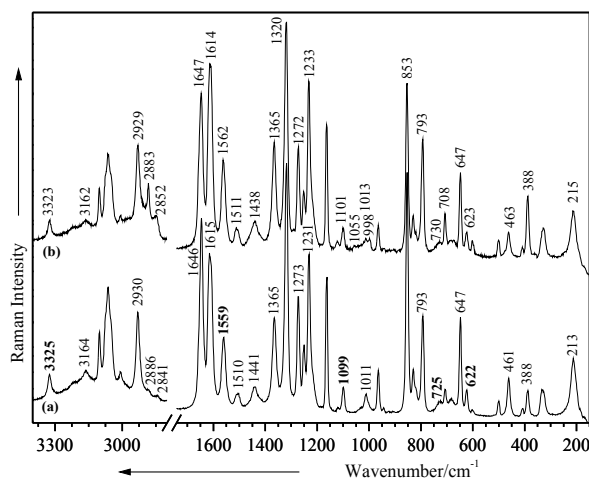
Figure VI.1.2.3. Micro-Raman spectra of recrystallized normal (a) and sinus (b) paracetamol. Excitation: 514.5 nm, 200 mW (a,b).

On the other side, the normal paracetamol (Fig. VI.1.2.3a) presents also three enhanced bands in comparison with the sinus paracetamol (Fig. VI.1.2.3b) and the solid state spectra of paracetamol (Fig. VI.1.2.1). The bands observed at 1320, 853, and 461 cm^{-1} can be increased in relative intensities due to lactose and talc presence; these exhibiting very strong bands[607,608,613] at 1335, 851, and 477 cm^{-1}.

The Raman spectra of the two types of paracetamol solutions are presented in Fig. VI.1.2.4. One can observe that both tablet types include bands, which are specific for the monoclinic form as well as for the orthorhombic form of paracetamol. The bold typed peaks are characteristic for the form I (monoclinic) of paracetamol and the normal typed frequencies are representative for the form II (orthorhombic) of paracetamol[566,483-589,592,596]. Looking at both spectra (Fig. VI.1.2.4a,b) one can state that in the solution, both paracetamol types contain a mixture of those two forms, monoclinic and orthorhombic.

The pH dependence Raman spectra of normal and sinus paracetamol aqueous solutions in the basic and acidic pH range are presented in Figs. VI.1.2.5, VI.1.2.6 and VI.1.2.7, VI.1.2.8, respectively.

The paracetamol molecule can be treated as a slightly acidic compound because of the OH group presence in the para-position[614].
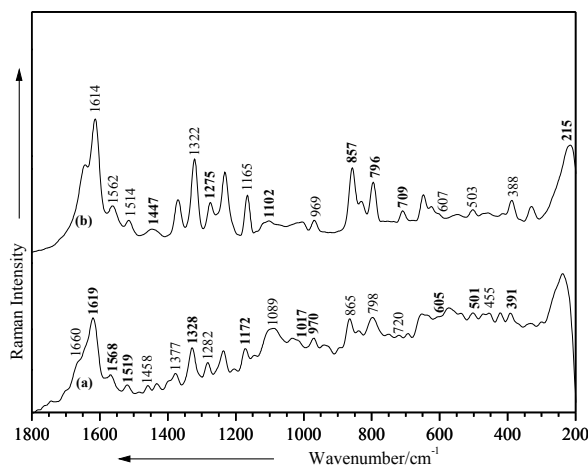
Figure VI.1.2.4. Raman spectra of normal (a) and sinus (b) paracetamol solution
(3.3x10^{-1} M). Excitation: 514.5 nm (a,b), 200 mW (a,b).

In the Raman spectra of normal paracetamol solution at basic pH values (Fig. VI.1.2.5) a significant broadening of the 1619 cm^{-1} band together with its two neighboring shoulders, at 1696 and 1660 cm^{-1}, is observable. This band at 1619 cm^{-1}, in the basic pH range, is 12 cm^{-1} red shifted (1606 cm^{-1}) and may be assigned to the asymmetrical C=C aromatic and C-N stretching modes (Fig. VI.1.2.5, pH 13); the shoulders at 1696 and 1660 cm^{-1} attributed to the CNH and C=O (amide I) stretching mode are importantly red shifted with the increasing of the pH value (1689 and 1637 cm^{-1}, Fig. VI.1.2.5, pH 13). The weak band at 1568 cm^{-1}, 20 cm^{-1} red shifted in the basic pH range, can be due to the in plane N-H bending mode (amide II).
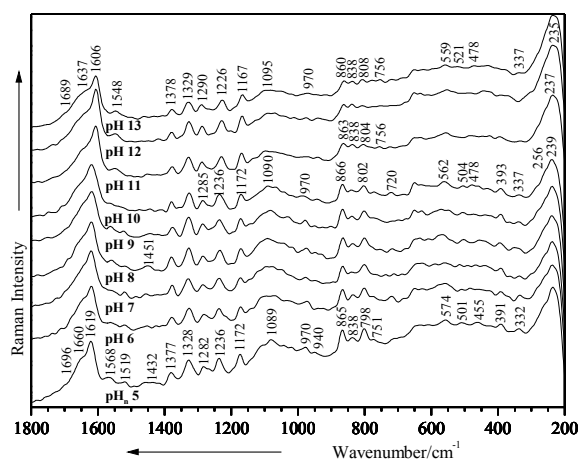
Figure VI.1.2.5. Raman spectra of 3.3x10^{-1} M normal paracetamol solution at different basic pH values.
Excitation: 514.5 nm, 200 mW.

By analogy with the normal paracetamol, in the Raman spectra of sinus paracetamol at basic pH values (Fig. VI.1.2.6) a significant increasing in relative intensity and 14 cm^{-1} red shifting of the band at

1614 cm^{-1}, which is attributed to the C=C aromatic and C-N stretching modes, can be observed (Fig. VI.1.2.6, pH 13).
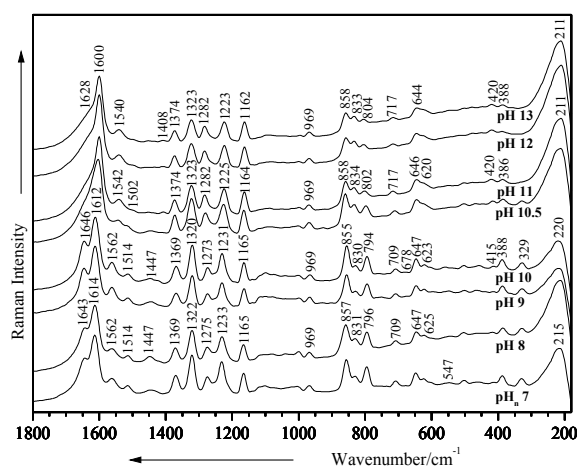
Figure VI.1.2.6. Raman spectra of 3.3x10^{-1} M sinus paracetamol solution at different basic pH values. Excitation: 514.5 nm, 200 mW.

Moreover, the strong band at 1643 cm^{-1} that corresponds to the C=O (amide I) stretching mode, decreases in relative intensity, becomes a shoulder beginning with pH 10.5, and is 15 cm^{-1} red shifted; the weak medium band at 1562 cm^{-1} becomes broader, is 22 cm^{-1} red shifted, and can be due to the in plane N-H bending mode (amide II) (Fig. VI.1.2.6, pH 13).

Furthermore, the weak signal at 1432 cm^{-1}, as a contribution of the asymmetrical CH$_3$ bending and phenyl stretching modes of the normal paracetamol, becomes broader and is 29 cm^{-1} blue shifted in the basic pH range, while the medium band at 1377 cm^{-1} is slightly decreased in relative intensity and is attributed to the symmetrical CH$_3$ bending mode. The signal corresponding to the C-N stretching mode (amide III) (1328 cm^{-1}) decreases in relative intensity, whereas the band corresponding to the C-O and C-N stretching modes (1282 cm^{-1}) increases in relative intensity in the basic pH range (Fig. VI.1.2.5, pH 13). With the increasing of pH, one can also observe, first a broadening and then a red shifting (20 cm^{-1}) of the phenyl-N bending mode (1236 cm^{-1}), by comparing it to the adjacent band (1172 cm^{-1}) assigned to phenyl-N and COH bending modes, which remain approximately constant in relative intensity in the basic pH range (Fig. VI.1.2.5) and is slightly red shifted (5 cm^{-1}).

In contrast to the normal paracetamol, in the Raman spectra of the sinus paracetamol (Fig. VI.1.2.6), the weak peak at 1447 cm^{-1}, with the same assignment as in the case of normal paracetamol, seems to increase in relative intensity at pH 8 and after that, beginning with pH 9 becomes broader and disappears at basic pH value. The next two bands (1369 and 1323 cm^{-1}) in the Raman spectra of the sinus paracetamol, which were attributed as well as for normal paracetamol, decrease in relative intensities and are slightly blue shifted. The peak at 1275 cm^{-1} is 5 cm^{-1} blue shifted and increases in relative intensity, whereas the signal at 1233 cm^{-1} becomes broader, is slightly decreased in relative intensity, and 10 cm^{-1} red shifted (Fig. VI.1.2.6, pH 13). The bands at 865, 838, and 798 cm^{-1} from the Raman spectra of normal paracetamol (Fig. VI.1.2.5, at pH 5 to 10) are slightly decreased in relative intensity, become weaker with

the pH increasing, and are slightly shifted; they are attributed to the out of plane C-C skeletal deformation, to the out of plane C-H bending mode, and to the phenyl-N bending mode, respectively. The similar bands from the Raman spectra of the sinus paracetamol observed at 857, 831, and 796 cm^{-1} (Fig. VI.1.2.6), decrease in relative intensity, are changed in shape, and are slightly blue shifted. The weak band at 574 cm^{-1}, which corresponds to the out of plane phenyl-N deformation mode of the normal paracetamol, is slightly decreased in relative intensity and 15 cm^{-1} red shifted in the basic pH range (Fig VI.1.2.5, pH 13), whereas in the case of sinus paracetamol, the analogous band at 547 cm^{-1} decreases in relative intensity and then disappear (Fig. VI.1.2.6, pH 9-13). In general, all bands, due to C-N, N-H, phenyl-N, COH, and C=O vibration modes of paracetamol become weaker and are red shifted; this already suggests the deprotonation of paracetamol in the basic pH range.
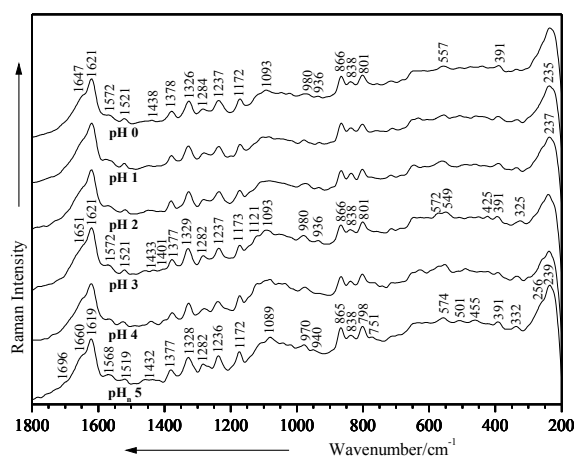
Figure VI.1.2.7. Raman spectra of 3.3x10^{-1} M normal paracetamol solution at different acidic pH values. Excitation: 514.5 nm, 200 mW.

Comparing Figs. VI.1.2.5 and VI.1.2.7, the Raman spectra of the normal paracetamol solutions remain mainly unchanged in the pH range from 5 to 3. Small differences can be observed in the 1700-1000 cm^{-1} spectral region at pH 2, whereas at pH 1 the disappearance of the shoulder at 1696 cm^{-1} and the blue shift of all bands from this spectral region was observed. Additionally, in the 1000-700 cm^{-1} region the band at 838 cm^{-1} increases in relative intensity (Fig. VI.1.2.7, pH 2) and can be due to the out of plane C-H bending mode. One can perceive that the out of plane phenyl-N deformation mode (574 cm^{-1}) is represented by two weak peaks at pH 3 (572 and 549 cm^{-1}) (Fig. VI.1.2.7) and at pH 0 remain a unique band, which is 17 cm^{-1} red shifted (557 cm^{-1}). In the low wavenumber region, the band at 332 cm^{-1} is changed in shape, relative intensity, is 7 cm^{-1} red shifted (325 cm^{-1} at pH 3, Fig. VI.1.2.7), and may be due to the out of plane phenyl-N deformation mode.

Thus, the fully protonated normal paracetamol molecule predominates at low pH values[603,614-616]. Finally, taking into account the major changes in the band shape attributed to phenyl-N Raman bands at acidic pH values, a protonation of the NH group is very likely. Comparing Figs. VI.1.2.6 and VI.1.2.8, the Raman spectra of the sinus paracetamol remain unchanged in the pH range from 7 to 0, which demonstrate that at the neutral pH 7, the sinus paracetamol exists in the zwitterionic form.

SERS spectra of the paracetamol on thin films

The SERS spectra of the normal and sinus paracetamol (8×10^{-2} M) are presented in Figs. VI.1.2.9 and VI.1.2.10 in comparison with the Raman spectra of the bulk solution (3.3×10^{-1} M) at pH 5 and 7, respectively. Large differences in band positions and relative intensities are observed, allowing the presumption of a chemisorbed species.
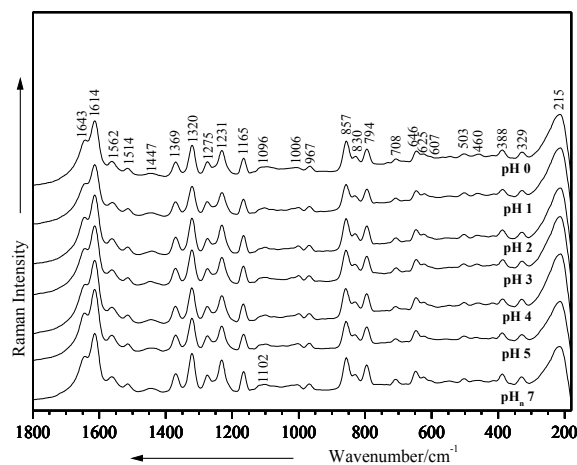
Figure VI.1.2.8. Raman spectra of 3.3×10^{-1} M sinus paracetamol solution at different acidic pH values. Excitation: 514.5 nm, 200 mW.

The SERS spectra were recorded on two types of island films with different roughnesses (2.9 and 1.9 Å). The microscopical images of the paracetamol solutions on both types of thin films can be observed in Figs. VI.1.2.9e,f and VI.1.2.10e,f. The negatively charged drug was expected to preserve the aggregation status and hence the Ag surface potential[324]. Since the SERS signal is concentration sensitive, in order to discuss the behavior to adsorption of the paracetamol on the silver films, the SERS spectrum at 8×10^{-2} M was chosen here for the adsorption geometry proposal.

Theoretically, the paracetamol molecule can interact with the Ag film surfaces *via* several functional groups. The negative charge of the C-O$^-$ moiety from the hydroxyl group situated in the para-position of the paracetamol, however, leads to a Coulombian repulsion[539,540] due to the negative potential of the Ag surface. One possibility for paracetamol to chemisorb is provided by the presence of the lone pair electrons of the nitrogen and oxygen atoms from the amide group. In this case, according to the surface selection rules[108], the amide I, II, and III bands are expected to be enhanced.

Another possibility for the paracetamol to chemisorb is through the π electrons of the phenyl ring. In accordance to the electromagnetic selection rules proposed by Creighton[108], and Moskovits and Suh[344], the C-H stretching mode should be relatively enhanced when the C-H bond is perpendicular to the metal surface plane as compared to the case in which the C-H bond lies parallel to the surface.

The observed bands in the SERS spectra (Figs. VI.1.2.9, VI.1.2.10) support in part all three considerations. More specifically, the very intense bands in the SERS spectra (1454, 1372, and 1326 cm^{-1} for the normal and 1454, 1371, and 1326 cm^{-1} for the sinus paracetamol, Figs. VI.1.2.9b,c and VI.1.2.10b,c, red and blue shifted, respectively, from the Raman spectra of the bulk solution, Figs.

VI.1.2.9a, VI.1.2.10a) assigned to the symmetrical C=O stretching mode (amide I), to the H$_3$C-C=O stretching and symmetrical CH$_3$ bending modes, and to the C-N stretching (amide III) mode are preponderantly due to the amide group that is now in a close vicinity of the Ag surfaces with a flat orientation of the skeleton ring (Figs. VI.1.2.9d, VI.1.2.10d).
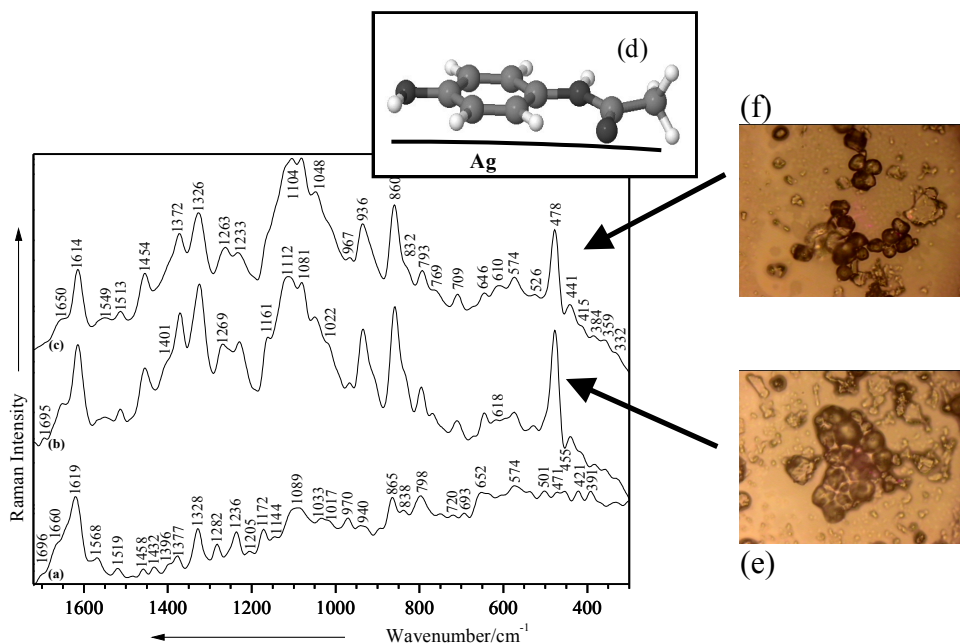
Figure VI.1.2.9. Raman spectrum of 3.3x10^{-1} M normal paracetamol solution (pH 5) (a), SERS spectra of 8x10^{-2} M normal paracetamol on thin films with 2.9 Å (b) and 1.9 Å (c) roughnesses and its proposed orientation on the silver surface (d). Excitation: 514.5 nm (a-c), 200 mW (a) and 50 mW (b,c). Microscopical images of the normal paracetamol solution (8x10^{-2} M) after drying on the silver films with 2.9 Å (e) and 1.9 Å (f) roughnesses.

Moreover, the medium bands observed in the SERS spectra of the normal paracetamol at 1263 and 1233 cm^{-1} (19 and 3 cm^{-1} red shifted from the Raman spectrum of the solution), which are due to the C-N and phenyl-N stretching modes of the amide group are changed in the shape. In the case of the sinus paracetamol, the medium bands observed in the SERS spectra at 1270 and 1233 cm^{-1} (5 and 2 cm^{-1} red shifted from the Raman spectra of the solution) have the same assignment as for the normal paracetamol and are changed in the shape. The medium bands at 1172 cm^{-1} (for the normal paracetamol) and at 1164 cm^{-1} (for the sinus paracetamol) in the Raman spectra of the solution become shoulders in the SERS spectra, are 11 and 1 cm^{-1} red shifted, and can be attributed to the C-OH bending modes.

The medium signal at 1089 cm^{-1} in the Raman spectrum of the normal paracetamol solution is split in the SERS spectrum in three peaks and one shoulder (1104, 1081, 1048 and 1022 cm^{-1}), which were assigned to the C-OH stretching, asymmetrical C-O-C stretching, CCC bending, and C-OH and phenyl bending modes, respectively. In the case of the sinus paracetamol, the unresolved signal between 1102 and 1000 cm^{-1}, increases in relative intensity in the SERS spectra, where three bands (1119, 1079, 1047 cm^{-1}) and one shoulder (1022 cm^{-1}) with the same assignment as for the normal paracetamol can be observed. Besides, these interactions generate the presence of the amide group to bend near the surface, with a flat orientation of the phenyl ring on the metallic surface.

This contribution is supported by the importantly increasing in relative intensity of the band at 936 cm^{-1} (in the SERS spectra of both normal and sinus paracetamol, Figs. VI.1.2.9b,c and VI.1.2.10b,c),

which are due to the out of plane C-H deformation of the phenyl ring, by the strong increase in relative intensity of the bands at 860 cm^{-1} (SERS spectra of normal paracetamol) and 858 cm^{-1} (SERS spectra of sinus paracetamol), which were attributed to the C-H and C-C out of plane skeletal deformations, and by the increase in relative intensity of the peaks at 646, 610 cm^{-1} (SERS spectrum of the normal paracetamol, Fig. VI.1.2.9c) and 615 cm^{-1} (SERS spectrum of the sinus paracetamol, Fig. VI.1.2.10c) that can correspond to the out of plane phenyl-N deformation modes.
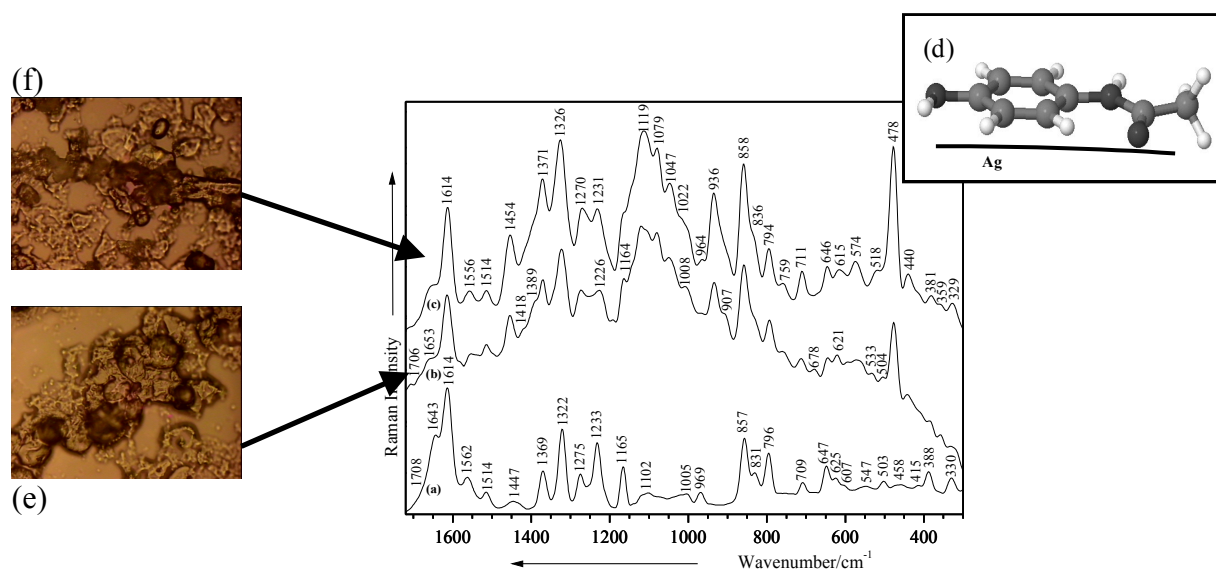
Figure VI.1.2.10. Raman spectrum of 3.3x10^{-1} M sinus paracetamol solution (pH 7) (a), SERS spectra of 8x10^{-2} M sinus paracetamol on thin films with 2.9 Å (b) and 1.9 Å (c) roughnesses and its proposed orientation on the silver surface (d). Excitation: 514.5 nm (a-c), 200 mW (a) and 50 mW (b,c). Microscopical images of the sinus paracetamol solution (8x10^{-2} M) after drying on the silver films with 2.9 Å (e) and 1.9 Å (f) roughnesses.

The very intense bands at 478 cm^{-1}, in the SERS spectra of the normal and sinus paracetamol were assigned to the Ag-O stretching mode[584]. The interaction of the metals with amide groups can occur *via* two different orientations when binding to the C=O and N-H groups[541]. In general, the Ag$^+$ affinity of an amide group depends to a large extent on the interaction of the Ag$^+$ ion with the side chain. This interaction is dictated by two factors: the intrinsic Lewis acid strength of the substituent and the amount of the steric strain introduced by forming the rings[494]. Alkyl groups stabilize positive charges inductively and not by direct coordination. This results in small increases in Ag$^+$ affinities, with the stabilization increasing with the size of the alkyl group. The paracetamol molecule binds to the silver colloidal surface through the lone pair electrons of the nitrogen and oxygen atoms of the amide group and π electrons of the phenyl ring, in a flat orientation (Figs. VI.1.2.9d and VI.1.2.10d). This assumption is supported by the Ag-O[584,494] and Ag-N[584,496] stretching modes, which can be detected at 478 and 441 cm^{-1} for the normal paracetamol and at 478 and 440 cm^{-1} for the sinus paracetamol, respectively.

Conclusions

The FT- and micro-Raman spectra of both paracetamol tablets were recorded and the marker bands of the characteristic functional groups were identified. The presence of the monoclinic form of paracetamol in the solid state of both types was also proved.

The micro-Raman spectra of the paracetamol after recrystallization on the glass surfaces show

that the normal paracetamol contains a mixture between monoclinic and orthorhombic forms, while the sinus paracetamol contains just the monoclinic form. The most important bands of some excipients, added in the drug production could be identified.

Analyzing the Raman spectra of both types of the paracetamol solutions, the existence of the mixture between monoclinic and orthorhombic forms and of the protonated species of normal and sinus paracetamol on going from basic to acidic pH values could be distinguished.

SERS spectra of paracetamol could be recorded even at low concentrations with a conventional SERS setup (8×10^{-2} M). The surface selection rules, along with the data from literature, have reasonably explained the adsorbate structures on the metal surface. A strong chemical interaction of both types of paracetamol with the silver film surfaces was observed at concentration of 8×10^{-2} M through the lone pair electrons of the nitrogen and oxygen atoms from the amide group and through the π electrons of the phenyl ring in a flat orientation.

VI.2 Antimalarial drugs

Raman and surface-enhanced Raman scattering (SERS) were employed to probe the interaction of the antimalarial drugs chloroquine (CQ) and mefloquine (MQ) with haematin. NIR-SERS spectra of both quinoline derivatives were obtained from a colloidal gold surface. Strong chemical interactions of each drug with the Au particles were observed and the similarities of the two NIR-SERS spectra allowed to predict a similar orientation geometry for both of drugs on the colloidal surface, namely through the quinoline skeletal part of each molecular structure.

Separately, the adsorption behavior of haematin on the Au colloid was studied under nonresonant conditions. In addition, both haematin-antimalarial drug systems (CQ and MQ) were prepared and investigated by NIR-SERS.

VI.2.1 Malaria and antimalarial drugs

Malaria is a global tropical disease with about 3 million deaths per year[617,618]. Owing to the increasing number of resistant strains of *Plasmodium falciparum*, new antimalarial drugs, among them quinoline derivatives, are needed. For therapeutic treatments, the free heme released in the parasite food vacuole is considered as an attractive pharmacological target: it is the most specific target that can be utilized since it comes from the hemoglobin digestion by the parasite in infected erythrocytes[619]. As the precise mechanisms of both heme aggregation and quinoline transport, are not exactly known many of quinoline-based compounds have been investigated. However, precise structure-activity relationships for optimal antimalarial activity remain unclear[620]. The difficulty of determining exact structure-function relationships arises from the dual requirements that heme polymerization inhibitors not only disrupt the process of hemozoin formation but also concentrate within the digestive vacuole of the parasite, which is the site of heme aggregation[620].

In spite of the huge amount of available pharmaceutical and medical data related to the

antimalarials and their possible inhibition effects[617-629], only few vibrational spectroscopic characterizations of several quinoline derivatives[630-633] and, recently, of haematin[634-636] have been published. The haematin-chloroquine mechanism interaction was recently reported using resonance Raman (RR) spectroscopy[634]. Polarization-resolved (RR) spectra of haematin and its complex with CQ were recorded under Q-band resonance conditions in order to monitor the binding of the drug to the heme structure. A noncovalent interaction in the electronic ground state of the CQ-heme complex was concluded[634].

Surface-enhanced Raman scattering (SERS) has been proven to trigger exciting opportunities in the field of biomedical spectroscopy[637,638], where it allows to study structural-functional properties of biologically relevant molecules, which are often present in extremely small concentrations at physiological level. SERS combines the structural information available by Raman spectroscopy with ultrasensitive detection limits, allowing a detection down to the single-molecule level[637].
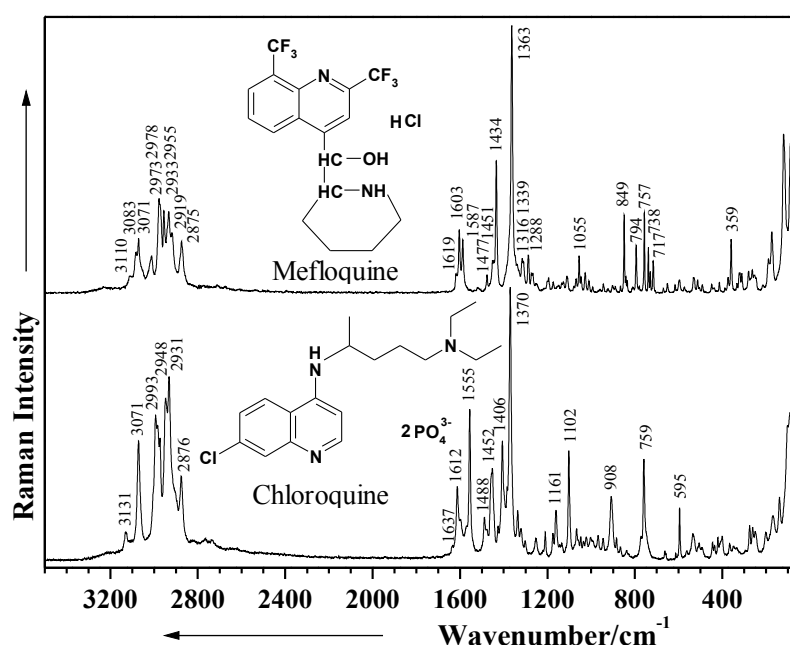
Figure .2.1.1. FT-Raman spectra of chloroquine diphosphate and mefloquine hydrochloride together with their molecular structures. Excitation: 1064 nm, 400 mW.

In particular, SERS with colloidal gold nanoparticles is attractive for biomedical applications[639]. It was shown[639] that gold nanostructures have comparably good SERS enhancement factors as compared to silver structures when near-infrared excitation is applied. The uniform size distribution, the chemical stability, and the optical properties of the Au colloidal surface provide important advantages in performing SERS experiments with light-sensitive molecules.

RR data[634,635] of haematin and haematin-CQ complex[634] have been recently published, but, to the best of our knowledge, SERS investigations of the antimalarial drugs or of the monomeric precursor, haematin, have not been reported.

When RR spectroscopy is employed to investigate the chromophore-containing species in the presence of a drug, the available information is selectively related to the structure of chromophore and its

possible perturbation caused by the drug. When the drug targets the nonchromophore part of the macromolecular structure, this information is unavailable using RR spectroscopy. In order to overcome this disadvantage, the use of SERS spectroscopy is the proper alternative, providing information about adsorbed molecular species[630,633,638], their functional groups involved in adsorption, the influence of the environmental pH conditions on adsorption, interaction between a specific drug and the target molecule upon adsorption on a proper surface, the mechanisms at the interface, etc.

VI.2.2 Electronic absorption spectra

The gold colloid displays characteristic optical properties, which have to be considered from the point of view of the electromagnetic mechanism[108,426,641], associated with the SERS effect. The absorption spectra of the pure gold colloid and the drug-colloid system for both antimalarial drugs are presented in the Figs. VI.2.2.2 and VI.2.2.3, respectively. The absorption bands of colloids are due to the plasmon excitation. The pure colloids show a plasmon resonance at ~534 nm.
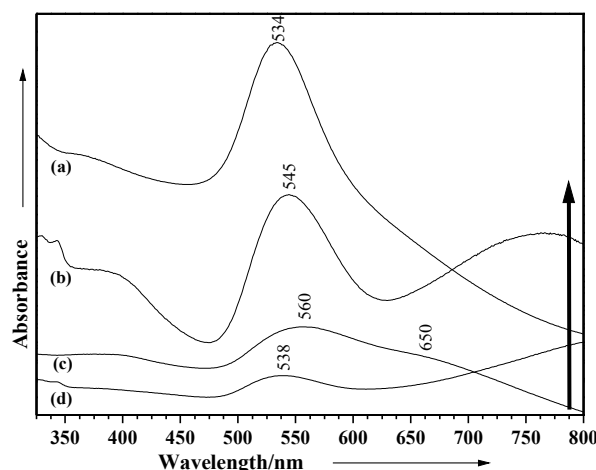
Figure VI.2.2.1. Absorption spectra of the gold colloid (Au) (a), haematin-CQ-Au (b), haematin-Au (c), and CQ-Au (d). The arrow indicates the excitation wavelength employed for NIR-SERS.

Upon addition of the drug solution, in both cases a red-shifted new band was observed at about 791 nm, indicating an aggregation of the Au particles in the presence of the drug. This result suggests the possibility of using the NIR-SERS excitation of the surface plasmon resonance of the aggregated particles in the presence of the respective drug.

Upon addition of haematin to the Au colloid, a decrease and a broadening of the absorption band was observed with the newly developed band at about 650 nm having a tendency to NIR shifting (Fig. VI.2.2.2c). This fact further supports motivation for NIR-SERS investigation on haematin species. The haematin-CQ and haematin–MQ systems (1:1 molar ratios), however, exhibit different absorption patterns upon addition to the Au colloid (Figs. VI.2.2.1b and VI.2.2.2b respectively).

In the case of haematin-CQ, the new band at 760 nm was well defined, whereas in the case of haematin-MQ, this new expected band has only a tendency to slowly develop, indicating a smaller degree

of particles aggregation in the presence of the molecular species then anticipated.
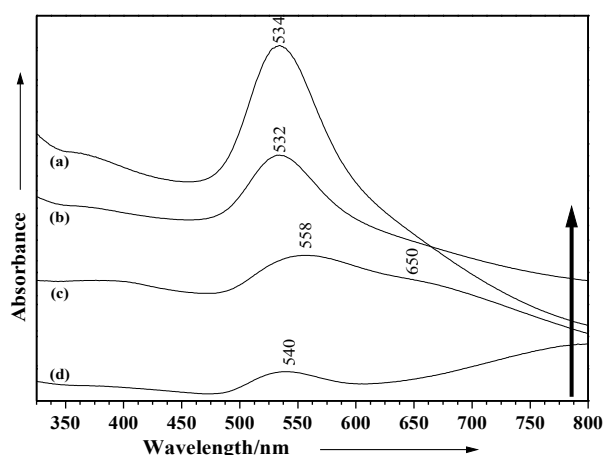
Figure VI.2.2.2. Absorption spectra of the gold colloid (Au) (a), haematin-MQ-Au (b), haematin-Au (c), and MQ-Au (d). The arrow indicates the excitation wavelength employed for NIR-SERS.

VI.2.3 NIR-SERS spectra

The recorded spectra of CQ, haematin, CQ-haematin (1:1 molar ration) are presented in the Fig. VI.2.3.1 and those of MQ and MQ-haematin system, in Fig. VI.2.3.2.

CQ and MQ on gold colloid

The collected vibrational FT-Raman and NIR-SERS data of the two drug species are summarized in Tables VI.2.3.1, VI.2.3.2, respectively. The proposed assignment[642] is based on the recently reported theoretical DFT calculations of several quinoline derivatives[630-632].
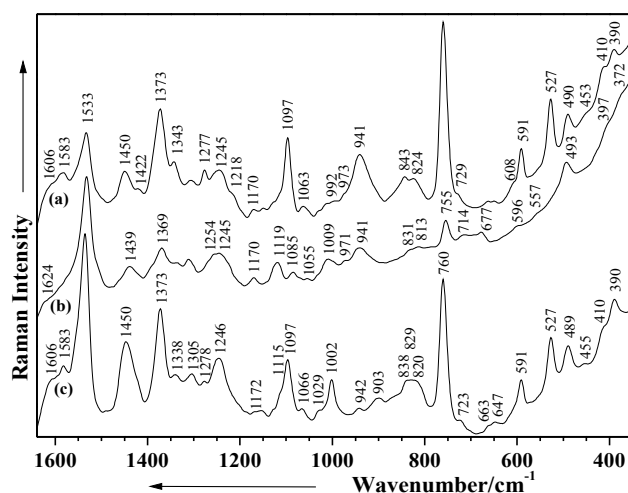
Figure VI.2.3.1. NIR-SERS spectra of CQ-haematin system (a), haematin (b), and CQ (c) on gold colloid. Excitation: 785 nm, 30 mW.

The well-known possibilities of adsorption on a metal surface, namely, physisorption and chemisorption[108,426,641], support the explanation of the electromagnetic mechanism of enhancement. In the case of physisorbed species, the Raman and SERS spectra are similar in relative intensities and band

positions. Additionally, when the CT (chemical enhancement) mechanism contributes to the total enhancement, the resulting SERS spectra are completely different from the corresponding normal Raman spectra. Comparing the NIR-SERS spectra with the Raman spectra of the two individual drugs, one can notice large differences in the relative intensities and band positions, which can be explained in terms of strong chemical interaction between the molecule and the Au nanoparticles.

Taking into account the information from the electronic spectra, one can conclude the formation of a CQ-Au SERS complex, where the charge transfer (CT) between the electron density of the surface plasmon and those of the molecule takes place. The 785 nm line employed for excitation of the SERS spectra matches exactly the resonance condition for this CT band. Theoretically, the CQ species could be chemisorbed through the lone pairs of each N atom, Cl atom, or through the π-ring system.
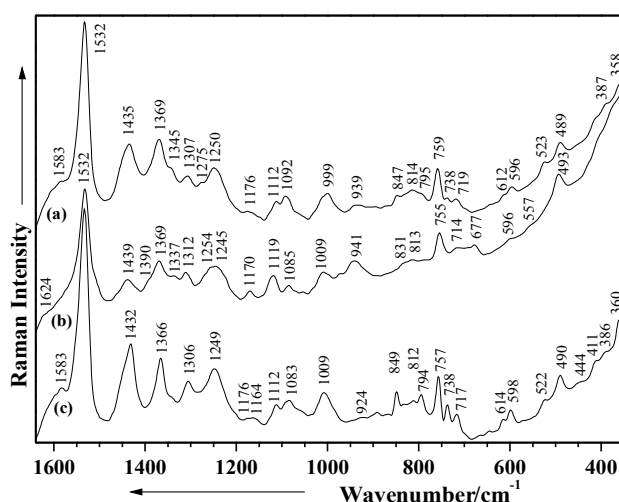
Figure VI.2.3.2. NIR-SERS spectra of MQ-haematin system (a), haematin (b),
and MQ (c) on gold colloid. Excitation: 785 nm, 30 mW.

Table VI.2.3.1. Vibrational FT-Raman and NIR-SERS data (cm^{-1}) of chloroquine diphosphate (CQ) and their assignments.

FT-Raman (cm^{-1})	NIR-SERS Au colloid (cm^{-1})	Vibrational Assignment
3131 w	-	ν_{as}(N-H)
3071 s	-	ν_s(N-H)
2993 s	-	ν_{as}(C-H) aromatic
2984 s	-	ν_s(C-H) aromatic
2973 s	-	ν_s(C-H)
2948 s	2944 m	ν_{as}(CH$_3$)
2931 s	-	ν_{as}(CH$_2$)
2903 sh	-	ν_s(CH$_2$)
2876 m	2859 m	ν_s(CH$_3$)
1637 w	-	δ(N-H) amine
1612 ms	1606 sh	ν(C=N), δ(N-H)
1598 sh	1583 m	ν quin. ring
1571 sh	-	ν(CCC), ν(C=N ring)
1555 s	1533 vs	ν(C=N ring)
1488 wm	1492 w	ν(C-C)ring, νC$_2$H$_5$
1476 sh	-	ν(C-C) ring
1452 ms	1450 ms	ν(C-C), δ(C-H), ν_{as}(-CH$_3$+CH$_2$) aliphatic
1426 w	-	ν(C-C), δ(C-H) ring
1406 s	-	ν(C-C), δ(C-H) ring

1385 m	-	ν(C-C) benzene ring
1370 vvs	1373 s	ν(CCC) quin., $ν_s$(C-CH$_3$) aliphatic
1336 wm	1338 m	ν(C-C), δ(C-H) ring
1321 w	-	ν(C-C)
1302 w	1305 m	ip δ(C-H), amine
	1278 m	ν(C-N)
1253w	1246 m	ν(C-C)quin., ν(C-N)amine
1210 w	1212 sh	ν(C-CH$_3$), ν tertiary diethyl amine
1175 w	1172 w	ν(C-C)
1161 wm	1157 w	ν(C-C), secondary aliphatic amine
1144 w	-	ν quin. ring
1135 w	1128 sh	ν quin. ring
1102 s	1097 m	ν(Cl-quin.)
1066 w	1066 w	ν(P=O)
1048 sh	-	ν(PO$_4^{3-}$)
1036 w	-	pyr. trigonal stretch
1023 w	1029 sh	ν(P-O)
1003 w	1002 m	ν quin
991 sh	-	pyr. ring breath
968 w	-	ν benz., op δ(C-H), C-dialkylamine
945 w	942 w	ν(C-C)
908 m	903 wm	op δ(C-H)
884 w	-	op δ(C-H) ring, aliphatic
867 w	-	ν(C-N-C), op δ(C-H)
837 w	838 m	op δ(C-H)
827 w	829 m	$ν_{as}$(C-N)
801 vw	-	op δ(C-H)
771 sh	-	τ(C-H) quin.
759 s	760 s	δ(N-H) amine, CH$_3$, ip ring def
745 sh	723 sh	ν(C-Cl), op δ(N-H)
663 vw	663 vw	δ(quin.-Cl), τ(C-H) quin.
658 vw	647 vw	τ(C-H) quin.
613 vw	-	δ(C-H), δ amine
595 m	591 m	δ(quin., C-Cl)
562 vw	-	op δ(C-C), (C-H)
535 w	527 m	op δ(C-N-C)
505 w	-	op δ(CCN)
492 vw	489 m	op δ quin., δ secondary aliphatic amine
434 w	390 m	−
255 w	-	δ(O-P-O)
	252 vvs	Au-N
249 w	-	τ(C-H) quin.
201 w	-	τ and δ quin.
168 wm	-	lattice vibrations
137 m	-	lattice vibrations
99 s	-	lattice vibrations
88 s	-	lattice vibrations

Table VI.2.3.2.Vibrational FT-Raman and NIR-SERS data (cm^{-1}) of mefloquine hydrochloride (MQ) and their assignments.

FT-Raman (cm^{-1})	NIR-SERS Au colloid (cm^{-1})	Vibrational Assignment
3110 w	-	$ν_{as}$(N-H)
3083 m	-	$ν_s$(C-H)
3071 m	-	$ν_s$(C-H) aromatic
3011 m	-	$ν_s$(C-H)
2978 ms	-	ν(CH, CH$_2$)
2973 sh	-	ν(CH)
2955 ms	-	$ν_{as}$(CH)
2933 ms	-	$ν_{as}$(CH$_2$)
2918 m	2920 m	$ν_s$(CH$_2$)
2875 m	2870 m	$ν_s$(CH) bridge
1619 w	-	δ(N-H), ν(C=C)
1603 ms	-	ν quin. ring
1587 m	1583 m	ν(C=C)
1555 vw	1532 vs	ν(C=N), ν(C=C)
	-	ν(C-C)ring
1477 w	-	ν(C-C) ring

1451 w	-	ν(C=N), ν(C-C)
1434 s	1432 m	ν(C-C), δ(C-H) ring
	-	ν(C-C) adsorbed quin. ring
1363 vvs	1366 m	ν(CCC) quin.
1339 w	1343 sh	δ(C-H) ring+ν(CF)
1316 w	-	ν(-CF$_3$)
	1306 m	ip δ(C-H)
1288 wm	-	ν(C-N), ν(-CF$_3$)
1253 w	1249 m	νC-C) quin., ν(C-N)amine
1195 w	-	ν(C-O)
1174 w	1176 w	ν(C-C), ν(N-H)
1149 vw	1164 w	ν(C-C), δ(C-H)
	-	ν quin. ring
1111 w	1112 w	ν quin., ν(-C-F)
1069 w	1083 wm	ν quin.
1055 wm	-	ν piperidine ring
1046 w	-	ip δ(C-H)
1027 w	-	pyr. trigonal stretch
1010 w	1009 m	ν quin.
993 vw	-	ν pyr. (breath)
960 vw	-	ν(C-C)
944 vw	-	δ(C-C-OH)
903 vw	-	ν(C-C)
889 vw	891 w	γ(O-H)
866 vw	867 w	ν(C-N-C) piperidine
849 ms	849 w	ip δ(C-H), piperidine breathing
835 w	833 w	ip δ(C-H), piperidine stretch
808 vw	812 w	op δ(C-H)
794 m	-	op δ(C-H)
757 ms	-	γ[(N-H), CH], ip ring def.
738 m	717 wm	op δ(C-H)
729 wm	-	δ(C-F), op δ(C-H)
717 wm	-	δ(CF$_3$), op δ(C-H)
670 w	665 w	τ(C-H) quin.
651 w	645 w	τ(C-H) quin.
616 w	614 w	δ(quin., CF$_3$)
595 w	598 wm	ip δ(CNC), δ(OH)
532 w	522 w	op δ(C-C), (C-H)
492 w	490 m	op δ(CH), γ(OH)
359 m	360 m	δ quin.
	250 vvs	Au-N
188 w	-	τ(C-H) quin.
173 wm	-	τ and δ quin., lattice vibrations

Abbreviations: s-strong, m-medium, w-weak, v-very, sh-shoulder, ν-stretching, δ–bending, τ-torsion, ip-in plane, op-out of plane, pyr.-pyridine moiety, quin.-quinoline ring.

According to the surface selection rules[108,643], the vibrational modes that have the polarizability tensor component perpendicular with the respect of the surface will be predominantly enhanced, whereas those having large tensor components parallel to the surface will result in weak SERS bands. Moreover, for molecules with a planar structure, the orientation geometry at the surface could be predicted from the relative intensity of the in-plane and out-of-plane C–H modes[644]. In the case of adsorption through the π-ring system, a characteristic red shift of the SERS bands together with their broadening on passing from Raman to SERS is usually observed

Analyzing the NIR–SERS spectrum of CQ (Fig. VI.2.3.1c) the strongest band at 1533 cm^{-1} has the corresponding Raman band at 1555 cm^{-1} (Fig. VI.2.1.1, Table VI.2.3.1), which was assigned to the C=N stretching mode of the ring. Significant red shift from the Raman position was observed for the most representative quinoline ring-stretching modes present in the SERS spectrum (Table VI.2.3.1). A blue shift of the enhanced vibrational modes, as expected of a supposed N-adsorption, was not observed;

therefore, a perpendicular staking of the skeletal molecular plane with respect of the surface would be less probable. One significant band at 1373 cm^{-1} (ring-stretching mode) from the NIR-SERS spectrum, however, was blue shifted with 3 cm^{-1} from its corresponding normal Raman position, which did suggest a quinoline N-adsorption. A tilted orientation of the skeletal ring would explain the decrease in the relative intensity of the SERS mode at 1373 cm^{-1} in comparison to FT-Raman (Table VI.2.3.1). Adsorption through one or both of the N atoms from the dialkylamine substitute was not consistent since the corresponding modes are less representative in the SERS spectrum.
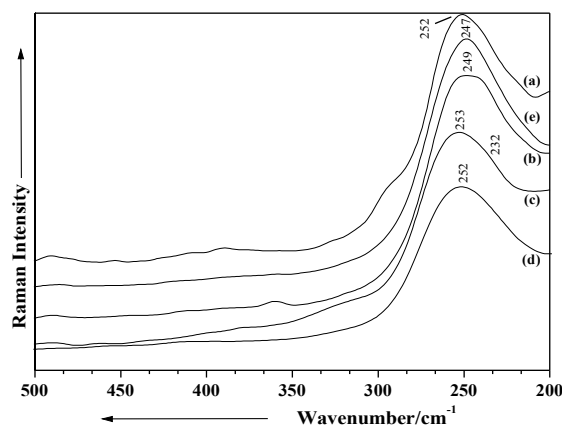
Figure VI.2.3.3. Low wavenumber region of the NIR-SERS spectra of CQ (a), MQ (b), haematin (c), haematin-CQ (d), and haematin-MQ (e).

Analyzing the low-wavenumber spectral range (Fig. VI.2.3.3a), a huge and broad SERS band located at 252 cm^{-1} was observed. This band is usually assigned to the Au–N and Au–Cl (when the Cl^{-} ions are present) stretching modes. Taking into account these considerations, the results suggest a flat rather than tilted orientation of the quinoline ring to the Au surface, where the N ring could be close enough for a CT mechanism. In the case of MQ, remarkable similarity with CQ in the SERS behavior has been observed, suggesting that the common skeletal structure is located in the close vicinity of the Au colloidal surface. The very strong band at 1532 cm^{-1} similar to CQ, along with the representative enhanced modes at 1583, 1432, 1366, 1249, 1009, 757, 490, 360 and 250 cm^{-1} are present (Fig. VI.2.3.2, Table VI.2.3.2). The red-shift character of the most prominent skeletal stretching modes, except for the 3 cm^{-1} blue shift of the band at 1366 cm^{-1}, the less significant piperidine moiety modes enhancement, and the presence of the band at 250 cm^{-1} suggest a tilted to flat orientation of the quinoline ring with respect to the Au surface with an N-adsorption conditioned by the steric configuration of both trifluoromethyl substituents of the MQ skeletal ring.

NIR-SERS spectrum of haematin

The observed vibrational Raman and NIR–SERS data of haematin adsorbed on Au colloid are summarized in the Table VI.2.3.3, together with the proposed assignments[634,635,645]. In the NIR–SERS spectrum the dominant band is located at 1532 cm^{-1}, whereas the totally symmetric stretching modes are less enhanced (Table VI.2.3.3). For the non-totally symmetric modes, appreciable SERS enhancements are observed.

The characteristic vibrational feature in the spin state region (1650-1500 cm^{-1}) of haematin could also reflect the dynamics of the porphyrin perturbation under different excitation energies of the laser lines, together with the change in haematin orientation on the surfaces.

Table VI.2.3.3. Raman and NIR-SERS data of haematin (cm^{-1}) for the 785 nm excitation line.

NIR-SERS Au colloid (cm^{-1})	Raman^{ref} (cm^{-1})	Vibrational assignment^{ref}
1624 sh	1626 s	ν_{10} B$_{1g}$ (C$_a$C$_m$)
	1591 sh	ν_{37} E$_u$ (C$_b$C$_b$)
	1571 s	ν_2 A$_{1g}$ (C$_b$C$_b$), ν_{19} A$_{2g}$ (C$_a$C$_m$)
	1553 s	ν_{11} B$_{1g}$ (C$_b$C$_b$)
1532 vs	1533 sh	ν_{38} E$_u$ (C$_a$C$_m$)
	1491	ν_3 A$_{1g}$ (C$_a$C$_m$)
	1453	ν_{28} B$_{2g}$ (C$_a$C$_m$)
1439 w	1435	δ_s (=CH$_2$) (1)
1390 sh	1404	ν_{29} B$_{2g}$ (C$_a$C$_b$)
1369 m	1373 s	ν_4 A$_{1g}$ (C$_a$N)
1337 w	1340	δ_s (=CH$_2$) (2)
1312 wm	1309 w	ν_{21} A$_{2g}$ δ(C$_m$H), δ_s (CH=)
1254 m	1260 m	ν_4, ν_9 A$_{1g}$
1245 m	-	?
	1228	ν_{13} B$_{1g}$
1170 w	1170 w	ν_{30} B$_{2g}$
1119 m	1127 ms	ν_{22} A$_{2g}$ (C$_a$N)
1085 w	1089	δ_{as} (=CH$_2$)
1055 w	-	?
1009 m	1008 w	γ(CH=)
971 w	-	?
941 m	-	?
831 w	-	?
813 w	806 wm	ν_6 A$_{1g}$ δ(C$_a$C$_m$C$_a$)
755 ms	756 ms	ν_{33}, ν_{34} A$_{1g}$
714 w	722	ν_{16} B$_{1g}$ δ (C$_a$NC$_a$)
677 w	675 w	ν_7 A$_{1g}$ δ (C$_b$C$_a$N)
596 w	-	?
557 w	555	ν_{49} δ(C$_a$C$_b$C$_b$)
493 w	492	pyr. fold ?
387 sh		?
358 sh		?
251 vvs		Au-O
232 sh		Au-N

Abbreviations: w-weak, m-medium, s-strong, sh-shoulder, op-out of plane. ν_2-ν_7 skeletal modes of porphyrine ring, pyr.-pyridine moiety, ref-(634-636,647). C$_a$-carbon atoms bonded to N; C$_m$-'middle' carbon (N-C$_a$-C$_m$-C$_a$-N);C$_b$-the others carbons from the porphyrine ring. Assignment follows the assumed D$_{4h}$ symmetry foe metallo-porphyrins[647].

The haematin molecule on the Au surface will experience an enhanced electric field from the metal in addition to the electric field from the incident light, thus will scatter light with an enhanced intensity compared to an isolated molecule. This contribution to SERS does not require direct bonding between the adsorbate and the metal surface; increased sensitivity has been recorded up to 40 Å from the metal surface. In the charge-transfer mechanism, the enhancement effect is dependent on the nature of the molecules involved. It includes transfer of charge from the metal surface through a bond. The enhancement mechanism requires new electronic transitions between adsorbate and metal (absorption band at 650 nm), made possible when haematin is at the surface. This mechanism accounts for the high specificity of SERS to the first layer of adsorbed molecules.

Owing to the NIR excitation, which is preresonant to a weak absorption band of haematin[635] but resonant to surface plasmons, RR scattering from the heme is considered to be negligible.

Preresonance still gives selectivity or sensitivity for the species containing the chromophore, but the scattering intensities are dependent on the molecular orientation at the surface, providing more information on the nature of the bonding.

In previous investigations, surface-enhanced resonance Raman scattering (SERRS) has also been used to investigate biological molecules[638,645,646,648]; for example, studies of enzymes on proteins are well known[648]. The intense bands in the spectra correspond to those found in resonance, but the relative intensities do vary when compared to resonance. It was shown[648] that the band at 1375 cm^{-1} (v_4) is a marker for the oxidation state. By gradually titrating cytochrome c into a silver colloid, adsorption layers on the surface have been built up from below to above monolayer coverage. When this occurs, there is a relative intensity change in a number of the bands. Specifically, the ratio of the intensity of the band at 1375 cm^{-1} (A_{1g}, v_4) to the band at 1640 cm^{-1} (B_{1g}, v_{10}) changes. By plotting this intensity, the formation of the monolayer could be monitored[648]. The reason for this change is that SER(R)S provided the effect, contains an appreciable SERS contribution, depends on selection rules related to those from SERS alone. Thus, as the monolayer builds up on the surface, the protein packs and the orientation of the heme in the protein relative to the surface changes. This change is reflected in the relative intensity changes between v_4 and v_{10}. In fact, at close-to-monolayer coverage, more subtle reorganization of the layer occurred.

Taking into account these considerations, at our concentration values of about 10^{-5} M, in the case of haematin, the marker band for the oxidation state is located at 1369 cm^{-1} (Fig. VI.2.3.1b). The band at 1533 cm^{-1} is believed to correlate with the porphyrin core size[645]. The slight decrease in its wavenumber on passing from Raman to SERS (Table VI.2.3.3) implies an expansion of the porphyrin ring, a plausible consequence of the increased interactions between the pyrrole nitrogen atoms and the metal surface. The possibility that the haematin adopts a denatured geometry upon chemisorption and that the heme group is situated in a smaller gap within the aggregates cannot be excluded. A nonbonded interaction between the pyrrole N atoms and a presumable drug species would affect the position of this band in the SERS spectra of the hematin-drug complexes.

SERS of haematin-drug systems

Individually, considering haematin in the presence of CQ, the NIR-SERS spectrum of haematin is affected in relative intensities and positions of several bands. The NIR-SERS spectrum of haematin-CQ system is more similar to those of the CQ except for the dominance of the band at 760 cm^{-1}, which becomes the strongest (Fig. VI.2.3.1a). This fact could also suggest a preference of CQ adsorption instead of haematin on the Au particles. Such coverage effect of the active sites of metal only with the CQ species would not allow to observe contributions from haematin raised above.

Following the metallo-porphyrin ring modes of the haematin in the presence of CQ antimalarial drug under the surface plasmon resonance, the band at 1373 cm^{-1} (shifted from 1369 cm^{-1} in the SERS of pure haematin) increases in relative intensity, but dramatically overlaps with the CQ contribution. The position of the band at 1533 cm^{-1} was found to be unaffected, suggesting that the pyrrole N atoms of the porphyrin macrocycle are not involved into a possible interaction with the drug. A significant increase in the relative intensity of the band located at 941 cm^{-1} (porphyrin skeletal mode) was observed. Therefore,

the hypothesis of CQ adsorption as the first monolayer up to the coverage effect of the active metal sites could be excluded. The relative intensities of the bands attributable to the adsorbed CQ are different in the case of the haematin-CQ system, indicating changes in the attached geometry of CQ when the haematin coexists. More probably, the heme core upon adsorption becomes sensitive to the presence of CQ as an axial π acceptor ligand (the wavenumber increased from 1369 to 1373 cm^{-1}). This hypothesis would also explain the enhancement of the porphyrin mode at 941 cm^{-1}.

In the low-wavenumber spectral range, the band shape (Fig. VI.2.3.3d) attributable to the molecule-Au bond is different from that of the individual species (pure haematin or CQ). This fact further supports the presumably interaction of the haematin and CQ species upon adsorption. The contribution of the CQ aliphatic chain was not observed in the spectrum of the haematin-CQ system, suggesting that this moiety of CQ is not involved into the interaction of the two species. The involvement into this possible interaction is more predictable for the quinoline ring.

The haematin-MQ system adsorbed on Au particles displays specific SERS changes in the relative intensities and band positions as compared to those of either haematin-Au or MQ-Au SERS systems. The strongest band at 1532 cm^{-1} being characteristic for both species, remains unshifted, whereas the marker band at 1369 cm^{-1} of haematin is significantly increased relative to those at 759 cm^{-1} (Fig. VI.2.3.2a). Small increases by 2-3 cm^{-1} of the modes mostly associated to the quinoline stretching were also observed. These modifications could be explained as in the case of CQ-haematin system, in terms of individual adsorption of each species through the chemisorption mechanism, where the first monolayer could contain both MQ and haematin, or through the interaction between the two species upon adsorption. Taking a closer inspection of the band positions, the small shifts and relative intensities modification observed in the band positions of the MQ-haematin system suggest that an individual adsorption or physical coexistence of the two species would be less probable. A perturbed geometry upon coadsorption resulting from their interaction would be responsible for this spectral change. Therefore, the SERS data seems to support an interaction between the haematin and MQ upon adsorption on Au particles, where the pyrimidine moiety of MQ is less involved. However, it would be speculative to predict the interaction geometry at this point. Further experimental SERS data on these compounds at the physiological pH values of the infected erythrocytes are certainly necessary to get more insight into the physical chemistry of antimalarial complex mechanisms.

As resumed by Pagola et al.[622], their previous studies have established that the quinoline antimalarial drugs are associated with the detoxification of hemozoin by crystallization. The proposed mechanisms for such a drug action were classified into three categories: (*i*) direct binding of the drug to heme monomers or dimers in solution, which interferes with the crystallization of hemozoin; (*ii*) enzymatic inhibition of a protein that catalyzes hemozoin crystallization, and (*iii*) chemisorption of the drug onto the crystallized hemozoin, leading to inhibition of further heme aggregation. The first and third point raised by Pagola et al.[622] were investigated in depth using surface-enhanced Raman spectroscopy. Since the micro-Raman spectra of hemozoin encapsulated within the food vacuole of a *Plasmodium falciparum* infected erythrocyte and of haematin were found to be identical[636], and the band at 1374 cm^{-1}

assigned to A_{1g} modes observed upon 780 nm line excitation was used for Raman imaging of hemozoin within its natural environment[636], the present NIR-SERS results[649] open the possibility to further investigate the haematin-drug systems *in vivo*.

VI.2.4 Conclusions

FT-Raman and NIR-SERS spectra of chloroquine diphosphate and mefloquine hydrochloride were recorded and discussed.

The first NIR-SERS spectroscopic investigation of haematin in the presence of two widely used antimalarial drugs is reported. The modifications in the spectra of each haematin-drug systems could be explained in terms of interaction between the two species, where the aliphatic chain of CQ or the pyrimidine moiety in the case of MQ, were less involved into interaction upon adsorption on Au particles. The heme core was supposed to become sensitive to the presence of the respective quinoline skeletal ring as an axial ligand upon adsorption on the metal particles.

The present results strongly motivate further NIR-SERS investigations in order to get more insight into the *in vivo* mechanisms of malaria pigment-drug interaction and resistance.

The above mentioned work (Chapter VI) has been the result of a collaboration with **Conf. Dr. S. Cîntă Pînzaru** and **MSc. L. M. Andronie** from Babes-Bolyai University, Cluj-Napoca, Romania.

Chapter VII

Theoretical and experimental IR and Raman studies on binding mode in lanthanide complexes

---

"I consider nature a vast chemical laboratory in which all
kinds of composition and decompositions are formed.
Vegetation is the basic instrument the creator uses to set
all of nature in motion."

(Antoine Lavoisier, French chemist 1743-1794)

VII.1 3,5 Pyrazoledicarboxylic acid and its lanthanide complexes

New La(III), Ce(III), and Nd(III) complexes with 3,5-pyrazoledicarboxylic acid (HPy) were synthesized and characterized with elemental analysis, IR, and Raman spectroscopies. Significant differences in the IR and Raman spectra of the complexes were observed as compared to the spectra of the ligand. The metal-ligand binding mode was studied on the basis of theoretical and experimental data. B3PW91 and B3LYP methods with 6-311++G** and LANL2DZ basis sets were successfully applied to study the molecular and vibrational structures as well as the conformational behavior of the neutral ligand and its new La(III) complex. The theoretical calculations of HPy suggested bidentate binding mode through the carboxylic oxygen atoms. Detailed vibrational analysis of HPy and lanthanide-Py systems based on both the calculated and experimental spectra confirmed the suggested metal-ligand binding mode. The density functional theory (DFT) calculated geometries, harmonic vibrational wavenumbers including IR and Raman scattering activities for the ligand and its lanthanide complexes were in good agreement with the experimental data, a complete vibrational assignment being proposed.

VII.1.1 Study motivation

3,5-Pyrazoledicarboxylic acid (HPy), known both as a multiple proton donor and acceptor, can use its carboxylate oxygen and pyrazole nitrogen atoms, which are highly accessible to metals, to form both monodentate and/or multidentate M-O and M-N bonds[650,651]. The coordinated structural motifs thus generated can then readily form hydrogen bonded networks[650,652]. To date, the majority of known supramolecular assemblies are synthesized by direct reactions of metal salts with various ligands.
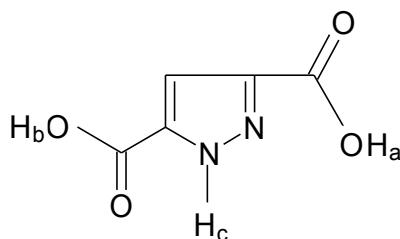
Figure VII.1.1.1. Molecular structure of the ligand 3,5-pyrazoledicarboxylic acid together with the three protons with different protonation power.

This ligand possesses three protons of different protonation power (H_a, H_b, and H_c in Fig. VII.1.1.1). Although both H_a and H_b are attached to carboxylic oxygen atoms, the two experience quite different coordination environments. The H_c in this ligand is linked to a nitrogen atom, and is more difficult to deprotonate than the other two hydrogen atoms. The difference in the binding power of these protons allows to deprotonate them at different pH levels. The flexible, multifunctional coordination sites of this ligand also give a high likelihood for generation of coordination polymers with high dimensionality. Its functional groups (carboxylate and pyrazole ring) bind to metals selectively. For

instance, the "harder" lanthanide metals coordinate more preferably to oxygen atoms than to the "softer'" nitrogen atoms, while the latter show a strong tendency to bind to transition metals. Cadmium (d^{10} configuration) was selected as a metal center in Pan et al.[652] because of its ambiability to form bonds with both nitrogen and oxygen atoms.

This ligand has demonstrated versatile coordination modes during the formation of numerous coordination frameworks, that is why it was a challenge for us to obtain new lanthanide(III) coordination complexes with 3,5-pyrazoledicarboxylic acid, especially in view of their application as anticancer agents. To the best of our knowledge, little is known about lanthanide(III) coordination compounds with 3,5-pyrazoledicarboxylic acid and such kind of lanthanide(III) complexes, possessing cytotoxic activity have not been previously reported. Recently published studies on rare-earth metal coordination compounds involving biologically active coumarin derivatives as ligands showed that a number of human tumor cell lines are very sensitive to the lanthanide complexes[653].

VII.1.2 Equilibrium structure of the neutral ligand, conformations, hydrogen bonding

Because no crystal structure data were yet reported on 3,5-pyrazoledicarboxylic acid, its structure was optimized at different level of theories (B3PW91/6-311++G**, B3PW91/LANL2DZ, B3LYP/6-311+G**, B3LYP/LANL2DZ) and compared with those of identical or similar functional groups of pyrazole from literature[650]. The calculated structural parameters of 3,5-pyrazoledicarboxylic acid are listed in Table VII.1.3.1 and the labelling of the atoms is shown in Fig. VII.1.3.1. As one can notice, there is a very good agreement between the theoretically determined parameters of 3,5-pyrazoledicarboxylic acid and its La(III) complex and the experimental values available in the literature[650]. 3,5-pyrazoledicarboxylic acid (Fig. VII.1.3.1) belongs to the C_s point group having only one symmetry element, the molecular plane[650].
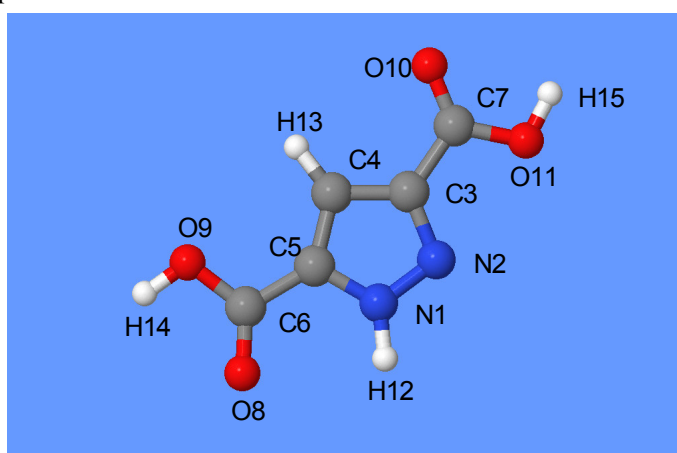
Figure VII.1.3.1. B3LYP/LANL2DZ optimized geometry of
3,5-pyrazoledicarboxylic acid molecule.

As shown in Table VII.1.3.1, the calculated N1-N2 bond lengths with different methods of the 3,5-pyrazoledicarboxylic acid molecule vary from 131.8 to 135.7 pm, which is somewhere between the length of a N-N single bond (145 pm) and that of a N=N double bond (125 pm)[34]. The N1-H12 bond

distance in this compound is calculated to be about 101.1-101.3 pm. Our theoretical values are in excellent agreement with experimental data[654] and with other theoretical studies on similar compounds[525,650]. The bond strength C5-N1, which has the average calculated at 134.9 pm is higher than that of the N2-C3 bond that is 135.4 pm (Table VII.1.3.1)[307,308]. These values are situated between the length of a C-N single bond (147 pm) and that of a C=N double bond (129 pm)[312]. Therefore, the calculated data suggest an extended π electron delocalization over the pyrazole system[313,314]. The elongation of the bond length supports the charge delocalization from C5-N1 and C4-C5 bond lengths, and the localization over the pyrazole ring[655]. The C4-C5 bond length, belonging to the pyrazole ring, calculated with different methods is shorter than the length of a C-C single bond (154 pm) and higher than of a C=C double bond (134 pm)[311]. All the bond lengths of the pyrazole ring are situated between the normal single and double bonds (Table VII.1.3.1) and are in a good agreement with previously reported theoretical[34,525,650,655] and experimental studies[654].

The average calculated of the C3-C7 and C5-C6 bond lengths are 146.3 and 147.3 pm, respectively, which are more appropriate from a C-C single bond (154 pm) as a C=C double bond (134 pm)[311]. The calculated dihedral angles corresponding to both carboxyl groups O8-C6-O9-H14, O10-C7-O11-H15, O8-C6-C5-N1, and O11-C7-C3-N2 are 0.0° (Table VII.1.3.1, Fig. VII.1.3.1) and come to demonstrate that both carboxyl groups are planar, and situated in the same plan with the pyrazole group. The two carboxyl groups of the 3,5-pyrazoledicarboxylic acid twist to an approximately equal and opposite extent with respect to the pyrazole ring. In our study this is revealed by the C3-C7-O11 (113.5°), C5-C6-O9 (112.5°) average calculated angles (Fig. VII.1.3.1, Table VII.1.3.1), the difference between C6-O9 and C7-O11 bonds being a 60° rotation. This conformation is characteristic to the β form of the odd diacids[515]. The two carbon-oxygen bonds for each carboxylate group do not differ in bond length values (Table VII.1.3.1) suggesting that the carbon oxygen single bonds are not coordinated[410,411].

Table VII.1.3.1. Selected calculated structural parameters of 3,5-pyrazoledicarboxylic acid in comparison with the available experimental data.

	Exp.[650,662]	Calcd.			
		B3LYP		B3PW91	
		6-311++G**	LANL2DZ	6-311++G**	LANL2DZ
Bond-lengths (pm)					
N1-N2	135.7; 137.0; 136.1	132.4	135.7	131.8	135.1
N2-C3	136.1; 136.8; 133.1	134.2	136.9	133.9	136.6
C3-C4	143.0; 141.6; 140.7	141.1	142.4	140.8	142.0
C4-C5	136.0; 137.2; 137.0	138.1	139.5	138.0	139.2
C5-N1	148.2; 134.0; 134.4	136.7	138.7	136.2	138.2
C5-C6		146.6	146.3	146.4	146.0
C3-C7		147.7	147.3	147.4	147.0
C6-O8	120.8; 121.3	121.1	124.7	120.9	124.4
C6-O9	131.4; 138.8	134.8	138.0	134.1	137.4
O9-H14	96.8	96.9	98.4	96.8	98.2
C3-O10	120.8	120.9	124.5	120.8	124.3
C3-O11	131.4	134.7	138.0	134.2	137.4
O11-H15	101.0; 98.0	96.9	98.5	96.7	98.2
C4-H13	110.1; 108.0; 107.5	107.6	107.8	107.7	107.8
N1-H12	101.9; 100.4; 101.0	101.1	101.3	101.1	101.2
Angles (°)					
C5-N1-N2	114.8; 114.0; 111.7	113.4	113.0	113.6	113.2
N1-N2-C3	107.9; 107.0; 104.9	104.7	104.2	104.6	104.2

N2-C3-C4	111.0; 111.8; 111.6	111.6	111.6	111.8	111.6
C3-C4-C5	104.0; 104.0; 104.9	104.3	105.0	104.2	104.8
C4-C5-N1	107.5; 106.6	106.1	106.3	106.0	106.2
N1-C5-C6	118.2	119.6	120.0	119.4	120.0
C4-C5-C6	130.7	134.3	133.7	134.5	133.7
N2-C3-C7	123.0	123.0	123.3	123.0	123.3
C4-C3-C7	124.2	125.4	125.1	125.4	125.1
C3-C4-H13	128.0; 126.9	127.7	127.3	127.8	127.3
N2-N1-H12	122.0; 119.0	120.7	120.4	120.7	120.4
O8-C6-O9	125.4	123.9	123.3	124.0	123.4
C6-O9-H14	110.6	107.5	111.0	107.2	111.0
O10-C7-O11	125.4	123.4	122.6	123.5	122.7
C7-O11-H15	108.3	106.8	110.3	106.5	110.3
C5-C6-O9	114.9	112.5	112.6	112.6	112.5
C3-C7-O11	115.4	113.4	113.7	113.4	113.7
C5-C6-O8		123.6	124.1	123.4	124.1
C3-C7-O10		123.2	123.7	123.1	123.7
C5-N1-H12	127.7; 127.3	126.0	126.6	125.7	126.4
C5-C4-H13	128.2	127.9	127.8	128.1	127.8
Dihedral angles					
O8-C6-O9-H14		0.0	0.0	0.0	0.0
O10-C7-O11-H15		0.0	0.0	0.0	0.0
O8-C6-C5-N1		0.0	0.0	0.0	0.0
O11-C7-C3-N2		0.0	0.0	0.0	0.0

VII.1.3 Theoretical study of the La-Py binding mode

Because no crystal structure data were yet reported on the La(III) complex of 3,5-pyrazoledicarboxylic acid molecule, its structure was optimized with Gaussian 03 program at different level of theories (B3PW91/LANL2DZ, B3LYP/LANL2DZ) and compared with those of identical or similar functional groups of lanthanide complexes from literature[34,525,650,654-656]. The calculated structural parameters of La(III) complex of 3,5-pyrazoledicarboxylic acid are presented in Table VII.1.4.1 and the labelling of the atoms is shown in Fig. VII.1.4.1. Our theoretical determined parameters are in a very good agreement with the experimental values available in the literature[34,525,650,654-656].
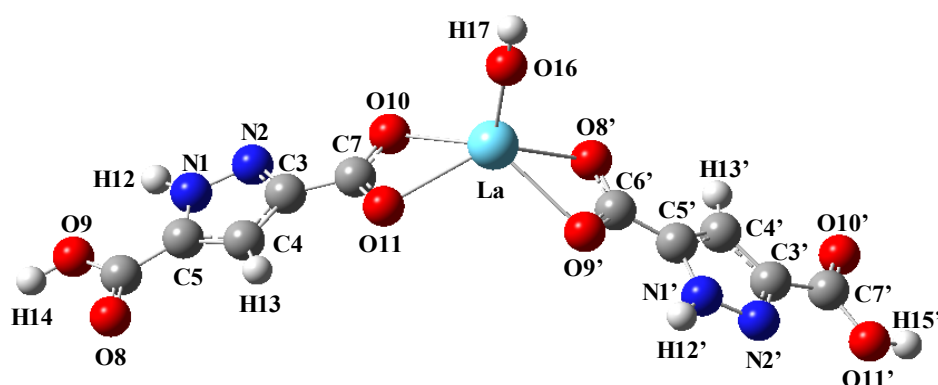
Figure VII.1.4.1. B3LYP/LANL2DZ optimized geometry of the La(III) complex
of 3,5-pyrazoledicarboxylic acid.

The calculated N1-N2 and N1'-N2' bond lengths (Table VII.1.4.1) with different methods of the

La(III) complex of 3,5-pyrazoledicarboxylic acid have the same values around 135.0 pm, which vary between the single bond length (145 pm) and the double bond length (125 pm)[34]. The N1-H12 and N1'-H12' bond distances in this compound are calculated to be about 101.1-101.3 pm and are in good agreement with experimental and theoretical values on similar compounds available in literature[650, 656]. As shown in Table VII.1.4.1, the C-N bond lengths of the compound are situated between 136.7 and 138.8 pm. Our theoretical values are higher than that of a C=N double bond (129 pm) and shorter than the length of a C-N single bond (147 pm)[312-314]. These calculated values suggest an extended π delocalzation over the pyrazole rings[312-314]. The elongation of the bond length supports the charge delocalization from C5-N1 (C5'-N1') and C4-C5 (C4'-C5') bond lengths and the localization over the pyrazole rings[655]. All bond distances of pyrazole rings are situated between the values of a normal single and double bonds (Table VII.1.4.1). We can assert that our density functional calculations are in good concordance with previous reported theoretical[650] and experimental[650,654] studies.

Table VII.1.4.1. Selected calculated structural parameters of La(III) complex of 3,5-pyrazoledicarboxylic acid in comparison with the available experimental data.

| | Exp.[650,662] | Calcd. | |
| | | B3LYP | B3PW91 |
		LANL2DZ	LANL2DZ
Bond-lengths (pm)			
N1-N2	135.7; 136.1; 136.5	135.6	135.0
N2-C3	132.8; 136.3; 136.1; 134.0	137.0	136.7
C3-C4	141.6; 142.0; 143.0; 141.6; 143.6	142.4	142.0
C4-C5	136.4; 140.7; 136.0; 137.2; 137.0	139.6	139.3
C5-N1	134.0; 133.9; 134.4	138.8	138.3
C5-C6	151.4	146.3	146.0
C3-C7	150.3	147.1	146.8
C6-O8	123.5; 127.0; 120.8; 121.3	123.9	123.6
C6-O9	139.5; 138.8	139.7	139.1
O9-H14	96.8	98.3	98.1
O9'-La	258.3; 262.4; 246.0; 255.0; 258.6	255.2	254.7
O8'-La	252.3; 261.3; 247.0; 255.0; 257.5	255.7	254.3
C3-O10	128.4; 129.0; 131.4	130.7	130.3
C3'-O10'	123.5; 127.0; 120.8	124.5	124.3
C3-O11	135.2; 129.0; 131.4	131.7	131.3
C3'-O11'	138.1; 138.8	138.1	137.5
O11-La	252.1; 253.9; 246.0; 253.0; 255.2	253.8	252.9
O10-La	253.0; 250.6; 245.0; 246.4; 252.0	252.9	252.0
O11'-H15'	96.8; 101.0; 98.0	98.5	98.2
C4-H13	108.0	107.8	107.8
N1-H12	100.4; 101.0	101.3	101.1
La-O16	182.6; 246.0; 237.9; 213.0; 217.8	216.3	215.3
O16-H17	96.8	96.8	96.6
Angles (°)			
C5-N1-N2	115.3; 114.8; 111.7; 114.0	113.0	113.2
N1-N2-C3	108.9; 107.9; 107.0; 104.9; 103.4	104.3	104.2
N2-C3-C4	111.0; 111.8	111.5	111.5
C3-C4-C5	118.9; 104.0; 104.0	105.0	104.8
C4-C5-N1	107.5	106.2	106.2
N1-C5-C6	122.2; 118.2	122.7	122.8
C4-C5-C6	130.7	131.0	131.0
N2-C3-C7	123.0	121.9	121.9
C4-C3-C7	119.6; 123.3; 124.2	126.6	126.6
C3-C4-H13	117.9; 128.0	127.2	127.3
N2-N1-H12	122; 119.0	120.4	120.4
O8-C6-O9	121.0; 125.4	123.0	123.0
O8'-C6'-O9'	123.5	119.7	119.8

C6-O9-H14	108.1; 110.6	111.3	111.3
C6'-O9'-La	92.7; 92.7	94.0	93.4
C6'-O8'-La	91.2; 94.1	93.5	93.9
O10-C7-O11	119.3	118.9	119.1
O10'-C7'-O11'	121.3; 125.4	122.5	122.5
C7-O11-La	95.5	94.4	93.6
C7-O10-La	94.1	93.7	94.9
C7'-O11'-H15'	107.8; 108.3	110.1	110.2
C5-C6-O9	114.9	110.3	110.4
C3-C7-O11	115.4	118.8	118.7
C5-C6-O8	127.5	126.7	126.6
C3-C7-O10	123.3	122.9	122.2
C5-N1-H12	127.7	126.6	126.4
C5-C4-H13	128.0	127.7	127.8
O10-La-O11	63.8; 48.8; 67.1; 59.5	53.0	53.1
O8'-La-O9'	68.2; 47.8; 67.1; 60.6	52.7	52.8
O11-La-O9'	108.3	105.3	105.5
O10-La-O8'	109.9	106.4	106.3
O10-La-O16	110.4	113.6	113.6
O11-La-O16	111.9	114.1	114.2
O9'-La-O16	114.8	114.1	113.9
O8'-La-O16	116.2	114.1	113.9
La-O16-H17		179.5	179.4
Dihedral angles (°)			
O8-C6-O9-H14		-0.1	-0.1
O10'-C7'-O11'-H15'		0.0	0.0
O8-C6-C5-N1		180.0	180.0
O10'-C7'-C3'-N2'		-180.0	-180.0
C3'-C7'-O11'-H15'		-180.0	-180.0
C5-C6-O9-H14		180.0	179.9
C7-O11-La-O9'		-132.2	-132.2
C6'-La-O9'-O11		131.6	131.6
C7-O10-La-O8'		130.6	130.8
C6'-O8'-La-O10		-131.6	-131.8
C4-C3-C7-O11		-0.7	-0.8
C4'-C5'-C6'-O8'		0.1	0.2
N2-C3-C7-O10		-0.5	-0.6
N1'-C5'-C6'-O9'		0.5	0.4

The coordinated structural motifs thus generated can then readily form hydrogen bonds[657,658]. The C-C distances of the boundary rings are about 140.0-148.0 pm (Table VII.1.4.1). The C-OH distances are about 137 pm. The bond distances of the carboxyls, when they are involved in a hydrogen bond, are 130.0 pm and are shorter in free carboxyl groups (Table VII.1.4.1)[650]. The average calculated of the C3-C7 (C3'-C7') and C5-C6 (C5'-C6') bond lengths are 147.0 and 146.1 pm, which come close to a C-C single bond (154.0 pm) as a C=C double bond (134.0 pm)[311]. The average calculated of the C6-O8 and C6-O9 bond lengths (123.8 and 139.4 pm) are in good agreement with the average calculated of similar bond distances from the free 3,5-pyrazoledicarboxylic acid (122.8 and 136.1 pm) (Table VII.1.3.1). The same situation can be observed from the C3'-O10' and C3'-O11' bond distances, which have an average calculated of 124.4 and 137.8 pm in comparison with C3-O10 and C3-O11 bond length of the free 3,5-pyrazoledicarboxylic acid (122.6 and 136.1 pm). Considering these affirmations and taking into account that the dihedral angles of the free carboxyl groups, O8-C6-O9-H14 and O10'-C7'-O11'-H15' are almost 0.0°, we can deduce that both free carboxyl groups are planar. Because of calculated dihedral angles O8-C6-C5-N1 and O10'-C7'-C3'-N2' that are 180° and -180°, we can also assert that both planar carboxyl groups are in the same plane with the pyrazole ring (Table VII.1.4.1, Fig. VII.1.4.1).

The other two carboxyl groups participate to lanthanum-ligand binding mode formation. From our calculations with different methods of the La(III) complex of 3,5-pyrazoledicarboxylic acid, the C6'-O8', C6'-O9', C3-O10, and C3-O11 bond distances are importantly changed as follows: the average calculated of C6'-O8' bond length (130.4 pm) becomes higher than the correspondent C-O bond distance of free 3,5-pyrazoledicarboxylic acid, whereas the average calculated of C6'-O9' bond length (131.6 pm) becomes shorter that the same bond distance of the free compound. Similarly, the average calculated of C3-O10 (130.5 pm) is higher that the same bond of the free sample, while the average calculated of C3-O11 (131.5 pm) is shorter that the same distance in the free compound (Table VII.1.3.1, Table VII.1.4.1).

The mentioned changes confirm a π delocalization between lanthanum and both carboxyl groups, which take part in La-Py binding formation[410,411]. Considering that carboxyl groups of the La(III) complex of 3,5-pyrazoledicarboxylic acid twist to an approximately equal and opposite extent with the respect to the pyrazole rings (C5-C6-O9=110.3°, C3-C7-O11=113.7°, C5'-C6'-O9'=118.7°, and C3'-C7'-O11'=113.7°) and the differences between C6-O9···C7-O11 and C6'-O9'···C7'-O11' bonds being a 60° rotation, we can discuss about β conformation form of the odd diacids[515]. The two sets of carbon-oxygen bonds for each carboxylate group do not differ in bond distance between themselves (Table VII.1.4.1) but differ from the free calculated form of 3,5-pyrazoledicarboxylic acid suggesting that in the La(III) complex of 3,5-pyrazoledicarboxylic acid the carbon-oxygen single bonds are coordinated[410,411]. Because of the carboxyl groups, the 3,5-pyrazoledicarboxylic acid works as a π-acceptor ligand[650,657].

The average calculated of La-O bond lengths: La-O8' (255.0 pm), La-O9' (254.9 pm), La-O10 (252.4 pm), La-O11 (253.3 pm) agrees with the experimental bond length for β conformation form of the odd diacids and is specific for the monometallic complexes of lanthanum[650]. The increasing of M-O distances is related to decreasing of O-M-O angles[659]. In our work this can be observed as follows: O8'-La-O9' (52.7°) and O10-La-O11 (53.1°) (Table VII.1.4.1)[650,659]. The C-O and C-C bond length changes in the organic part of La complexes can be caused by the formation of a conjugated bond system with the ligand[650]. The average calculated bond angles (C6'-O8'-La) and (C6'-O9'-La) are the same value (93.7), whereas (C7-O10-La) and (C7-O11-La) are quite different (94.3° and 94.0°, respectively). From these values we can conclude that the La-O-C$_{aryl}$ linkages are not linear[660]. This assertion can be certified by the following calculated angles: O10-La-O8' (106.3°) and O11-La-O9' (105.4°) (Table VII.1.4.1).

The hydroxyl group attached to the lanthanum atom is almost linear, the calculated angle La-O16-H17 varies between 179.4-179.5°. The La-O16 bond distance is shorter that the distances between La and each oxygen of the carboxyl groups (215.8 pm) and the O16-H17 bond length has a value (96.7 pm), which is appropriate from the normal O-H bond length[650].

VII.1.4 Vibrational characterization of the Ln complexes of 3,5-pyrazoledicarboxylic acid

The vibrational fundamentals from the IR and Raman spectra, presented in Figs. VII.1.5.1 and VII.1.5.3, were analyzed by comparing these modes with those from the literature[650,660] in combination

with the results of our DFT calculations (i.e., harmonic vibrational wavenumbers and their Raman scattering activities). In Table VII.1.5.1 the selected calculated and experimental Raman and SERS data together with their tentative assignment are given. Examination of the Fig. VII.1.5.1, which shows the IR spectra of 3,5-pyrazoledicarboxylic acid and its lanthanide complexes, discloses some point of interest. The stretching vibrations around 3500 cm^{-1} in all spectra are attributed to the secondary aromatic amine.

This agrees with the observations from the literature that all hydrogen atoms attached to pyrazole nitrogen are not deprotonated. In the 3600-2700 cm^{-1} region we can observe the N1-H12 stretching mode as a shoulder at 3353 cm^{-1} for the Hpy (Fig. VII.1.5.1a), as a very strong band for the La(III) complex (3405 cm^{-1}) (Fig. VII.1.5.1b), as a strong and medium strong band for Ce(III) (3378cm^{-1}) (Fig. VII.1.5.1c) and Nd(III) (3404 cm^{-1}) (Fig. VII.1.5.1d) complexes. The presence of the NH stretching vibration mode in this wavenumber region is characteristic to the dimer structure of HPy[515,650]. Furthermore, for the dimer structures, the OH stretching mode are presents at 3220 cm^{-1} for the HPy as a strong band, at 3229 cm^{-1} and 3228 cm^{-1} for the La(III) and Ce(III) complexes, as shoulders, and is absent in the IR spectrum of the Nd(III) complex.

Moreover, the bands characteristics for dimmer structures of the ligand (Fig. VII.1.5.2) between 3200-1800 cm^{-1} are missing in the spectra of the complexes. The bands at around 3100 cm^{-1} in the IR spectra of the 3,5-pyrazoledicarboxylic acid and its lanthanide complexes can be attributed to the C4-H13 stretching mode.
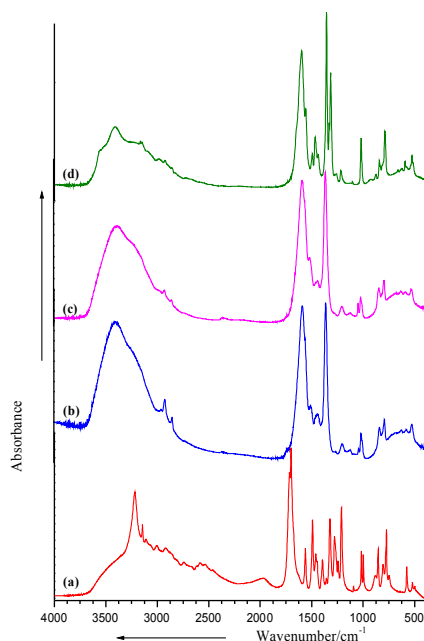
Figure VII.1.5.1. IR spectra of 3,5-pyrazoledicarboxylic acid (a), and its La(III) (b), Ce(III) (c), and Nd(III) (d) complexes.

In the hydrogen bonded dimer form[650] the OH stretching band in the IR centers is situated around 3000 cm^{-1} and its superimposed band shoulders assigned to overtones and combinations of bands near 1420 and 1300 cm^{-1} (due to the OH bending mode and C-O stretching mode) enhanced Fermi resonance with the broad OH stretching band. When the carbonyl is hydrogen bonded but not dimerized, a bond active in both IR and Raman spectra appears in the 1730-1705 cm^{-1} wavenumber region. In our spectra no

band can be observed in this region in the Raman spectra of HPy and its complexes. The dimer form is best characterized by the Raman band in the 1680-1640 cm^{-1} range[525,650] and by two IR bands: at about 1290 cm^{-1} (in plane C-OH bending mode) and somewhat weaker band, which is seen at 1440-1395 cm^{-1} (C-O stretching mode)[39,661].

The wavenumber region 2700-2500 cm^{-1} in the IR spectra of the 3,5-pyrazoledicarboxylic acid and its complexes with La(III), Ce(III), and Nd(III), is typical for strongly hydrogen bonded intermolecular complexes due to a strong anharmonic coupling (Fermi resonance) of the NH stretching vibrations with overtones and combinations of lower wavenumber modes of the bonded molecules[40-42].
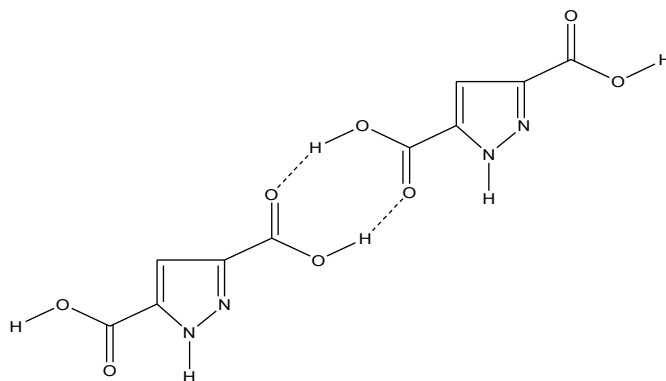
Figure VII.1.5.2. The suggested dimmer structure of the 3,5-pyrazoledicarboxylic acid (**Dr. I. Kostova**).

The very strong band in the IR spectrum of the HPy at 1700 cm^{-1} was assigned to the asymmetrical stretching mode of the C=O groups, while the shoulder at 1633 cm^{-1} corresponds to the symmetrical C=O stretching modes. In the Raman spectrum of the same compound, the asymmetrical stretching mode is represented by the very strong band at 1679 cm^{-1}, while the symmetrical stretching vibration was attributed to the shoulder at 1641 cm^{-1}. In the IR spectra of the lanthanide complexes, these bands are absent, while in their Raman spectra only the symmetrical stretching mods are present (Fig. VII.1.5.3; Tables VII.1.5.1, VII.1.5.2).

In the IR spectra of HPy and its Ln(III) complexes (Fig. VII.1.5.1) the medium and very strong bands at 1560 cm^{-1} (HPy), 1587 cm^{-1} (La(III) complex), 1585 cm^{-1} (Ce(III) complex), and 1596 cm^{-1} (Nd(III) complex) were assigned to the symmetrical stretching mode of the pyrazole ring, while in the Raman spectra this vibrational mode is distinguished for the HPy by the weak peak at 1558 cm^{-1}, for the La(III) complex by the shoulder at 1570 cm^{-1} and by the medium band at 1557 cm^{-1}, and for the Ce(III) and Nd(III) complexes, by the strong bands at 1549 and 1554 cm^{-1}, respectively (Fig. VII.1.5.3).

All these bands are shifted to lower wavenumbers (Tables VII.1.5.1, VII.1.5.3). Other bands connected with the pyrazol ring stretching modes in the IR spectra are the bands at 1460, 1395, 1357, 1018 cm^{-1} (for the HPy), the bands at 1438, 1361, 1017 cm^{-1} (for the La(III) complex), 1438, 1361 cm^{-1} (for the Ce(III) complex), and 1437, 1356 cm^{-1} (for the Nd(III) complex). In the Raman spectra, the pyrazole ring stretching modes are presented as follows: 1464, 1436, 1356, 1090, 1003 cm^{-1} (for the HPy), 1458, 1426, 1343, 1002 cm^{-1} (for the La(III) complex), 1418 cm^{-1} (for the Ce(III) complex), and 1457, 1426, 1346 cm^{-1} (for the Nd(III) complex). These bands are shifted in the Raman spectra of the complexes. Such observed shifting is indicative of the participation of the carboxyl groups in metal-

ligand bonding, which therefore affects the C-O, and C-C stretching vibrations as well as the C-OH and OCO bending vibrations of the pyrazole moieties[650]. The in plane bending modes of the pyrazole ring can be observed at around 1500 cm^{-1} for both IR and Raman spectra of the lanthanide complexes and only at 998 cm^{-1} (IR) and 988 cm^{-1} (Raman) for the HPy, whereas the out of plane bending modes of the pyrazole and CH bond have been observed around 880-600 cm^{-1} for HPy and its lanthanide complexes (Figs. VII.1.5.1, VII.1.5.3; Tables VII.1.5.1-VII.1.5.3).
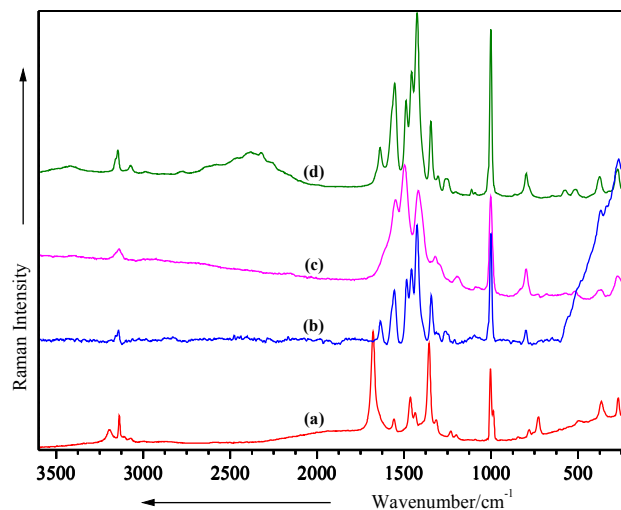
Figure VII.1.5.3. Raman spectra of 3,5-pyrazoledicarboxylic acid (a) and its La(III) (b), Ce(III) (c), and Nd(III) (d) complexes. Excitation: 514.5 nm, 50 mW.

The bands around 1320 cm^{-1}, strong in IR and weak in Raman, can be due to the asymmetrical C-O stretching mode, whereas the bands around 1200 cm^{-1} almost weak in IR and very weak in Raman, were attributed to the symmetrical C=O stretching mode[411]. The ring bending vibration and the skeletal deformation bands of free HPy, mainly in the 1090-270 cm^{-1} wavenumber region, show considerable changes on complex formation (Fig. VII.1.5.3). This may be attributed to the distortion of the pyrazole rings upon metalation. The new bands at about 510 cm^{-1}, which appear only in the IR and Raman spectra of the Ce(III) and Nd(III) complexes, can be due to the metal-oxygen vibrations. The new band at 524 cm^{-1} in the IR spectrum and the new one at 513 cm^{-1} in the Raman spectrum, which appear only fort he La complex, can be due to the metal-oxygen interactions[650]. In the low wavenumber region of the Raman spectrum of HPy (Fig. VII.1.5.3) the medium band at 366 cm^{-1} is slightly shifted to the higher wavenumbers in the Raman spectra of the lanthanides complex and becomes weaker. This one and its new neighbouring band at 343 cm^{-1} (La(III) complex) can be due to the metal-oxygen vibration modes[650]. The metal affects the carboxylate anion as well as the ring structure. The carboxylic acids interact with the metals as symmetric, bidentate carboxylate anions and both oxygen atoms of the carboxylate are symmetrically bonded to the metal[650] (Fig. VII.1.4.1). In this sense, we can observe in the Raman spectra of the La complex a shoulder at 224 cm^{-1} and in the Raman spectra of the Ce(III) and Nd(III) complexes, the bands at about 210 cm^{-1}, which can be due to the O-M-O vibration modes[650].

The binding mode of the ligand to Ce(III) and Nd(III) ions was elucidated by recording the IR

and Raman spectra of the complexes as compared with those of the free ligand. Examination of the Fig. VII.1.5.1, which shows the IR spectra of HPy and its new complexes with La (III), Ce(III), and Nd(III), discloses some point of interest. In general the strong peaks in the spectra of the complexes are around 1600-1400 cm^{-1}, which is characteristic for the expected adsorption for asymmetric and symmetric vibrations for uni- and bidentate carboxylate groups[662]. That is why we suggest the structure of the Ce(III) and Nd(III) complexes as presented on Fig. VII.1.5.4 (**Dr. I. Kostova**).
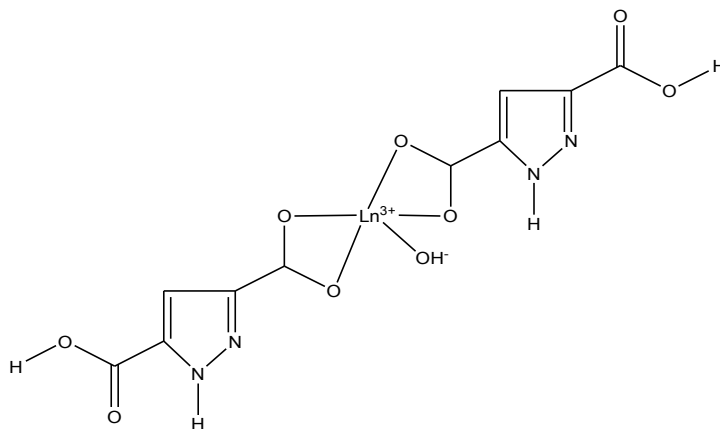
Fig. VII.1.5.4. The proposed structure of the Ce(III) and Nd(III) complexes with 3,5-pyrazoledicarboxylic acid.

VII.1.5 Conclusions

The complex of 3,5-pyrazoledicarboxylic acid with La(III), Ce(III), and Nd(III) were obtained for the first time using a new method of synthesis, which has not been reported in the literature so far. The composition of the new lanthanide complexes was characterized by elemental analysis and the empirical formula of the compounds was determined.

The geometry of the 3,5-pyrazoledicarboxylic acid was computed and optimized with B3PW91/6-311++G**, B3PW91/LANL2DZ, B3LYP/6-311++G**, and B3LYP/LANL2DZ methods, while the geometry of the new La(III) complex of 3,5-pyrazoledicarboxylic acid was computed and optimized with B3PW91/LANL2DZ and B3LYP/LANL2DZ methods.

The metal-ligand binding mode in the new La(III) complex of 3,5-pyrazoledicarboxylic acid was demonstrated through DFT modelling of La(III)-3,5-pyrazoledicarboxylic acid structure: 3,5-pyrazoledicarboxylic acid binds to La(III) ion through the oxygen atoms of the carboxylic groups.

IR and Raman spectra of the 3,5-pyrazoledicarboxylic acid and its La(III), Ce(III), and Nd(III) complexes were recorded and the marker bands of characteristic functional groups were identified, in order to use them as data bank for further application in trace analysis of rare-earth complexes. The vibrational study of 3,5-pyrazoledicarboxylic acid and its lanthanide complexes, based on both IR and Raman vibrational data, helped to gain a deeper insight into the coordination behavior of the ligand and the coordination polyhedron of its lanthanide complexes.

Table VII.1.5.1. Selected calculated and experimental IR and Raman wavenumbers (cm^{-1}) of 3,5-pyrezoledicarboxylic acid (HPy) and its La(III) complex ([La(Py)]) and their tentative assignment.

IR		Calcd. IR freqs. [HPy]				Calcd. IR freqs. [La(Py)]		Raman solid		Vibrational assignment
		B3PW91		B3LYP		B3PW91	B3LYP			
HPy	La(Py)	LANL2DZ	6-311++G**	LANL2DZ	6-311++G**	LANL2DZ	LANL2DZ	HPy	La(Py)	Refs. 650,662
1968 w										ν_{asym} (COO)
1717 vs	1735 vw	1716		1698		1743	1725			ν_{sym} (COO)
1700 vs		1710		1692		1710	1693	1679 vs		ν_{asym} (C=O
1633 sh						1633	1615	1641 sh	1634 w	ν_{sym} (C=O)
	1587 vs	1601	1604	1585	1590	1610	1594	1588 w	1570 sh	ν_{sym} (ring)
1560 m						1564	1547		1557 m	ν_{sym} (ring)
1492 s	1508 m	1524	1519		1501	1486	1510		1485 m	δ_{ip} (ring)
1460 m		1459	1476	1507	1457	1458	1463	1464 m	1458 m	ν (N=N); ν (ring)
1395 sh	1438 m	1436	1450	1440	1433	1424	1437	1436 wm	1426 s	ν (ring); ν (C-O)
1357 m	1361 vs	1375	1383	1420		1364	1362	1356 vs	1343 m	ν (ring)
1322 s		1332	1350	1357	1363	1327	1316	1316 w	1317 vw	ν (C-O)
1278 ms	1266 vw			1320	1337	1264	1251		1264 vw	δ_{op} (CH); δ (C-OH)
1244 m		1281	1288	1270	1279	1253	1243	1231 w		δ_{ip} (CH); ν (COC)
1210 s	1199 w	1222	1244	1200	1225	1214	1197	1201 w		ν_{sym} (C=O)
1094 w	1123 vw	1158	1168	1153	1152	1142	1136	1133 vw		δ_{ip} (NH)
	1041 w	1081	1092	1090	1089	1031	1070	1090 vw		ν (ring); δ (CH)
1018 m	1017 wm	1021	1030	1012	1025	1007	1023	1003 s	1002 s	δ_{ip} (CH); ν (ring)
998 m		984	998	976	994	990	997	988 ms		δ_{ip} (ring)
881 wm			884		885	940	939	897 vw		δ_{op} (CH); δ_{op} (ring)
852 m	838 wm							844 vw		δ_{op} (CH)
806 wm		794	797	787	792	810	803	782 vw	801 w	δ_{op} (CH)
772 ms	790 m	777	779	766	773	801	795			δ_{op} (CH)
747 wm		771	733	759		771	759	756 sh		δ_{op} (CH)
	625 w	713	716	708	729	691	686	729 wm	654 vw	δ (OCO)
577 m	578 w	585	571	579	609	580	575	605 vw	563 vw	δ_{op} (ring)
	524 w	555	552	552	547	517	514		513 vw	ν (M-O)
499 w	475 sh	495	504	492	502	500	498	495 vw		δ (OCO)
						382	380	366 m	376 w	ν (skeletal)
		323	328	322	326	375	373		343 vw	ν (M-O)
		266		264		279	278	270 m	277 w	δ_{op} (skeletal)
			322		224	267	267		224 sh	ν (O-M-O)

Abbreviation: vw – very weak; w – weak; m – medium; ms – medium strong; s – strong; vs – very strong; sh – shoulder; υ – stretching; δ – bending; sym – symmetric; asym – asymmetric; ip – in-plane; op – out-of-plane, M – metal, ring – pyrazole ring.

Table VII.1.5.2. Selected calculated and experimental IR wavenumbers (cm⁻¹) of 3,5-pyrazoledicarboxylic acid (HPy) and its Ce(III) ([Ce(Py)]) and Nd(III) ([Nd(Py)]) complexes and their tentative assignments.

| Calcd. IR freqs. | | | | IR | | | Vibrational assignment |
| B3PW91 | | B3LYP | | | | | |
LANL2DZ	6-311++G**	LANL2DZ	6-311++G**	HPy	[Ce(Py)]	[Nd(Py)]	Ref. 662
3347		3331		3353 sh	3378 s	3404ms	ν (NH)
	3294		3285	3220 s	3228 sh		ν (OH)
				3144 wm	3165 sh	3163 wm	ν (CH)
				3109 w	3101 sh	3092 sh	ν (CH)
				3064 sh	3070 sh		ν (CH)
				3002 w	3003 sh	2984 w	ν (=C-H)
				2920 w	2924 vw	2924 w	ν (CH)
				2876 sh	2854 vw	2855 w	ν (C-C-H)
				1968 w			νasym (COO)
1716		1698		1717 vs			νsym (COO)
1710		1692		1700 vs			νasym (C=O)
				1633 sh			νsym (C=O)
1601	1604	1585	1590	1560 m	1585 vs	1596 s	νsym (ring)
1524	1519		1501	1492 s	1513 m	1494 w	δip (ring)
1459	1476	1507	1457	1460 m		1467 m	ν (N=N); ν (ring)
1436	1450	1440	1433		1438 wm	1437 wm	ν (ring)
1375	1383	1420		1395 sh			ν (ring)
1332	1350	1357	1363	1357 m	1361 vs	1356 vs	ν (ring); δ (OH)
1332		1320	1337	1322 s		1315 s	ν (C-O)
1281	1288	1270	1279	1278 ms		1272 w	δop (CH)
1222	1244		1225	1244 m			δip (CH); ν (COC)
1222	1188	1200	1181	1210 s	1200 w	1217 w	νsym (C=O)
1158	1168	1153	1152				δip NH; ν (ring)
1081	1092	1090	1089	1094 w	1043 m	1104 vw	ν (ring); ν (CH)
1021	1030	1012	1025	1018 m	1017 m	1019 m	δip (CH); δop (CH); ν (ring)
984	998	976	994	998 m			δip (ring)
	884		885	881 wm		875 vw	δop (CH); δop (ring)
				852 m	840 m	843 wm	δop (CH)
794	797	787	792	806 wm	790 m	809 sh	δop (CH)
777	779	766	773	772 ms		788 m	δop (CH)
771	733	759	773	747 wm			δop (CH)
713	716	708	729				δ (OCO)
585	571	579	609	577 m	581 w	593 w	δop (ring)
555	552	552	547	522 w	527 w	526 w	δop (NH)
495	504	492	502		508 sh	515 sh	ν (M-O)
445	460	443	458	499 w		452 wv	δ (OCO)

Abbreviations: vw – very weak; w – weak; m – medium; ms – medium strong; s – strong; vs – very strong; sh – shoulder; υ - stretching; δ - bending; sym – symmetric; asym – asymmetric; ip – in plane; op – out of plane; M – metal.

Table VII.1.5.3. Selected calculated and experimental Raman wavenumbers (cm^{-1}) of 3,5-pyrazoledicarboxylic acid (Hpy) and its Ce(III) ([Ce(Py)]) and Nd(III) ([Nd(Py)]) complexes and their tentative assignments.

| Calcd. | | | | Raman solid | | | Vibrational assignment |
| B3PW91 | | B3LYP | | | | | |
LANL2DZ	6-311++G**	LANL2DZ	6-311++G**	HPy	Ce(Py)$_2$	Nd(Py)$_2$	Ref. 662
3348		3332				3417 vw	ν (NH)
	3295		3285				ν (OH)
				3137 m	3139 wm	3145 wm	ν (CH)
				3111 w			ν (CH)
				3071 w		3071 w	ν (CH)
						1996 sh	ν$_{asym}$ (COO)
1710		1698		1679 vs			ν$_{asym}$ (C=O)
1601		1691		1641 sh	1620 sh	1637 wm	ν$_{sym}$ (C=O)
1524	1604	1585	1590	1558 w	1549 s	1554 s	ν$_{sym}$ (ring)
	1476	1507	1501		1498 vs	1489 ms	δ$_{ip}$ (ring)
1459	1450	1440	1457	1464 m		1457 s	ν (N=N); ν (ring)
1436		1420	1433	1436 w/m	1418 s	1426 vs	ν (ring)
	1383			1390 sh			ν (ring)
1375		1357	1363	1356 vs		1346 ms	ν (ring); δ (C-OH)
1332	1350	1320	1337	1316 w	1322 m	1305 w	ν (C-O)
1280	1288	1270	1279		1299 sh		δ$_{op}$ (CH)
1222	1244		1225	1231 w	1257 sh	1260 w	δ$_{ip}$ (CH); ν (COC)
	1188	1200	1181	1201 w	1195 wm	1204 vw	ν$_{sym}$ (C=O)
1158	1168	1153	1152	1133 vw		1112 vw	δ$_{ip}$ NH; ν (ring)
1081	1092	1090	1089	1090 vw	1089 vw	1093 vw	ν (ring); ν (CH)
1021	1030	1012	1025	1003 s	1002 s	1002 vvs	δ$_{ip}$ (CH); δ$_{op}$ (CH); ν (ring)
984	998	976	994	988 ms			δ$_{ip}$ (ring)
	884		885	897 vw			δ$_{op}$ (CH); δ$_{op}$ (ring)
				844 vw	857 sh	863 vw	δ$_{op}$ (CH)
	797	787	792		798 m	798 wm	δ$_{op}$ (CH)
794	779	766	773	782 vw			δ$_{op}$ (CH)
771		759		756 sh			δ$_{op}$ (CH)
713	733	708	729	729 w/m	730 vw/ 680	648 vw	δ (OCO)
585	571	579	609	605 vw	572 vw	572 w	δ$_{op}$ (ring)
555	552	552	547		518 w	515 w	ν (M-O)
323	328	322	326	366 m	368 w	376 wm	ν (M-O)
217	222	218	224		210 wm	212 sh	ν (O-M-O)

Abbreviations: vw – very weak; w – weak; m – medium; ms – medium strong; s – strong; vs – very strong; sh – shoulder; ν - stretching; δ - bending; sym – symmetric; asym – asymmetric; ip – in plane; op – out of plane; M – metal.

VII.2 Orotic acid and its lanthanide complexes

The complexes of La(III), Ce(III), and Nd(III) were synthesized by reaction of lanthanide (Ln(III)) nitrate with sodium salt of orotic acid in amounts equal to metal: ligand molar ratio of 1:2. The structure of the final complexes was determined by means of vibrational (IR and Raman) spectra and elemental analysis. The geometry of orotic acid (HOA) was computed and optimized with the Gaussian 03 program using the B3PW91/6-311++G**, B3PW91/LANL2DZ, B3LYP/6-311++G**, and B3LYP/LANL2DZ methods, while the geometry of the La(III) complex of orotic acid was also at first calculated and optimized with the B3PW91/LANL2DZ and B3LYP/LANL2DZ methods. Detailed vibrational analysis of HOA and Ln(III)-OA systems based on both the calculated and experimental spectra confirmed the suggested metal-ligand binding mode.

The calculated geometries, harmonic vibrational wavenumbers including IR and Raman scattering activities for the ligand and its La(III) complex were in good agreement with the experimental data, a complete vibrational assignment being proposed.

VII.2.1 Orotic acid and its utility

The coordination chemistry of orotic acid (2,6-dioxo-1,2,3,6-tetrahydropyrimidine-4-carboxylic acid, vitamin B_{13}, Fig. VII.2.1.1) has been an area of great activity. Orotic acid occupies a unique position in biology by being the only effective precursor in the biosynthesis of pyrimidine bases of nucleic acids in living organisms[663]. Metal orotates are widely applied in medicine. Platinum, palladium and nickel orotate complexes have been screened as therapeutic agents for cancer. More recent interest has focused on the proposed biological carrier function of orotic acid and the corresponding anionic species for metal ions, which is held responsible for the successful application of orotate complexes in curing syndromes associated with a deficiency of a variety of metals such as calcium, magnesium, zinc or iron[663].
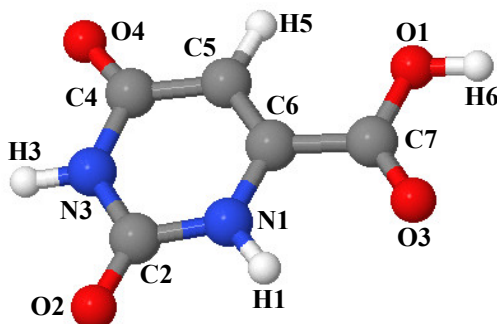
Figure VII.2.1.1. B3LYP/LANL2DZ optimized geometry of orotic acid together with its labeling.

Orotic acid (H_3L), (Fig. VII.2.1.1), acts as a diacid in aqueous solution, with the acidic function suggested to be located on the carboxylic group (pK_{a1}=2.09) and on the N3 site (pK_{a2}=9.45). The

monobasic form, hydroorotate, H_2L^-, appears to predominantly form complexes with coordination through the carboxyl oxygen atoms. Compounds with the Zn(II) and Mg(II) cations, where the H_2L^- anion does not enter the inner coordination sphere of the cation have also been reported. The multifunctionality of the hydroorotate, H_2L^- and orotate, HL^{2-} anions offers interesting possibilities in crystal engineering as a versatile ligand for supramolecular assemblies. The coordinated orotate anions exhibit a ligand surface with double or triple hydrogen-bonding capabilities, depending on the metal coordination mode, and has thus a potential to adopt several modes of interligand hydrogen bonding to allow the formation of extended, self-assembled structures.

This ligand has demonstrated versatile coordination modes during the formation of coordination frameworks, that is why it was a challenge for us to obtain new lanthanide(III) coordination complexes with orotic acid, especially in view of their application as anticancer agents[663].

The complexes of orotic acid with La(III), Ce(III), and Nd(III) were identified and characterized with elemental analysis, IR and Raman spectroscopies. For estimation of the most preferred reactive sites of orotic acid for electrophilic attack and metal binding, its geometry was calculated. The La(III)-orotic acid binding mode was elucidated on the basis of DFT calculations of the molecular and vibrational structures of orotic acid and its La(III)-OA model systems.

VII.2.2 Theoretical investigations of the orotic acid and its La(III) complex

The calculated structural parameters of orotic acid and its new La(III) complex are listed in Tables VII.2.2.1, VII.2.2.2 and the labeling of the atoms is shown in Figs. VII.2.1.1 and VII.2.2.1. As one can notice, there is a very good agreement between the theoretically determined parameters of orotic acid and its La(III) complex, and the experimental values available in the literature[311,312,663,664].

Orotic acid structure has been calculated and previously published data[665] helped us to better characterize its lanthanide complexes structure. The optimized molecular structure of orotic acid is very similar to the structure obtained by X-Ray diffraction (Table VII.2.2.1)[663-667]. The orotic acid molecule has a planar structure (Fig. VII.2.1.1). Orotic acid may exist with a syn- or anti-orientations of the carboxylic group[668]. The molecular geometry of orotic acid was fully optimized; the global minimum on the potential energy surface was characterized and identified. The carboxyl group seems to have a syn-orientation (Fig. VII.2.1.1), orientation that is specific in the solid phase of the orotic acid[668].

As shown in Table VII.2.2.1, the average calculated of N3-C4 bond length of orotic acid is 141.0 pm, which is very close to the normal N-C single bond (147 pm). The calculated N1-C2, N3-C2, and N1-C6 bond lengths with different methods of the orotic acid molecule vary from 136.9 to 140.1 pm, which is somewhere between the length of a N-C single bond (147 pm) and that of a N=C double bond (129 pm)[312]. From all the N-C bonds, the N1-C6 and N1-C2 are the shortest; this indicates a considerable π-electron delocalization within the C5-C6-N1-C2 skeleton[669]. The N1-H1 and N3-H3 bond distances in this compound are calculated to be about 101.2-101.7 pm. Our theoretical values are in excellent agreement with experimental data[667] and with other theoretical studies on similar compounds[666,668].

The C4-C5 bond length belonging to the uracil ring calculated with different methods, which vary from 145.9 pm to 146.8 pm, is shorter than the length of a C-C single bond (154 pm) and longer than that of a C=C double bond (134 pm)[311]. The average calculated of the C5-C6 bond length is 135.6 pm, which is a bit longer than a C=C double bond[311,664], and comes to confirm the π-electron delocalization. The C6-C7 bond length vary between 148.8 and 149.6 pm, respectively, which are more appropriate from a C-C single bond (154 pm) rather than a C=C double bond (134 pm)[311,664].

Table VII.2.2.1. Selected calculated structural parameters of orotic acid in comparison with the available experimental data.

	Exp. Refs. 663,664	Calcd.			
		B3LYP		B3PW91	
		6-311++G**	LANL2DZ	6-311++G**	LANL2DZ
Bond-lengths (pm)					
N1-C2	135.9; 137.5; 139.0; 137.8	138.9	140.0	138.5	139.5
C2-N3	138.1; 138.4; 138.7; 138.0	138.9	140.1	138.5	139.7
N3-C4	136.8; 138.1; 137.1; 139.0	140.6	141.8	140.1	141.3
C4-C5	143.3; 144.7; 144.9; 143.5	146.2	146.8	145.9	146.4
C5-C6	136.5; 135.2; 135.0; 136.1	135.0	136.4	134.9	136.1
C6-N1	136.9; 136.7; 138.5; 134.6	137.5	139.0	136.9	138.5
C6-C7	149.8; 152.8; 150.6; 152.9	149.6	149.2	149.2	148.8
C7-O1	130.6; 126.4; 134.8; 125.8	134.1	137.2	133.6	136.7
C7-O3	124.0; 124.5; 123.1; 125.6	120.7	124.3	120.5	124.1
C2-O2	125.4; 123.6; 122.4; 122.4	121.0	124.7	120.8	124.4
C4-O4	124.6; 124.0; 122.7; 125.5	121.5	125.1	121.3	124.9
O1-H6	102.0; 102.0	96.9	98.4	96.8	98.2
N1-H1	94.0; 94.0	101.3	101.7	101.2	101.6
N3-H3	89.0; 89.0	101.3	101.7	101.2	101.6
C5-H5	103.0; 103.1	107.8	108.1	107.9	108.1
Angles (°)					
C6-N1-C2	122.7; 118.9; 123.9; 118.1	123.7	123.2	123.7	123.2
N1-C2-N3	114.7; 117.9; 114.7; 116.2	112.9	113.5	112.9	113.5
C2-N3-C4	124.8; 126.9; 127.5; 127.3	128.1	127.6	128.3	127.7
N3-C4-C5	115.5; 116.0; 113.7; 112.4	113.7	114.1	113.6	114.1
C4-C5-C6	119.0; 122.5; 120.5; 121.4	119.6	119.6	119.5	119.5
C5-C6-N1	121.7; 124.4; 125.3; 122.9	122.0	122.1	122.1	122.1
N1-C6-C7	114.1; 113.9; 114.0; 113.1	113.4	113.8	113.3	113.7
C5-C6-C7	125.3; 120.7; 124.7; 123.4	124.6	124.2	124.6	124.2
C6-C7-O1	114.1; 117.4; 113.1; 114.8	113.1	113.1	113.1	113.1
C6-C7-O3	120.5; 118.8; 122.6	122.5	123.0	122.5	122.9
C7-O1-H6	105.0	107.8	111.7	107.5	111.7
O1-C7-O3	124.5; 127.6; 127.6; 126.4	124.4	123.9	124.4	124.0
C6-N1-H1	121.0; 122.0	118.9	119.2	118.8	119.2
C2-N1-H1	114.1	117.4	117.5	117.6	117.6
N1-C2-O2	123.0; 123.2; 123.3; 123.3	123.2	123.1	123.3	123.1
N3-C2-O2	121.2; 122.1; 120.5; 119.5	123.8	123.4	123.8	123.4
C2-N3-H3	116.0	115.5	115.7	115.4	115.7
C4-N3-H3	117.0; 117.1	116.4	116.7	116.3	116.7
N3-C4-O4	119.5; 122.4; 119.4; 121.5	121.0	120.7	121.0	120.7
C5-C4-O4	125.5; 123.9; 128.2; 126.4	125.3	125.2	125.4	125.2
C4-C5-H5		118.5	118.7	118.6	118.8
C6-C5-H5	124.0	121.9	121.7	121.9	121.7
Dihedral angles (°)					
N1-C6-C7-O3		0.0	0.0	0.0	0.0
H1-N1-C6-C7		0.0	0.0	0.0	0.0
C5-C6-C7-O1		0.0	0.0	0.0	0.0
H5-C5-C6-C7		0.0	0.0	0.0	0.0
O2-C2-N1-H1		0.0	0.0	0.0	0.0
O2-C2-N3-H3		0.0	0.0	0.0	0.0
O4-C4-N3-H3		0.0	0.0	0.0	0.0

O4-C4-C5-H5	0.0	0.0	0.0	0.0
O3-C7-O1-H6	0.0	0.0	0.0	0.0
C6-C7-O1-H6	-180.0	-180.0	-180.0	-180.0
C2-N1-C6-C7	-180.0	-180.0	-180.0	-180.0
C4-C5-C6-C7	-180.0	-180.0	-180.0	-180.0

The calculated C7-O3 bond distance is situated between 120.5 pm and 124.3 pm, which is longer than a normal C=O double bond (120 pm), while the C7-O1 bond length varies from 133.6 pm to 137.2 pm being shorter than a normal C-O single bond (143 pm)[407,408]. The difference in the carboxyl bond lengths C7-O1 and C7-O3 as compared to the normal single and double bond lengths suggests that the negative charge and the double bond are delocalized[407,408].

The O3-C7-O1 calculated angle varies from 123.9° to 124.4° and The calculated dihedral angle corresponding to the carboxyl group O3-C7-O1-H6 is 0.0° (Table VII.2.2.1, Fig. VII.2.1.1) and comes to demonstrate that the carboxyl group is planar, in the same plan with the uracil ring.

Both average calculated carbon-oxygen bond lengths belong to the uracil ring are appropriate values to a double C=O bond length (120 pm) as follows: 122.7 pm for the C2-O2 bond length and 123.2 pm for the C4-O4 bond distance (Fig. VII.2.1.1, Table VII.2.2.1). The two carbon-oxygen bonds of the carboxylate group do not differ in bond length values (Table VII.2.2.1) suggesting that the carbon-oxygen single bond is not coordinated[411,666].

The calculated dihedral angles C5-C6-C7-O1, H5-C5-C6-C7, N1-C6-C7-O3, and H1-N1-C6-C7 are 0.0° (Table VII.2.2.1) as well as O2-C2-N1-H1, O2-C2-N3-H3, O4-C4-N3-H3, and O4-C4-C5-H5. These values come to prove that the orotic acid molecule is planar. The planarity of the orotic acid molecule can be observed through the corresponding angles of the uracil ring, which are almost the same values as in the literature (Table VII.2.2.1)[663,666,669].

The calculated N1-C2 and N1'-C2' bond lengths (Table VII.2.2.2) with different methods of the La(III) complex of orotic acid have the same values around 139.7 pm, which vary between the single N-C bond length (147 pm) and the double N=C bond length (129 pm)[312]. The N1-H1 and N1'-H1' bond distances in this compound are calculated to be about 101.6-101.8 pm and are in good agreement with experimental and theoretical values on similar compounds available in literature[666,668]. As shown in Table VII.2.2.2, the other C-N bond lengths of the La(III) complex are situated between 139.7 pm and 141.8 pm. Our theoretical values are higher than that of a C=N double bond (129 pm) and shorter than the length of a C-N single bond (147 pm)[312,663]. These calculated values suggest an extended π delocalzation over the uracil rings[655] (Fig. VII.2.2.1). The elongation of the bond length supports the charge delocalization from C4-C5 (C4'-C5') and C5-C6 (C5'-C6') bond lengths and the localization over the uracil rings[663]. All bond distances of both uracil rings are situated between the values of a normal single and double bonds (Table VII.2.2.2). We can assert that our density functional calculations are in good concordance with previously reported studies[663-669].

The coordinated structural motifs thus generated can then readily form hydrogen bonds[657,658]. The C-C distances of the boundary rings are about 148.4-150.7 pm (Table VII.2.2.2). The C-O distances are about 130.0 pm. The bond distances of the carboxyls, when they are involved in a hydrogen bond, are 130.0 pm and are shorter than in free carboxyl groups (Table VII.2.2.2)[663]. The calculated averages of the

C6-C7 (C6'-C7') bond lengths are 148.6 and 150.5 pm, which come closer to a C-C single bond (154.0 pm) than to a C=C double bond (134.0 pm)[311].
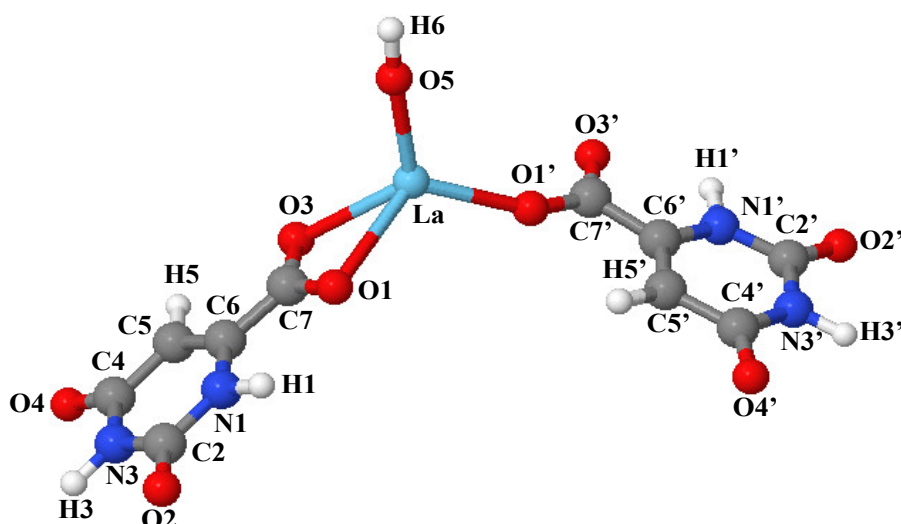
Figure VII.2.2.1. B3LYP/LANL2DZ optimized geometry of La(III) complex of orotic acid together with its atoms labeling.

Orotic acid usually acts as a bidentate dianionic ligand chelating to one metal ion through the deprotonated carboxylic group and the adjacent nitrogen atom. Although in our complex one of carbonyl oxygen of two orotate ligands remains free, and this unusual coordination mode may be ascribed to the high affinity of lanthanide ions for oxygen[670,671]. The La(III) atom is at least four-coordinate, with bonds to two oxygen atoms from the carboxylate of one of the orotate ligands, to one carboxyl oxygen atom of different orotate ligand, and to one oxygen atom from hydroxyl anion (Fig. VII.2.2.1). The La-O distances are in the range from 214.5 pm to 254.2 pm (Table VII.2.2.2). The complex is mononuclear and each local coordination unit around the metal ion contains two orotate ligands and one OH⁻ ion[663,664].

Table VII.2.2.2. Selected calculated structural parameters of La(III) complex of orotic acid in comparison with the available experimental data.

	Exp. Refs. 663,664	Calcd.	
		B3LYP LANL2DZ	B3PW91 LANL2DZ
Bond-lengths (pm)			
N1-C2	136.3; 135.9; 137.5; 139.0; 137.8	139.9	139.5
C2-N3	137.3; 138.1; 138.4; 138.7; 138.0	140.2	139.7
N3-C4	136.4; 136.8; 138.1; 137.1; 139.0	141.8	141.3
C4-C5	143.3; 141.9; 144.7; 144.9; 143.5	146.8	146.4
C5-C6	154.6; 136.5; 135.2; 135.0; 136.1	136.4	136.2
C6-N1	136.9; 136.7; 138.5; 134.6	138.9	138.4
C6-C7	149.8; 152.8; 150.6; 152.9; 152.1	148.8	148.4
C7-O1	130.6; 126.4; 134.8; 125.8; 126.7	131.4	131.1
C7-O3	124.0; 124.5; 123.1; 125.6; 122.5	130.3	129.9
C2-O2	125.4; 123.6; 122.4; 122.4; 122.6	124.6	124.4
C4-O4	124.6; 124.0; 122.7; 125.5; 122.1	125.1	124.8
O1-La	258.3; 262.4; 246.0; 255.0; 258.6	254.2	253.2
O1'-La	237.9 ; 246.0	229.0	228.2
O3-La	252.3; 261.3; 247.0; 255.0; 257.5	255.3	254.4
La-O5	237.9; 246.0; 182.7; 213.0; 217.8	215.5	214.5
O5-H6	102.0; 102.0; 96.8	96.9	96.7
N1-H1	94.0; 94.0	101.7	101.6
N3-H3	89.0; 89.0	101.7	101.6

C5-H5	103.0; 103.1	108.1	108.1
Angles (°)			
C6-N1-C2	122.7; 118.9; 123.9; 118.1; 118.7	123.2	123.1
N1-C2-N3	114.7; 117.9; 114.7; 116.2; 117.2	113.5	113.5
C2-N3-C4	126.4; 124.8; 126.9; 127.5; 127.3	127.6	127.7
N3-C4-C5	115.5; 116.0; 113.7; 112.4; 112.1	114.0	114.0
C4-C5-C6	119.0; 117.8; 122.5; 120.5; 121.4	119.6	119.5
C5-C6-N1	121.7; 124.4; 118.2; 125.3; 122.9	122.2	122.2
N1-C6-C7	114.1; 116.5; 114.0; 113.1; 113.6	115.3	115.3
C5-C6-C7	121.7; 125.3; 120.7; 124.7; 123.4	122.5	122.5
C6-C7-O1	114.1; 116.7; 117.5; 117.4; 113.1	118.5	118.4
C6-C7-O3	120.5; 118.8; 114.9; 114.3; 122.6	121.5	121.4
C7-O1-La	94.1; 92.7	93.7	93.6
C7'-O1'-La		152.0	151.7
C7-O3-La	94.1; 92.7	93.5	93.3
O1-C7-O3	124.5; 127.6; 128.3; 127.6; 126.4	120.0	120.2
C6-N1-H1	121.0; 122.0	119.0	118.9
C2-N1-H1	114.1	117.8	117.9
N1-C2-O2	123.0; 123.2; 123.3; 123.3	123.1	123.1
N3-C2-O2	121.2; 119.0; 122.1; 120.5; 119.5	123.4	123.4
C2-N3-H3	116.0	115.7	115.6
C4-N3-H3	117.0; 117.1	116.7	116.6
N3-C4-O4	119.5; 118.6; 122.4; 119.4; 121.5	120.8	120.8
C5-C4-O4	125.5; 123.9; 128.2; 126.4	125.2	125.2
C4-C5-H5	117.9; 118.2	119.1	119.2
C6-C5-H5	124.0	121.4	121.3
O1-La-O5	111.9	114.7	114.6
O3-La-O5	116.2	117.0	117.1
O1'-La-O5	114.8	116.9	116.7
Dihedral angles (°)			
N1-C6-C7-O3		-179.8	-179.8
N1-C6-C7-O1		0.0	0.0
H1-N1-C6-C7		-0.1	-0.1
C5-C6-C7-O1		180.0	179.9
C7-O1-La-O5		105.9	106.1
C7'-O1'-La-O5		-67.0	-66.8
C7-O3-La-O5		-101.4	-101.3

Both carboxyl oxygens of one of the orotate ligand, the carboxyl oxygen from the other one orotate ligand, and one oxygen from hydroxyl anion participate to La(III)-ligand binding mode formation. From our calculations with different methods of the La(III) complex of orotic acid, the C7-O1, C7'-O1', and C7-O3 bond distances are considerably changed in the complex in comparison to the free ligand (Tables VII.2.2.1 and VII.2.2.2) as follows: the average calculated of C7-O1 bond length (131.3 pm) becomes shorter that the correspondent C-O bond distance of free orotic acid, whereas the average calculated of C7'-O1' bond length (133.4 pm) turns out to be shorter that the same bond distance of the free compound. Similarly, the average calculated of C7-O3 (130.1 pm) is higher that the same bond of the free sample, while the average calculated of C7'-O3' bond length (131.5 pm), which is not engaged in coordination, is shorter that the same distance in the free compound (Tables VII.2.2.1 and VII.2.2.2). The mentioned changes confirm a π delocalization between La(III) and both carboxyl groups, which take part in La(III)-orotic acid binding formation[411,663,669]. The three carbon-oxygen bonds of carboxylate groups do not differ in bond distance between themselves (Tables VII.2.2.2) but differ from the free calculated form of orotic acid suggesting that in the La(III) complex of orotic acid the carbon-oxygen single bonds are coordinated[411]. Because of the carboxyl groups, the orotic acid works as a π-acceptor ligand[657].

The average calculated of La-O bond lengths: La-O1 (253.7 pm), La-O1' (228.6 pm), La-O3 (254.8 pm), La-O5 (215.0 pm) agree with the literature[670,671] and are specific for the monometallic complexes of lanthanum[663]. The increasing of M-O distances is related to decreasing of O-M-O angles[659]. In our work this can be observed as follows: O1-La-O5 (114.7°) and O1'-La-O5 (116.8°) (Table VII.2.2.2)[659]. The C-O and C-C bond length changes in the organic part of lanthanum complexes can be caused by the formation of a conjugated bond system with the ligand[663]. The average calculated bond angles (C7-O1-La) and (C7-O3-La) have the same value (93.5°), whereas (C7'-O1'-La) is quite different (151.9°). From these values we can conclude that the La-O-C$_{aryl}$ linkages are not linear[660]. This assertion can be certified by the following calculated angles: O3-La-O5 (117.1°) and O1-La-O1' (115.1°) (Table VII.2.2.2, Fig. VII.2.2.1). The hydroxyl group attached to the La(III) atom is almost linear, the calculated angle La-O5-H6 being 177.5°. The La-O5 bond distance is shorter that the distances between lanthanum and the oxygens of the carboxyl groups (215.0 pm) and the O5-H6 bond length has a value (96.8 pm), which is appropriate for the normal O-H bond length[546].

VII.2.3 Vibrational spectroscopy

The vibrational fundamentals from the IR and Raman spectra, presented in Figs. VII.2.3.1 and VII.2.3.2, were analyzed by comparing these modes with those from the literature[666,669] in combination with the results of our DFT calculations. In Tables VII.2.3.1 and VII.2.3.2 the selected calculated and experimental IR and Raman data together with their attempted assignments are given.
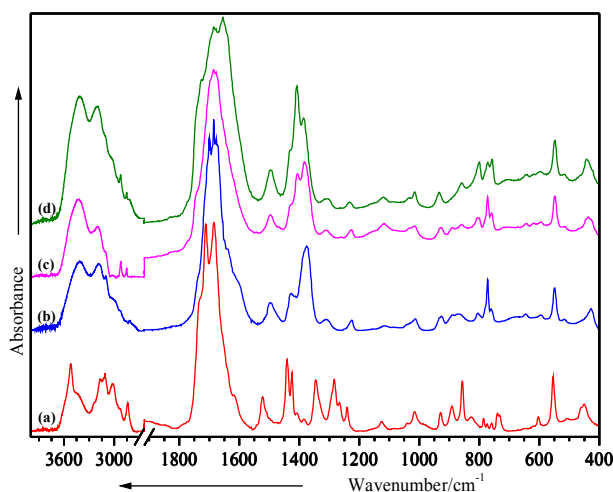
Figure VII.2.3.1. IR spectra of orotic acid (a) and its La(III) (b), Ce(III)(c), and Nd(III) (d) complexes.

In the 3600-2000 cm^{-1} spectral region of the IR spectrum, the OH and NH stretches give rise to medium IR bands (Figs. VII.2.3.1 and VII.2.3.2). The assignment of the OH and NH bands is quite difficult because they appear overlapped in the same spectral region, and the involvement of these groups in hydrogen bonds affects their wavenumbers and produces a relevant band broadening[669]. In the IR spectra, the medium bands at 3520 cm^{-1} (orotic acid), 3410 cm^{-1} (La(III) complex), 3437 cm^{-1} (Ce(III)

complex), and at 3415 cm^{-1} (Nd(III) complex) were assigned to the NH stretching modes, while the shoulder at 3232 cm^{-1} (orotic acid), the medium bands at 3190 cm^{-1} (La(III) complex), 3197 cm^{-1} (Ce(III) complex), and 3215 cm^{-1} (Nd(III) complex) were attributed to the OH stretching modes (Fig. VII.2.3.1, Tables VII.2.3.1 and VII.2.3.2).

When the carbonyl is hydrogen bonded but not dimerized, a bond active in both IR and Raman spectra appears at 1730-1705 cm^{-1}. In our IR spectra, one very strong band can be observed in this region, at 1712 cm^{-1} for orotic acid, absent for the La(III) complex, and at 1743 and 1726 cm^{-1} for the Ce(III) and Nd(III) complexes, respectively, which were assigned to the symmetrical stretching mode of $C2=O2$ and to the N-H stretching mode. In this region one can observe a medium band at 1715 cm^{-1} in the Raman spectrum of the free ligand, two shoulders at 1747 and 1714 cm^{-1} in the Raman spectrum of the La(III) complex, two, one very weak and one medium strong, peaks at 1745 and 1688 cm^{-1} in the Raman spectrum of the Ce(III) complex, and two, one very weak and one strong signals at 1744 and 1755 cm^{-1} in the Raman spectrum of the Nd(III) complex (Fig. VII.2.3.2). The dimer form is best characterized by the Raman band in the 1680-1640 cm^{-1} range[663,664] and by the two IR bands: at about 1290 cm^{-1} (in plane C-OH bending mode) and somewhat weaker band, which may be seen in the 1440-1395 cm^{-1} wavenumber region (C-O stretching mode) (Figs. VII.2.3.1 and VII.2.3.2; Tables VII.2.3.1 and VII.2.3.2)[39,661].

The wavenumber region 2700-2500 cm^{-1} in the IR spectra of the orotic acid and its lanthanide complexes is typical for strongly hydrogen bonded intermolecular complexes due to a strong anharmonic coupling (Fermi resonance) of the NH stretching vibrations with overtones and combinations of lower wavenumber modes of the bonded molecules[40].
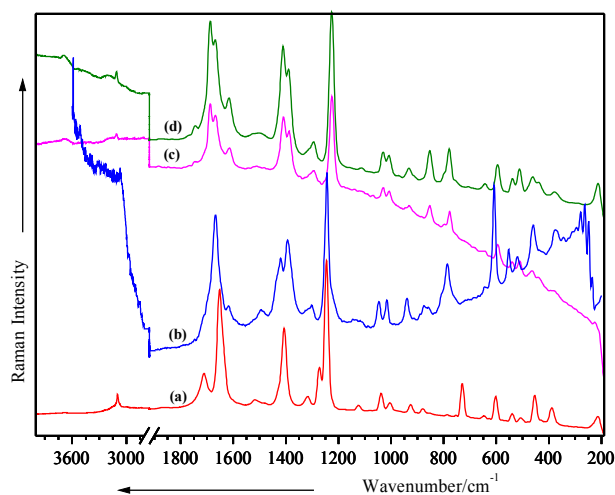
Figure VII.2.3.2. Solid state Raman spectra of orotic acid (a) and its La(III) (b), Ce(III) (c), and Nd(III) (d) complexes. Excitation: 784.8 nm, 35 mW (a,b); 514.5 nm, 50 mW (c,d).

The very strong bands at 1684 cm^{-1} (IR spectrum of orotic acid), 1685 cm^{-1} (IR spectrum of La(III) complex), 1686 cm^{-1} (IR spectrum of Ce(III) complex), and 1685 cm^{-1} (IR spectrum of Nd(III) complex) were assigned to the symmetrical stretching modes of $C4=O4$, $C4'=O4'$ and to the C6=C5, C6'=C5' stretching modes (Fig. VII.2.3.1). In the Raman spectra, these vibrations can be observed as very strong bands at 1657 cm^{-1} for orotic acid, 1668 cm^{-1} for its La(III) complex, 1668 cm^{-1} for the Ce(III)

complex, and 1669 cm^{-1} for the Nd(III) complex (Fig. VII.2.3.2). In the IR spectra of orotic acid and its lanthanide complexes, the shoulders at 1617 cm^{-1} for the orotic acid and 1641, 1678, and 1655 cm^{-1} for its La(III), Ce(III), and Nd(III) complexes, respectively, were attributed to the C=C and C=O stretching contributions, whereas in the Raman spectra these vibrational modes are distinguish for the orotic acid through the shoulder at 1615 cm^{-1}, through the weak band at 1619 cm^{-1} for its La(III) complex, and through the weak medium bands at 1614 and 1617 cm^{-1} for its Ce(III) and Nd(III) complexes.

The asymmetrical COO$^-$ stretching mode, absent in the IR spectra of Ce(III) and Nd(III) complexes, was observed as a medium band at 1522 cm^{-1} (in the IR spectrum of orotic acid), a shoulder at 1604 cm^{-1} (in the IR spectra of La(III) the complex), while in the Raman spectra this vibration was detected only for the free ligand as a weak band at 1522 cm^{-1} (Figs. VII.2.3.1 and VII.2.3.2). The symmetrical COO$^-$ stretching mode was observed in the IR spectra as weak bands at 1407 cm^{-1} for the orotic acid, as strong, medium, and medium strong peaks at 1375, 1406, and 1408 cm^{-1} for its La(III), Ce(III), and Nd(III) complexes, while in the Raman spectra this vibration appears as a strong peak at 1414 cm^{-1} for the free ligand and as strong bands at 1394, 1409, and 1411 cm^{-1} for its Ln complexes (Figs. VII.2.3.1, VII.2.3.2; Tables VII.2.3.1, VII.2.3.2).

The C-O stretching mode, which appears as medium strong and medium bands in the IR spectra, at 1442 cm^{-1} for orotic acid and at 1498 cm^{-1} for its lanthanide complexes, in the Raman spectra is represented by a shoulder at 1508 cm^{-1} for orotic acid, by a weak peak at 1495 cm^{-1} for the La(III) complex, and by two very weak peaks at 1511 and 1502 cm^{-1} for the Ce(III) and Nd(III) complexes. In the 1800-900 cm^{-1} spectral region of the IR spectra, the medium strong and medium bands at 1424 and 1426 cm^{-1} for the free ligand and its La(III) complex, as well as the shoulder at 1424 cm^{-1} for its Ce(III) complex (Figs. VII.2.3.1) can be due to the stretching modes of N-H and N'-H', respectively. These vibrations are rather different and shifted in the Raman spectra: at 1436 cm^{-1} for the free ligand, at 1420 cm^{-1} for the La(III) complex, and absent in the IR spectra of the Ce(III) and Nd(III) complexes.

The C5'-H5' and N1'-H1' bending modes were attributed to the medium band at 1345 cm^{-1} in the IR spectrum of the orotic acid, while in the IR spectra of the complexes they are absent in the case of La(III), and present as weak bands at 1312 and 1308 cm^{-1} in the case of Ce(III) and Nd(III) complexes, respectively (Figs. VII.2.3.1). In the Raman spectra these vibrations can be observed for the ligand and for the complexes. The C5-H5, N1-H1, and C-OH bending modes are present in the IR spectra as well as in the Raman spectra. In the IR spectra they are observed at 1284 cm^{-1} for the free ligand, at 1311 cm^{-1} for the La(III) complex, and absent for Ce(III) and Nd(III) complexes, while in the Raman spectra they are detected at 1282 cm^{-1} and 1302 cm^{-1}, for the free ligand and its La(III) complex, respectively and absent for the other two complexes.

The weak band at 1266 cm^{-1}, which can be observed only in the IR spectrum of the orotic acid can be due to the C=O bending mode and to the symmetrical stretching mode of N1-C2-N3. The weak peak at 1241 cm^{-1} that appears in the IR spectrum of the free ligand and only in the IR spectra of its Ce(III) and Nd(III) complexes (1227, 1232 cm^{-1}), was assigned to the stretching modes of C2-N3-C4 and C6=C5-C4. In the Raman spectra these vibrations appear as very strong bands for the ligand as well as for

its lanthanide complexes. The presence of the second ligand molecule in the lanthanide complexes is revealed by the C2'-N3'-C4' and C6'=C5'-C4' stretching modes, which were attributed to both bands from the IR and Raman spectra of the complex (1205 and 1226 cm^{-1}) and in the same mode to the in plane bending modes of C5'H5' and N1'H1', which were assigned to both the bands from the IR and Raman spectra of the complex (1119 and 1114 cm^{-1}).

The bands around 1015 cm^{-1}, weak in IR and medium in Raman spectra, can be due to the symmetrical C=O stretching mode, whereas the band around 930 cm^{-1} almost weak in IR and medium in Raman spectra, were attributed to the symmetrical C(ring)-C(carboxyl) bridge bond stretching mode. The uracilate ring bending vibration and the skeletal deformation bands of the free orotic acid, mainly in the 900-300 cm^{-1} wavenumber region, show considerable changes on complex formation (Figs. VII.2.3.1 and VII.2.3.2; Tables VII.2.3.1 and VII.2.3.2). These changes may be attributed to distortion of the uracilate rings upon coordination. The new bands at 428, 441, 437 cm^{-1} in the IR spectra and at 434, 437, 443 cm^{-1} in the Raman spectra, which appear only for the La(III), Ce(III), and Nd(III) complexes, can be due to the lanthanide-oxygen interactions[669]. In the low wavenumber region of the Raman spectrum of orotic acid (Fig. VII.2.3.2), the medium strong band at 395 cm^{-1} is importantly shifted to the short wavenumber region in the Raman spectra of the La(III), Ce(III), and Nd(III) complexes (375, 383, 379 cm^{-1}) and becomes weaker. These bands can be due to the lanthanide-oxygen vibration modes[663,664].

The metal affects the carboxylate anion as well as the ring structure[663,664]. The carboxylic acids interact with the metals as symmetric[335,336]. Both oxygen atoms of the carboxylate groups are symmetrically bonded to the metal[347]. Moreover, we can observe in the Raman spectra of the lanthanide complexes weak peaks at 306, 225, and 213 cm^{-1}, which can be due to the O1-M-O3 vibration modes (Table VII.2.3.1 and VII.2.3.2)[663,664]. The complexes described above demonstrate once more the versatility of the orotate ligand, which adopts different coordination modes.

VII.2.4 Conclusions

The geometry of the orotic acid was computed and optimized with B3PW91/6-311++G**, B3PW91/LANL2DZ, B3LYP/6-311++G**, and B3LYP/LANL2DZ methods, while the geometry of the new La(III) complex of orotic acid was computed and optimized with B3PW91/LANL2DZ and B3LYP/LANL2DZ methods.

Orotic acid binds to the La(III) ion through both oxygen atoms of the carboxylic group from one of the ligands, one carboxyl oxygen from the other one ligand, and one OH$^-$ ion. The density functional calculations revealed that the mode of binding was bidentate through the carboxylic oxygen atoms with one of the orotic acid and monodentate through the carboxylic oxygen with the other one of the orotic acid. The vibrational analysis performed for the studied species, orotic acid and its lanthanide complexes, helped to explain the vibrational behavior of the ligand vibrational modes, sensitive to interaction with lanthanide atoms. The vibrational study gave evidence for the coordination mode of the ligand to Ln(III) ion and hence it was in agreement with the other theory prediction.

Table VII.2.3.1. Selected calculated and experimental IR and Raman wavenumbers (cm^{-1}) of orotic acid (HOA) and its La(III) complex ([La(OA)]) and their tentative assignment.

| Calcd. (HOA) | | | | Raman | | IR | | Calcd [La(OA)] | | Vibrational assignment |
| B3PW91 | | B3LYP | | | | | | B3PW91 | B3LYP | |
LANL2DZ	6311++G**	LANL2DZ	6311++G**	HOA	[La(OA)]	HOA	[La(OA)]	LANL2DZ	LANL2DZ	Ref. 663,664
3620	3607	3602	3591			3520 m	3410 m	3609	3593	ν (NH)
3312	3266	3297	3256	3144 sh		3232 sh	3190 m	3306	3291	ν (OH)
1747	1787	1727	1764		1747 sh			1746		ν$_{asym}$ (C7=O3, C7'=O3')
1733		1714		1715 m	1714 sh	1712 vs		1727	1726	ν$_{sym}$ (C2=O2, C2'=O2'); ν(NH, N'H')
1667	1687	1686		1657 vs	1668 vs	1684 vs	1685 vs	1675	1708	ν$_{sym}$ (C4=O4, C4'=O4'); ν(C6=C5, C6'=C5')
		1650	1670	1615 sh	1619 w	1617 sh	1641 sh	1635	1658	ν$_{sym}$ (C=C); ν(C=O)
1536	1539		1524	1522 w		1522 m	1604 sh	1527	1529	ν$_{asym}$ (COO⁻)
		1519		1508 sh	1495 w	1442 ms	1498 m	1472	1447	ν (C-O)
1428	1413	1419	1411	1436 sh	1420 ms	1424 ms	1426 m	1429	1421	ν (NH, N'H')
1395	1407	1391	1391	1414 s	1394 ms	1407 w	1375 s	1400	1383	ν$_{sym}$ (COO⁻); ν$_{asym}$ (N1-C2-N3)
1337	1394	1380	1320	1326 w	1318 vw	1345 m		1328	1339	δ (C5'H5', N1'H1')
	1317	1331		1282 m	1302 w	1284 m	1311 w	1311	1322	δ (C5H5, N1H1); δ (C-O-H)
						1266 w		1263		δ (C=O); ν$_{sym}$ N1-C2-N3
1265		1245		1254 vs	1244 vs	1241 w		1261	1243	ν (C2-N3-C4, C6=C5-C4)
	1226		1212		1205 sh		1226 w		1240	ν (C2'-N3'-C4', C6'=C5'-C4')
1154	1191	1146	1180	1134 w	1145 vw	1125 w		1139	1131	δ$_{ip}$ (C5H5, N1H1)
1118	1125	1107	1118		1119 vw		1114 vw	1138	1128	δ$_{ip}$ (C5'H5', N1'H1')
1019	1025	1012	1021	1047 m	1047 m	1042 vw		1029	1022	ν (C5=C6-N1); ν$_{sym}$ (C=O)
1006	1009	996	1000	1011 m	1016 m	1015 w	1014 w	1012	1019	ν (C5'=C6'-N1'); ν$_{sym}$ (C'=O')
922	922			933 m	939 m	930 w	926 w	931	931	ν (Cring-Cca)
910		912	913		914 sh			916	915	CH op def.
		909			889 w					ν (C5C4, C5'C4')
				887 w	874 w	892 w		896	894	ν (Cring-Cca); CH op def.
	860		863	862 vw	860 w	856 m	867 w			δ$_{op}$ (NH); δ$_{op}$ (ring)
827		816			810 sh	826 w		829	817	δ$_{op}$ (NH)
					804 sh		804 w	803	793	δ$_{op}$ (C=O); δ$_{op}$ (NH)
787	795	778	790	792 w	787 m	786 w	772 ms	780	789	δ$_{op}$ (COOH)
770	756	762	751	753 sh	757 sh	758 vw		761	771	δ$_{op}$ (NH); CH op def.
715	735	711	732	736 s		740 w		755	750	ν$_{sym}$ (COO⁻)
698	689	692	685		704 vw			700	701	δ$_{op}$ (NH, CO, CH)
659	679	654	674	653 w	643 w		645 w	634	632	op (ring, ring') def.
614	617	608	610	608 s	608 vs	603 w	595 w	622	618	ν (La-O5)
563	573	560	571	546 m	553 m	555 m	549 ms	548	547	ring' def.; δ (La-O1')
527	529	527	530	513 w	519 w	507 vw	517 vw	527	527	ring def.; δ (La-O1, La-O3)
483	455	481	456	460 ms	460 m	451 w		450	447	δ (O5H6)
424	431	422	429		434 sh		428 w	435	434	ν (ring-Cca); ν (La-O1, La-O3)

Table VII.2.3.2. Selected calculated and experimental IR and Raman wavenumbers (cm^{-1}) of orotic acid (HOA) and its Ce(III) ([Ce(OA)]) and Nd(III) ([Nd(OA)]) complexes together with their tentative assignment.

| Calcd. (HOA) | | | | Raman | | | IR | | | Vibrational assignment |
| B3PW91 | | B3LYP | | | | | | | | Ref. 663,664 |
LANL2DZ	6311++G**	LANL2DZ	6311++G**	HOA	[Ce(OA)]	[Nd(OA)]	HOA	[Ce(OA)]	[Nd(OA)]	
3620	3607	3602	3591		3688 vw	3685 vw	3520 m	3437 m	3415 ms	ν (NH)
3312	3266	3297	3256		3183 sh	3215 sh	3232 sh	3197 wm	3215 m	ν (OH)
1747	1787	1727	1764		1745 vw	1744 vw	1732 sh	1743 sh	1726 sh	ν$_{asym}$ (C7=O3, C7'=O3')
1733		1714		1711 m	1688 ms	1688 s	1712 vs			ν$_{sym}$ (C2=O2, C2'=O2'); ν(NH, N'H')
1667	1687	1686		1657 vs	1668 m	1669 ms	1684 vs	1686 vs	1685 vs	ν$_{sym}$ (C4=O4, C4'=O4'); ν(C6=C5, C6'=C5')
		1650	1670	1615 sh	1614 wm	1617 wm	1617 sh	1678 sh	1655 vs	ν$_{sym}$ (C=C); ν(C=O)
1536	1539		1524	1522 w			1522 m			ν$_{asym}$ (COO⁻)
		1519		1508 sh	1511 vw	1502 vw	1442 ms	1498 wm	1498 wm	ν (C-O)
1428	1413	1419	1411	1436 sh			1424 ms	1424 sh		ν (NH, N'H')
1395	1407			1414 s	1409 s	1411 s	1407 w	1406 m	1408 ms	ν$_{sym}$ (COO⁻); ν$_{asym}$ (N1-C2-N3)
		1391	1391		1387 ms	1390 ms		1383 s	1386 m	ν$_{sym}$ (COO⁻); ν$_{asym}$ (N1-C2-N3)
1337	1394	1380	1320	1326 w	1294 w	1293 w	1345 m	1312 w	1308 w	δ (C5'H5', N1'H1')
	1317	1331		1282 m			1284 m			δ (C5H5, N1H1); δ (C-O-H)
1265	1226	1245	1212	1254 vs	1225 vs	1226 vs	1241 w	1227 w	1232 w	ν (C2-N3-C4, C6=C5-C4)
1118	1125	1107	1118	1134 w			1125 w	1119 w	1121 w	δ$_{ip}$ (C5H5, N1H1)
1019	1025	1012	1021	1047 m	1030 wm	1031 wm	1042 vw	1032 sh	1038 sh	ν (C5=C6-N1); ν$_{sym}$ (C=O)
1006	1009	996	1000	1011 w	1008 wm	1008 wm	1015 w	1015 w	1015 w	ν (C5'=C6'-N1'); ν$_{sym}$ (C'=O')
922	922			933 wm	931 w	933 w	930 w	929 w	933 w	ν (Cring-Cca)
910		912	913	887 w			892 w	889 vw		ν (ring-Cca); CH op def.
827	860	909	863	862 vw	853 wm	853 m	856 m	858 vw	858 w	δ$_{op}$ (NH); δ$_{op}$ (ring)
							826 w	806 w	800 wm	δ$_{op}$ (C=O); δ$_{op}$ (NH)
787	795	778	790	792 w	777 wm	778 m	786 w	772 wm	771 wm	δ$_{op}$ (COOH)
770	756	762	751	753 sh			758 vw	759 w	757 wm	δ$_{op}$ (NH); CH op def.
715	735	711	732	736 s			740 w			ν$_{sym}$ (COO⁻)
659	679	654	674	653 w	644 vw	643 vw		644 vw	643 vw	τ (ring, ring')
								618 vw	618 vw	
614	617	608	610	608 s	595 wm	595 wm	603 w	593 vw	596 vw	ν (M-O5)
563	573	560	571	546 m	539 w	539 w	555 m	549 wm	548 wm	ring' def.; δ (M-O1')
527	529	527	530	513 w	511 w	513 wm	507 vw	516 vw	516 vw	ring def.; δ (M-O1, M-O3)
483	455	481	456	460 ms	465 w	461 w	451 w	473 sh	464 sh	δ (O5H6)
424	431	422	429		441 w	440 w		437 w	443 w	ν (ring-Cca); ν (M-O1, M-O3)
395	405	395	406	395 ms	383 vw	379 w				ν (ring'-C'ca)
331	338	329	336	215 wm	225 w	213 wm				δ (O1-M-O3)

Abbreviations: vw – very weak; w – weak; m – medium; ms – medium strong; s – strong; vs – very strong; sh – shoulder; ν – stretching; δ – bending; sym – symmetric; asym – asymmetric; ip – in plane; op – out of plane; ring – uracil ring; ca – carboxylate; M – metal.

VII.3 5-Aminoorotic acid and its lanthanide complexes

The structure of the lanthanide complexes of 5-aminoorotic acid were determined by means of elemental analysis, IR and Raman spectroscopies. Significant differences in the IR, and Raman spectra of the complexes were observed as compared to the spectra of the ligand. The geometry of 5-aminoorotic acid was computed and optimized with the Gaussian 03 program employing the B3PW91 and B3LYP methods with the 6-311++G** and LANL2DZ basis sets, while the geometry of the La(III) complex of 5-aminoorotic acid was also calculated and optimized with B3PW91/LANL2DZ and B3LYP/LANL2DZ methods. The density functional calculations revealed that the binding mode in the complex was bidentate through the carboxylic oxygen atoms. Detailed vibrational analysis of 5-aminoorotic acid and its Ln(III) systems based on both the calculated and experimental spectra confirmed the suggested metal-ligand binding mode.

VII.3.1 What difference does it make the 5-aminoorotic acid?

Despite the interest in orotate metal complexes, the coordination chemistry of the orotic acid derivatives has received scantily attention[672]. One of these derivatives is 5-aminoorotic acid (5-amino-2,6-dioxo-1,2,3,6-tetrahydropyrimidine-4-carboxylic acid, Fig. VII.3.1.1) which has relatively unknown coordination chemistry.
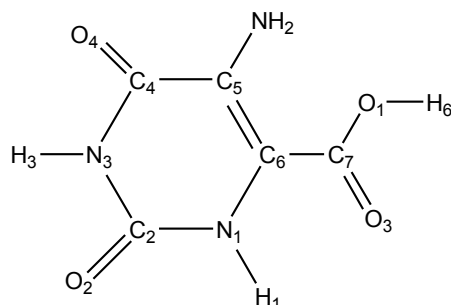
Figure VII.3.1.1. Molecular structure of the 5-aminoorotic acid (HAOA).

The complexes were identified and characterized with elemental analysis, IR and Raman spectroscopies. For estimation of the most preferred reactive sites of 5-aminoorotic acid for electrophilic attack and metal binding, its geometry was calculated and optimized. The binding mode of the 5-aminoorotic acid to the Ln(III) atoms was elucidated on the basis of DFT calculations of the molecular and vibrational structures of 5-aminoorotic acid and its La(III) model systems.

The content of the metal ion was determined after mineralization. The water content in the complexes was determined by Karl Fisher analysis. IR and Raman spectroscopies have confirmed the nature of the complex. The data of the elemental analysis of the Ln(III) complexes serve as a basis for the determination of their empirical formula (**Dr. I. Kostova**).

The binding mode of the HAOA ligand to lanthanide ions was elucidated by recording the IR and

Raman spectra of the complex in comparison with those of the free ligand.

VII.3.2 Geometry optimization

Because no crystal structure data are available for HAOA and its La(III) complex, their structures were optimized at different levels of theory (B3PW91/6-311++G**, B3PW91/LANL2DZ, B3LYP/6-311++G**, B3LYP/LANL2DZ) and compared with literature data for compounds containing identical or similar functional groups[672]. The calculated structural parameters of HAOA and its new La(III) complex are listed in Tables VII.3.2.1 and VII.3.2.2 and the labeling of the atoms is shown in Figs. VII.3.2.1 and VII.3.2.2. As one can notice, there is a very good agreement between the theoretically determined parameters of HAOA and its La(III) complex, and the experimental values available in the literature[672].

Previously published X-Ray diffraction data[665-668] about orotic acid helped us characterize the geometry of HAOA. The optimized molecular structure of HAOA is very similar to the structure of orotic acid obtained by X-Ray diffraction (Table VII.3.2.1)[666,667]. The HAOA molecule has a planar structure. The calculated N1-C6-C7-O3 dihedral angle is 0.0°, which suggests that the carboxylic group seem to have an anti-orientation (Fig. VII.3.2.1), orientation that can be specific to the solid state of the HAOA[668]. In this conformation of HAOA, the existence of the intramolecular hydrogen bondings would be highly probable.

As shown in Table VII.3.2.1, the average calculated of N-C bond lengths of HAOA may have values similar to a normal N-C single bond (147 pm) or to a normal N=C double bond (129 pm)[312]. Particularly, the N5-C5 calculated bond length vary between 134.6 and 136.2 pm, which is rather near to a normal double N=C distance (129 pm)[312] and can suggest a delocalization of the lone pair electrons of the nitrogen atom over the pyrimidine ring. The other two, N1-C2 and N3-C4 bonds, which have also short length values come to indicate a considerable π-electron delocalization within the N1-C2O2-N3-C4O4 skeleton[669]. All the N-H bond distances in this compound, calculated to be about 101.9-100.5 pm, are in very good agreement with the experimental data[667] and with other theoretical studies on similar compounds[666,668]. The calculated C4-C5 bond length belongs to the pyrimidine ring vary from 148.7 pm to 149.6 pm, which is shorter than that of a C-C single bond (154 pm)[311]. This shortening can be due to the π-electron and to the lone pair electron of the N5 atom delocalization[669]. The calculated average of the C5-C6 bond length is 137.8 pm being a bit longer than that of a C=C double bond[311,407,665] and comes to confirm also the π-electron delocalization. Both calculated averages of the carbon-oxygen bond lengths belonging to the pyrimidine ring are values which are similar to a double C=O bond length (120 pm): 123.1 pm for the C2-O2 bond length and 123.6 pm for the C4-O4 bond distance (Fig. VII.3.2.1, Table VII.3.2.1). The calculated C7-O3 bond distance is situated between 121.1 pm and 124.9 pm, which is longer than that of a normal C=O double bond (120 pm), whereas the C7-O1 bond length vary from 135.6 pm to 139.8 pm which is shorter than that of a normal C-O single bond (143 pm)[408,410]. The difference in the carboxyl bond lengths C7-O1 and C7-O3 as compared to the normal single and double bond lengths suggests that the negative charge and the double bond are delocalized[407,408,410], and that the C-O single

bond can be coordinated[410,411].

The O3-C7-O1 calculated angle, which varies from 121.6° to 122.4° and the calculated dihedral angle corresponding to the carboxyl group O3-C7-O1-H6, which measures 0.0° (Table VII.3.2.1, Fig. VII.3.2.1) demonstrate that the carboxyl group is planar, in the same plan with the pyrimidine ring. The planarity of the HAOA molecule may be demonstrated through the calculated dihedral angles: C5-C6-C7-O1, N5-C5-C6-C7, N1-C6-C7-O3, and H1-N1-C6-C7 , which measure 0.0° (Table VII.3.2.1), as well as O2-C2-N1-H1, O2-C2-N3-H3, and O4-C4-N3-H3 dihedral angles. Moreover, the calculated dihedral angles C4-C5-N5-H5', C6-C5-N5-H5, N5-C5-C6-C7, and O4-C4-C5-N5 are 0.0° (Table VII.3.2.1) and come to show that the amino group is situated in the same plan with the aromatic ring[407,666,669].
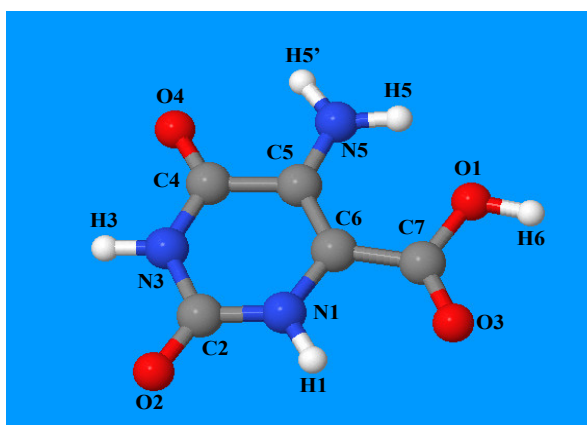
Figure VII.3.2.1. B3LYP/LANL2DZ optimized geometry of 5-aminoorotic acid together with its atoms labeling.

The HAOA has a good ability to adopt several modes of intramolecular hydrogen bonding[410,411,669], which take place between the coordinated carboxylate O1 and one of the protons of the coordinated amino group (C7-O1···H5=207.2 pm), between the pyrimidine carbonyl oxygens O4 and the other one of the protons of the coordinated amino group (C4-O4···H5'=223.9), and between the uncoordinated carboxylate O3 and the imido N1-H1 group (N1-H1···O3=230.6) (Table VII.3.2.1, Fig. VII.3.2.1). Taking into account the average calculated of the hydrogen bonds lengths, the latter seems to be particularly strong. The intramolecular hydrogen bonds play an important role in the crystal packing.

Metal complexes of pyrimidine nitrogen bases, as La(III) complex of HAOA, are studied in order to assist in elucidating the effect of lanthanide ions on the pyrimidine derivative structure. We discuss the geometry optimization of La(III) complex of HAOA in terms of the nature of the bonding and the possible structural types. Through the DFT calculations with different bases, HAOA coordinates to the La(III) atom as a dianion and the complex contains three HAOA ligands (Fig. VII.3.2.2)[672,673]. The calculated N-C bond lengths of the La(III) complex of HAOA belonging to the pyrimidine ring from all three ligands (Table VII.3.2.2) have for each of the ligands the same values (Table VII.3.2.2), which varies between the single N-C bond length (147 pm) and the double N=C bond length (129 pm)[312,407,665-669]. Opposite to this, the N-C bond distances linked to the ring are shorter (N5-C5=135.5 pm). These calculated values suggest an extended π delocalzation over the pyrimidine rings[312,669]. All the calculated bond distances of pyrimidine rings are values situated between the normal single and double bonds (Table

VII.3.2.2) and are in good concordance with previous reported studies[311,312,407-411,665-669].

The coordinated structural motifs thus generated can then readily form hydrogen bonds[672]. The C-C distances of the boundary rings are about 149.5-138.6 pm (Table VII.3.2.2). The changes in C-C bond lengths from the pyrimidine rings in the complex are not longer than 0.3 Å. This can be caused by the formation of a conjugated bond system in HAOA ligands. The C-C bridge bonds between pyrimidine rings and carboxylic groups in the complex are shorter with 1.4 and 1.5 Å (Table VII.3.2.2), respectively, as in the free ligands (Table VII.3.2.1). This shortening in the bond lengths can be also produced because of the conjugated bond system formation.

Table VII.3.2.1. Selected calculated structural parameters of 5-aminoorotic acid in comparison with the available experimental data.

	Exp. Ref. 672	Calcd.			
		B3LYP		B3PW91	
		6-311++G**	LANL2DZ	6-311++G**	LANL2DZ
Bond-lengths (pm)					
N1-C2	136.3; 137.5; 139.0; 137.8	136.4	137.6	136.1	137.2
C2-N3	138.4; 138.7; 138.0; 144.2	140.5	141.6	140.0	141.1
N3-C4	138.1; 137.1; 139.0; 138.1	137.8	138.8	137.3	138.4
C4-C5	143.3; 144.7; 144.9; 143.5	149.2	149.6	148.7	149.1
C5-C6	136.5; 135.0; 136.1; 136.5	137.2	138.6	137.0	138.3
C6-N1	136.9; 138.5; 134.6; 144.2	140.3	141.5	139.7	141.0
C6-C7	149.8; 149.8; 152.8; 150.6	146.1	145.7	145.8	145.3
C7-O1	130.6; 134.8; 125.8; 126.8	136.3	139.8	135.6	139.1
C7-O3	124.0; 124.5; 123.1; 125.6	121.3	124.9	121.1	124.7
C2-O2	125.4; 123.6; 122.4; 124.0	121.4	125.0	121.2	124.8
C4-O4	123.7; 124.6; 124.0; 122.7	121.9	125.6	121.7	125.3
O1-H6	102.0; 102.0	96.9	98.3	96.7	98.2
N1-H1	94.0; 94.0	101.2	101.7	101.2	101.6
N3-H3	89.0; 89.0	101.3	101.7	101.2	101.6
C5-N5	134.6	135.1	136.2	134.6	135.8
N5-H5		100.5	101.1	100.5	101.1
N5-H5'		100.9	101.4	100.9	101.3
C4-O4···H5'		225.1	229.2	223.5	228.0
C7-O1···H5		210.6	203.8	210.8	203.6
N1-H1···O3		229.0	233.4	227.6	232.3
Angles (°)					
N1-C2-N3	114.7; 114.7; 116.2; 117.2	112.7	113.3	112.7	113.3
C2-N3-C4	126.4; 124.8; 126.9; 127.5	128.0	127.5	128.2	127.6
C4-C5-C6	119.0; 117.8; 122.5; 120.5	118.2	118.3	118.1	118.3
C5-C6-N1	121.7; 118.2; 125.3; 122.9	120.3	120.3	120.3	120.3
N1-C6-C7	113.9; 114.0; 113.1; 113.6	112.9	113.4	112.9	113.4
C5-C6-C7	125.3; 120.7; 124.7; 123.4	126.9	126.3	126.8	126.3
C6-C7-O1	114.1; 117.4; 113.1; 114.8	113.8	113.9	113.8	113.9
C6-C7-O3	120.5; 114.9; 114.3; 122.6	123.9	124.5	123.8	124.4
C7-O1-H6	105.0; 106.0	106.8	110.0	106.6	110.1
O1-C7-O3	124.5; 127.6; 127.6; 126.4	122.2	121.6	122.4	121.7
C6-N1-H1	121.0; 122.0	117.0	117.2	116.8	117.2
C2-N1-H1	114.1	117.5	117.8	117.6	117.8
N1-C2-O2	123.0; 123.2; 123.3	125.3	125.0	125.3	125.0
N3-C2-O2	121.2; 119.0; 122.1; 120.5	122.0	121.7	122.0	121.7
Dihedral angles					
N1-C6-C7-O3		0.0	0.0	0.0	0.0
H1-N1-C6-C7		0.0	0.0	0.0	0.0
C5-C6-C7-O1		0.0	0.0	0.0	0.0
N5-C5-C6-C7		0.0	0.0	0.0	0.0

O2-C2-N3-H3	0.0	0.0	0.0	0.0
O4-C4-C5-N5	0.0	0.0	0.0	0.0
O3-C7-O1-H6	0.0	0.0	0.0	0.0
C6-C5-N5-H5	0.0	0.0	0.0	0.0
C4-C5-N5-H5'	-0.1	0.0	0.0	0.0

The average calculated of the carbonyl C-O distances from the pyrimidine rings are around 124.8 pm for the bonds referred to the C2 and 125.3 pm for those of the C4, and they are longer than in the free ligands, but not longer than 0.2 Å, suggesting also the coordinated system formation. HAOA as a derivative of the orotic acid can act, usually, as a bidentate dianionic ligand chelating to one metal ion through the deprotonated carboxylic group and the adjacent nitrogen atom[672].
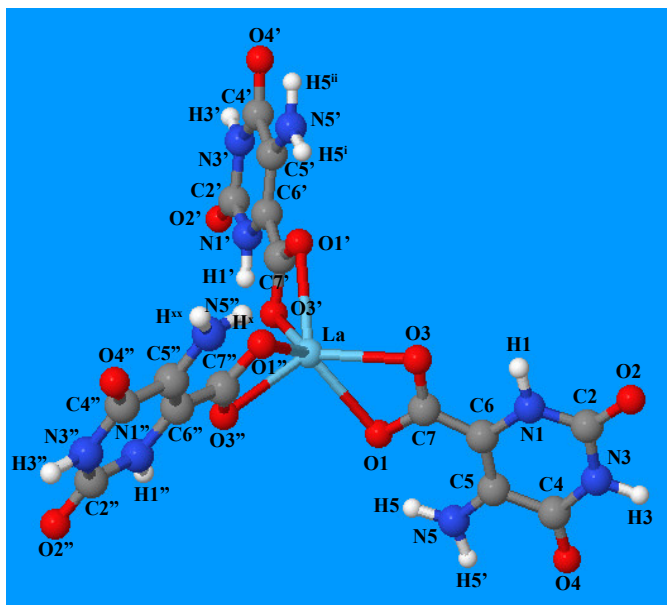
Figure VII.3.2.2. B3LYP/LANL2DZ optimized geometry of La(III) complex of 5-aminoorotic acid together with its atoms labeling.

Table VII.3.2.2. Selected calculated structural parameters of La(III) complex of 5-aminoorotic acid in comparison with the available experimental data.

	Exp. Ref. 672	Calcd.	
		B3LYP LANL2DZ	B3PW91 LANL2DZ
Bond-lengths (pm)			
N1-C2	136.3; 136.3; 135.9; 137.5; 137.8; 136.3	137.6	137.3
C2-N3	138.4; 138.7; 138.0; 137.8; 145.0; 150.8	141.8	141.3
N3-C4	136.9; 136.4; 138.1; 137.1; 139.0; 137.1	138.9	138.5
C4-C5	143.3; 141.9; 144.7; 144.9; 147.7; 150.7	149.5	149.0
C5-C6	154.6; 136.5; 135.2; 135.0; 136.1; 136.4	138.9	138.6
C6-N1	136.9; 138.5; 139.5; 146.0; 150.8	141.3	140.8
C6-C7	149.8; 149.8; 152.8; 148.5; 151.2	144.2	143.9
C7-O1	130.6; 130.6; 134.8; 127.5; 130.4	132.8	132.4
C7-O3	124.4; 124.0; 124.5; 125.6; 125.3; 130.4	132.3	131.9
C2-O2	125.4; 123.6; 122.6; 123.2; 121.0	125.0	124.7
C4-O4	123.7; 124.6; 124.0; 122.7; 125.5; 122.1	125.4	125.2
N1-H1	103.0; 103.1	101.6	101.5
N3-H3	103.0; 103.1	101.7	101.6
C5-N5	134.6	135.8	135.3
N5-H5	103.0; 103.1	101.6	101.5
N5-H5'	103.0; 103.1	101.4	101.3
La-O1	258.3; 262.4; 246.0; 255.0; 258.6	252.9	251.9
La-O3	252.3; 261.3; 247.0; 255.0; 257.5	250.7	249.6
C4-O4···H5'		234.3	233.5

C7-O1···H5		203.3	201.9
C4'-O4'···H5[ii]		233.7	233.3
C7'-O1'···H5[i]		204.6	201.8
C4"-O4"···H5[xx]		234.1	233.4
C7"-O1"···H5[x]		203.1	201.9
N1-H1···O3		233.7	233.0
N1'-H1'···O3'		233.2	233.1
N1"-H1"···O3"		233.8	232.9
Angles (°)			
C6-N1-C2	122.7; 118.9; 123.9; 118.1; 118.7	124.6	124.6
N1-C2-N3	114.7; 117.9; 114.7; 116.2; 117.2	113.5	113.5
C2-N3-C4	126.4; 124.8; 126.9; 127.5; 127.3	127.7	127.8
N3-C4-C5	115.5; 116.0; 113.7; 112.4; 112.1; 112.8	115.1	115.1
C4-C5-C6	119.0; 117.8; 122.5; 120.5; 121.4; 111.3	118.5	118.5
C5-C6-N1	121.7; 124.4; 118.2; 125.3; 122.9; 120.5	120.5	120.5
N1-C6-C7	114.1; 113.9; 116.5; 114.0; 113.1; 113.6	116.3	116.4
C5-C6-C7	121.7; 125.3; 120.7; 124.7; 123.4	123.2	123.1
C6-C7-O1	116.7; 117.5; 117.4; 113.1; 114.8; 117.8	121.8	121.7
C6-C7-O3	120.5; 118.8; 114.9; 122.6; 118.7; 117.6	120.5	120.5
O1-C7-O3	124.5; 127.6; 128.3; 127.6; 126.4	117.7	117.8
C6-N1-H1	114.1	117.3	117.2
C2-N1-H1	121.0; 122.0	118.1	118.1
N1-C2-O2	123.0; 123.2; 123.3; 123.3	125.0	125.0
N3-C2-O2	121.2; 119.0; 122.1; 120.5; 119.5	121.5	121.5
C2-N3-H3	116.0	115.0	115.0
C4-N3-H3	117.0; 117.1	117.2	117.2
N3-C4-O4	119.5; 118.6; 122.4; 119.4; 121.5	123.0	123.1
C5-C4-O4	125.5; 123.9; 128.2; 126.4	121.8	121.8
C7-O1-La	94.1; 92.7	93.8	93.7
C7-O3-La	94.1; 92.7	95.0	94.9
O1-La-O3	63.8; 47.95; 66.5; 67.4	53.5	53.6
O1-La-O3"	100.2	101.0	100.9
O3-La-O1"		101.2	101.1
O3-La-O1'		101.2	101.1
O1-La-O3'		101.9	101.8
O1'-La-O1"	95.0, 99.7	97.6	97.6
O3'-La-O3"	107.0	105.4	105.4

In our La(III) complex of HAOA all of oxygen atoms from the carboxyl groups are involved in the binding to La(III) ion and this coordination mode may be ascribed to the high affinity of lanthanide ions to oxygen[672]. The La(III) ion is quite symmetrically six-coordinate, with bonds to each two oxygen atoms from the carboxylate groups of the HAOA (Fig. 4). The coordination polyhedron of the central atom in the La(III) complex of HAOA is trigonal-prismatic[672], in which the correspondent O-La-O angles of the complex vary between 53.6° and 101.8° (Table VII.3.2.2, Fig. VII.3.2.2). The La-O distances are in the range from 249.0 pm to 253.8 pm (Table VII.3.2.2). The carboxylate groups exhibit bidentate coordination; the La(III) complex of HAOA, formed in this way, is mononuclear and each local coordination unit around the metal ion contains one 5-aminoorotate ligands[672]. The calculated C-O bond distances of the carboxylate groups from the complex are values similar to those of the free ligand (around 132.5 pm) (Tables VII.3.2.1 and VII.3.2.2), values which could confirm that they are involved in hydrogen bonds formation[672]. Moreover, a π-electron delocalization between the lanthanum ion and the carboxylate groups, which take part in the La(III)-HAOA binding formation[410,411669], should be possible. Because of the carboxylate groups presence, the HAOA works as a π-acceptor ligand[672].

The calculated average of the La-O bond lengths agrees with the literature[672] and is specific for the monometallic complexes of the lanthanum[672]. The increasing of M-O distances is related to decreasing

of O-M-O angles[672]. The calculated average angles (C7-O1-La) and (C7-O3-La), which have the same values for all the ligands (92.2°-95.3°), may prove that the La-O-C$_{aryl}$ linkages are not linear[672]. This assertion can be certified by the calculated O-La-O angles (Table VII.3.2.2, Fig. VII.3.2.2). It should be mentioned that different kinds of hydrogen bonds[672] are observed in the complex: hydrogen bonding of coordinated carboxylic oxygen and the proton of the nitrogen atom (N1-H1···O3=233.3 pm); hydrogen bonding of uncoordinated carbonylic oxygen from the pyrimidyne rings and one of the protons of the amino groups (C4-O4···H5'=233.7 pm), and hydrogen bonding of the coordinated carboxylic oxygen and other proton of the amino groups (C7-O1···H5=202.7 pm).

VII.3.3 Vibrational spectroscopy

The vibrational fundamentals from the IR and Raman spectra, presented in Figs. VII.3.3.1 and VII.3.3.2, were analyzed by comparing these modes with those from the literature[665,666,669,672] in combination with the results of our DFT calculations. In the Tables VII.3.3.1 and VII.3.3.2 the selected calculated and experimental IR and Raman data together with their attempted assignment are given.

Figure VII.3.3.1. IR spectra of 5-aminoorotic acid (a) and its La(III) (b),
Ce(III) (c), and Nd(III) (d) complexes.

In the 3600-2000 cm^{-1} spectral region from the IR spectrum the CH and NH stretches give rise to medium IR bands (Figs. VII.3.3.1, VII.3.3.2). The assignment of the CH and NH bands is quite difficult because they occur overlapped in the same spectral region, and the involvement of these groups in hydrogen bonds affects their wavenumbers and produces a relevant band broadening[669,672]. In the IR spectra, the strong band at 3457 cm^{-1} (HAOA), the medium bands at 3479 and 3448 cm^{-1} (La(III) complex), the medium peaks at 3480 cm^{-1} and 3450 cm^{-1} (Ce(III) complex), and the medium signals at 3478 and 3450 cm^{-1} (Nd(III) complex) were assigned to the NH stretching modes from the pyrimidine rings (Tables VII.3.3.1 and VII.3.3.2)[672,674], while the bands at 3333 cm^{-1} and 3044 cm^{-1} in the IR spectrum of HAOA, as well as the bands at 3339 cm^{-1}, 3263 cm^{-1}, and 3038 cm^{-1} (IR spectrum of La(III) complex), the peaks at 3340, 3258, and 3035 cm^{-1} (IR spectrum of Ce(III) complex), and the signals at 3339, 3251,

and 3038 cm^{-1} (IR spectrum of Nd(III) complex) were attributed to the CH stretching modes[672,674] (Fig. VII.3.3.1; Tables VII.3.3.1, VII.3.3.2). In the Raman spectra, the CH and NH stretching vibrations are present for the ligand and complex (Tables VII.3.3.1, VII.3.3.2; Fig. VII.3.3.2). The NH$_2$ asymmetrical stretching mode that is absent in the IR and Raman spectra of the ligand, can be seen in the IR and Raman spectra of the complexes: at 3361 cm^{-1} (IR) and 3357 cm^{-1} (Raman) for the La(III) complex, at 3362 cm^{-1} (IR) and 3356 cm^{-1} (Raman) for the Ce(III) complex, and at 3361 cm^{-1} (IR) and 3351 cm^{-1} (Raman) for the Nd(III) complex, whereas the symmetrical NH$_2$ stretching mode is present in both IR and Raman spectra of the ligand and only in the IR spectra of the lanthanide complexes.

In the IR spectra, bands with medium and weak intensities for the ligand and complex, can be observed at about 2800 cm^{-1}, and they are typical for strongly hydrogen bonded intermolecular complexes due to a strong anharmonic coupling (Fermi resonance) of the NH stretching vibrations with overtones and combinations of lower frequency modes of the bonded molecules[40-42]. Besides, one very strong band can be observed in 1730-1690 cm^{-1} region at 1691 cm^{-1} in the IR spectrum of the ligand and one medium band around 1700 cm^{-1} in each IR spectra of the complexes, which were assigned to the symmetrical stretching mode of C2=O2 and to the NH stretching mode (Fig. VII.3.3.1). The medium bands from the IR spectra at 1566 cm^{-1} (ligand) 1556 cm^{-1} (La(III) complex), and 1555 cm^{-1} (Ce(III) and Nd(III) complexes), as well as the medium peaks from the Raman spectra at 1560 cm^{-1} (ligand), 1542 cm^{-1} (La(III) complex), and 1542 cm^{-1} (Ce(III) and Nd(III) complexes) were attributed to the C5-C6 stretching and in plane NH bending modes (Tables VII.3.3.1, VII.3.3.2). The next pyrimidine ring vibrations, as N-C and N-H bending modes, can be observed in the 1520-1490 cm^{-1} wavenumber region. The symmetrical COO$^-$ stretching mode was observed in the IR spectra through medium and strong bands at 1405 cm^{-1} (ligand), 1390 cm^{-1} (La(III) complex), 1391 cm^{-1} (Ce(III) and Nd(III) complexes), while in the Raman spectra this vibration appears through strong peaks at 1384, 1386 and 1389 cm^{-1} only for the complexes (Figs. VII.3.3.1, VII.3.3.2).

The in plane C7-O1H6 bending mode appears only in the Raman spectrum of the free ligand as a medium strong signal at 1341 cm^{-1}. In the IR spectra, the medium band at 1312 cm^{-1} for HAOA, as well as the medium signals at 1304 cm^{-1} for the La(III) complex and 1306 cm^{-1} for the Ce(III) and Nd(III) complexes, were attributed to the C7-O1 stretching modes (Fig. VII.3.3.1), while in the Raman spectra these vibrations can be observed as a weak peak at 1301 cm^{-1} for the ligand and as medium/strong signals, shifted to lower wavenumber region, at 1295 cm^{-1} for the La(III) complex and 1293 cm^{-1} for the Ce(III) and Nd(III) complexes. The in plane NH$_2$ and C-O bending modes are detected only in the IR spectra, at 1255 cm^{-1} for the free ligand and blue shifted by 33-44 cm^{-1} for the complexes (1290, 1288, 1299 cm^{-1}), whereas the in plane NH and CH bending modes appear in both IR and Raman spectra of the free ligand and the complexes. In the IR spectra these can be seen at 1234 cm^{-1} (HAOA), 1237 cm^{-1} (lanthanide complexes), while in the Raman spectra they are blue shifted (8 cm^{-1} for the ligand) and red shifted (7, 4 cm^{-1} for the complexes).

The very weak signal at 989 cm^{-1} in the IR spectrum of the ligand (absent in the IR spectrum of the complexes), which was assigned to the trigonal pyrimidine ring breathing mode, can not be observed

in the corresponding Raman spectra. The very weak peak at 767 cm^{-1} from the IR spectra of the ligand and the weak bands around 775 cm^{-1} from the IR spectra of its lanthanide complexes seem to be absent in the Raman spectrum of the ligand and increased in relative intensity in the Raman spectra of the complexes (the same position, 763 cm^{-1} in all the spectra of the complexes). These vibration were attributed to the in plane C7-O3 bending and NH$_2$ wagging modes.
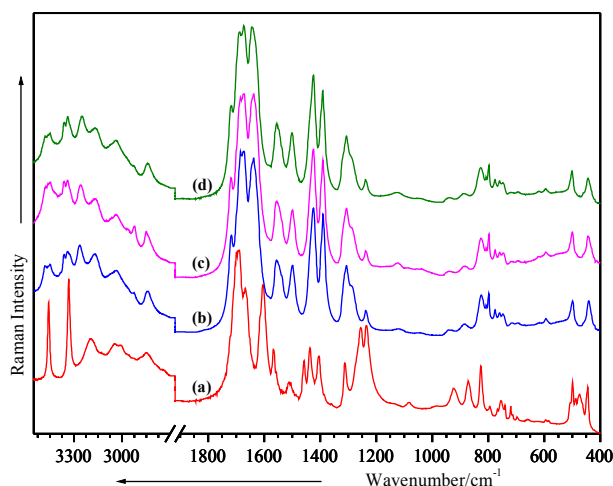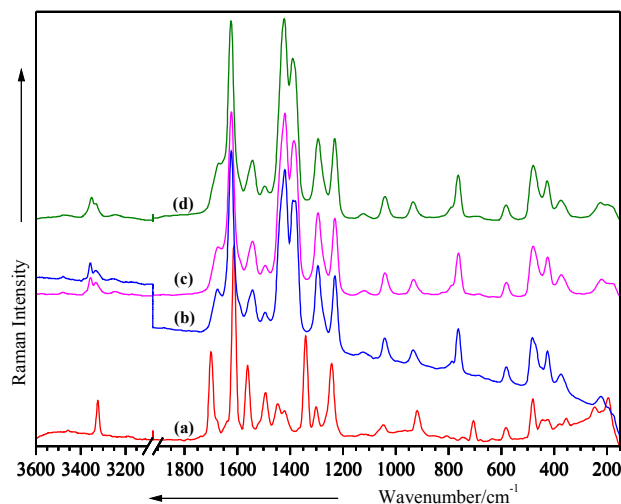

Figure VII.3.3.2. Raman spectra of 5-aminoorotic acid (a) and its La(III) (b), Ce(III) (c), and Nd(III) (d) complexes. Excitation: 514.5 nm, 100 mW (a-d).

In general, between the IR and Raman spectra of the ligand in comparison to the same spectra of the metal complexes we can assert wavenumber shifting, increases and/or decreases in relative intensities, and appearance and/or disappearing of bands. These changes can be caused by a decrease in the force constants of the bonds and polarization of the C-C, C-H bonds in the pyrimidine rings. The formation of complexes with lanthanide atoms perturb not only the aromatic systems of the rings, but also the quasiaromatic systems. The metal affects the M-O bonds and this effect is transferred to the C-O bonds. After that, the force constant of the OCC$_{ring}$ bond is changed, which is reflected in the displacement of electronic charge around bonds between heterocyclic rings, and heterocyclic rings and protons. The pyrimidine ring bending vibration and the skeletal deformation bands of the free ligand, mainly in the 900-300 cm^{-1} wavenumber region, show considerable changes on the complex formation (Figs. VII.3.3.1, VII.3.3.2; Tables VII.3.3.1, VII.3.3.2). These changes may be attributed to the pyrimidine rings distorsion upon complexation. The spectra in the frequency region below 600 cm^{-1} are of particularly interest, since they provide information about metal-ligand vibrations. The new band at 617 cm^{-1} and the new shoulder at 521 cm^{-1} (La(III) complex), the new band at 620 cm^{-1} and the new shoulder at 548 cm^{-1} (Ce(III) complex), as well as the new band at 619 cm^{-1} and the shoulder at 551 cm^{-1} (Nd(III) complex), only in the IR spectra of the complexes, which are absent in their Raman spectra, can be due to the La-O interactions.

In the low wavenumber region from the Raman spectra of the complexes (Fig. VII.3.3.2), the bands that can be due to the La-O vibrations are the bands about 425 cm^{-1}, which are increased in relative intensity as compared to the Raman spectrum of the ligand. Besides, the appearance of a new shoulder at

422 cm^{-1} in the IR spectrum of the La(III) complex confirms the presence of the La-O interaction.

The ionic potential of the metal is the most important parameter responsible for the influence of the metal on the rest of the molecule. The carboxylic acids may interact with the metals as symmetric, bidentate carboxylate anions. In this sens, we can observe in the Raman spectra of the La(III), Ce(III), and Nd(III) complexes, weak peaks at 224 cm^{-1}, at 220, 179 cm^{-1}, and 225, 198 cm^{-1}, respectively, which can be due to the O1-La-O3 vibration modes (Tables VII.3.3.1 and VII.3.3.2).

Metal complexes of pyrimidine nitrogen bases, as lanthanide complexes of 5-aminoorotic acid, are studied in order to assist in elucidating the effect of La(III), Ce(III), and Nd(III) ions on the pyrimidine derivative structure. We discussed the geometry optimization of La(III) complex of 5-aminoorotic acid in terms of the nature of the bonding and the possible structural types. Through the DFT calculations with different bases, the 5-aminoorotic acid coordinates to the La(III) atom as a dianion and the complex contains three 5-aminoorotic ligands (Fig. VII.3.2.2). 5-aminoorotic acid as a derivative of orotic acid can, usually, act as a bidentate dianionic ligand chelating to one metal ion through the deprotonated carboxylic group and the adjacent nitrogen atom. In the optimized geometry of the La(III) complex of 5-aminoorotic acid, all of the oxygen atoms from the carboxylate groups are involved in the binding to La(III) atom and this coordination mode may be ascribed to the high affinity of lanthanide ions for oxygen. The La(III) atom is quite symmetrically six-coordinate, with bonds to each two oxygen atoms from the carboxylate groups of the 5-aminoorotate ligands (Fig. VII.3.2.2)[672]. We suppose that the coordination polyhedron of the central atom in the Ce(III) and Nd(III) complexes of 5-aminoorotic acid is a distorted octahedron in the same way as for the La(III) complex of 5-aminoorotic acid[672]. The carboxylate groups exhibit bidentate coordination; the Ce(III) and Nd(III) complexes of 5-aminoorotic acid, formed in this way, are monuclear and each local coordination unit around the metal ion contains one 5-aminoorotate ligand.

VII.3.4 Conclusions

The complexes of La(III), Ce(III), and Nd(III) with 5-aminoorotic acid have been synthesized through a new method and characterized by elemental and spectral (IR, Raman) analyses.

The geometry of 5-aminoorotic acid was computed and optimized with the Gaussian 03 program using the B3PW91/6-311++G**, B3PW91/LANL2DZ, B3LYP/6-311++G**, and B3LYP/LANL2DZ methods, while the geometry of its La(III) complex was calculated and optimized with B3PW91/LANL2DZ and B3LYP/LANL2DZ methods.

The metal-ligand binding mode in the lanthanide complexes of 5-aminoorotic acid was explained through modeling of La(III)-5-aminoorotic acid structure: 5-aminoorotic acid binds to the La(III) atom through both the oxygen atoms of the carboxylic group from all three ligands; the central atom La(III) is six-coordinated and forms together with the ligands a distorted octahedron structure. The density functional calculations together with the vibrational assignments revealed that the mode of binding was bidentate through the carboxylic oxygen atoms.

Table VII.3.3.1. Selected calculated and experimental IR and Raman wavenumbers (cm^{-1}) of 5-aminoorotic acid (HAOA) and its La(III) complex [La(AOA)] and their tentative assignment.

| IR | | Calcd. IR freqs. [HAOA] | | | | Calcd. IR freqs. [La(AOA)] | | Raman solid | | Vibrational assignment |
| | | B3PW91 | | B3LYP | | B3PW91 | B3LYP | | | |
HAOA	[La(AOA)]	LANL2DZ	6-311++G**	LANL2DZ	6-311++G**	LANL2DZ	LANL2DZ	HAOA	[La(AOA)]	Refs. 672,674
	3479 m	3595	3597	3579	3583	3554	3542		3478 vw	ν(N1H1)
3457 s	3448 m							3456 vw		ν(N3H3)
	3361 m								3357 w	$ν_{as}$(NH$_2$)
3333 s	3339 m							3323 m	3333 w	ν(CH)
	3263 m								3257 vw	ν(CH)
3196 m	3171 m							3166 vw		$ν_s$(NH$_2$)
3044 w/m	3038 w									ν(CH)
3011 w/m	2928 sh									ν(CH)$_{ring}$
2850 w	2841 w/m									Bonded NH···O
1691 vs	1718 m	1719	1698	1700	1752	1715	1696	1699 m		ν(NH); $ν_s$(C2=O2)
	1684 vs	1692		1675	1676	1685	1664			$ν_s$(C4=O4)
1667 s	1673 vs	1682		1663		1682	1662	1678 sh	1673 m	$ν_s$(C4=O4); $ν_{as}$(COO$^-$)
1604 s	1637 vs	1620	1589	1617	1592	1618	1612	1612 vs	1623 vs	ν(C5-C6); NH$_2$ sciss
1566 m	1556 m	1561	1547	1545	1537	1586	1571	1560 m	1542 w/m	$δ_{ip}$(N1H1, N5H5); ν(C5C6)
1511 w	1499 m					1449	1439	1492 w/m	1494 w	δ(NC); ν(ring); $δ_{ip}$(N3H3)
1457 m		1444	1430	1434	1424	1445	1436	1447 w		$δ_{ip}$(N1H1, N1C2N3)
1436 m	1424 s	1418	1422	1410	1412	1426	1412	1421 w	1420 vs	$δ_{ip}$(N3H3)
1405 m	1390 s	1403	1400	1385	1390	1410	1404		1384 s	$δ_{ip}$(N1H1, N1C2N3); $ν_s$(COO$^-$)
		1346	1325	1330	1311	1316	1340	1341 m/s		$δ_{ip}$(C7-O1H6)
1312 m	1306 m	1318	1301	1300	1293	1282	1295	1301 w	1295 m/s	ν(C7-O1)
1255 m/s	1290 sh	1280		1267		1281	1268			$δ_{ip}$(NH$_2$, C-O1, C-O3)
1234 m/s	1237 w		1249		1233	1140	1230	1242 m	1230 m/s	$δ_{ip}$(NH,CH)
1140 sh	1122 vw	1186	1177	1180	1169	1138	1132		1124 vw	ν(NC)
1083 vw		1092	1121	1080	1112		1130	1047 vw	1041 w	ν(C6-O, C6-C7)
989 sh		1009	1013	1000	1005	1014	1005			Trigonal ring breath
924 w	941 sh	918	919	908	912	944	935	919 w/m	933 w/m	$δ_{op}$(CC, CN)
871 w/m	884 vw	830				831	824			wagg (N1H1···O, N3H3···O)
826 m	825 m	828	827	819	822	804	819			δ(C6-C7, C-H)
795 vw	798 m	793	781	786	777	801	796	809 vw	788 sh	$δ_{op}$(O3C7O1)
767 vw	775 w		776		775	769	760		763 m	$δ_{ip}$(C7O3); NH$_2$ wagg
754 w	759 w	761		752		753	748	748 vw		$δ_{op}$(C2=O2, C4=O4)
740 w	747 w	745	743	737	739	746	739			$δ_{op}$(N3H3, N1H1)
719 w	715 vw					732	722	706 w		$δ_{op}$(C2=O2, C4=O4)
696 vw	694 vw	692	686	687	687	692	687			$δ_{op}$ (N1H1, N3H3, NH$_2$)
	617 vw	648	677	622	673	643	637			ν(La-O)
595 vw	594 vw	630	609		603	576	635			τ(NH$_2$)

584 vw		588	583	583	578	573	571	582 w	581 w/m	δ_{op}(N-H)
	521 sh	560	569	556	550	494	568			ν(La-O)
499 m	499 m	553				493	492			δ_{op}(O1H6)
488 w		479	481	477	481	481	480	482 w/m	480 m	τ(ring)
474 w/m	459 sh	468	450	467	453	464	461			δ_{op}(N3H3, N5H5)
446 m	441 m	430	436	427	435	435	442	445 w		τ(C2O2, C4O4, COO)
	422 sh	401	411	401	411	434	434	425 sh	425 w/m	τ(C2O2, ring)
		371		367		378	377	381 vw	375 w	op def. ring; ν(La-O)
		351	360	353	363	374	370	356 vw	339 sh	τ(NH$_2$, C4O4)
		335	334	337	336	333	337	249 w		τ(NH$_2$)
		219				257	257		224 w	ν(O-La-O)
		195	197	198	200	197	196	196 w	196 sh	τ(ring); δ(O-La-O)

Abbreviation: vw – very weak; w – weak; m – medium; ms – medium strong; s – strong; vs – very strong; sh – shoulder; ν – stretching; δ – bending; τ – torsion; s– symmetric; as– asymmetric; def. – deformation; ip – in plane; op – out of plane; ring – pyrimidine ring; sciss – scissoring; wagg – wagging.

Table VII.3.3.2. Selected calculated and experimental IR and Raman wavenumbers (cm^{-1}) of 5-aminoorotic acid (HAOA) and its Ce(III) [Ce(AOA)] and Nd(III) [Nd(AOA)] complexes and their tentative assignment.

IR			Calcd. IR freqs. [HAOA]				Raman solid			Vibrational assignment
			B3PW91		B3LYP					
HAOA	[Ce(AOA)]	[Nd(AOA)]	LANL2DZ	6-311++G**	LANL2DZ	6-311++G**	HAOA	[Ce(AOA)]	[Nd(AOA)]	
	3480 m	3478 m	3595	3597	3579	3583		3479 vw	3478 vw	ν(N1H1)
3457 s	3450 m	3450 m					3456 vw			ν(N3H3)
	3362 m	3361 m						3356 w	3351 w	ν_{as}(NH$_2$)
3333 s	3340 m	3339 m					3323 m	3333 w	3333 w	ν(CH)
	3258 m	3251 m						3247 vw	3247 vw	ν(CH)
3196 m	3166 w/m	3169 w/m					3166 vw			ν_s(NH$_2$)
3044 w/m	3035 w/m	3038 w/m								ν(CH)
3011 w/m	2961 vw	2998 sh								ν(CH)$_{ring}$
2850 w	2850 w/m	2837 w/m								Bonded NH···O
	1718 s	1718 s	1719			1752				
1691 vs	1685 vs	1688 vs	1692	1698	1700		1699 m			ν(NH); ν_s(C2=O2)
	1673 vs	1672 vs	1682		1675	1676	1678 sh	1672 w/m	1669 w/m	ν_s(C4=O4)
1667 s	1637 vs	1643 vs			1663					ν_s(C4=O4); ν_{as}(COO$^-$)
1604 s			1620	1589	1617	1592	1612 vs	1623 vs	1623 vs	ν(C5-C6); NH$_2$ sciss
1566 m	1555 m	1555 m	1561	1547	1545	1537	1560 m	1542 w/m	1542 w/m	δ_{ip}(N1H1, N5H5); ν(C5C6)
1511 w	1499 m	1501 m					1492 w/m	1494 w	1495 w	δ(NC); ν(ring); δ_{ip}(N3H3)
1457 m			1444	1430	1434	1424	1447 w			δ_{ip}(N1H1, N1C2N3)

1436 m	1424 s	1424 s	1418	1422	1410	1412	1421 w	1420 vs	1421 vs	δ_{ip}(N3H3)
1405 m	1391 s	1391 s	1403	1400	1385	1390		1386 s	1389 s	δ_{ip}(N1H1, N1C2N3); ν_s(COO$^-$)
			1346	1325	1330	1311	1341 m/s			δ_{ip}(C7-O1H6)
1312 m	1306 ms	1306 ms	1318	1301	1300	1293	1301 w	1293 m	1293 m	ν(C7-O1)
1255 m/s	1288 sh	1289 sh	1280		1267					δ_{ip}(NH$_2$, C-O1, C-O3)
1234 m/s	1237 w	1237 w		1249		1233	1242 m	1230 m	1230 m	δ_{ip}(NH,CH)
1140 sh	1123 vw	1123 vw	1186	1177	1180	1169		1118 vw	1123 vw	ν(NC)
1083 vw		1042 sh	1092	1121	1080	1112	1047 vw	1041 w	1041 w	ν(C6-O, C6-C7)
989 sh			1009	1013	1000	1005				Trigonal ring breath
924 w	940 vw	938 vw	918	919	908	912	919 w/m	933 w	934 w	δ_{op}(CC, CN)
871 w/m	885 vw	887 vw	830							wagg (N1H1$\cdots$O, N3H3$\cdots$O)
826 m	825 m	826 m	828	827	819	822				δ(C6-C7, C-H)
795 vw	798 m	798 m	793	781	786	777	809 vw	787 sh	791 sh	δ_{op}(O3C7O1)
767 vw	775 w	776 w		776		775		763 w/m	763 w/m	δ_{ip}(C7O3); NH$_2$ wagg
754 w	759 w	760 w	761		752		748 vw			δ_{op}(C2=O2, C4=O4)
740 w	746 w	748 w	745	743	737	739				δ_{op}(N3H3, N1H1)
719 w	719 vw	719 vw					706 w			δ_{op}(C2=O2, C4=O4)
696 vw	694 vw	693 vw	692	686	687	687		687 vw	690 vw	δ_{op} (N1H1, N3H3, NH$_2$)
	620 vw	619 vw	648	677	622	673				ν(M-O)
595 vw	594 vw	595 vw	630	609		603				τ(NH$_2$)
584 vw			588	583	583	578	582 w	581 w	582 w	δ_{op}(N-H)
	548 sh	551 sh	560	569	556	550				ν(M-O)
499 m	500 m	501 m		553						δ_{op}(O1H6)
488 w			479	481	477	481	482 w/m	480 m	480 m	τ(ring)
474 w/m			468	450	467	453				δ_{op}(N3H3, N5H5)
446 m	443 m	444 m	430	436	427	435	445 w			τ(C2O2, C4O4, COO)
			401	411	401	411	425 sh	425 w/m	427 w/m	τ(C2O2, ring)
			371		367		381 vw	373 w	375 w	op def. ring; ν(M-O)
			351	360	353	363	356 vw			τ(NH$_2$, C4O4)
			335	334	337	336	249 w			τ(NH$_2$)
				219				220 w	225 w	ν(O-M-O)
			195	197	198	200	196 w	179 w	198 w	τ(ring); δ(O-M-O)

Abbreviation: vw – very weak; w – weak; m – medium; ms – medium strong; s – strong; vs – very strong; sh – shoulder; ν – stretching; δ – bending; τ – torsion; s– symmetric; as– asymmetric; def. – deformation; ip – in plane; op – out of plane; ring – pyrimidine ring; sciss – scissoring; wagg – wagging; M – metal.

Chapter VIII

Summary/Zusammenfassung

Summary

The present work combines the vibrational spectroscopy and the accurate density functional theory (DFT) calculations on the investigation of several well-known classes of food additives (colors, preservatives, and flavor enhancers), of medicines (anti-inflammatory, anti-malarial drugs), and of three types of lanthanide complexes of a few pharmaceutically active compounds. A short part of the current work, namely Chapter IV, addresses to the vibrational dephasing of the C-O and C-C stretching modes in the hydrogen bonded binary system of tetrahydrofuran (THF) with water ($C_4H_8O\cdots HOH$).

Infrared and Raman spectroscopy were employed for the characterization of the ground state molecular structure. Moreover, resonance Raman (RR) spectra contain additional information on the resonantly enhanced excited state molecular structure. Surface enhanced Raman scattering (SERS) allows one to determine the interaction and adsorption site of active agents on a metal substrate. Furthermore, density functional theory (DFT) calculations were carried out for an exact assignment of the vibrational spectra. The DFT computed molecular geometries of the species of interest reproduced the crystal structure data very well and in conjunction with IR and Raman measurements helped us to clarify the structures of the compounds, for which no experimental data were available; and this especially for the new lanthanide complexes.

The first chapter introduces briefly the general subject matter of the work. The various projects are related to recent research developments in the respective chapters. The second chapter concentrates on the theoretical background of vibrational spectroscopy and theoretical calculations.

The third chapter brings one in contact with the studied samples, the experimental procedures (solutions and substrates processing, synthesis) which were used, the description of the apparatus and computational details.

In the fourth chapter the focus is set on the study of vibrational relaxations, such as vibrational dephasing, one of the most powerful tools to investigate the dynamical processes in the liquid phase of the matter, having the possibility to identify two principal mechanisms for interpreting the relaxation process. The first process, population relaxation, involves a change in the quantum state of the relevant normal mode, while the second one, dephasing, is related to the phase decay of the vibrational wavefunction. Since THF is the simplest model compound for understanding the vibrations of the furanose ring of RNA and DNA backbones and water (H_2O) is an omnipresent solvent in biological systems, the plot of ratio, I_{hyb}/I_{main} vs. mole fraction of C_4H_8O, was used as a Raman marker to locate the hydrophilic site of the membrane with directly biological significance.

Chapter V, after a short overview on food additives employment and classification, presents a detailed characterization and identification study of five well-known food additives (E102, E211, E127, E132, and E621) by combining vibrational spectroscopy with density functional theory calculations. FT-Raman spectrum in solid state and Raman/RR spectra of all food additives at different concentrations, were recorded in order to use them as data bank for further applications in trace analysis of food products. Overall, the SERS results indicate that with excitation at frequencies close to those of the Ag plasmon resonance and out of the dye resonance condition, SERS investigations are possible upon lowering concentration. However the SERS effect is much weaker than required for complex applications like food analysis. Therefore, for this purpose, the SERRS investigations would be more effective.

The E102 additive was found to feature an extended π electron delocalization over the pyrazole system with the sodium sulfonate groups lying on the opposite sides of the conjugated azo linkages, which makes the connection between one of the phenyl rings and the pyrazole ring. The difference between the C10-N9 and N8-C4 bonds being a 180° rotation, and the calculated bond distances from 179.2 pm to 186.6 pm for the C13-S20 bond suggest the presence of intermolecular hydrogen bonds.

As a monoazo dye, E102 reveals the distinguishing azochromophore group –N8=N9– subject to azo hydrazone form in appropriate solutions. In the pH dependent Raman spectra, a drastic photoprocess would lead to corresponding Raman changes with the appearance of the photoproducts signal, which was not observed in our spectra in basic conditions. More probably, the present modifications observed at pH values over 9, are due to the ionisation related to the OH groups of the structure, which affects the vibrational behaviour of the O6-C5-C4-N8=N9-C involved modes, where the azo-hydrazone tautomers are possible. Taking into account the major changes in the band shape attributed to the azo bridge at pH 2 values, one can conclude a possible protonation of this part.

The observed bands in the SERS spectrum support the consideration that the phenyl 1 ring is in a close vicinity of the Ag particles with a perpendicular orientation of the pyrazole ring and its attached OH functional group, as well as the presence of the C3-COO⁻ functional group, negatively charged, to bend near the surface, along the C3-C bond. Lowering the concentration generates a reorientation of the phenyl skeletal plane with respect to the silver surface. The pyrazole ring bands are less representative in the SERS spectra, suggesting that this part of the molecular structure is less involved into adsorption.

In the case of E211, two types of available preservative, commercial and pure, were studied. The

differences between the Raman spectra of the pure and commercial E211 lead us to the assumption that several impurities are present in the commercial substance. Because of contamination in the manufacturing process, some heavy metals, most notably lead, are often found in the finished products. The E211 used in the food industry can contain in small doses arsenic, lead, and mercury. From the Raman spectra of E211 at different pH values, the Raman behavior at pH 3 shows the undissociated molecular form of the sodium benzoate, while at pH 5 the E211 seems to be dissociated.

A strong chemical interaction of E211 with the silver colloidal particles was observed under micromolar concentrations through the lone pair electrons of the oxygen atoms of the carboxylate anion in a perpendicular orientation. The SERS spectra of E211 at acidic pH values were recorded and revealed the same orientation through the carboxylate anion.

According to our DFT calculations, the molecular conformation of E127 is planar except for the benzoate moiety, which lies nearly perpendicular to the xanthene ring (71.8°). This angle agrees with previously X-Ray data and because its value is smaller that 87.7°, we can confirm the existence of the quinoid (sodium salts) form of the food dye. Also specifically for the quinoid form of E127 are that the bonds and angles of the xanthene ring indicate normal values as a three range benzenes. Usually, the cationic xanthene structures are stabilized in a quinoid form.

From the SERR spectra at concentration of 0.39×10^{-7} and according to our optimized geometry of the E127, we suppose that the E127 molecule can lie parallel to the xanthene ring and with the benzoate group perpendicular to the silver colloidal particles along with the carboxylate group. Taking into account the vibrational modes assignment, the strong chemical interaction of E127 with the silver colloidal particles at the concentration of 0.39×10^{-8} M can be assumed through both benzene and xanthene rings. The xanthene ring lies tilted on the silver surface through the O26 and I22 atoms and the benzene ring seems to be quite perpendicular to the silver surface. At the concentration of 0.39×10^{-9}, the E127 molecule is adsorbed on the silver surface through the carboxylate group and the I23, I24 atoms of the xanthene ring in a tilted orientation of the xanthene ring and a perpendicular orientation of the benzene ring, whereas at concentration of 0.39×10^{-10} a tilted orientation of the E127 molecule through π electrons of the benzene ring and the oxygens and iodine atoms of the xanthene ring is being proposed.

The pH dependent SERR spectra of E127 in the acidic range confirm the anion-induced charge transfer complex formation in the silver colloid; the monoanionic form of the molecule is present and it can be adsorbed on the silver colloidal particles through the xanthene ring, in a vertical orientation. The basic pH dependent SERR spectra come to demonstrate the deprotonation of the E127 molecule in the non-polar solvents and the presence of the lactone form. The molecule lies in a perpendicular orientation on the silver colloidal particles through the carboxylate moiety from the lactone structure of the molecule.

From DFT studies one can conclude that the E132 molecule is quite planar except for both sulphonic groups, with a symmetry center placed at the C9=C9' bridge bond level. Both sulphonic groups exhibit trigonal pyramid symmetry and they are situated on both sides of the symmetry bridge bond, with both double bonded oxygen atoms in opposite directions. Both sulphonic groups are rotated by 97.2° (calculated average) from the molecular plane. From our DFT calculations, we can deduce that the

molecule exhibits a preference for the *trans* conformer and, in this case, hydrogen bonding can take place between the hydrogen atom of the N-H bonds and the oxygen atom of the C=O bonds. The stable protonated structures of E132 are characterized by two slightly strong N^+-H···O=C hydrogen bonds, which restrict the accessible conformational space.

The Raman spectrum of E132 in solid state and the RR spectra in aqueous solution were recorded and the marker bands were identified. E132 could be detected in aqueous solution down to micromolar levels with RR, at nanomolar concentrations with SERR spectroscopy on sodium citrate-reduced silver colloid, and down to micromolar levels with SERR spectroscopy on island films with various roughnesses.

The surface selection rules together with the data from literature can explain the adsorbate structures on the metal surfaces. A strong chemical interaction of E132 with the silver colloidal particles is observed at nanomolar concentrations after 12 hours from the aggregation; the interaction taking place through the lone pair electrons of the two oxygen atoms of the $-SO_3^-$ groups, symmetric bidentate.

The chemical interaction of E132 with the island films is observed down to micromolar concentrations and the binding modes on the metallic surface are different when the molecule is excited with the green laser line, the interaction taking place through the lone pair electrons of two oxygen atoms of the $-SO_3^-$ groups, one oxygen atom and one nitrogen atom of the pyrrolidone ring, in a tilted orientation; when the molecule is excited with the red laser line, though, the molecule binds to the silver surface through the π electrons distributed over the pyrrolidone and phenyl rings and through the negative oxygen ions of both $-SO_3^-$ groups, in a perpendicular orientation.

Raman and SERS spectra of MSG were recorded at different concentrations. This study may serve as a reference for further Raman spectroscopic applications in trace analysis of food products.

The geometry of E621 was computed and optimized with different basis and methods of the Gaussian 03 program, demonstrating that both forms of E621 possess different geometries that can be explained by the molecule protonation possibilities. The results from the FT-Raman spectrum are consistent with the zwitterionic structure of E621 in the solid state.

Analyzing the Raman spectra of the solutions could evidence two changes in the molecular identity of E621 on going from basic to acidic pH values. The quantitatively protonated form of MSG dominates at low pH values.

SERS spectra of MSG were recorded even at very low concentrations down to 10^{-5} M. A strong chemical interaction of E621 with the colloidal particles was observed, involving an adsorption *via* the lone pairs of the nitrogen atom and the oxygen atoms of the carboxyl group. The surface selection rules along with our theoretical results are subject to explain the adsorbate structure on the metal surface at different concentrations and pH values.

The sixth chapter concentrates on the anti-inflammatory and anti-malarial drugs monitoring. The Raman spectra of the different aspirin tablets can be employed for differentiating the buffered and unbuffered pharmaceutical species. The two distinct species of aspirin were found to be slightly different chemisorbed on the silver surface.

The FT- and micro-Raman spectra of both types of paracetamol tablets were recorded and the marker bands of the characteristic functional groups were identified. The presence of the monoclinic form of paracetamol in the solid state of both types was also proved.

The micro-Raman spectra of the paracetamol after recrystallization on the glass surfaces shows that the normal paracetamol contains a mixture between monoclinc and orthorhombic forms, while the sinus paracetamol contains just the monoclinic form. The most important bands of some excipients, added in the drug production could be identified.

Analyzing the Raman spectra of both types of the paracetamol solutions, the existence of the mixture between monoclinic and orthorhombic forms and of the protonated species of normal and sinus paracetamol on going from basic to acidic pH values could be distinguished.

SERS spectra of paracetamol could be recorded even at low concentrations with a conventional SERS setup (8×10^{-2} M). The chemical interaction of both types of paracetamol with the silver film surfaces was observed at concentration of 8×10^{-2} M through the lone pair electrons of the nitrogen and oxygen atoms from the amide group and through the π electrons of the phenyl ring in a flat orientation.

The first NIR-SERS spectroscopic investigation of haematin in the presence of two widely used antimalarial drugs is reported. The modifications in the spectra of each haematin-drug systems could be explained in terms of interaction between the two species, where the aliphatic chain of CQ or the pyrimidine moiety in the case of MQ, were less involved into interaction upon adsorption on Au particles. The heme core was supposed to become sensitive to the presence of the respective quinoline skeletal ring as an axial ligand upon adsorption on the metal particles.

Once again, it has been shown why these two complementary methods became so popular among chemists, especially since major progresses in Raman excitation (lasers), detection techniques (CCD cameras, FT-techniques) and unambiguous signal assignment by DFT calculations have been achieved.

By combining these two methods, the auspicious results obtained on the new potentially biologically active lanthanide complexes of pharmaceutically active compounds (Chapter VII), made us confident of the power of theoretical calculations in aiding the interpretation of IR and Raman spectra by solving some interesting issues. Consequently, the IR and Raman spectra of new potentially biologically active lanthanide complexes, that were synthesized by our coworkers, were discussed with the assistance of the accurate results obtained from DFT calculations (structural parameters, harmonic vibrational wavenumbers, Raman scattering activities), and many previously incomplete assignments have been analyzed and improved.

The IR and Raman study together with the DFT calculations results on 3,5-pyrazoledicarboxylic acid, orotic acid, 5-aminoorotic acid, and their La(III), Ce(III), Nd(III) complexes demonstrates the metal-ligand binding mode in the new Ln(III) complexes. Moreover, the metal-ligand binding mode in the new La(III) complex of 3,5-pyrazoledicarboxylic acid was demonstrated through DFT modelling of La(III)-3,5-pyrazoledicarboxylic acid structure: 3,5-pyrazoledicarboxylic acid binds to La(III) ion through the oxygen atoms of the carboxylic groups. IR and Raman spectra of the 3,5-pyrazoledicarboxylic acid and its La(III), Ce(III), and Nd(III) complexes were recorded and the marker bands of characteristic

functional groups were identified, in order to use them as data bank for further application in trace analysis of rare-earth complexes. The vibrational study of 3,5-pyrazoledicarboxylic acid and its lanthanide complexes, based on both IR and Raman vibrational data, helped to gain a deeper insight into the coordination behavior of the ligand and the coordination polyhedron of its lanthanide complexes.

Orotic acid binds to the La(III) ion through both oxygen atoms of the carboxylic group from one of the ligands, one carboxyl oxygen from the other ligand, and one OH$^-$ ion. The density functional calculations revealed that the mode of binding was bidentate through the carboxylic oxygen atoms with one of the orotic acids and monodentate through the carboxylic oxygen with the other one of the orotic acids. The vibrational analysis performed for the studied species, orotic acid and its lanthanide complexes, helped to explain the vibrational behavior of the ligand vibrational modes, sensitive to interaction with lanthanide atoms. The vibrational study gave evidence for the coordination mode of the ligand to Ln(III) ion and hence it was in agreement with the other theory prediction.

5-Aminoorotic acid binds to the La(III) atom through both oxygen atoms of the carboxylic group from all three ligands; the central atom La(III) is six-coordinated and forms together with the ligands a distorted octahedron structure. The density functional calculations together with the vibrational assignments revealed that the mode of binding was bidentate through the carboxylic oxygen atoms.

Overall, the results provide a benchmark illustration of the virtues of DFT in aiding the interpretation of rich vibrational spectra attainable for larger polyatomic adsorbates by using SERS, as well as in furnishing detailed insight into the relation between the vibrational properties and the nature of the Ag substrate-adsorbate bonding. Therefore, we strongly believe that quantum chemical calculations will become a matter of rapidly growing scientific and practical interest in SERS. We also tried to find out the method, which could fit best the experimental results. We used the DFT methods (BLYP, B3LYP, BPW91, B3PW91), as well as the basis sets LANL2DZ, 6-31+G(d), 6-311+G(d), and 6-311++G**. The first calculations indicated the B3PW91/LANL2DZ combination as the most reliable one for the lanthanide systems and the less expensive one, due to its accuracy and computational efficiency. In fact, almost all the DFT-based methods, particularly when allied with the LANL2DZ basis set, yielded results, which were significantly closer to the experimental values than those of the traditional Hartree-Fock and the Møller-Plesset (MP2) electron correlation methods. It is now clear that quantum mechanical DFT calculations represent an indispensable complement not only for the spectroscopical studies in chemistry, but they can also help for a better understanding and exploring of other young fields in physical chemistry, such as SERS.

The experiments and results presented in this work demonstrate that vibrational spectroscopy in conjunction with quantum chemical calculations have a large applicability for the investigation of the molecular structure. In particular, resonance Raman spectroscopy proved to be a valuable method to obtain information about the initial dynamics and excited state structure of photochemically active systems. Moreover, Raman, SERS, and SERRS spectroscopies brought an important contribution in the understanding of the structure-activity relationship of several pharmaceuticals.

Zusammenfassung

In der vorliegenden Arbeit wurden Schwingungsspektroskopie und exakte Dichtefunktionaltheorie-Berechnungen (DFT, density functional theory) für Untersuchungen an einigen bekannten Klassen von Lebensmittelzusatzstoffen (Farbstoffe, Konservierungsmittel und Geschmacksverstärker), Medikamenten (entzündungshemmende Arzneimittel, Anti-Malaria-Arzneimittel) und drei verschiedenen Lanthanidkomplextypen einiger pharmazeutisch-aktiver Substanzen verwendet. Ein kurzer Teil der aktuellen Arbeit, nämlich Kapitel IV, befasst sich mit Schwingungsdephasierung der C-O und C-C Streckschwingungsmoden an dem Wasserstoffbrücken-gebunden binären System von THF und Wasser ($C_4H_8O\cdots HOH$).

Infrarot- und Raman-Schwingungsspektroskopie wurden zur Charakterisierung der Molekülstruktur im Grundzustand angewandt. Außerdem enthalten Resonanz-Raman (RR)-Spektren zusätzliche Informationen über die Molekülstruktur der resonant angeregten Zustände. Oberflächen-verstärkte Raman-Streuung (SERS) erlaubt es, die Wechselwirkungs- und die Adsorptionsstelle der aktiven Wirkstoffe an Metalloberflächen zu bestimmen. Des Weiteren wurden Dichtefunktionaltheorie-(DFT) Rechnungen zur exakten Modenzuordnung in den Schwingungsspektren durchgeführt. Die DFT-berechneten Molekülgeometrien der interessierenden Spezies stimmten sehr gut mit den Kristallstrukturdaten überein und waren zusammen mit Infrarot- und Raman-Messungen hilfreich bei der Aufklärung derjenigen Substanzstrukturen, für welche keine experimentellen Daten verfügbar waren, und dies besonders für die neuen Lanthaniden-Komplexen.

Das erste Kapitel gibt eine Einführung zum Themengebiet der Arbeit. Die Beziehung der verschiedenen Projekte zu aktuellen Entwicklungen in der Forschung wird in den entsprechenden Kapiteln hergestellt. Das zweite Kapitel konzentriert sich auf die theoretischen Hintergründe der Schwingungsspektroskopie und der DFT-Rechnungen.

Im dritten Kapitel werden die untersuchten Proben vorgestellt, sowie die eingesetzten experimentellen Arbeitsmethoden (Herstellung der Lösungen und der Substrate und Synthesen), die Beschreibung der Geräte und Einzelheiten zu den DFT-Rechnungen.

Im vierten Kapitel wird auf die Untersuchung der Schwingungsrelaxation eingegangen, z.B. in Form der Schwingungsdephasierung, welche als nützliches Hilfsmittel zur Erforschung dynamischer Prozesse in der flüssigen Phase eingesetzt werden kann. Das gibt die Möglichkeit, zwei hauptsächliche Mechanismen für die Erklärung des Relexationsprozesses zu identifizieren. Der erste Prozess, die Besetzungsrelaxation, beinhaltet eine Änderung des Quantenzustandes der relevanten Normalmode, während der zweite Prozess, die Dephasierung, mit der Phasenrelaxation der Wellenfunktion zusammenhängt. Weil THF das einfachste Modell zum Verständnis der Schwingungen des Furanoserings der RNA- und DNA-Rückgrate ist und Wasser das allgegenwärtige Lösungsmittel in biologischen

Systemen ist, wurde die Auftragung vom Verhältnis I_{hyb}/I_{main} gegen den Molenbruch des THF als Raman-Marker benutzt um die hydrophile Stelle der Membran mit unmittelbar biologischer-Signifikanz zu lokalisieren.

Das Kapitel V stellt, nach einer kurzen Übersicht über die Anwendung und die Klassifizierung der Lebensmittelzusatzstoffe, eine detaillierte Untersuchung für die Charakterisierung und die Identifizierung von fünf weit verbreiteten Lebensmittelzusatzstoffen (E102, E211, E127, E132 und E621) durch Kombination von Schwingungsspektroskopie mit Dichtefunktionaltheorie-Rechnungen vor. Das FT-Raman-Spektrum des Festkörpers und Raman/RR-Spektren von allen Lebensmittelzusatzstoffen mit verschiedenen Konzentrationen wurden aufgenommen, um sie als Datenbank für weitere Anwendungsmöglichkeiten in der Spurenanalyse von Lebensmittelprodukten zu benutzen. Allgemein zeigen die SERS-Ergebnisse, dass bei Verwendung von Anregungswellenlängen in der Nähe der Plasmonresonanz des Silbers und außerhalb der elektronischen Resonanz des Farbstoffes, SERS-Untersuchungen bei niedrigen Konzentrationen möglich sind. Allerdings ist der SERS-Effekt viel schwächer als erforderlich, um komplizierte Anwendungen wie Lebensmittelanalysen durchzuführen. Deswegen könnten für diesen Zweck SERRS-Untersuchungen erfolgreicher sein.

Es wurde festgestellt, dass E102 eine erweiterte π-Elektronen-Delokalisierung über das Pyrazolsystem besitzt, wobei die Natriumsulfonatgruppen auf entgegengesetzten Seiten der konjugierten Azobindungen liegen, welche die Verbindung zwischen einem der Phenylringe und dem Pyrazolring herstellen. Die Differenz zwischen den C10-N9 und N8-C4 Bindungen entspricht einer 180°-Drehung, und die berechneten Bindungsabstände von 179,2 pm bis 186,6 pm für die C13-S20 Bindung deuten auf die Anwesenheit intermolekularer Wasserstoffbrückenbindungen hin.

Als ein Mono-Azofarbstoff weist E102 die charakteristische Azochromophorgruppe -N8=N9- auf, welche in geeigneter Lösung eine Azohydrazonform bildet. In den pH-abhängigen Raman-Spektren würde ein drastischer Photoprozess zu entsprechenden Raman-Veränderungen mit Auftreten eines Photoproduktsignals führen, was in unseren Spektren unter alkalischen Bedingungen nicht beobachtet wurde. Es ist wahrscheinlicher, dass die vorhandenen Änderungen, die bei pH-Werten größer als 9 beobachtet wurden, auf die Ionisierung der OH-Gruppen der Struktur zurückzuführen sind. Dies beeinflusst das Schwingungsverhalten der O6-C5-C4-N8=N9-C Moden, wo die Azohydrazontautomere möglich sind. Unter Berücksichtigung der größten Änderungen des Bandenprofils, die der Azobrücke bei pH 2 zugeordnet wurden, kann man auf eine mögliche Protonierung des oben genannten Teils schließen.

Die beobachteten Banden im SERS-Spektrum unterstützen die Vermutung, dass sich der Phenylring 1 sehr nahe an den Silberpartikeln befindet, mit senkrechter Orientierung des Pyrazolrings und seiner verknüpften OH-Gruppe, und dass eine negativ geladene C3-COO⁻-Gruppe vorhanden ist, die sich entlang der C3-C-Bindung nahe der Oberfläche anlagert. Eine Konzentrationsabsenkung bewirkt eine Reorientierung der Phenylgerüstebene in Bezug auf die Silberoberfläche. Die Pyrazolringbanden sind in den SERS-Spektren weniger ausgeprägt, was nahe legt, dass dieser Teil der Molekülstruktur weniger in die Adsorption einbezogen ist.

Im Falle von E211 wurden zwei Sorten des erhältlichen Konservierungsmittels, kommerziell und

rein, untersucht. Die Differenzen zwischen den Raman-Spektren des kommerziellen und des reinen E211 führen uns zu der Annahme, dass mehrere Verunreinigungen in der kommerziellen Substanz vorhanden sind. Aufgrund von Verunreinigungen während des Verarbeitungsprozesses, werden verschiedene Schwermetalle v.a. Blei häufig in den Endprodukten gefunden. Das E211, das in der Lebensmittelindustrie verwendet wird kann in kleinen Dosen Arsen, Blei und Quecksilber enthalten. Gemäß den Raman-Spektren des E211 bei verschiedenen pH-Werten zeigt das Raman-Verhalten bei pH 3 die undissoziierte molekulare Form des Natriumbenzoates, während bei pH 5 das E211 dissoziiert zu sein scheint.

Eine starke chemische Wechselwirkung des E211 mit den kolloidalen Silberpartikeln unter mikromolaren Konzentrationen konnte durch die freien Elektronenpaare der Sauerstoffatome der senkrecht orientierten Carboxylatgruppe beobachtet werden. Die SERS-Spektren des E211 bei sauren pH-Werten wurden aufgenommen und zeigten die gleiche Orientierung durch die Carboxylatgruppe.

In Übereinstimmung mit unseren Dichtefunktionaltheorie-Rechnungen ist die molekulare Konformation des E127 planar mit Ausnahme des Benzoatrestes, der fast senkrecht zu dem Xanthenring liegt (71,8°). Dieser Winkel stimmt mit zuvor veröffentlichten Röntgenstrukturuntersuchungen überein. Weil der Winkel kleiner als 87,7° ist, können wir die Existenz der Quinoidform (Natriumsalze) des Farbstoffs bestätigen. Ebenfalls besonders für die Quinoidform des E127 ist, dass die Bindungen und die Winkel des Xanthenrings, normale Meßwerte wie die eines aromatischen Dreiringsystems aufzeigen. Gewöhnlich sind die kationischen Xanthenstrukturen in einer Quinoidform stabilisiert.

Von dem SERR-Spektrum bei einer Konzentration von $0,39 \times 10^{-7}$ M und in Übereinstimmung mit unserer optimierten Geometrie des E127, nehmen wir an, dass das E127-Molekül mit dem Xanthenring parallel und mit der Benzoatgruppe, ebenso wie mit der Carboxylatgruppe, senkrecht zu den Silberkolloidpartikeln liegen kann. Unter Beachtung der Schwingungsmodenzuordnung, kann die starke chemische Wechselwirkung des E127 mit den Silverkolloidpartikeln bei einer Konzentration von $0,39 \times 10^{-8}$ M durch Benzol- und Xanthenringe angenommen werden. Der Xanthenring liegt gekippt auf der Silberoberfläche durch die O26- und I22-Atome, und der Benzolring scheint ziemlich senkrecht zu der Silberoberfläche zu sein. Bei einer Konzentration von $0,39 \times 10^{-9}$ M ist das E127-Molekül über die Carboxylatgruppe und die I23-, I24-Atome des Xanthenrings, mit dem Xanthenring gekippt und mit dem Benzolring senkrecht, auf der Silberoberfläche adsorbiert. Bei einer Konzentration von $0,39 \times 10^{-10}$ M wird hingegen eine gekippte Orientierung des E127-Moleküls durch die π-Elektronen des Benzolrings, durch die Sauerstoff- und die Jodatome des Xanthenrings vorgeschlagen.

Die pH-abhängigen SERR-Spektren des E127 im sauren Bereich bestätigen die Anionen-induzierte Bildung von Charge-Transfer-Komplexen in dem Silberkolloid. Es liegt die monoanionische Form des Moleküls vor, und dieses kann an den Silberkolloidpartikeln durch den Xanthenring in einer vertikalen Orientierung adsorbiert werden. Die alkalischen pH-abhängigen SERR-Spektren zeigen die Protonierung des E127-Moleküls in unpolaren Lösungsmittel und das Vorliegen der Laktonform. Das Molekül liegt senkrecht auf den Silberkolloidpartikeln durch den Carboxylatrest der Laktonform des Moleküls.

Aus den Dichtefunktionaltheorie-Untersuchungen kann man schließen, dass das E132-Molekül mit Ausnahme der beiden Sulfongruppen nahezu planar ist, wobei sich ein Symmetriezentrum auf Höhe der C9=C9'-Brücke befindet. Beide Sulfongruppen zeigen die Trigonal-Pyramiden-Symmetrie und befinden sich auf zwei Seiten der Bindungsbrücke, wobei die doppelt gebundenen Sauerstoffatome jeweils gegensinnig ausgerichtet sind. Beide Sulfongruppen sind um 97,2° (berechneter Durchschnitt) aus der Molekülebene herausgedreht. Die Dichtefunktionaltheorie-Rechnungen legen eine Präferenz für das Trans-Konformer nahe, und in diesem Fall kann die Wasserstoffbrückenbindung zwischen dem Wasserstoffatom der N-H-Bindungen und dem Sauerstoffatom der C=O-Bindungen ausgebildet werden. Die stabile protonierte Struktur des E132 ist durch zwei mäßig starke N^+-$H\cdots O$=C Wasserstoffbrückenbindungen, die die Anzahl der möglichen Konformere begrenzt, charakterisiert.

Das Raman-Spektrum des Festkörpers des E132-Moleküls und die RR-Spektren der wässrigen Lösungen wurden aufgenommen, und die Markerbanden wurden identifiziert. E132 konnte in wässriger Lösung bis zu mikromolarer Konzentration mit RR, mit nanomolarer Konzentration mit der SERR-Spektroskopie an dem Natriumzitrat reduzierten Silberkolloid und auch bis zu mikromolarer Konzentration mit der SERR-Spektroskopie an rauen Silberfilmen mit verschiedener Rauigkeit, detektiert werden.

Die Oberflächen-Auswahlregeln gemeinsam mit den Daten aus der Literatur können die Adsorbatstrukturen an den Metalloberflächen erklären. Die starke Wechselwirkung des E132 mit den Silberkolloidpartikeln wurde bei nanomolarer Konzentration 12 Stunden nach der Aggregation beobachtet. Die symmetrisch-bidentate Wechselwirkung findet durch die freien Elektronenpaare von zwei Sauerstoffatomen der -SO_3^- Gruppen statt.

Die chemische Wechselwirkung des E132 mit den rauen Silberfilmen wird bis zu mikromolarer Konzentration und mit verschiedenen Orientierungen an den Metalloberflächen beobachtet. Wenn das Molekül mit grünem Laserlicht angeregt wird, findet die Wechselwirkung durch die freien Elektronenpaare der Sauerstoffatomen der -SO_3^- Gruppen, sowie einem Sauerstoffatom und einem Stickstoffatom des Pyrolidonrings, der sich in einer gekippten Orientierung befindet, statt. Wenn das Molekül mit rotem Laserlicht angeregt wird, bindet das Molekül an der Silberoberfläche durch die π-Elektronen, die über die Pyrolidon- und Phenylringe verteilt sind, und durch die negativen Sauerstoffionen der beiden -SO_3^- Gruppen, die sich in einer senkrechten Orientierung befinden.

Raman- und SERS-Spektren des MSG wurden bei verschiedenen Konzentrationen aufgenommen. Diese Untersuchung könnte als Referenz für weitere Raman-spektroskopische Anwendungen in der Spurenanalyse vor Lebensmittelprodukten dienen.

Die Geometrie des E621 wurde mit verschiedenen Basissätzen und Funktionalen des Gaussian03-Programms berechnet und optimiert. Anhand von DFT-Rechnungen kann gezeigt werden, dass beide Formen des E621 verschiedene Geometrien besitzen, die durch die unterschiedlichen Protonierungsmöglichkeiten des Moleküls erklärt werden können. Die Ergebnisse des FT-Raman-Spektrums sind mit der Zwitterionenstruktur des Festkörpers des E621 im Einklang.

Die Analyse der Raman-Spektren der Lösungen ergab beim Übergang von alkalischen zu sauren

pH-Werten zwei Änderungen bezüglich der molekularen Eigenschaften des E621. Die quantitativ protonierte Form des E621 dominiert bei niedrigen pH-Werten.

SERS-Spektren des MSG wurden auch für sehr niedrige Konzentrationen (bis zu 10^{-5} M) aufgenommen. Es wurde eine starke chemische Wechselwirkung des E621 mit den Kolloidpartikeln beobachtet, bei der eine Adsorption über die freien Elektronenpaare des Stickstoffatoms und der Sauerstoffatome der Carboxylgruppe beteiligt ist. Die Oberflächen-Auswahlregeln zusammen mit unseren theoretischen Ergebnissen können die Grundlage zur Erklärung der Adsorbatstruktur an der Metalloberfläche bei verschiedenen Konzentrationen und pH-Werten bilden.

Im sechsten Kapitel werden Messungen an entzündungshemmenden und anti-Malaria-aktiven Arzneimitteln vorgestellt. Die Raman-Spektren von verschiedenen Aspirin-Tabletten können für die Differenzierung der gepufferten und ungepufferten pharmazeutischen Spezies verwendet werden. Es wurde festgestellt, dass diese zwei Spezies des Aspirin leicht unterschiedlich an der Silberoberfläche chemisorbiert sind.

Es wurden FT- und Mikro-Raman-Spektren der beiden Arten von Paracetamol-Tabletten aufgenommen und die Marker-Banden der charakteristischen funktionellen Gruppen identifiziert; auch wurde für beide Paracetamol-Arten das Vorliegen der monoklinen Form im Festkörper bestätigt. Die Mikro-Raman-Spektren des Paracetamol nach der Rekristallisation auf den Glasoberflächen zeigen, dass das normale Paracetamol eine Mischung der monoklinen und orthorhombischen Formen enthält, während das Sinus-Paracetamol nur die monokline Form enthält. Die wichtigste Banden einiger Hilfsstoffe, die bei der Herstellung der Medikamente zugesetzt werden, konnten identifiziert werden.

Durch die Analyse der Raman-Spektren der beiden verschiedenen Paracetamol-Lösungen konnte das Vorliegen einer Mischung zwischen monokliner und orthorhombischer Form nachgewiesen werden, und beim Übergang von alkalischen zu sauren pH-Werten konnten protonierte Spezies von normalem und Sinus-Paracetamol unterschieden werden.

SERS-Spektren von Paracetamol konnten sogar bei niedrigen Konzentrationen (8×10^{-2} M) mit einem normalen SERS-Aufbau aufgenommen werden. Bei einer Konzentration von 8×10^{-2} M wurde eine chemische Wechselwirkung beider Paracetamol-Arten mit den Silberfilm-Oberflächen durch die Freien Elektronenpaare des Stickstoff- und des Sauerstoffatoms der Amidgruppe und durch die π-Elektronen des flach ausgerichteten Phenylrings festgestellt.

Es wird die erste NIR-SERS-spektroskopische Untersuchung von Hämatin in Gegenwart von zwei weit verbreiteten Anti-Malaria-Arzneimitteln beschrieben. Die Änderungen in den Spektren der betreffenden Hämatin-Arzneimittel-Systeme konnten mit Bezug auf die Interaktion zwischen den beiden Spezies erklärt werden, wobei die aliphatische Kette von CQ und der Pyrimidinrest im Falle von MQ bei der Adsorption an Goldpartikeln weniger an der Wechselwirkung beteiligt sind. Es kann angenommen werden, dass der Hämkern sensitiv wird für die Anwesenheit eines entsprechenden Chinolinskelett-Rings, der als axialer Ligand an die Metalloberfläche adsorbiert.

Einmal mehr konnte gezeigt werden, weshalb die beiden sich ergänzenden Methoden, Schwingungsspektroskopie und DFT-Rechnungen bei Chemikern weit verbreitet sind, vor allem seitdem

große Fortschritte bei der Laser-Anregung, den Detektionstechniken (CCD-Kameras, FT-Techniken) sowie bezüglich eindeutiger Bandenzuordnungen durch DFT-Rechnungen gemacht worden sind.

Die durch die Kombination beider Methoden gewonnenen vielversprechenden Ergebnisse zu den neuen, potentiell biologisch aktiven Lanthaniden-Komplexen pharmazeutisch aktiver Substanzen (Kapitel VII) überzeugten uns von der Leistungsfähigkeit der Dichtefunktionaltheorie-Rechnungen als Hilfsmittel bei der Auswertung von IR- und Raman-Spektren um verschiedene interessante Problemstellungen zu lösen. Deswegen wurden die IR- und Raman-Spektren neuer potentiell biologisch aktiver Lanthaniden-Komplexe, die von unseren Kooperationspartnern synthetisiert wurden, mit Hilfe exakter Ergebnisse aus DFT-Rechnungen (Strukturparameter, harmonische Schwingungswellenzahlen, Raman-Streuaktivitäten) besprochen, und viele vorher unvollständige Zuordnungen wurden analysiert und verbessert.

Die IR- und Raman-Untersuchungen zusammen mit den Ergebnissen aus Dichtefunktionaltheorie-Rechnungen von 3,5-Pyrazoldicarboxylsäure, Orotsäure, 5-Aminoorotsäure und ihrer La(III)-, Ce(III)- und Nd(III)-Komplexe geben Auskunft über die Art der Metall-Ligand-Bindung in den neuen Ln(III)-Komplexen. Desweiteren wurde die Art der Metall-Ligand-Bindung in den neuen La(III)-Komplexen der 3,5-Pyrazoldicarboxylsäure durch die Dichtefunktionaltheorie-Modellierung der La(III)-3,5-Pyrazoldicarboxylsäure-Struktur gezeigt: 3,5-Pyrazoldicarboxylsäure bindet über die Sauerstoffatome der Carboxylgruppen an das La(III)-Ion. IR- und Raman-Spektren von 3,5-Pyrazoldicarboxylsäure und ihrer La(III)-, Ce(III)- und Nd(III)-Komplexe wurden aufgenommen und die Banden zugeordnet, um sie als Datenbank für weitergehende Anwendungen in der Spurenanalyse der Seltenen Erden-Komplexe zu benutzen. Die schwingungsspektroskopische Untersuchung der 3,5-Pyrazoldicarboxylsäure und ihrer Lanthaniden-Komplexe, basierend auf IR- und Raman-Schwingungsdaten, half, Einsicht über das Koordinationsverhalten des Liganden und das Koordinationspolyeder der Lanthaniden-Komplexe zu erhalten.

Orotsäure bindet an das La(III)-Ion durch beide Sauerstoffatome der Carboxylgruppe eines Liganden, einem Carboxylsauerstoff eines weiteren Liganden und einem OH⁻-Ion. Die DFT-Rechnungen belegten die bidentate Bindung durch die Carboxylsauerstoffatome der einen Orotsäure und die monodentate Bindung durch einen Carboxylsauerstoff der anderen Orotsäure. Die Schwingungsanalysen, die für die Orotsäure und ihre Lanthaniden-Komplexe ausgeführt wurden, waren hilfreich bei der Erklärung des Verhaltens der sensitiv auf die Komplexierung reagierenden Schwingungsmoden des Liganden. Die schwingungsspektroskopische Untersuchung gab Auskunft über die Art der Koordination des Liganden zum Ln(III)-Ion und war in Übereinstimmung mit anderen Theorievoraussagen.

5-Aminoorotsäure bindet an das La(III)-Atom durch jeweils beide Sauerstoffatome der Carboxylgruppen von allen drei Liganden. Das Zentralatom ist sechsfachkoordiniert und bildet zusammen mit den Liganden eine verzerrte Oktaederstruktur. Die DFT-Rechnungen zusammen mit der Modenzuordnung zeigt, dass bidentate Bindungen über die Carboxylsauerstoffatome ausgebildet werden.

Zusammenfassend lässt sich sagen, dass die Ergebnisse eine überzeugende Darstellung für die Stärken der Dichtefunktional-Theorie liefern; vor allem im Hinblick auf die Interpretation von Schwingungsspektren mit hoher Modendichte, die für größere polyatomare Adsorbate bei Verwendung

der SERS-Technik erhalten werden können, wie auch im Hinblick auf eine detaillierte Einsicht in die Beziehung zwischen Schwingungseigenschaften und der Art der Silbersubstrat-Adsorbat-Bindung. Daher sind wir der Meinung, dass DFT-Rechnungen in Verbindung mit SERS von zunehmenden wissenschaftlichen und praktischen Interesse sein werden. Dabei haben wir ebenfalls versucht diejenige Methode herauszufinden, die die experimentellen Ergebnisse am besten wiedergibt. Wir haben die DFT-Methoden BLYP, B3LYP, BPW91 und P3PW91 sowie die Basissätze LANL2DZ, 6-31+G(d), 6-311+G(d) und 6-311++G** benutzt. In den ersten Rechnungen stellte sich die B3PW91/LANL2DZ-Kombination als die zuverlässigste und am wenigsten Rechenzeit-intensive für die Lanthanidensysteme heraus. Tatsächlich lieferten fast alle DFT-basierten Methoden, besonders in Verbindung mit dem LANL2DZ-Basissatz, Ergebnisse, die deutlich näher an den experimentellen Werten lagen als jene aus traditionellen Hartree-Fock- und Møller-Plesset-Elektronen-Korrelations-Methoden. Dies macht deutlich, dass quantenmechanische DFT-Rechnungen nicht nur eine unverzichtbare Ergänzung für spektroskopische Untersuchungen in der Chemie bilden, sondern auch Hilfsmittel sein können für ein besseres Verständnis und die Erforschung anderer neuer Fachrichtungen in der Physikalischen Chemie, wie zum Beispiel SERS.

Die Experimente und Ergebnisse, die in dieser Arbeit präsentiert wurden, demonstrieren, dass die Schwingungsspektroskopie in Verbindung mit quantenchemischen Rechnungen für die Untersuchung molekularer Strukturen ausgezeichnet geeignet ist. Insbesonders hat sich die Rezonanz-Raman-Spektroskopie als eine nützliche Methode zum Erhalt von Informationen über die anfängliche Dynamik und die Struktur des angeregten Zustandes der photochemisch-aktiven Systeme erwiesen. Darüber hinaus leisten Raman-, SERS- und SERRS-Spektroskopie einen wichtigen Beitrag zum Verständnis der Struktur-Aktivitäts-Beziehung von verschiedenen Arzneimitteln.

Bibliography

1. Braude EA. *Nature (London ,UK)* 1945; **155**: 733.
2. Duncan ABF, Matsen FA. in *Chemical Application of Spectroscopy*, West W Ed., Interscience, New York, 1956; **V**.
3. Gillam AE, Stern ES. *Electronic Absorption Spectroscopy*, Edward Arnold, London, 1957; **2**.
4. Glick D, Greenberg LJ. *Anal. Chem.* 1959; **31**: 42A.
5. Rao CNR. *Ultra-violet and visible Spectroscopy. Chemical Applications*, Butterworth&Co. Ltd.: London, 1961; **1,2**.
6. Biquard D. *Ann. Chim. Appl.* 1933; **20**: 97.
7. Brown HC, McDaniel DH, Hafliger O. in *Determination of Organic Structures by Physical Methods*, Braude EA and Nachod FC Eds., Academic Press, New York, 1955; **14**.
8. Grynkiewicz G, Poenie M, Tsien RY. *J. Biol. Chem.* 1985; **260**: 3340.
9. Lakowicz JR. *Principles of Fluorescence Spectroscopy*, Plenum Press, New York, 1983.
10. Lewis GN, Kasha M. *J. Am. Chem. Soc.* 1945; **67**: 994.
11. West W. *Chemical Applications of Spectroscopy*, Interscience, New York, 1956; **VI**.
12. Guilbault GG. *Practical Fluorescence*, Second Ed., Marcel Dekker, Inc.: New York, 1990.
13. Hallam HE. in *Infra-Red Spectroscopy and Molecular Structure. An Outline of the Principles*, Davies M. Ed., Elsevier, Amsterdam, 1963; **XII**: 405-440.
14. Josien ML. *Molecular Spectroscopy*, Proc. V[th] Eur. Congress, Amsterdam, Butterworth Sci., London, 1962.
15. Hallam HE. *Spectroscopy*, Proc. Institute of Petroleum Hydrocarbon Res. Group IIIrd Conf., London, 1962; 245.
16. Williams RL. *Ann. Rept. Progr. Chem. (Chem. Soc. London)*, 1962; **58**: 34.
17. Cutmore EA, Hallam HE. *Trans. Faraday Soc.* 1962; **58**: 40.
18. Gordy W, Stanford SC. *J. Chem. Phys.* 1940; **8**: 170.
19. Lord RC, Nolin B, Stidham HD. *J. Am. Chem. Soc.* 1955; **77**: 1365.
20. Bayliss NS, Cole ARH, Little LH. *Spectrochim. Acta* 1959; **15**: 12.
21. Tuomikoski P. *J. Chem. Phys.* 1952; **20**: 1054.
22. Kasha M. *Disc. Faraday Soc.* 1950; **9**: 14.
23. McConnel H. *J. Chem. Phys.* 1952; **20**: 700.
24. Bayliss NS, McRae EG. *J. Phys. Chem.* 1954; **58**: 1002.
25. Pauling L. *The Nature of the Chemical Bond,* 2nd Ed., Cornell University Press, New York, 1948.
26. Forbes WF, Templeton JF. *Canad. J. Chem.* 1958; **36**: 180.
27. Forbes WF, Knight AR. *Canad. J. Chem.* 1959; **37**: 334.
28. Pimentel GC, McClellan AL. *The Hydrogen Bond*, Freeman WH&Co., London, 1960.
29. Blinc R, Hadži D. *Hydrogen Bonding*, Pergamon, London, 1959.
30. Singh RK, Asthana BP, Verma AL, Pathak CM. *Chem. Phys. Lett.* 1997; **278**: 35.

31. Singh RK, Bhriguvansh P, Asthana BP, Verma AL. *Chem. Phys. Lett.* 1998; **296**: 611.
32. Schlücker S,Singh RK, Asthana BP, Popp J, Kiefer W. *J. Phys. Chem. A* 2001; **105**: 9983.
33. Asthana BP, Kiefer W. *Vibrational Spectra and Structure*,Durig JR Ed., Elsevier, Amsterdam, 1993; **20**: 127.
34. Exner K, Fischer G, Bahr N, Beckmann E, Lugan M, Yang F, Rihs G, Keller M, Hunkler D, Knothe L, Prinzbach H. *Eur. J. Org. Chem.* 2000; **2000**: 763.
35. Castaneda J, Denisov GS, Kucherov SY, Schreiber VM, Shurukhina AV. *J. Mol. Struct.* 2003; **660**: 25.
36. Bratoz S, Hadži D, Sheppard N. *Spectrochim. Acta* 1956; **8**: 249.
37. Gonzalez-Sanchez F. *Spectrochim. Acta* 1958; **12**: 17.
38. Hadži D, Sheppard N. *Proc. Roy. Soc. A* 1953; **216**: 247.
39. Lin-Vien D, Colthup NB, Fateley WG, Grasselli JG. *The Handbook of Infrared and Raman Characteristic Frequencies of Organic Molecules*, Jovanovich HB Ed., Academic Press Inc., San Diego, 1991; 140.
40. Dollish FR, Fateley WG, Bentley FF. *Characteristic Raman Frequencies of Organic Compounds*, John Wiley&Sons Inc., Pittsburgh, Pennsylvania, 1974; 128.
41. Orza JM, Garcia MV, Alkorta I, Elguero J. *Spectrochim. Acta A* 2000; **56**: 1469.
42. Szabo A, Cesljevic VI, Kovacs A. *Chem. Phys.* 2001; **270**: 67.
43. Gilli G, Gilli P. *J. Mol. Struct.* 2000; **552**: 1.
44. Coulson CA. in *Hydrogen Bonding*, Hadži D Ed., Pergamon Press, New York, 1959.
45. Morokuma K. *J. Chem. Phys.* 1971; **55**: 1236.
46. Stevens ED, Lehmann MS, Coppens P. *J. Am. Chem. Soc.* 1977; **99**: 2829.
47. Pimentel GC. *J. Chem. Phys.* 1951; **19**: 446.
48. Reid C. *J. Chem. Phys.* 1959; **30**: 182.
49. Kollman PA, Allen LC. *J. Am. Chem. Soc.* 1970; **92**: 6101.
50. Parr RG, Yang W. *Density-Functional Theory of Atoms and Molecules*, Oxford University Press, New York, 1989.
51. Geerlings P, De Proft F, Langenaeker W. *Chem. Rev.* 2003; **103**: 1793.
52. Chermette H. *J. Comput. Chem.* 1999; **20**: 129.
53. Parr RG, Donnelly RA, Levy M, Palke WE. *J. Chem. Phys.* 1978; **68**: 3801.
54. Kohn W, Becke AD, Parr RG. *J. Phys. Chem.* 1996; **100**: 12974.
55. Pearson RG. *J. Chem. Educ.* 1999; **76**: 267.
56. Sanderson RT. *Science* 1951; **114**: 670.
57. Thar J, Kirchner B. *J. Phys. Chem. A* 2006; **110**: 4229.
58. Atkins PW. *Molecular Quantum Mechanics*, Clarendon Press, Oxford, 1970.
59. Placzek G, Rayleigh-Streuung und Raman-Effekt, *Handbuch der Radiologie*, Marx E Ed., Akad. Verlag, Leipzig, 1934; **VI**: 205-374.
60. Long DA. *Raman Spectroscopy*, McGraw-Hill Ed., UK, London, 1977; **4**: 74-110.
61. Evans JC. in *Infra-Red Spectroscopy and Molecular Structure. An Outline of the Principles*, Davies M Ed., Elsevier, Amsterdam, 1963; **VI**: 199-225.
62. Tu AT. *Raman spectroscopy in biology. Principles and Applications*, Wiley J&Sons, New York, 1982; **1**: 3-43.
63. Demtröder W. *Laser Spectroscopy. Basic Concepts and Instrumentation*, Springer Verlag Berlin, Heidelberg, 1981.
64. Freeman SK. *Application of Laser Raman Spectroscopy*, Wiley, New York, 1974.
65. Chalmers JM, Griffiths PR. *Handbook of Vibrational Spectroscopy*, Wiley J&Sons, Chichester Baffins Lane, UK, 2002; **1**.
66. Durig JR, Sullivan JF. in *Non-Linear Raman Spectroscopy and Its Chemical Applications*, Kiefer W& Long DA Eds., Reidel D Publ. Co., 1982; 33-50.
67. Mills IM. in *Infra-Red Spectroscopy and Molecular Structure. An Outline of the Principles*,Davies M Ed., Elsevier, Amsterdam, 1963; **V**: 166-198.
68. Hollas JM. *Modern Spectroscopy*, 2nd Ed., Wiley J&Sons, Baffins Lane, UK, 1992; **6**: 128-183.
69. Barnes AJ, Orville WJ. *Vibrational Spectroscopy–Modern Trends*, Elsevier Sci., Amsterdam, Holland, 1977.
70. Bunker PR. *Molecular Symmetry and Spectroscopy*, Academic Press Inc., New York, 1979.
71. Jodl HJ. *Vibrational Spectra and Structure. A series of advances*, Durig JR Ed., Elsevier, Amsterdam, Holland, 1984; **13**.
72. Niquist RA. *Interpreting Infrared, Raman, and NMR Spectra*, Academic Press, San Diego, 2001; **1**.
73. Brandt ES, Cotton TM. in *Physical Methods of Chemistry*, 2nd Ed.,Rossiter BW&Baetzold RG Eds., John Wiley&Sons, New York, 1993; **IXB**.
74. Schrader B. in *Infrared and Raman Spectroscopy*, Schrader B Ed., VCH Weinheim, 1995; **2**.
75. Chempeney DC. *Fourier Transforms and their Physical Applications*, Academic Press, London, 1973.
76. Marshall AG, Verdun FR. *Fourier Transforms in NMR, Optical and Mass Spectroscopy*, Elsevier, Amsterdam, 1990.
77. Felker PM, Maxton PM, Schaeffer MW. *Chem. Rev.* 1994; **94**: 1787.
78. Fellgett PB. *Infrared Phys.* 1984; **24**: 95.
79. Jacquinot P. *J. Opt. Soc. Am.* 1954; **44**: 761.
80. Jacquinot P. *Infrared Phys.* 1984; **24**: 99.

81. Champion PM, Albrecht AC. *Ann. Rev. Phys. Chem.* 1982; **33**: 353.

82. Johnson BB, Peticolas WL. *Ann. Rev. Phys. Chem.* 1976; **27**: 465.

83. Siebrand W, Zgierski M. *Resonance Raman Spectroscopy–A Key to Vibronic Coupling*, in *Excited State*, Lim EC Ed., Academic Press, New York, 1979; **1**: 1-36.

84. Myers AB, Mathies RA. *Resonance Raman Intensities: A Probe of Excited State Structure and Dynamics*, in *Biological Applications of Raman Spectroscopy*, Spiro TG Ed., Wiley, New York, 1988; **1**: 1-58 .

85. Brandmüller J, Kiefer W. Physicist's view, 50 years of Raman Spectroscopy, *Spex Speaker* 1978; **23**: 310.

86. Fleischmann M, Hendra PJ, McQuillan AJ. *Chem. Phys. Lett.* 1974; **26**: 163.

87. Jeanmaire DL, Van Duyne RP. *J. Electroanal. Chem.* 1977; **84**: 1.

88. Albrecht MG, Creighton JA. *J. Am. Chem. Soc.* 1977; **99**: 5215.

89. Van Duyne RP. in *Chemical and Biochemical Applications of Laser*, Moore CB Ed., Academic Press, New York, 1979; **4**.

90. Furtak TE, Reyes J. *Surf. Sci.* 1980; **93**: 351.

91. Lee TK, Birman JL. *J. Raman Spectrosc.* 1981; **10**: 140.

92. Krasser W, Renaouprez AJ. *J. Raman Spectrosc.* 1981; **11**: 425.

93. Loo BH. *J. Chem. Phys.* 1981; **75**: 5955.

94. Creighton JA, Eadon DG. *J. Chem. Soc, Faraday Trans.* 1991; **87**: 3881.

95. Kerker M Ed., *Selected Papers on Surface Enhanced Raman Scattering*, SPIE Milestone Series, Washington, 1990; **MS 10**.

96. Sequaris JM, Koglin E. *Fresenius' Z. Anal. Chem.* 1985; **321**: 758.

97. Torres EL, Winefordner JD. *Anal. Chem.* 1987; **59**: 1626.

98. Munro CH, Smith WE, Armstrong DR, White PC. *J. Phys. Chem.* 1995; **99**: 879.

99. Moskovits M. *J. Chem. Phys.* 1982; **77**: 4408.

100. Moskovits M, Suh JS. *J. Phys. Chem.* 1984; **88**: 1293.

101. Gao X, Davies JP, Weaver MJ. *J. Phys. Chem.* 1990; **94**: 6858.

102. Cooney RP, Mahoney MR, McQuillan AJ. *Advances in Infrared and Raman spectroscopy*, Clark RJH& Hester RE Eds., Heyden, Philadelphia, 1982; **9**: 188.

103. Campion A, Mullins DR. *Chem. Phys. Lett.* 1983; **94**: 576.

104. Campion A, Mullins DR. *Surf. Sci.* 1985; **158**: 263.

105. Seki H. *J. Electron Spectrosc. Relat. Phenom.* 1986; **39**: 289.

106. Mrozek MF, Wasileski SA, Weaver MJ. *J. Am. Chem. Soc.* 2001; **123**: 12817.

107. Chang RK. *Ber. Bunsen. Ges. Phys. Chem.* 1987; **91**: 296.

108. Creighton JA. *Spectroscopy of surface*, Clark RJH&Hester RE Eds., Wiley, New York, 1988; 37.

109. Murray CA. *Surface Enhanced Raman Scattering*, Chang RK&Furtak TE Eds., Plenum, New York, 1982; 203.

110. Cotton TM, Uphaus RA, Möbius D. *J. Phys. Chem.* 1986; **90**: 6071.

111. Chang RK, Laube BL. *CRC Crit. Rev. Solid State Mater. Sci.* 1984; **12**: 1.

112. Barz F, Gordon II JG, Philpott MR, Weaver MJ. *Chem. Phys. Lett.* 1982; **91**: 291.

113. Metiu H, Das P, *Annu. Rev. Phys. Chem.* 1984; **35**: 507.

114. Wokaun A. *Solid State Phys.* 1984; **38**: 223.

115. Chew H, McNulty PJ, Kerker M. *Phys. Rev. A* 1976; **13**: 396.

116. Wang DS, Chew H, Kerker M. *Appl. Opt.* 1980; **19**: 2256.

117. Kerker M, Wang DS, Chew H. *Appl. Opt.* 1980; **19**: 4159.

118. Wang DS, Kerker M. *Phys. Rev. B* 1981; **24**: 1777.

119. Chew H, Wang DS, Kerker M. *Phys. Rev. B* 1983; **28**: 4169.

120. Kerker M, Siiman O, Wang DS. *J. Phys. Chem.* 1984; **88**: 3168.

121. Kerker M. *The Scattering of Light and Other Electromagnetic Radiation*, Academic Press, New York, 1969.

122. Blatchford CG, Campbell JR, Creighton JA. *Surf. Sci.* 1981; **108**: 411.

123. Siiman O, Bumm LA, Callaghan R, Blatchford CG, Kerker M. *J. Phys. Chem.* 1983; **87**: 1014.

124. Lyon WA, Nie SM. *Anal. Chem.* 1997; **69**: 3400.

125. Emory SR, Haskins WE, Nie SM. *J. Am. Chem. Soc.* 1998; **120**: 8009.

126. Kneipp K, Kneipp H, Manoharan R, Hanlon EB, Itzkan I, Dasari RR, Feld MS. *Appl. Spectrosc.* 1998; **52**: 1493.

127. Krug JT, Wang GD, Emory SR, Nie SM. *J. Am. Chem. Soc.* 1999; **121**: 9208.

128. Kneipp K, Kneipp H, Itzkan I, Dasari RR, Feld MS. *Chem. Phys.* 1999; **247**: 155.

129. Michaels AM, Nirmal M, Brus LE. *J. Am. Chem. Soc.* 1999; **121**: 9932.

130. Xu H, Bjerneld EJ, Käll M, Börjesson L. *Phys. Rev. Lett.* 1999; **83**: 4357.

131. Constantino CJL, Lemma T, Antunes PA, Aroca R. *Anal. Chem.* 2001; **73**: 3674.

132. Moskovits M. *Proc. XVIIIth ICORS*, Minsk J, Jalsovszky G, Keresztury G Eds., Budapest, Hungary, 2002; 53.

133. Kneipp K, Wang Y, Kneipp H, Itzkan I, Dasari RR, Feld MS. *Phys. Rev. Lett.* 1996; **76**: 2444. Kneipp K, Kneipp H, Kneipp J. *Account Chem. Res.* 2006; **39**: 443.

134. Haslett TL, Tay L, Moskovits M. *J. Chem. Phys.* 2000; **113**: 1641.

135. Moskovits M, DiLella DP. *Surface Enhanced Raman Scattering*, Chang RK&Furtak TE Eds., Plenum, New York, 1982; 243.

136. Otto A. *Appl. Surf. Sci.* 1980; **6**: 309.
137. Otto A. *J. Raman Spectrosc.* 1991; **22**: 743.
138. Guzonas DA, Irish DE, Atkinson GF. *Langmuir* 1990; **6**: 1102.
139. Watanabe T, Kawanami O, Honda K, Pettinger B. *Chem. Phys. Lett.* 1983; **102**: 565.
140. Roy D, Furtak TE. *Chem. Phys. Lett.* 1986; **124**: 299.
141. Lombardi JR, Birke RL, Lu TH, Xu J. *J. Chem. Phys.* 1986; **84**: 4174.
142. Adrian FJ. *J. Chem. Phys.* 1982; **77**: 5302.
143. Wetzel H, Gerischer H, Pettinger B. *Chem. Phys. Lett.* 1981; **78**: 392.
144. Birke RL, Lombardi JR. *Surface-Enhanced Raman Scattering*, Gale RJ Ed., *Spectroelectrochemistry: Theory and Practice*, Plenum, New York, 1988; 263.
145. Persson BNJ. *Chem. Phys. Lett.* 1981; **82**: 561.
146. Gersten JI, Birke RL, Lombardi JR. *Phys. Rev. Lett.* 1979; **43**: 147.
147. Stacy AA, Van Duyne RP. *Chem. Phys. Lett.* 1983; **102**: 365.
148. Siiman O, Lepp A, Kerker M. *J. Phys. Chem.* 1983; **87**: 5319.
149. Zeman EJ, Carron KT, Schatz GC, Van Duyne RP. *J. Chem. Phys.* 1987; **87**: 4189.
150. Rodger C, Smith WE, Dent G, Edmondson M. *J. Chem. Soc., Dalton Trans.* 1996; **5**: 791.
151. Kneipp K, Wang Y, Dasari RR, Feld MS. *Appl. Spectrosc.* 1995; **49**: 780.
152. Xu Y, Zheng Y. *Anal. Chim. Acta* 1989; **225**: 227.
153. Munro CH, Smith WE, White PC. *Analyst* 1995; **120**: 993.
154. Hildebrandt P, Stockburger M. *J. Raman Spectrosc.* 1986; **17**: 55.
155. Pineda AC, Ronis D. *J. Chem. Phys.* 1985; **83**: 5330.
156. Persaud I, Grossman WEL. *J. Raman Spectrosc.* 1993; **24**: 107.
157. Cotton TM, Schultz SG, Van Duyne RP. *J. Am. Chem. Soc.* 1982; **104**: 6528.
158. Hildebrandt P, Spiro TG. *J. Phys. Chem.* 1984; **88**: 5935.
159. Nie S, Castillo CG, Bergbauber KL, Kuck JFR, Nabiev IR, Yu NT. *Appl. Spectrosc.* 1990; **44**: 571.
160. Sokolov KV, Lutsenko SV, Nabiev IR, Nie S, Yu NT. *Appl. Spectrosc.* 1991; **45**: 1143.
161. Macdonald IDG, Smith WE, Munro AW. *FEBS Lett.* 1996; **396**: 196.
162. Nabiev I, Baranov A, Chourpa I, Beljebbar A, Sockalingum GD, Manfait M. *J. Phys. Chem.* 1995; **99**: 1608.
163. Kaul BB, Holt RE, Schlegel VL, Cotton TM, *Anal. Chem.* 1988; **60**: 1580.
164. Mullen KI, Wang D, Crane LG, Carron KT. *Anal. Chem.* 1992; **64**: 930.
165. Xi K, Sharma SK, Taylor GT, Muenow DW. *Appl. Spectrosc.* 1992; **46**: 819.
166. Hidalgo M, Montes R, Laserna JJ, Ruperez A. *Anal. Chim. Acta* 1996; **318**: 229.
167. Tsai WH, Boerio FJ, Clarson SJ, Montaudo G. *J. Raman Spectrosc.* 1990; **21**: 311.
168. Markwort L, Hendra PJ, *J. Electroanal. Chem.* 1995; **397**: 225.
169. Furtak TE, Trott G, Loo BH. *Surf. Sci.* 1980; **101**: 374.
170. Pettinger B, Wenning U. *Chem. Phys. Lett.* 1978; **56**: 253.
171. Efrima S. *Modern Aspects of Electrochemistry*, Conway BE, White RE, Bockris JO'M Eds., Plenum, New York, 1985; **16**: 253ff.
172. Gao P, Patterson ML, Tadayyoni MA, Weaver MJ. *Langmuir* 1985; **1**: 173.
173. Macomber SH, Furtak TE, Devine TM. *Chem. Phys. Lett.* 1982; **90**: 439.
174. Chen TT, Von Raben KU, Owen JF, Chang RK, Laube BL. *Chem. Phys. Lett.* 1982; **91**: 494.
175. Devine TM, Furtak TE, Macomber SH. *J. Electroanal. Chem. Interfacial Electrochem.* 1984; **164**: 299.
176. Loo BH. *Ann. Rep. INCRA*, Project No. 341, 1982.
177. Carron KT, Xue GI, Lewis ML. *Langmuir* 1991; **7**: 2.
178. Laserna JJ, Campiglia AD, Winefordner JD. *Anal. Chim. Acta* 1988; **208**: 21.
179. Sutherland WS, Laserna JJ, Angebranndt MJ, Winefordner JD. *Anal. Chem.* 1990; **62**: 689.
180. Lee PC, Meisel D. *Chem. Phys. Lett.* 1983; **99**: 262.
181. Heard SM, Grieser F, Barraclough CG. *Chem. Phys. Lett.* 1983; **95**: 154.
182. Sheng RS, Zhu L, Morris MD. *Anal. Chem.* 1986; **58**: 1116.
183. Blatchford CG, Siiman O, Kerker M. *J. Phys. Chem.* 1983; **87**: 2503.
184. Wetzel H, Gerischer H, Pettinger B. *Chem. Phys. Lett.* 1982; **85**: 187.
185. Carey Lea M. *Am. J. Sci.* 1889; **37**: 476.
186. Creighton JA, Blatchford CG, Albrecht MG. *J. Chem. Soc.; Faraday Trans. 2* 1979; **75**: 790.
187. Lee PC, Meisel D. *J. Phys. Chem.* 1982; **86**: 3391.
188. Munro CH, Smith WE, Garner M, Clarkson J, White PC. *Langmuir* 1995; **11**: 3712.
189. Siiman O, Feilchenfeld H. *J. Phys. Chem.* 1988; **92**: 453.
190. Fu S, Zhang P, *J. Raman Spectrosc.* 1992; **23**: 93.
191. Miller SK, Baiker A, Meier M, Wokaun A. *J. Chem. Soc., Faraday Trans. 1* 1984; **80**: 1305.
192. Xue G, Dong J. *Anal. Chem.* 1991; **63**: 2393.
193. Ruperez A, Laserna JJ. *Anal. Chim. Acta* 1994; **291**: 147.
194. Aroca R, Martin F. *J. Raman Spectrosc.* 1985; **16**: 156.
195. Albano EV, Daiser S, Miranda R, Wandelt K. *Surf. Sci.* 1985; **150**: 367.

196. Chalmers JM, Griffiths PR. *Handbook of Vibrational Spectroscopy*, Wiley J&Sons, Chichester Baffins Lane, UK, 2002; **2**.
197. Sennett RS, Scott GD. *J. Opt. Soc. Am.* 1950; **40**: 203.
198. Schlegel VL, Cotton TM. *Anal. Chem.* 1991; **63**: 241.
199. Hansma PK, Elings VB, Marti O, Bracker CE. *Science* 1988; **242**: 209.
200. Hohenberg P, Kohn W. *Phys. Rev. B* 1964; **136**: 864.
201. Kohn W, Sham LJ. *Phys. Rev. A* 1965; **140**: 1133.
202. Levy M. *Proc. Natl. Acad. Sci. (USA)* 1979; **76**: 6062.
203. Parr RG, WangW. *Density Functional Theory of Atoms and Molecules*, Oxford Press, New York, 1989.
204. Jensen F. *Introduction to Computational Chemistry*, Wiley J&Sons, Baffins Lane, UK, 1999.
205. St.-Amant A. *Reviews in Computational Chemistry*, Lipkowitz KB&Boyd DB Eds., Wiley, New York, 1996; **7**: 217.
206. Ziegler T. *Chem. Rev.* 1991; **91**: 651.
207. Szabo A, Ostlund NS. *Modern Quantum Chemistry : Introduction to Advanced Electronic Structure Theory*, 1ˢᵗ Ed. Revised, McGraw-Hill, New York, 1989.
208. Hehre WJ, Radom L, Schlyer PvR, Pople JA. *Ab Initio Molecular Orbital Theory*, Wiley J&Sons, New York, 1986.
209. Dahl JP, Avery J. Eds. *Local Density Approximation in Quantum Chemistry and Solid State Physics*, Plenum, New York, 1984.
210. Vosko SH, Wilk L, Nusair M. *Can. J. Phys.* 1980; **58**: 1200.
211. Labanowski JK, Jan K. *Density Functional Methods in Chemistry*, Andzelm JW Ed., Springer, New York, 1991.
212. Papai I, St.-Amant A, Ushio J, Salahub D. *Int. J. Quantum Chem., Quantum Chem. Symp.* 1990; **24**: 29.
213. Bartelett RJ, Stanton JF. *Reviews in Computational Chemistry*, Lipkowitz KB&Boyd DB Eds., VCH Publishers, New York, 1994; **5**: 65-169.
214. Andzelm J, Wimmer E. *J. Chem. Phys.* 1992; **96**: 1280.
215. Johnson BG, Gil PMW, Pople JA. *J. Chem. Phys.* 1993; **98**: 5612.
216. Ceperley DM. *Phys. Rev. B* 1978; **18**: 3126.
217. Ceperley DM, Adler BJ. *Phys. Rev. Lett.* 1980; **45**: 566.
218. Perdew JP, Zunger A. *Phys. Rev. B* 1981; **23**: 5048.
219. Becke AD. *The challenge of d and f electrons*, *ACS Symp. Ser.* Salahub DR&Zerner MC Eds., Am. Chem. Soc., Washington, DC, 1989; **394**: 165.
220. Becke AD. *J. Chem. Phys.* 1992; **96**: 2155.
221. Becke AD. *J. Chem. Phys.* 1992; **97**: 9173.
222. Sim F, St.-Amant A, Papai I, Salahub DR. *J. Am. Chem. Soc.* 1992; **114**: 4391.
223. Mlynarski P, Salahub DR. *Phys. Rev. B* 1991; **43**: 1399.
224. Perdew JP, Wang Y. *Phys. Rev. B* 1986; **33**: 8800.
225. Perdew JP. *Phys. Rev. B* 1986; **33:** 8822.
226. Becke AD. *Phys. Rev. A* 1988; **38**: 3098.
227. Miehlich B, Savin A, Stoll H, Preuss H. *Chem. Phys. Lett.* 1989; **157**: 200.
228. Perdew JP, Chevary JA, Vosko SH, Jackson KA, Pederson MR, Singh DJ, Fiolhais C. *Phys. Rev. A* 1992; **46**: 6671.
229. Langreth DC, Mehl MJ. *Phys. Rev. B* 1983; **28**: 1809.
230. Fan LY, Ziegler T. *J. Chem. Phys.* 1991; **94**: 6057.
231. Laasonen K, Csajka F, Parrinello M. *Chem. Phys. Lett.* 1992; **194**: 172.
232. Lee C, Yang W, Parr RG. *Phys. Rev. B* 1988; **37**: 785.
233. Becke AD. *J. Chem. Phys.* 1993; **98**: 1372.
234. Becke AD. *J. Chem. Phys.* 1993; **98**: 5648.
235. Slater JC. *Phys. Rev.* 1930; **36**: 57.
236. Boys SF. *Proc. R. Soc. (London) A* 1950; **200**: 452.
237. Clementi E, Corongiu G, Aida M. *Modern Techniques in Computational Chemistry*, Clementi E Ed., ESCOM Sci. Publishers, Leiden, 1990.
238. Henre WJ, Ditchfield R, Pople JA. *J. Phys. Chem.* 1972; **56**: 2257.
239. Binkely JS, Pople JA. *J. Am. Chem. Soc.* 1980; **102**: 939.
240. Krishnan R, Binkely JS, Seeger R, Pople JA. *J. Chem. Phys.* 1980; **72**: 650.
241. Frisch MJ, Pople JA, Binkely JS. *J. Chem. Phys.* 1984; **80**: 3265.
242. Wadt WR, Hay PJ. *J. Chem. Phys.* 1985; **82**: 284.
243. Hay PJ, Wadt WR. *J. Chem. Phys.* 1985; **82**: 270 .
244. Hay PJ, Wadt WR. *J. Chem. Phys.* 1985; **82**: 299.
245 Dunning Jr. TH, Hay PJ, in *Modern Theoretical Chemistry*,Schaefer HF IIIʳᵈ Ed., Plenum, New York, 1976; **3:** 1-28.
246. Bachrach SM. *Reviews in Computational Chemistry*, Lipkowitz KB&Boyd DB Eds., VCH Publishers, New York, 1994; **5**: 171.

247. Reed AE, Weinstock RB, Weinhold F. *J. Chem. Phys.* 1985; **83**: 735.
248. Reed AE, Weinhold F. *J. Chem. Phys.* 1985; **83**: 1736.
249. Reed AE, Curtiss LA, Weinhold F. *Chem. Rev.* 1988; **88**: 899.
250. Lödwin P-O. *Phys. Rev.* 1955; **97**: 1474.
251. Mulliken RS, Ermler WC. *Diatomic Molecules: Results of Ab Initio Calculations*, Academic Press, New York, 1977; 33-38.
252. Collins JB, Steitwieser A. *J. Comput. Chem.* 1980; **1**: 81.
253. Davidson ER. *Reduced Density Matrices in Quantum Chemistry*, Academic Press, New York, 1976.
254. McWeeney R, Sutcliffe BT. *Methods of Molecular Quantum Mechanics*, Academic Press, New York, 1969.
255. Sutherland WS, Winefordner JD. *J. Colloid Interface Sci.* 1992; **148**: 129.
256. Rivas L, Sanchez-Cortes S, Garcia-Ramos JV, Morcillo G. *Langmuir* 2000;**16**: 9723.
257. Frisch MJ, Trucks GW, Schlegel HB, Gill PMW, Johnson BG, Robb MA, Cheeseman JR, Keith T, Peterson GA, Montgomery JA, Rhaghavachari K, Al-Laham MA, Zakrzewski VG, Ortiz JV, Foresman JB, Ciolowski J, Stefanov BB, Nanayakkara A, Challacombe M, Peng CY, Ayala PY, Chen W, Wong MW, Andres JL, Replogle ES, Gomberts R, Martin RL, Fox DJ, Binkley JS, Defrees DJ, Baker J, Stewart JP, Head-Gordon M, Gonzales C, Pople JA. *Gaussian 98*; Revision A7; Gaussian Inc.: Pittsburgh PA, 1998.
258. Frisch MJ, Trucks GW, Schlegel HB, Scuseria GE, Robb MA, Cheeseman JR, Montgomery Jr. JA, Vreven T, Kudin KN, Burant JC, Millam JM, Iyengar SS, Tomasi J, Barone V, Mennucci B, Cossi M, Scalmani G, Rega N, Petersson GA, Nakatsuji H, Hada M, Ehara M, Toyota K, Fukuda R, Hasegawa J, Ishida M, Nakajima T, Honda Y, Kitao O, Nakai H, Klene M, Li X, Knox JE, Hratchian HP, Cross JB, Adamo C, Jaramillo J, Gomperts R, Stratmann RE, Yazyev O, Austin AJ, Cammi R, Pomelli C, Ochterski JW, Ayala PY, Morokuma K, Voth GA, Salvador P, Dannenberg JJ, Zakrzewski VG, Dapprich S, Daniels AD, Strain MC, Farkas O, Malick DK, Rabuck AD, Raghavachari K, Foresman JB, Ortiz JV, Cui Q, Baboul AG, Clifford S, Cioslowski J, Stefanov BB, Liu G, Liashenko A, Piskorz P, Komaromi I, Martin RL, Fox DJ, Keith T, Al-Laham MA, Peng CY, Nanayakkara A, Challacombe M, Gill PMW, Johnson B, Chen W, Wong MW, Gonzalez C, Pople JA. *Gaussian 03*, Revision B04, Gaussian Inc.: Pittsburgh PA, 2003.
259. Lee C, Yang W, Parr RG. *Phys. Rev. B* 1988; **37**: 785.
260. Perdew JP. *Electronic Structure of Solids*, Ziesche P, Eschrig H Eds., Akademie Verlag, Berlin, 1991; 11.
261. Perdew JP, Wang Y. *Phys. Rev. B* 1992; **45**: 13244.
262. Dunning Jr. TH, Hay PJ. *Modern Theoretical Chemistry*, Schaefer HF Ed., Plenum, New York, 1976; **3**: 805.
263. Yamaguchi Y, Frisch M, Gaw JF, Schaefer HF, Binkley S. *J. Chem. Phys.* 1986; **84**: 2262.
264. Ojha AK, Srivastava SK, Peica N, Schlücker S, Kiefer W, Asthana BP. *J. Mol. Struct.* 2005; **735-736**: 349.
265. Asthana BP, Takahashi H, Kiefer W, *Chem. Phys. Lett.* 1983; **94**: 41.
266. Oxtoby DW. *J. Phys. Chem.* 1983; **87**: 3028.
267. Moressi A, Sassi P, Paolantoni M, Santini S, Cataliotti RS. *Chem. Phys.* 2000; **254**: 337.
268. Thomas Jr. GJ, Tsuboi M. *Adv. Biophys. Chem.* 1993; **3**: 1.
269. Strajbl M, Baumruk V, Florian J. *J. Phys. Chem. B* 1998; **102**: 1314.
270. Schweitzer KS, Chandler D. *J. Chem. Phys.* 1982; **76**: 2296.
271. Pagán YM, Ben-Amotz D, *J. Phys. Chem. B* 2000; **104**: 7858.
272. Ojha AK, Srivastava SK, Koster J, Shukla MK, Leszczynski J, Asthana BP, Kiefer W. *J. Mol. Struct.* 2004; **689**: 127.
273. Srivastava SK, Ojha AK, Koster J, Shukla MK, Leszczynski J, Asthana BP, Kiefer W. *J. Mol. Struct.* 2003; **661-662**: 11.
274. Singh RK, Singh SN, Asthana BP, Pantak CM. *J. Raman. Spectrosc.* 1994; **25**: 423.
275. Bodarev AF, Mardaeva AI. *Opt. Spectrosc.* 1973; **67**: 67.
276. Anderson PW. *J. Phys. Soc. Jpn.* 1954; **9**: 316.
277. Kubo R, Tomita K. *J. Phys. Soc. Jpn.* 1954; **9**: 888.
278. Müller LJ, Vanden Bout D, Berg M. *J. Chem. Phys.* 1993; **99**: 810.
279. Fischer SF, Laubereau A. *Chem. Phys. Lett.* 1978; **55**: 189.
280. Knapp EW, Fischer SF. *J. Chem. Phys.* 1982; **76**: 4730.
281. Asthana BP, Kiefer W, Knapp EW. *J. Chem. Phys.* 1984; **81**: 3774.
282. European Parliament and Council Directive 87/107/EEC (1988) on the approximation of the laws of the Member States concerning food additives authorised for use in foodstuffs intended for human consumption, *Official Journal of the European Communities*, 11.02.1989; **L40**: 27-33.
283. Saltmarsh M Ed., *Essential Guide to Food Additives,* Leatherhead Food RA Publishing, 2000; 1-322.
284. Wilson BG, Bahna SL. *Ann. Allergy Asthma Immunol.* 2005; **95**: 499.
285. World Health Organisation (1987). Principles for the Safety Assessment of Food Additives and Contaminants in Food. Environmental Health Criteria 70. International Programme on Chemical Safety (IPCS) in cooperation with the Joint FAO/WHO Expert Committee on Food Additives (JECFA). World Health Organisation, Geneva.
286. International Life Sciences Institute, *Food allergy and other adverse reactions to food,* Concise Monograph Series ILSI Europe, Avenue E. Mounier 83, Box 6, B-1200 Brussels, Belgium, 1994; 1-22.
287. Blackburn C, McClure PJ. *Foodborne pathogens: hazards, risk analysis and control*, CRC Press, 2002.
288. Branen A, Davidson P, Salminen S. *Food additives*; Marcel Dekker, New York, 1989; 83-137.

289. Juhlia L. *Int. J. Dermatol.* 1980; **19**: 548.

290. Virchow C, Szczeklik A, Bianco S, Schmitz-Schumann M, Juhl E, Robuschi M, Damonte C, Menz G, Serwonska M. *Respiration* 1988; **53**: 20.

291. Czech W, Schopf E, Kapp A. *Inflamm-Res*. 1996; **44**: 291.

292. Bircher AJ, Haldimann D, Weber J. *Allergy Clin. Immunol. Int*. 1996; **8**: 109.

293. Wedi B, Elsner J, Kapp A. *Allergy Clin. Immunol. Int*. 1996; **8**: 113.

294. Zuberbier T, Chantraine-Hess S, Hartmann K. *Acta Derm. Venereol* (Stockh) 1995; **75**: 484.

295. Petrus M, Bonaz S, Causse E, Micheau P, Rhabbour M, Netter JC, Bildstein G. *Allerg. Immunol.* 1997; **29**: 36.

296. Devlin J, David TJ. *Arch. Dis. Child.* 1992; **67**: 709.

297. Egger J, Wilson J, Carter CM, Turner MW, Soothill JF. *The Lancet* 1983; **322**: 865.

298. Madsen C. *Environ. Toxicol. Pharmacol.* 1997; **4**: 163.

299. Young E. *Environ. Toxicol. Pharmacol.* 1997; **4**: 111.

300. Giger A., *Pure Appl. Chem.* 2002; **74**: 1383.

301. Lancaster FE, Lawrence JF. *Food Addit. Contam.* 1999; **16**: 381.

302. Walker R. *Food and Cosmetics Toxicol.* 1970; **8**: 659.

303. Chung KT. *Mutat. Res.* 1983; **114**: 269.

304. Gicquell J, Carles M, Bodot H. *J. Phys. Chem.* 1979; **83**: 699.

305. Saha A, Das C, Goswami S, Peng SM. *Indian J. Chem. Sect. A* 2001; **40A**: 198.

306. Campos-Fernandez CS, Galan-Mascaros GR, Smucker BW, Dunbar KR. *Eur. J. Inorg. Chem.* 2003; **2003**: 988.

307. Dinda J, Ray U, Mostafa G, Lu TH, Usman A, Razak IA, Chantrapromma S, Fun HK, Sinha C. *Polyhedron* 2003; **22**: 247.

308. Ray US, Mostafa G, Lu TH, Sinha C. *Crystal Engineering* 2002; **5**: 95.

309. Byabartta P, Jasimuddin S, Ghosh BK, Sinha C, Slawin AMZ and Woollins JD. *New J. Chem.* 2002; **26**: 1415.

310. Lu TH, Misra TK, Lin PC, Liao FL, Chung CS. *Polyhedron* 2003; **22**: 535.

311. Allen FR, Kennard O, Watson DG, Brammer L, Orpen AG, Taylor R. *J. Chem. Soc. Perkin Trans.* 1987; **2**: S1.

312. Dinda J, Bag K, Sinha C, Mostafa G, Lu TH. *Polyhedron* 2003; **22**: 1367.

313. Dai Z, Peng B, Chen X. *Dyes and Pigments* 1999; **40**: 219.

314. Lye J, Freeman HS, Mason ME, Singh P. *Dyes and Pigments* 1999; **42**: 107.

315. Freeman HS, McIntosh SA, Singh P. *Dyes and Pigments* 1997; **35**: 11.

316. Anwar SO, Oikawa H, Nakanishi H. *Chem. Mater.* 2000; **12**: 1162.

317. Van Haverbeke L, Janssens JF and Herman MA *Intern. J. Environ. Anal. Chem.* 1981; **10**: 205.

318. Stobbaerts RF, Van Haverbeke L, and Herman MA. *J. Food Sci.* 1983; **48**: 521.

319. Sett P, Paul N, Brahma SK, Chattopadhyay S. *J. Raman Spectrosc.* 1999; **30**: 611.

320. McAnally G, McLaughlin C, Brown R, Robson DC, Faulds K, Takley DR, Smith WE and Graham D. *Analyst* 2002; **127**: 834.

321. Cîntă Pînzaru S, Pavel I, Peica N, Leopold N *Asian Chem. Lett.* 2004; **8**: 39.

322. Genç N. *Water SA* 2004; **30**: 399.

323. Barros AA, Rodrigues JA, Almeida PJ. *Anal. Chim. Acta* 1993; **273**: 539.

324. Faulds K, Littleford RE, Graham D, Dent G, Smith WE. *Anal. Chem.* 2004; **76**: 592.

325. de Mendonca AJG, Cardoso CMP, Juusola PM. *Fluid Phase Equilibria* 2003; **214**: 87.

326. Van Hove JLK, Kishnani P, Muenzer J, Wenstrup RJ, Summar ML, Brummond MR, Lachiewicz AM, Millington DS, Kahler SG. *Am. J. Med. Gen.* 1995; **59**: 444.

327. Green TP, Marchessault RP, Freese DK. *J. Pediatr.* 1983; **102**: 785.

328. Breitkreutz J, El-Saleh F, Kiera C, Kleinebudde P, Wiedey W. *Eur. J. Pharm. Biopharm.* 2003; **56**: 255.

329. Breitkreutz J, Bornhöft M, Wöll F, Kleinebudde P. *Eur. J. Pharm. Biopharm.* 2003; **56**: 247.

330. Davis BA, Raubertas RF, Pearson SK, Bowen WH. *Caries Res.* 2001; **35**: 331.

331. Baird-Parker AC, Silliker JH Eds., *Microbial Ecology of Foods*, Academic Press, New York, 1980; **1**: 126.

332. Lambert RJ, Stratford M. *J. Appl. Microbiol.* 1999; **86**: 157.

333. Chipley JR, Branen AL Davidson PM Eds., *Antimicrobials in foods*, Decker M, New York, 1983; 11.

334. Lewandowski W, Dasiewicz B, Koczon P, Skierski J, Dobrosz-Teperek K, Swislocka R, Fuks L, Priebe W, Mazurek AP. *J. Mol. Struct.* 2002; **604**: 189.

335. Wang K, Li YS. *Vib. Spectrosc.* 1997; **14**: 183.

336. Boerio FJ, Hong PP, Clark PJ, Okamoto Y. *Langmuir* 1990; **6**: 721.

337. Koczon P, Lewandowski W, Mazurek AP. *Vib. Spectrosc.* 1999; **20**: 143.

338. Bajdor K, Koczon P, Wieckowska E, Lewandowski W. *Int. J. Quantum Chem.* 1997; **62**: 385.

339. Moscibroda P, Baranska H, Tinti A, Lewandowski W. *Vib. Spectrosc.* 1995; **9**: 69.

340. Kwon CH, Kim HL, Kim MS. *J. Chem. Phys.* 2002; **116**: 10361.

341. Christiansen O, Stanton JF, Gauss J. *J. Chem. Phys.* 1998; **108**: 3987.

342. Badr Y, Mahmoud MA. *J. Mol. Struct.* 2005; **749**: 193.

343. Huang ZY, Yang CY, Zhuang ZX, Wang XR, Lee FSC. *Anal. Chim. Acta* 2004; **509**: 77.

344. Moskovits M, Suh JS. *J. Am. Chem. Soc.* 1986; **108**: 4711.

345. Szlyk E, Lakomska I. *Polish J. Chem.* 2002; **76**: 1399.

346. Morzyk-Ociepa B, Michalska D. *Spectrochim. Acta A* 2003; **59**: 1247.
347. Kwon YJ, Son DH, Ahn SJ, Kim MS, Kim K. *J. Phys. Chem.* 1994; **98**: 8481.
348. Sanchez-Cortes S, Garcia-Ramos JV. *J. Raman Spectrosc.* 1998; **29**: 365.
349. Pavel I, Szeghalmi A, Moigno D, Cîntă S, Kiefer W. *Biopolymers (Biospectroscopy)* 2003; **72**: 25.
350. Holmes WC, Scanlan JT. *Constery* 1927; **49**: 1594.
351. Zipfel E, Grezes R, Seiffert W, Zimmermann HW. *Histochemistry* 1982; **75**: 539.
352. Clark G. *Staining Procedures*, 4ᵗʰ Ed., Williams&Wilkins, Baltimore, 1989.
353. Evans L. *J. Chromatogr. A* 2003; **991**: 275.
354. Berzas Nevado JJ, Rodriguez Flores J, Villasenor Llerena MJ, Rodriguez Farinas N. *Talanta* 1999; **48**: 895.
355. Berzas Nevado JJ, Rodriguez Flores J, Villasenor Llerena MJ, Rodriguez Farinas N. *Anal. Chim. Acta* 1999; **391**: 353.
356. Chernov'yants MS, Gol'eva VE, Pyshchev AI. *J. Anal. Chem.* 2003; **58**: 139.
357. Ebato Y, Kato Y, Onishi H, Nagai T, Machida Y. *Drug Develop. Res.* 2003; **58**: 253.
358. Gustafsson H, Flood K, Berge OG, Brodin E, Olgart L, Stiller CO. *Exp. Neurol.* 2003; **182**: 427.
359. Phaechamud T, Koizumi T, Ritthidej GC. *Int. J. Pharm.* 2000; **198**: 97.
360. Katayama K, Kato Y, Onishi H, Nagai T, Machida Y. *Int. J. Pharm.* 2002; **248**: 93.
361. Yamabe K, Kato Y, Onishi H, Machida Y. *J. of Controlled Release* 2003; **90**: 71.
362. Dass CR. *S. Pac. J. Nat. Sci.* 2001; **19**: 18.
363. Yu W, Kappila T, Hultenby K, Persson JK, Xu XJ, Wiesenfeld-Hallin Z. *J. Peripher. Nerv. Syst.* 2000; **5**: 209.
364. Shin Y, Yoo DI. J. *Appl. Polym. Sci.* 1998; **67**: 1515.
365. Velasco GN, Pereiro GR, Diaz MEG. *Spectrochim. Acta A* 1995; **51**: 895.
366. Diaz MEG, Pereiro GR, Velasco GN. *Analyst* 1995; **120**: 457.
367. Chan MA, Lam SK, Lo D. *J. Fluoresc.* 2002; **12**: 327.
368. Perez-Ruiz T, Martinez-Lozano C, Tomas V, Fenoll J. *Analyst* 2000; **125**: 507.
369. Kapadia GJ, Tokuda H, Sridhar R, Balasubramanian V, Takayasu J, Bu P, Enjo F, Takasaki M, Konoshima T, Nishino H. *Cancer Lett.* 1998; **129**: 87.
370. Karpliuk IA, Volkova IA, Volkova NA, Okuneva LA, Gogol AT, Rybakova KD. *Vopr. Pitan* 1984; **2**: 58.
371. Borzelleca JF, Hogan JB, Koestner A. *Food Chem. Toxicol.* 1985; **23**: 551.
372. Borzelleca JF, Hogan JB. *Food Chem. Toxicol.* 1985; **23**: 719.
373. Collins TFX, Black TN, Ruggels DI. *Toxicol. Ind. Health* 1993; **9**: 605.
374. Collins TFX, Black TN, O'Donnell Jr. MW, Shackelford ME, Bulhack P. *Food Chem. Toxicol.* 1993; **31**: 161.
375. Zijno A, Marcon F, Leopardi P, Salvotore G, Carere A, Crebelli R. *Food Chem. Toxicol.* 1994; **32**: 159.
376. Vorhees CV, Butcher RE, Bruner RL, Wootten V, Sobotka TJ, *Arch. Toxicol.* 1994; **53**: 253.
377. Tanaka T. *Food and Chem. Toxicol.* 2001; **39**: 447.
378. Abdel Aziz AH, Shouman SA, Attia AS, Saad SF. *Pharmacol. Res.* 1997; **35**: 457.
379. Mekkawy HA, Massoud AA, El-Zawahry AM. *Problems of Forensic Sciences (Z Zagadnień Nauk Sądowych)* 2000; **43**: 40.
380. Diemair W, Hausser H. *Z. Lebensmitt. Untersuch.* 1951; **92**: 1965.
381. Walsh JP, Shiels L, Lim EM, Bhagat CI, Ward LC, Stuckey BGA, Dhaliwal SS, Chew GT, Bhagat MC, Cussons AJ. *J Clin. Endocrinol. Metab.* 2003; **88**: 4543.
382. Levitan H. *Proc. Natl. Acad. Sci. USA* 1977; **74**: 2914.
383. Smith PA, Dombro K, Zidichouski J. *J. Pharmacol. Exp. Ther.* 1984; **230**: 221.
384. Ruiz M, Ingbar SH. *Endocrinology* 1982; **110**: 1613.
385. Vought RL, Brown FA, Wolff J. *J. Clin. Endocrinol.* 1972; 34: 747.
386. Mol JA, Docter R, Hennemann G, Visser TJ. *Biochm. Biophys. Res. Commun.* 1982; **120**: 28.
387. McCombs GB, Green ML, Root J. *J. Contemporary Dental Practice* 2001; **2**: 1.
388. Ma CQ, Li KA, Tong SY. *Anal. Chim. Acta* 1996 **333**: 83.
389. Drexhage KH. in *Progress in Optics*, Wolf E. Ed., North-Holland, Amsterdam, 1974; 163.
390. Cody V. *Acta Cryst. C*, 1987; **43**: 705.
391. Wang L, Roitberg A, Meuse C, Gaigalas AK. *Spectrochim. Acta A*, 2001; **57**: 1781.
392. Stomphorst RG, van der Zwan G, Van Zandvoort MAMJ, Sieval AB, Zuilhof H, Vergeldt FJ, Schaafsma TJ. *J. Phys. Chem. A* 2001; **105**: 4235.
393. Cavallo L, Moore MH, Corrie JET, Fraternali F. *J. Phys. Chem. A* 2004; **108**: 7744.
394. Nakanishi W, Hayashi S, Kusuyama Y, Negoro T, Masuda S, Mutoh H. *J. Org. Chem.* 1998; **63**: 8373.
395. Hoshiba T, Ida T, Mizuno M, Takaoka K, Endo K. *J. Mol. Struct.* 2002; **602-603**: 381.
396. van der Vlugt JI, Sablong R, Mills AM, Kooijman H, Spek AL, Meetsma A, Vogt D. *Dalton Trans.* 2003; **2003**: 4690.
397. Lettinga MP, Klarenbeek EM, Zuilhof H, Van Zandvoort MAMJ. *J. Fluoresc.* 1999; **9:** 265.
398. Hildebrandt P, Epding A, Vanhecke F, Keller S, Schrader B. *J. Mol. Struct.* 1995; **349**: 137.
399. Healy PC, Hocking A, Tran-Dinh N, Pitt JI, Shivas RG, Mitchell JK, Kotiw M, Davis RA. *Phytochem.* 2004; **65**: 2373.
400. Brito-Arias M, Tapia-Albarrán M, Padilla-Martínez I, Martínez-Martínez F, Espinosa G, Molins E, Espinosa E. *J. Chem. Crystallogr.* 1999; **29**: 759.

401. Okada K, Okada S. *J. Mol. Struct.* 1999; **510**: 35.
402. Rihs G, Weis CD. *Dyes and Pigments* 1991; **15**: 165.
403. Wang X, Song M, Long Y. *J. Solid State Chem.* 2001; **156**: 325.
404. Badejo IT, Karaman R, Pinkerton AA, Fry JL. *J. Org. Chem.* 1990; **55**: 4327.
405. Salni D, Sargent MV, Skelton BW, Soediro I, Sutisna M, White AH, Yulinah E. *Aust. J. Chem.* 2002; **55**: 229.
406. Kasmai HS, Liu R. *J. Chem. Soc. (Perkin Trans. 2)* 1997; **1997**: 1605.
407. Allen FH, Kirby AJ. *J. Am. Chem. Soc.* 1984; 106: 6197.
408. Suter HU, Nonella M. *J. Phys. Chem.* 1998; **102**: 10128.
409. Schneider AG, Schmalle HW, Arod F, Dubler E. *J. Inorg. Biochem.* 2002; **89**: 227.
410. Djordjevic C, Vuletic N, Jacobs BA, Lee-Renslo M, Sinn E. *Inorg. Chem.* 1997; **36**: 1798.
411. Kieninger M, Ventura ON, Suhai S. *Int. J. Quantum Chem.* 1998; **70**: 253.
412. Evans CJ, Clouthier DJ. *J. Chem. Phys.* 2002; **117**: 6439.
413. Rao PM, Rao GR. *J. Raman Spectrosc.* 1989; **20**: 609.
414. Friedrich HB, Onani MO, Munro OQ. *J. Organomet. Comp.* 2001; **633**: 39.
415. Lee M, Kim H, Lee YS, Kim MS. *J. Chem. Phys.* 2005; **122**: 244319.
416. Zheng X, Phillips DL. *Chem. Phys. Lett.* 1998; **296**: 173.
417. Ogata T, Kamitsuma M. *J. Mol. Struct.* 1995; **352-353**: 345.
418. Macías M, Gamboa A, Ulloa M, Toscano RA, Mata R. *Phytochem.* 2001; **58**: 751.
419. Skrdla PJ, Saavedra SS, Armstrong NR, Mendes SB, Peyghambarian N. *Anal. Chem.* 1999; **71**: 1332.
420. Hebbink GA, Grave L, Woldering LA, Reinhoudt DN, van Veggel FCJM. *J. Phys. Chem. A* 2003; **107**: 2483.
421. Yeow EKL, Slep LD, Chibisov AK, Braslavsky SE. *J. Phys. Chem.* 2003; **107**: 439.
422. Bailey RT, Cruickshank FR, Deans G, Gillanders RN, Tedford MC. *Anal. Chim. Acta* 2003; **487**: 101.
423. Peica N, Pavel I, Schlücker S. *Asian J. Phys.* 2006; submitted.
424. Majoube M, Henry M. *Spectrochim. Acta A* 1991; **47**: 1459.
425. Zhang H, Zhang M, Shen T. *Dyes and Pigments* 1999; **43**: 15.
426. Moskovits M. *Rev. Modern Phys.* 1985; **57**: 783.
427. Otto A, Mrozek I, Grabhorn H, Akemann W. *J. Phys. Condensed Matter* 1992; **4**: 1143.
428. Hildebrandt P, Stockburger H. *J. Phys. Chem.* 1984; **88**: 5985.
429. Endo T, Nakada N, Sato T, Shimada M. *J. Phys. Chem. Solids* 1988; **49**: 1423.
430. Wetzel H, Gerischer H, Pettinger B. *Chem. Phys. Lett.* 1981; **78**: 392.
431. Macomber SH, Furtak TE. *Solid State Commun.* 1983; **45**: 267.
432. Adams SK, Edwards DA, Richards R. *Inorg. Chim. Acta* 1975; **12**: 163.
433. Loffreda D, Dal Corso A, Baroni S, Savio L, Vattuone L, Rocca M. *Surface Sci.* 2003; **530**: 26.
434. Scherer JR, *Planar Vibrations of Chlorinated Benzenes*, Dow Chemical Co., Midland, Michigan, 1963.
435. Scherer JR. *Spectrochim. Acta A* 1968; **24**: 747.
436. Campbell M, Lecomte S, Smith WE. *J. Raman Spectrosc.* 1999; **30**: 37.
437. Chowdhury J, Pal P, Ghosh M, Misra TN. *J. Col. Int. Sci.* 2001; **235**: 317.
438. Regis A, Dumas P, Corset J. *Chem. Phys. Lett.* 1984; **107**: 502.
439. Vosgröne T, Meixner AJ. *J. Luminesc.* 2004; **107**: 13.
440. Vosgröne T, Meixner AJ. *Chem. Phys. Chem.* 2005; **6**: 154.
441. Gautier A, *Liebigs Ann. Chem.* 1867; **142**: 289.
442. Grandmougin E, Dessoulavy E. *Chem. Ber.* 1909; **42**: 358.
443. Mahadevan MM, Weitzman GA, Horgan S, Breckinridge S, Miller MM. *Reprod. Toxicol.* 1997; 7: 631-633.
444. Imoto S, Hasebe T. *J.J.C.O.* 1999; **29**: 11-15.
445. Korogi Y, Hirai T, Nishimura R, Hamatake S, Sakamoto Y, Murakami R, Baba Y, Arakawa A, Takahashi M, Uji Y. *A.J.R.* 1995; **165**: 1269-1272.
446. Yeung AT. *The Practice of Minimally Invasive Spinal Technique-AAMISMS*, **LLC-1ˢᵗ Ed.** 2000; 231-236.
447. Miller RW, Eady RR, Gormal C, Fairhurst SA, Smith BE. *Biochem. J.* 1998; **334**: 601-607.
448. Webb RK, Ralstan AC, Runciman WB. *Anaesthesia* 1991; **46**: 207-212.
449. Ralston AC, Webb RK, Runciman WB, *Anaesthesia* 1991; **46**: 291-295.
450. Arend A, Kolts I, *Ann. Anat.* 2002; **184**: 149.
451. Lee JH, Kim JW, Cho YK, Sohn CI, Jeon WK, Kim BI, Cho EY. *Am. J. Gastroent.* 2003; **98**: 1284-1288.
452. Basavaiah K, Swamy JM. *Anal. Sci.* 2001; **17**: 963-967.
453. Bader H, Hoigne J. *Water Res.* 1981; **15**: 449.
454. Grosjean D, Hisham MWM. *J. Air Waste Manage. Assoc.* 1992; **42**: 169.
455. Daul K, Niketic S, Rauzy C, Schläpfer CW. *Chem. Eur. J.* 2004; **10**: 721-727 ().
456. Mercero JM, Fowler JE, Ugalde JM. *J. Phys. Chem. A* 2000; **104**: 7053.
457. Day PN, Pachter R. *J. Chem. Phys.* 1997; **107**: 2990.
458. Luna A, Amekraz B, Tortajada J, Morizur JP, Alcamí M, Mó O, Yáñez M. *J. Am. Chem. Soc.* 1998; **120**: 5411.
459. Perrin CL. *Acc. Chem. Res.* 1989; **22**: 268.
460. Tortajada J, LeonE, Luna A, Mó O, Yáñez M. *J. Phys. Chem.* 1994; **98**: 12919.
461. Antonczak S, Ruiz-López MF, Rivail JL. *J. Am. Chem. Soc.* 1994; **116**: 3912.
462. Weiqun Z, Wen Y, Liqun X, Xianchen C. *J. Inorg. Chem.* 2005; **99**: 1314.

463. Peica N, Pavel I, Cîntă Pînzaru S, Rastogi VK, Kiefer W. *J. Raman Spectrosc.* 2005; **36**: 657.

464. Cartmell E, Fowels GWA. *Valency and Molecular Structure*, 4th Ed., Butterworths, London, 1977.

465. von Eller H. *Bull. Soc. Chim. Fr.* 1995; 1426, 1429, 1433, 1438, 1444.

466. Chen PC. *Int. J. Quantum Chem.* 1996; **60**: 681.

467. Szafran M, Dega-Szafran Z, Thaimattam R, Jaskólski M. *J. Mol. Struct.* 2004; **706**: 49.

468. Calligaris M, Melchior A, Geremia S, *Inorg. Chim. Acta* 2001; **323**: 89.

469. Rudner MS, Jeremic S, Petterson KA, Kent DR, Brown KA, Drake MD, Goddard WA, Roberts JD. *J. Phys. Chem. A* 2005; **109**: 9076.

470. Nagasawa Y, Taguri R, Matsuda H, Murakami M, Ohama M, Okada T, Miyasaka H, *Phys. Chem. Chem. Phys.* 2004; **6**: 5370.

471. Klipfel MW, Zamora MA, Rodriguez AM, Fidanza NG, Enriz RD, Csizmadia IG. *J. Phys. Chem. A* 2003; **107:** 5079.

472. El Firdoussi A, Esseffar M, Bouab W, Abboud JLM, Mó O, Yáñez M, Ruasse MF. *J. Phys. Chem. A* 2005; **109**: 9141.

473. Hammond RB, Roberts KJ, Docherty R, Edmondson M. *J. Phys. Chem. B* 1997; **101**: 6532.

474. Rodriguez JA, Pérez M, Jirsak T, Gonzáles L, Maiti A. *Surf. Sci.* 2001; **477**: L279.

475. Cao S, Tang JC, Zhu P, Wang L, Shen SL. *Phys. Rev. B* 2002; **66**: 045403.

476. Muchall HM. *ARKIVOC* 2001; **xii**: 82.

477. Lo WJ, Wu YJ, Lee YP. *J. Chem. Phys.* 2002; **117**: 6655.

478. Borrajo AMP, Gal JF, Maria PC, Decouzon M, Ripley DC, Buncel E, Thatcher GRJ. *J. Org. Chem.* 1997; **62**: 9203.

479. Brigatti MF, Galli E, Medici L. *Mineral. Mag.* 1997; **61**: 447.

480. Shadi IT, Chowdhry BZ, Snowden MJ, Witnall R. *Spectrochim. Acta A* 2003; **59**: 2201.

481. Shadi IT, Chowdhry BZ, Snowden MJ, Withnall R. *Chem. Comm.* 2004; **12**: 1436.

482. Nishimura S, Sasaki J, Kandori H, Matsuda T, Fukada Y, Maeda A. *Biochemistry* 1996; **35**: 13267.

483. Fitjer L, Gerke R, Lüttke W, Müller P, Usón I. *Tetrahedron* 1999; **55**: 14421.

484. Girotto EM, Gazotti WA, Tormena CF, De Paoli MA. *Electrochim. Acta* 2002; **47**: 1351.

485. Min ES, Nam SI, Lee MS, *Bull. Chem. Soc. Jpn.* 2002; **75**: 677.

486. Witke K, Brzezinka KW, Lamprecht I. *J. Mol. Struct.* 2003; **661-662**: 235.

487. Vandenabeele P, Bodé S, Alonso A, Moens L. *Spectrochim. Acta A* 2005; **61**: 2349.

488. Rode JE, Raczyńska ED, Górnicka E, Cz. Dobrowolski J, *J. Mol. Struct.* 2005; **749**: 51.

489. Górnicka E, Rode JE, Raczyńska ED, Dasiewicz B, Dobrowolski JC. *Vib. Spectrosc.* 2004; **36**: 105.

490. Meersman F, Wang J, Wu Y, Heremans K. *Macromolecules* 2005; **38**: 8923.

491. Sanchez LA, Birke RL, Lombardi JR. *J. Phys. Chem.* 1984; **88**: 1762.

492. Du Y, Fang Y. *Spectrochim. Acta A* 2004; **60**: 535.

493. Peica N, Cîntă Pînzaru S, Frosch T, Schmitt M, Popp J, Bringmann G, Kiefer W. Proc. "3rd International Conference on Materials for Advanced Technologies" (ICMAT), "9rd International Conference on Advanced Materials" (IUMRS–ICAM), *Singapore*, Singapore, Book of abstracts, 2005; July, 3-8.

494. Shoeib T, Siu KWM, Hopkinson AC. *J. Phys. Chem. A* 2002; **106**: 6121.

495. Morzyc-Ociepa B, Michalska D. *Spectrochim. Acta A* 2003; **59**: 1247.

496. Morzyc-Ociepa B, Michalska D. *Spectrochim. Acta A* 1999; **55**: 2671.

497. Weiss B. *Food Additive Safety and Evaluation*, Plenum Publishing Corporation, 1984; 221-250.

498. Collins-Williams C. *Ann. Allergy* 1983; **51**: 315-316.

499. Allen DH, Baker GJ. *New Engl. J. Med.* 1981; **305**: 1154-1155.

500. Reif-Lehrer L. *Federation Proc.* 1976; **35**: 2205-2211.

501. Claxton LD, Barry PZ. *Am J Public Health* 1977 **67**: 1037-1042.

502. Miller M. *Danger! Additives at Work*, London Food Commission, London, 1985.

503. Larsen PJ, Fledelius C, Knudsen LB, Tang-Christensen M. *Diabetes* 2001; **50**: 2530-2539.

504. Hirata AE, Alvarez-Rojas F, Carvalheira JBC, de Oliveira Carvalho CR, Dolnikoff MS, Saad MJA. *Life Sci.* 2003; 73: 1369-1381.

505. Hwang JJ, Jaeger K, Hancock J, Stupp SI. *J. Biomed. Mater. Res.* 1999; **47**: 504-515.

506. Wilkinson M, Wilkinson D, Wiesner G, Morash B, Ur E. *Neuroendocrinology* 2005; **81**: 19-30.

507. Chambille I. *J. Comp. Neurol.* 1998; **392**: 458-467.

508. Chambille I. *Brain Res.* 1998; **808**: 250-261.

509. Lin JY, Pan JT. *Brain Res. Bull.* 1999; **48**: 103-108.

510. Légrádi G, Lechan RM. *Endocrinology* 1998; **139**: 3262-3270.

511. Grön H, Borissova A, Roberts KJ. *Ind. Eng. Chem. Res.* 2003; **42**: 198-206.

512. Grön H, Mougin P, Thomas A, White G, Wilkinson D. *Ind. Eng. Chem. Res.* 2003; **42**: 4888-4898.

513. Hammond RB, Lai X, Roberts KJ. *Cryst. Growth Des.* 2004; **4**: 943-948.

514. Kusumoto I. *J. Nutr.* 2001; **131**: 2552-2555.

515. Thalladi VR, Nüsse M, Boese R. *J. Am. Chem. Soc.* 2000; **122**: 9227-9236.

516. Gopalan SS, Kumaradhas P, Kulkarni GU, Rao CNR. *J. Mol. Struct.* 2000; **521**: 97.

517. Dupré La Tour F, De Broglie MM. *C. R. Acad. Sci. Paris* 1935; **201**: 479.

518. Tortajada J, Leon E, Morizur JP, Luna A, Mó O, Yáňez M. *J. Phys. Chem.* 1995; **99**: 13890.

519. Igarashi M, Ishibashi T, Nishihira J, Tachikawa H. *Internet Electron. J. Mol. Des.* 2003; **2**: 712.

520. Bottoni A, Lanza CZ, Miscione GP, Spinelli D. *J. Am. Chem. Soc.* 2004; **126**: 1542-1550.

521. Sun W, Kinsel GR, Marynick DS. *J. Phys. Chem. A* 1999; **103**: 4113-4117.

522. Walling AE, Pargas RE, De Dios AC. *J. Phys. Chem. A* 1997; **101**: 7299.

523. IUPAC-IUB Commission on Biochemical Nomenclature, *Biochemistry* 1970; **9**: 3471.

524. Tarditi AM, Klipfel MW, Rodriguez AM, Suvire FD, Chasse GA, Farkas O, Perczel A, Enriz RD. *J. Mol. Struct. (Theochem)* 2001; **545**: 29-47.

525. Gomes JRB, Ribeiro da Silva MDM, Ribeiro da Silva MAV. *J. Phys. Chem. A* 2004; **108**: 2119-2130.

526. Laleveé J, Allonas X, Fouassier JP. *J. Am. Chem. Soc.* 2002; **124**: 9613-9621.

527. Walter W, Fleck T, Voss J, Gerwin M. *Justus Liebigs Ann. Chem.* 1975; **2**: 275.

528. Walter W, Staeglich P. *Spectrochim. Acta A* 1982; **38**: 815.

529. Matsumoto H, Li YJ, Wang YF, Chen TM, Kitamura M Nakaya, T. *Macromolecules* 1996; **29**: 2372-2377.

530. Ponomarenko EA, Waddon AJ, Bakeev KN, Tirrell DA, MacKnight WJ. *Macromolecules* 1996; **29**: 4340.

531. Kabisch G, Klose M. *J. Raman Spectrosc.* 1978; **7**: 311.

532. Silvi B, Perchard JP. *Spectrochim. Acta A* 1976; **32**: 23.

533. van der Ohe W. *J. Chem. Phys.* 1975; **62**: 3933.

534. López Navarrete JT, Hernández V, Ramírez FJ. *J. Raman Spectrosc.* 1994; **25**: 861-867.

535. Rosen RB, Kruger EF, Katz A, Alfano RR. *US Patent Appl. Publ.* Jul. 18, 2002; US2002/0095257 A1.

536. Shurvell HF, Bergin FJ. *J. Raman Spectrosc.* 1989; **20**: 163-168.

537. Edsall JT. *J. Chem. Phys.* 1937; **5**: 508-517.

538. Stacchiola D, Burkholder L, Zheng T, Weinert M, Tysoe WT. *J. Phys. Chem. B* 2005; **109**: 851-856.

539. Clementi E. *J. Chem. Phys.* 1981; **74**: 578-588.

540. Dudev T, Lin YL, Dudev M, Lim C. *J. Am. Chem. Soc.* 2003; **125**: 3168-3180.

541. Mercero JM, Fowler JE, Ugalde JM, *J. Phys. Chem. A* 1998; **102**: 7006-7012.

542. Ferguson RK, Boutros AR. *JAMA : The journal of the American Medical Association* 1970; **213**: 1186-1187.

543. Kaufman FL, Dubanksy AS. *Pediatrics* 1972; **49**: 610-611.

544. Levy G. *Pediatrics* 1978; **62**: 867-872.

545. Boczar M, Wójcik MJ, Szczeponek K, Jamróz D, Zięba A, Kawałek B. *Chem. Phys.* 2003; **286**: 63-79.

546. Binev IG, Stamboliyska BA, Binev YI. *J. Molec. Str.* 1996; **378**: 189-197.

547. Neault JF, Tajmir-Riahi HA. *J. Phys. Chem.* 1997; **101**: 114-116.

548. Neault JF, Naoui M, Manfait M, Tajmir-Riahi HA. *FEBS Letters* 1996: **382**: 26-30.

549. Payne RS, Rowe RC, Roberts RJ, Charlton MH, Docherty R. *J. Comput. Chem.* 1999; **20**: 262-273.

550. Wang C, Vickers TJ, Mann CK. *J. Pharm. Biomed. Anal.* 1997; **16**: 87-94.

551. Y. Wang, Y. S. Li, Z. Zhang, D. An, *Spectr. Acta A*, **59**, 589-594 **(2003)**.

552. Peica N, Andronie LM, Cîntă Pînzaru S, Kiefer W. *Studia Universitatis, Seria Physica* 2004; **XLIX**: 57.

553. Bacon TH, Hole JG, North M, Burnett I. *J. Clin. Pharm.* 2002; **53**: 629-636.

554. Sandrini M, Romualdi P, Capobianco A, Vitale G, Morelli G, Pini LA, Candeletti S. *Neuropeptides* 2001; **35**: 110.

555. Mitchell JR, Jollow DJ, Potter WZ, Davis DC, Gilette JR, Brodie BB. *J. Pharm. Exp. Ther.* 1973 **187**: 185.

556. Morgan S, Dorman S. *Letters* 2004; **27**: 99-101.

557. Florén CH, Thesleff P, Nilsson A. *Med. Scand.* 1987; **222**: 185-288.

558. Hinson JA. Biochemical toxicology of acetaminophen. In *Reviews in Biochemical Toxicology* Hodgson E, Bend JR, Philpot RM Eds., Elsevier, Amsterdam, 1980; **2**: 103-129.

559. M. W. Gemborys, G. W. Gribble, G. H. Mudge, *J. Med. Chem.*, **21** (1978) 649-652.

560. Sandler DP, Smith JC, Weinberg CR, Buckalew YM, Dennis VW, Blythe WB, Burgess WP. *N. Engl. J. Med.* 1989; **320**: 1238.

561. Richard AM, Hongslo JK, Boone PF, Holme JA. *Chem. Res. Toxicol.* 1991; **4**: 151-156.

562. Di Martino P, Conflant P, Drache M, Huvenne JP, Guyot-Hermann AM. *J. Therm. Anal.* 1997; **48**: 447-458.

563. Beyer T, Day GM, Price SL. *J. Am. Chem. Soc.* 2001; **123**: 5086-5094.

564. Rossi A, Savioli A, Bini M, Capsoni D, Massarotti V, Bettini R, Gazzaniga A, Sangalli ME, Giordano F. *Therm. Acta* 2003; **406**: 55-67.

565. Peterson ML, Morissette SL, McNulty C, Goldsweig A, Shaw P, LeQuesne M, Monagle J, Encina N, Marchionna J, Johnson A, Gonzalez-Zugasti J, Lemmo AV, Ellis SJ, Clima MJ, Almarsson JÖ. *J. Am. Chem. Soc.* 2002; **124**: 10958-10959.

566. Szelagiewicz M, Marcolli C, Cianferani S, Hard AP, Vit A, Burkhard A, Von Raumer M, Hofmeier UC, Zilian A, Francotte E, Schenker R. *J. Therm. Anal. Cal.* 1999; **57**: 23-43.

567. Kalantzi L, Reppas C, Dressman JB, Amidon GL, Junginger HE, Midha KK, Shah VP, Stavchansky SA, Barends DM, *J. Pharm. Sci.* 2006; **95**: 4-14.

568. Fabbiani FPA, Allan DR, David WIF, Moggach SS, Parsons S, Pulham CR, *Cryst. Eng. Comm.* 2004; **6**: 504.

569. Nichols G, Frampton CS. *J. Pharm. Sci.* 1998; **87**: 684-693.

570. Verwer P, Leusen FJJ. *Revs. Comp. Chem.* 1998; **12**: 327-365.

571. Espeau P, Céolin R, Tamarit JL, Perrin MA, Gauchi JP, Leveiller F. *J. Pharm. Sci.* 2005; **94**: 524-539.

572. Florence AJ, Shankland N, Shankland K, David WIF, Pidcock E, Xu X, Johnston A, Kennedy AR, Cox PJ, Evans JSO, Steele G, Cosgrove SD, Frampton CS. *J. Appl. Cryst.* 2005; **38**: 249-259.

573. Giordano F, Rossi A, Bettini R, Savioli A, Gazzaniga A, Novák C. *J. Therm. Anal. Cal.* 2002; **68**: 575-590.

574. Garekani HA, Ford JL, Rubinstein MH, Rajabi-Siahboomi AR. *Int. J. Pharm.* 2000; **208**: 87-99.

575. Prasad KVR, Ristic RI, Sheen DB, Sherwood JN. *Int. J. Pharm.* 2002; **238**: 29-41.

576. Mikhailenko MA. *J. Cryst. Growth* 2004; **265**: 616-618.

577. McGregor PA, Allan DR, Parsons S, Pulham CR. *J. Pharm. Sci.* 2002; **91**: 1308-1311.

578. Di Martino P, Guyot-Hermann AM, Conflant P, Drache M, Guyot JC. *Int. J. Pharm.* 1996; **128**: 1-8.

579. Binev IG, Vassileva-Boyadjieva P, Binev YI. *J. Mol. Struct.* 1998; **447**: 235-246.

580. Ramos ML, Tyson JF, Curran DL. *Anal. Chim. Acta* 1998; **364**: 107-116.

581. Merckle P, Kovar KA. *J. Pharm. Biomed. Anal.* 1998; **17**: 365-374.

582. Eustaquio A, Blanco M, Jee RD, Moffat AC. *Anal. Chim. Acta* 1999; **383**: 283-290.

583. Lin SY, Wang SL, Cheng YD. *J. Phys. Chem. Solids* 2001; **61**: 1889-1893.

584. Mohamed GG, El-Gamel NEA, Teixidor F. *Polyhedron* 2001; **20**: 2689-2696.

585. Terzyk AP. *Colloids and Surfaces A* 2001; **177**: 23-45.

586. Wang SL, Lin SY, Wei YS. *Chem. Pharm. Bull.* 2002; **50**: 153-156.

587. Fujiwara M, Chow PS, Ma DL, Braatz RD. *Cryst. Growth&Design* 2002; **2**: 363-370.

588. Sala S, Tassaing T, Ventosa N, Danten Y, Besnard M, Veciana J. *Chem. Phys. Chem.* 2004; **5**: 243-245.

589. Burgina EB, Baltakhinov VP, Boldyreva EV, Shakhtschneider TP. *Int. J. Struct. Chem.* 2004; **45**: 64-73.

590. Romero S, Bustamante P, Escalera B, Cirri M, Mura P. *J. Therm. Anal. Cal.* 2004; **77**: 541-554.

591. Dou. Y, Sun Y, Ren Y, Ren Y. *Anal. Chim. Acta* 2005; **528**: 55-61.

592. Ivanova BB. *J. Mol. Struct.* 2005; **738**: 233-238.

593. Dou Y, Sun Y, Ren Y, Ju P, Ren Y. *J. Pharm. Biomed. Anal.* 2005; **37**: 543-549.

594. Blanco M, Alcalá M. *Eur. J. Pharm. Sci.* 2006; **27**: 280-286.

595. Yu ZQ, Chow PS, Tan RBH. *Ind. Eng. Chem. Res.* 2006; **45**: 438-444.

596. Moynihan HA, O'Hare IP. *Int. J. Pharm.* 2002; **247**: 179-185.

597. Szostak R, Mazurek S. *Analyst* 2002; **127**: 144-148.

598. Al-Zoubi N, Koundourellis JE, Malamataris S. *J. Pharm. Biomed. Anal.* 2002; **29**: 459-467.

599. Wang Y, Li YS, Zhang Z, An D. *Spectrochim. Acta A* 2003; **59**: 589-594.

600. Day JS, Edwards HGM, Dobrowski SA, Voice AM. *Spectrochim. Acta A* 2004; **60**: 563-568.

601. Day JS, Edwards HGM, Dobrowski SA, Voice AM. *Spectrochim. Acta A* 2004; **60**: 1725-1730.

602. Thorley FC, Baldwin KJ, Lee DC, Batchelder DN. *J. Raman Spectrosc.* 2006; **37**: 335-341.

603. Terzyk AP, Rychlicki G, Biniak S, Łukaszewicz JP. *J. Colloid Interface Sci.* 2003; **257**: 13-30.

604. Szép A, Marosi G, Bálint M, Bódis A. *Proc. 8th Polymers for Advanced Technologies Int. Symp.* Budapest, Hungary, 13-16 September, 2005.

605. Szép A, Fekete P, Virgula J, Budavári Z, Marosi G. *Proc. 8th Polymers for Advanced Technologies Int. Symp.* Budapest, Hungary, 13-16 September; 2005.

606. Clarke F, Whitley A, Mamedov S, Adar F, Lewis N, Lee E. *Spectroscopy-Solutions for Materials Analysis*, an Advanstar Publ., Printed in U.S.A., June 2005.

607. Murphy BM, Prescott SW, Larson I. *J. Pharm. Biomed. Anal.* 2005; **38**: 186-190.

608. Vogel H, Wright JK, Jähnig F. *The EMBO Journal* 1985; **4**: 3625-3631.

609. Fechner PM, Wartewig S, Füting M, Heilmann A, Neubert RHH, Kleinebudde P. *AAPS Pharm. Sci.* 2003; **5**: 1.

610. Eichhorn SJ, Young RJ. *Cellulose* 2001; **8**: 197-207.

611. Agarwal UP. *Appita* 2005; **2005**: 377-384.

612. Bisby RH, Johnson SA, Tavender SM, Parker AW. *Science-Lasers Sci. Fac. Prog.* CLF Ann. Rep. 1996/1997.

613. Wang A, Freeman J, Kuebler KE. *Lunar and Planetary Science* 2002; **XXXIII**: 1374.

614. Terzyk AP. *J. Colloid Interface Sci.* 2004; **272**: 59-75.

615. Diniz JEM, Borges RS, Alves CN. *Theochem* 2004; **673**: 93-97.

616. Gracin S, Brinck T, Rasmuson ÅC. *Ind. Eng. Chem. Res.* 2002; **41**: 5114-5124.

617. Stevenson MM, Riley EM. *Nature Rev. Immunol.* 2004; **4**: 169.

618. Reinaldo TD, Osvaldo AS-F, José F-VD. *J. Braz. Chem. Soc.* 2002; **13**: 727.

619. Robert A, Benoit-Vical F, Dechy-Cabaret O, Meunier B. *Pure Appl. Chem.* 2001; **73**: 1173.

620. Ziegler J, Linck R, Wright DW. *Cur. Med. Chem.* 2001; **8**: 171.

621. Monti D, Vodopivec B, Basilico N, Olliaro P, Taramelli D. *Biochem.* 1999; **38**: 8858.

622. Pagola S., Stephens PW, Bohle DS, Kosar AD, Madsen SK. *Nature* 2000; **404**: 307.

623. Ridley RG. *Nature* 2002; **415:** 686.

624. Olliaro P. *Pharmacol. Ther.* 2001; **89**: 207.

625. Foley M, Tilley L. *Pharmacol. Ther.* 1988; **79**: 55.

626. Vippagunta SR, Dorn A, Ridley RG, Vennerstrom JL. *Biochim. Biophys. Acta* 2000; **1475:** 133.

627. Parapini S, Basilico N, Pasini E, Egan TJ, Olliaro P, Taramelli D, Monti D. *Exp. l Parasitology* 2000; **96:** 249.

628. Adams PA, Berman PAM, Egan TJ, Marsh PJ, Silver J. *J. Inorganic Biochem.* 1996; **63**: 69.

629. Nguyen-Cong V, Rode BM. *J. Chem. Inf. Comput. Sci.* 1996**; 36**: 114.

630. Bolboacă M, Kiefer W, Popp J. *J. Raman Spectrosc.* 2002; **33**: 207.

631. Puviarasan N, Arjunan V, Mohan S. *Turk J. Chem*. 2004; **28**: 53.

632. Krishnakumar V, Ramasami R. *Spectrochim. Acta A* 2005; **61**: 673.

633. Cîntă Pînzaru S, Leopold N, Pavel I, Kiefer W. *Spectrochim. Acta A* 2004; **60**: 2021.

634. Frosch T, Küstner B, Schlücker S, Szeghalmi A, Schmitt M, Kiefer W, Popp J. *J. Raman Spectrosc*. 2004; **35**: 819.

635. Bayden Wood R, Langford SJ, Cooke BM, Lim J, Glenister FK, Duriska M, Unthank JK, McNaughton D. *J. Am. Chem. Soc*. 2004; **126**: 9233.

636. Bayden Wood R, Langford S, Cooke B, Glenister F, Lim J, McNaughton D. *Febs Lett*. 2003; **554**: 247.

637. Kneipp K, Kneipp H, Bhaskaran Kartha V, Manoharan R, Deinum G, Itzkan I, Dasari RR, Feld MS. *Phys. Rev. E* 1998; **57**: 6281.

638. Cotton TM, Kim JH, Chumanov GD. *J. Raman Spectrosc*. 1991; **22**: 729.

639. Kneipp K, Kneipp H, Itzkan I, Dasari RR, Feld MS. *Current Science* 1999; **77**: 915.

640. Sutherland WS, Winefordner JD. *J. Colloid Interface Sci*. 1984; **99**: 270.

641. Champion A, Kambhampati P. *Chem. Soc. Rev*. 1988; **27**: 241.

642. Socrates G, *Infrared and Raman Characteristic Group Frequencies. Tables and Charts*, 3rd Eds., Wiley, 2001; 173.

643. Moskovits M, DiLella DP. *J. Chem. Phys*. 1980; **73**: 6068.

644. Moskovits M, Suh JS. *J. Phys. Chem*. 1988; **92**: 6327.

645. Crisanti MA, Spiro TG, English DR, Hendrickson DN, Suslik KS. *Inorg. Chem*. 1984; **23**: 3897.

646. Smulevich G, Spiro TG. *J. Phys. Chem*. 1985; **89**: 5168.

647. Choi S, Spiro TG, Langry KC, Smith KM, Budd DL, La Mar GN, *J. Am. Chem. Soc.*, **104** (1982) 4345.

648. Otto A. *J. Raman Spectrosc*. 2002; **33**: 593.

649. Cîntă Pînzaru S, Peica N, Küstner B, Schlücker S, Schmitt M, Frosch T, Faber JH, Bringmann G, Popp J. *J. Raman Spectrosc*. 2006; **37**: 326.

650. Peica N, Kostova I, Kiefer W. *Chem. Phys*. 2006; **325**: 411.

651. Pan L, Huang X, Li J, Wu Y, Zheng N. *Angew. Chem. Int. Ed. Engl*. 2000; **39**: 527.

652. Pan L, Huang XY, Li J. *J. Solid State. Chem*. 2000; **152**: 236.

653. Kostova I, Kostova R, Momekov G, Trendafilova N, Karaivanova M. *J. Tr. Elem. Med. Biol*. 2005; **18**: 219.

654. Billes F, Endrédi H, Jalsovszky G. *Theochem* 1999; **465**: 157.

655. Fukushima K, Iwahashi H. *Bull. Chem. Soc. Jpn*. 2004; **77**: 1671.

656. Jursic BS, Zdravkovski Z. *Theochem* 1995; **331**: 229.

657. Pan L, Ching N, Huang X, Li J. *Chem. Eur. J*. 2001; **7**: 4431.

658. Sakagami N, Nakahanada M, Ino K, Hioki A, Kaizaki S. *Inorg. Chem*. 1996; **35**: 683.

659. Mehring M, Mansfeld D, Schürmann M. *Z. Anorg. Allg. Chem*. 2004; **630**: 452.

660. Giesbrecht GR, Whitener GD, Arnold J. *J. Chem. Soc. (Dalton Trans.)* 2001; **2001**: 923.

661. Hadzi D, Sheppard N. *Proc. Roy. Soc. Ser. A* 1953; **216**: 247.

662. Kostova I, Peica N, Kiefer W. *J. Raman Spectrosc*. 2006; *accepted*.

663. Kostova I, Peica N, Kiefer W. *Polyhedron* 2006; *submitted*.

664. Kostova I, Peica N, Kiefer W. *J. Phys. Chem. A* 2006; *submitted*.

665. Baran EJ, Mercader RC, Hueso-Ureña F, Moreno-Carretero MN, Quiros-Olozabal M, Salas-Peregrin JM, *Polyhedron* 1996; **15**: 1717.

666. Hernanz A, Billes F, Bratu I, Navarro R. *Biopolymers (Biospectroscopy)* 2000; **57**: 187.

667. Takusawaga F, Shimada A. *Bull. Chem. Soc. Jpn*. 1973; **46**: 2011.

668 Hilal. R, Zaky ZM, Elroby SAK. *J. Mol. Struct. (Theochem)* 2004 **685**: 35.

669. Wysokiński R, Morzyk-Ociepa B, Głowiak T, Michalska D. *J. Mol. Struct. (Theochem)* 2002; **606**: 241.

670. Li X, Shi Q, Sun D, Bi W, Cao R. *Eur. J. Inorg. Chem*. 2004; **4**: 2747.

671. Sun D, Cao R, Liang Y, Hong M. *Chem. Lett*. 2001; **9**: 878.

672. Kostova I, Peica N, Kiefer W. *Chem. Phys*. 2006; **327**: 494.

673. Perlepes SP, Lazaridou V, Sankhla B, Tsangaris JM. *Bull. Soc. Chim. Fr*. 1990; **Sept.-Oct.**: 597.

674. Peica N, Kostova I, Kiefer W. *XXth ICORS* 20-25 August 2006, Yokohama, Japan, Book of abstracts, 152.

Word of Gratitude

A lot that cannot be said is at times best expressed in the words "**Thank you**". Here, I mention some of the countless number of persons who are *instrumental*, in more ways imaginable, for the *fruits* of my study and making my stay in Würzburg a delight.

To the following people I share my deepest gratitude.

Prof. Dr. Dr. hc Wolfgang Kiefer, for his uncompromised support for his students, which I consider a priceless gift in my journey as a PhD researcher, and for that peculiar way of providing me the challenge to strive, which has proven most useful for reaching the finish line with energy left for an extra mile - something I would not exchange for gold, and for those invaluable lessons on how to express thoughts into scientifically legible and explicable presentations. Prof. Dr. Jürgen Popp, PD Dr. Michael Schmitt, and Conf. Dr. Simona Cîntă Pînzaru for their careful mentoring at the crucial moments and for being my link to Raman spectroscopy, especially SERS, which attests to the possible applications of my study. Dr. Ioana Emilia Pavel for her guidance and expressing the joyous collaboration between theory and experiment by coming up with sharp scientific questions and insightful summaries. Dr. Irena Kostova and Prof. Dr. Vinod Kumar Rastogi, also for theirs guidance and keeping the spirits high despite our hectic preparations.

I also do not forget other professors and scientists whose influence and generous collaboration ever remain invaluable. Prof. Dr. Volker Engel, Prof. Dr. Ingo Fischer, Prof. Dr. Birendra P. Asthana, Dr. Sebastian Schlücker, Dr. Torsten Siebert, and Prof. Dr. Otto Dopfer for their enthusiasm and welcoming collaboration.

I do not forget Mrs. Ursula Müller, which was a constant source of support during my PhD, for the sagacious discussions, for all her efforts in organizational aspects especially at the beginning of my PhD study in Germany and for her *Käsekuchen* I had a taste. Her uninterrupted presence and her well-intentioned advice saved me many times from difficulties provided by lack of German language knowledge. Dr. R. Colditz for introducing me into the practical training together with Joachim and Ralph. Mrs. Gudrun Mühlrath, Mrs. Sabine Fuchs, and Mrs. Andrée Meyer for their assistance.

I would like to tank all my colleagues for the delightful ambiance at work. Dr. Krisztina Babocsi, Bernd Küstner, Dr. Nicolae Tarcea, Dr. Adriana Szeghalmi, and Dr. Benjamin Dietzek for theirs inspired presence, intuitive discussions during anyone's presentations, the cheering in the *Mensa*, sometimes *Kneipen* or movie theaters. Dr. Joachim Koster, Bernd Küstner, Dr. Benjamin Dietzek, and Dr. Ralph Geßner for the *German classes*, especially during the coffee and cigarette breaks. To Dr. Raman Maksimenka for reminding me that science is *cool* and that "nicotine is vitamine". Nele Welter for the possibility to switch always the *Messzeit*, without writing emails. Katrin , Anne, Jessy, Tim, Karina, Max for the laughters in the *Mensa*, *Cafeteria*, and coffee breaks. Bernd Küstner, Dr. Raman Maksimenka also for their help during my move-in into the Wittelsbacherstraße apartment and for the beers on the lawn in front of the House sitting on the sofa. Cristina Dem and Dr. Claudiu Dem for offering me accommodation during some Workshops in Jena and for the long-night entertainment together with Dr. Monica Baia, Dr. Lucian Baia, Dr. Nicolae Leopold, Dr. Nicolae Tarcea, and the help of high spirits and beers. Dr. Krisztina Babocsi, which was the best support for my adaptation to the German outlook and food. Horia Sorin Andrei for the connection to the computer's problems and his expertise was the key to the DFT calculations and helpful for the upcoming research regarding my PhD thesis. I had a lot of fun during the discussions and play-upon-words on various topics with Harald Bresch. For the nice moments spent in *Praktikum*, I would like to thank Dr. Nicola Solca, Dr. Stefanie Gräfe, Sofia Dembski, Mathias Barthel, Réne Lewinski, Philipp Marquetand, Stefan Dümmler.

I do not forget the permanent employees, whose acquaintance and backing up I could have never done without. Peter Popp for reconstructing the meaning of "*Halbzeit*" and for the computer's software. Belinda Böhm for the technical assistance and unconditional help in the laboratory. Flo for the short breaks in front of the Institute. Stefanie Schauberth for technical assistance and funny moments she provided with her way of always being in a good mood. Jürgen Zimmermann and Rainer Eck in the electronic workshop and Wolfgang Libler, Gerhard Bömmel, Thomas Schreckling, Ralf Kohrmann, Peter Lang in the mechanic workshop for providing me with high quality electronic and technical devices and because they were always *high spirits bringers*. Melanie Grom, who unconsciously reminded the old lessons, that a smile brings wonders. May she rest in peace.

Moving towards where the sun rises, I express my gratitude to the people's from the research group of Prof. Dr. Jürgen Popp, whom I met frequently in Jena, Würzburg, München, and also in Yokohama.

I would like to mention also the people I met during my studies in Würzburg, Ana, Bea, Smaranda, Minaewer, Armin, Roland, Maria, Rareş, Răzvan, Manfred, Dora, Ramona, Adela, Dani, Iulia,

Bruno whose presence will be ever agreeable. Erasmus students Oana Ponta, Carmen Mărcus, Cosmin Farcău, Sergiu Baidoc, Valerian Ciobotă, Claudia Popa, Cătălin Popa, Eliza Burean, with them I had a lot of fun. Specially thanks to Luisa Andronie for our fruitful collaboration.

Least forgotten is home. My late father who helped and encouraged me all the time. I do not have words to express my gratitude for all that he made. May he rest in peace. My mother, my sister, my brother-in-law, and my both nieces, for their warmth, and moral support. My mother who helped and understood me each time I had troubles. To my sister, Magda for helping my mother and for the interesting and funny discussions, which we had. To my brother-in-law, Florin for understanding and good advices. To my nieces, Mihaela and Alexandra for their kindness.

At last, but not at least, I would like cordially to thank Tibi. Without him and his support in the time of this research, I wouldn't have been able to complete my work. He always supported and encouraged me, giving me trust and force to go on, when the things were going aimlessly. He obviously brought his contribution to improve my knowledge of English language-finesses and making clear the real sense of some sentences. I would like to thank him too for his patience and for invaluable discussions with mostly constructive character.

Lebenslauf

Persönliche Daten

Vorname	Niculina
Name	Peica
Anschrift	Wittelsbacherstraße 2 97074 Würzburg
Geburtsdatum	29.02.1976
Geburtsort	Slatina, Rumänien
Staatsangehörigkeit	rumänisch
Familienstand	ledig

Studium

seit 08.2003	Institution: Bayerische Julius-Maximilians Universität Würzburg Abteilung: Institut für Physikalische Chemie; am Lehrstuhl für Physikalische Chemie II, Arbeitskreis Prof. Dr. Dr. h.c. Kiefer. Anschrift: Am Hubland, 97074 Würzburg, Deutschland Forschungsthema: "Schwingungsspektroskopie und dichtefunktionaltheoretische Berechnungen von biologischen Molekülen"
09.2002-06.2003	Institution: Babeş-Bolyai Universität Abteilung: Fakultät für Physik Anschrift: Kogălniceanu 1, 400084 Cluj-Napoca, Rumänien Fachrichtung: *Biophysik und medizinische Physik* Abschluss: **MSc.**
09.1998-06.2002	Institution: Babeş-Bolyai University Abteilung: Fakultät für Physik Anschrift: Kogălniceanu 1, 400084 Cluj-Napoca, Rumänien Fachrichtung: *medizinische Physik* Abschluss: **Diplom**
09.1996-05.1997	Institution: Fachhochschule für Krankenpflege Anschrift: Mânăstirii 39, 230076 Slatina, Rumänien Fach: Medizin Abschluss: **Pädiatrie (Kinderheilkunde)**
09.1990-06.1994	Institution: **Sanitätsschule (Krankenpflege)** Anschrift: Republicii 19, 240256 Râmnicu Vâlcea, Rumänien Fach: Medizin Abschluss: **Abitur, Krankenpflegerinnen-Abschluss**

Auszeichnungen/Preisverleihung

01.2003-05.2003	Nach sehr gutem Abschluss des Diploms Erhalt des Socrates-Erasmus-Stipendiums an der Universität Würzburg.
09.2001	Workshop mit Zertifikat *„Advanced Methods on Spectroscopic Analysis; Applications"* der Babeş-Bolyai Universität, Cluj-Napoca, Rumänien und Joseph Fourier Universität, Grenoble, Frankreich.
03.1996-11.1996	„Newstart II Formation in Neonatology" - berufliche Fortbildung (auf englisch) in Bukarest, Rumänien.
	Zahlreiche Auszeichnungen bei Schülerwettbewerben in den Fächern: Physik, Chemie, Fremdsprachen.

Berufserfahrungen

seit 10.2003	Wissenschaftliche Mitarbeiterin an der Universität Würzburg.
04.2001-12.2001	Berufstätigkeit: Krankenschwester Institution: Hausarzt Praxis Anschrift: Izlazului 11, 400655 Cluj-Napoca, Rumänien Fach: Allgemeinmedizin
10.1994-09.1998	Berufstätigkeit: Krankenschwester Institution: Landkreis Krankenhaus Slatina Olt Anschrift: Crişan 9-11, 230013 Slatina, Rumänien Fach: Neonatologie

Publications

Characterization of indigo carmine with surface-enhanced resonance Raman spectroscopy (SERRS) using silver colloids and island films, and theoretical calculations

N. Peica[1], W. Kiefer[1]

[1]*Institut für Physikalische Chemie, Universität Würzburg, Am Hubland, D-97074 Würzburg, Germany*

Theoretical and spectroscopic studies of 5-aminoorotic acid and its new lanthanide (III) complexes

I. Kostova[a], N. Peica[b], W. Kiefer[b]

[a]*Department of Chemistry, Faculty of Pharmacy, Medical University, 2 Dunav St., Sofia 1000, Bulgaria*
[b]*Institut für Physikalische Chemie, Universität Würzburg, Am Hubland, D-97074 Würzburg, Germany*

Raman, FT-IR, and DFT studies of 3,5-pyrazoledicarboxylic acid and its Ce(III) and Nd(III) complexes

Irena Kostova[a], Niculina Peica[b], Wolfgang Kiefer[b]

[a]*Department of Chemistry, Faculty of Pharmacy, Medical University, 2 Dunav St., Sofia 1000, Bulgaria*
[b]*Institut für Physikalische Chemie, Universität Würzburg, Am Hubland, D-97074 Würzburg, Germany*

Monosodium glutamate in its anhydrous and monohydrate form: differentiation by Raman spectroscopies and density functional calculations

N. Peica[1], C. Lehene[2], N. Leopold[2], S. Schlücker[1], W. Kiefer[1]

[1]*Institut für Physikalische Chemie, Universität Würzburg, Am Hubland, D-97074 Würzburg, Germany*
[2]*Faculty of Physics, Babeş-Bolyai University, Kogălniceanu 1, 400084 Cluj-Napoca, Romania*

Theoretical and spectroscopic studies of new lanthanum (III) complex of 5-aminoorotic acid

I. Kostova[a], N. Peica[b], W. Kiefer[b]

[a]*Department of Chemistry, Faculty of Pharmacy, Medical University, 2 Dunav St., Sofia 1000, Bulgaria*
[b]*Institut für Physikalische Chemie, Universität Würzburg, Am Hubland, D-97074 Würzburg, Germany*

Theoretical and experimental studies on binding mode of 3,5-pyrazoledicarboxylic acid in its new La(III) complex

Niculina Peica [a], Irena Kostova [b,*], Wolfgang Kiefer [a]

[a]*Institut für Physikalische Chemie, Universität Würzburg, Am Hubland, D-97074 Würzburg, Germany*
[b]*Department of Chemistry, Faculty of Pharmacy, Medical University, 2 Dunav St., Sofia 1000, Bulgaria*

Theoretical and spectroscopic studies of 3,5-pyrazoledicarboxylic acid and its new La(III) complex

Irena Kostova[a], Niculina Peica[b], Lodhi Rajive[c], Vinod K. Rastogi[c]

[a]*Department of Chemistry, Faculty of Pharmacy, Medical University, 2 Dunav St., Sofia 1000, Bulgaria*
[b]*Institut für Physikalische Chemie, Universität Würzburg, Am Hubland, D-97074 Würzburg, Germany*
[c]*Physics Department, CCS University, 250 004 Meerut, India*

"Perspectives in Vibrational Spectroscopy"

S. Cîntă Pînzaru[1], N. Peica[2], B. Küstner[2], S. Schlücker[2], M. Schmitt[3], J. Popp[3]

[1]*Physics Department, Babeş-Bolyai University, Kogălniceanu 1, 400084 Cluj-Napoca, Romania*
[2]*Institut für Physikalische Chemie, Universität Würzburg, Am Hubland, D-97074 Würzburg, Germany*
[3]*Institut für Physikalische Chemie, Universität Jena, Helmholtzweg 4, 07743 Jena, Germany*

FT-Raman and NIR-SERS characterization of the antimalarial drugs chloroquine and mefloquine and their interaction with hematin

S. Cîntă Pînzaru[1], N. Peica[2], B. Küstner[2], S. Schlücker[2], M. Schmitt[3], T. Frosch[3], J. H. Faber[4], G. Bringmann[4], and J. Popp[3]
[1]*Physics Department, Babeş-Bolyai University, Kogălniceanu 1, 400084 Cluj-Napoca, Romania*
[2]*Institut für Physikalische Chemie, Universität Würzburg, Am Hubland, D-97074 Würzburg, Germany*
[3]*Institut für Physikalische Chemie, Universität Jena, Helmholtzweg 4, 07743 Jena, Germany*
[4]*Institut für Organische Chemie, Universität Würzburg, Am Hubland, D-97074 Würzburg, Germany*

Surface-enhanced Raman spectroscopy employed in antimalarial mechanism of chloroquine drug upon hematin

S. Cîntă Pînzaru[1], N. Peica[2]; B. Kustner[2], S. Schlücker[2], M. Schmitt[3], T. Frosch[3], J. Popp[3], W. Kiefer[2]

[1]*Physics Department, Babeş-Bolyai University, Kogălniceanu 1, 400084 Cluj-Napoca, Romania*
[2]*Institut für Physikalische Chemie, Universität Würzburg, Am Hubland, D-97074 Würzburg, Germany*
[3]*Institut für Physikalische Chemie, Universität Jena, Helmholtzweg 4, 07743 Jena, Germany*

**Raman and SERS spectroscopy monitoring the interaction mechanism of
quinoline-derived antimalarial drugs with hematin**

S. Cîntă[1], N. Peica[2], B. Küstner[2], S. Schlücker[2], M. Schmitt[3], T. Frosch[3], J. Popp[3], W. Kiefer[2]

[1]*Molecular Spectroscopy Department, Babes-Bolyai University, Kogălniceanu 1, RO-400084 Cluj-Napoca, Romania*
[2]*Institut für Physikalische Chemie, Universität Würzburg, Am Hubland, D-97074 Würzburg, Germany*
[3]*Institut für Physikalische Chemie, Universität Jena, Helmholtzweg 4, D-07743 Jena, Germany*

**Vibrational characterization of E102 food additive by Raman, surface-enhanced Raman
spectroscopy, and theoretical studies**

N. Peica[1], I. Pavel[1,2], S. Cîntă Pînzaru[3], V. K. Rastogi[4], and W. Kiefer[1]

[1]*Institut für Physikalische Chemie, Universität Würzburg, Am Hubland, D-97074 Würzburg, Germany*
[2]*Department of Chemistry and Biochemistry, University of California at Santa Barbara, Santa Barbara, CA 93106-9510, USA*
[3]*Physics Department, Babeş-Bolyai University, Kogălniceanu 1, 400084 Cluj-Napoca, Romania*
[4]*Physics Department, CCS University, 250004 Meerut, India*

**Concentration dependent wavenumber shifts and linewidth changes of some prominent vibrational
modes of C_4H_8O investigated in a binary system (C_4H_8O + H_2O) by polarized Raman study and ab-initio calculations**

Animesh K. Ojha[a], Sunil K. Srivastava[a], N. Peica[b], S. Schlücker[b], W. Kiefer, B. P. Asthana[a]

[a]*Laser and Spectroscopy Laboratory, Department of Physics, Banaras Hindu University, Varanasi 221005, India*
[b]*Institut für Physikalische Chemie, Universität Würzburg, Am Hubland, D-97074 Würzburg, Germany*

**Buffered *versus* Unbuffered Aspirin Species Monitored by Raman and
Surface-Enhanced Raman Spectroscopy**

N. Peica[1], L. M. Andronie[2], S. Cîntă-Pînzaru[2], and W. Kiefer[1]

[1]*Institut für Physikalische Chemie, Universität Würzburg, Am Hubland, D-97074 Würzburg, Germany*
[2]*Babeş-Bolyai University, Physics Department, Kogălniceanu 1, 400084 Cluj-Napoca, Romania*

Concentration dependence Raman and SERS spectra of E 102 Food Additive

S. Cînta-Pînzaru[1], I. Pavel[2], N. Peica[2], N. Leopold[2]

[1]*Babeş-Bolyai University, Physics Department, Kogălniceanu 1, 400084 Cluj-Napoca, Romania*
[2]*Bayerische Julius-Maximilians Universität, Institut für Physikalische Chemie, Am Hubland, D-97074 Würzburg, Germany*

Studia Universitatis Babeş-Bolyai, Physica, 2, Special Issue, (2003) 504-506

Food additives study: vibrational approach

S. Cîntă-Pînzaru[1], N. Peica[2], I. Pavel[2], W. Kiefer[2]

[1]*Babeş-Bolyai University, Physics Department, Kogălniceanu 1, 400084 Cluj-Napoca, Romania*
[2]*Bayerische Julius-Maximilians Universität, Institut für Physikalische Chemie, Am Hubland, D-97074 Würzburg, Germany*

Journal of Optoelectronic and Advanced Materials, *submitted*

Raman and surface-enhanced Raman studies of the food additive sodium benzoate

N. Peica[1], C. Lehene[2], N. Leopold[2], O. Cozar[2], W. Kiefer[1]

[1]*Institut für Physikalische Chemie, Universität Würzburg, Am Hubland, D-97074 Würzburg, Germany*
[2]*Faculty of Physics, Babeş-Bolyai University, Kogălniceanu 1, 400084 Cluj-Napoca, Romania*

Polyhedron, *submitted*

**Binding mode of orotic acid, theoretical and spectroscopic studies
of its new lanthanum (III) complex**

I. Kostova[a], N. Peica[b], W. Kiefer[b]

[a]*Department of Chemistry, Faculty of Pharmacy, Medical University, 2 Dunav St., Sofia 1000, Bulgaria*
[b]*Institut für Physikalische Chemie, Universität Würzburg, Am Hubland, D-97074 Würzburg, Germany*

Journal of Physical Chemistry A, *submitted*

Orotic acid-DFT and vibrational

I. Kostova[a], N. Peica[b], W. Kiefer[b]

[a]*Department of Chemistry, Faculty of Pharmacy, Medical University, 2 Dunav St., Sofia 1000, Bulgaria*
[b]*Institut für Physikalische Chemie, Universität Würzburg, Am Hubland, D-97074 Würzburg, Germany*

Erklärung

Hiermit erkläre ich an Eides statt, dass ich die Dissertation

„Vibrational Spectroscopy and density functional theory calculations on biological molecules"

selbständig angefertigt und keine anderen als die von mir angegebenen Quellen und Hilfsmittel benutzt habe.

Ich erkläre außerdem, dass diese Dissertation weder in gleicher oder anderer Form bereits in einem Prüfungsverfahren vorgelegen hat.

Ich habe früher außer den mit dem Zulassungsgesuch urkundlich vorgelegten Graden keine weiteren akademischen Grade erworben oder zu erwerben versucht.

Würzburg, den 9. November 2006

....
(Niculina Peica)